Constraining the physicochemical conditions of star-forming gas : high angular resolution observations of the B335 Class 0 protostar

Victoria Cabedo Soto

To cite this version:

Victoria Cabedo Soto. Constraining the physicochemical conditions of star-forming gas : high angular resolution observations of the B335 Class 0 protostar. Other. Université Paris Cité, 2021. English. NNT : 2021UNIP7057 . tel-03610017

HAL Id: tel-03610017
https://theses.hal.science/tel-03610017

Submitted on 16 Mar 2022

HAL is a multi-disciplinary open access archive for the deposit and dissemination of scientific research documents, whether they are published or not. The documents may come from teaching and research institutions in France or abroad, or from public or private research centers.

L'archive ouverte pluridisciplinaire **HAL**, est destinée au dépôt et à la diffusion de documents scientifiques de niveau recherche, publiés ou non, émanant des établissements d'enseignement et de recherche français ou étrangers, des laboratoires publics ou privés.

Université de Paris
École doctorale 127: Astronomie Astrophysique
Laboratoire de Formation des Etoiles et du Milieu Interstellaire (LFEMI)

Constraining the physicochemical conditions of star-forming gas

High angular resolution observations of the B335 Class 0 protostar

VICTORIA CABEDO SOTO

THÈSE DE DOCTORAT D'ASTROPHYSIQUE

Dirigée par **Anaëlle J. Maury** & **Josep Miquel Girart**

Présentée et soutenue publiquement le 17 décembre 2021

Devant un jury composé de :

Sylvain Chaty	Professeur, Université de Paris	Président du Jury
Eva Wirström	Associate Proffesor, CUT	Rapporteur
Francesco Fontani	Astronomer, INAF	Rapporteur
José María Torrelles	Research Professor, ICE	Examinateur
Anaëlle J. Maury	Ingénieur-chercheur, CEA	Directrice de thèse
Josep Miquel Girart	Equivalent Professor, ICE	Co-directeur de thèse

Except where otherwise noted, this is work licensed under
https://creativecommons.org/licenses/by-nc-nd/3.0/fr/

She stretched herself up on tiptoe, and peeped over the edge of the mushroom, and her eyes immediately met those of a large blue caterpillar, that was sitting on the top, with its arms folded, quietly smoking a long hookah, and taking not the smallest notice of her or of anything else.
- **Alice in Wonderland**, Lewis Carrol (1865)

Abstract

The process of star formation is well known in a general aspect, however, a lot of details are still missing. Some questions, such as the mode and efficiency of the accretion process or the role of the magnetic field, are still open and are key to completely understand star formation. The aim of this work is to put constraints on some of the physical and chemical processes happening in a young star forming core during the first stages of the collapse. For this purpose, we obtained high angular resolution observations of the Class 0 protostellar object B335. This object, which is an isolated Bok Globule, is very well known as it is an excellent source to test theories of gravitational collapse during the low-mass star formation process. It has also been suggested as a good example of magnetically regulated collapse, as it presents a strongly pinched magnetic field morphology. Within the project, we obtained dust continuum and several molecular lines emission, probing scales from the envelope, around 4000 au, to the most inner part, at around 150 au, with the ALMA interferometer. Our data set has proven to be very heterogeneous in nature as well as to present complex gas kinematics, observed in complex molecular line profiles. Within our observations of rare isotpologues from CO, we observed double-peaked line profiles which could not be attributed to optically thin lines, as expected from the abundance of those molecules. We also studied the morphology of the line profiles at different offsets of the source, and found that they were not in agreement with the expected models of symmetric spherical collapse. We use these facts to study the infall modes on the source and modeled the line profiles to obtain the main parameters, such as the peak velocity, the velocity dispersion and the opacity. From this analysis we found that the observed emission was optically thin, and that each component of the double-peaked line profile had a linewidth typical from infall motions. Thus, we proposed that the two peaks were coming from two different gas reservoirs with different kinematics, i.e., the collapse is not symmetric and it is occurring along the exterior of the cavity walls. Since the double-peaked profiles appeared in other CO derivatives, such as HCO+ and DCO+, we kept this hypothesis of the two distinct velocity components to proceed with the derivation of the deuteration and the ionization fraction. Our values of the ionization fraction show that B335 lies in the upper range of the values computed from the literature for protostellar objects. Since we resolve the maps of the ionization fraction, we can see different tendencies that point to different ionization processes, i.e., ionization due to Cosmic Rays, probably enhanced due to the isolation of the object and the presence of an organized magnetic field, and ionization due to accretion radiation close to the protostar. We also compare the distribution of the ionization with the polarized dust emission, which is indicative of the morphology of the magnetic field. A good correlation is observed, where the largest values of the ionization fraction are correlated with the polarized continuum intensity. We also attempted for the first time to compute the effect of ambipolar diffusion in a Class 0 object, i.e., difference in the kinematics of neutral and ionic molecules. We were able to observe that both type of molecules present different ranges of the velocity dispersion, which suggests that the ions are coupled to the magnetic field. In summary, a better view of the interplay between the gas and the magnetic field is obtained, suggesting a good coupling of the two and pointing to the fact that collapse in B335 is strongly magnetically regulated.

Keywords: *Star formation; protostars; interferometry; deuteration; ionization; magnetic field*

Résumé

Le processus de formation des étoiles est bien connu dans ses grand lignes, cependant, beaucoup de détails manquent encore. Certaines questions, telles que le mode et l'efficacité du processus d'accrétion ou le rôle du champ magnétique, restent ouvertes et sont essentielles pour bien comprendre le processus de formation des étoiles. Le but de ce travail est de poser des contraintes sur certains des processus physiques et chimiques qui se produisent dans un jeune coeur protostellaire pendant les premières étapes de l'effondrement. Pur cela, nous avons obtenu des observations à haute résolution angulaire de la proto-ètoile de Classe 0 B335. Cet objet, qui est un globule isolé, est très connu car c'est une excellente source pour tester les théories de l'effondrement gravitationnel au cours du processus de formation des étoiles de faible masse. C'est aussi un objet prototypique car considéré comme un bon exemple d'effondrement régulé magnétiquement, car il présente une morphologie de champ magnétique sous forme de sablier, évocateur d'un champ fort étiré paru un potentiel gravitationel. Dans le cadre du projet, nous avons obtenu des observations de l'émission thermique du continuum de poussière et plusieurs raies moléculaires, en sondant des échelles de l'enveloppe, autour de 4000 au, jusqu'à la partie la plus interne, à environ 150 au, en utilisant l'interféromètre ALMA. Notre ensemble de données s'est avéré être de nature très hétérogène et présenter une cinématique du gaz structurée, se traduisant par des profiles complexes de raies moléculaires. Dans nos observations d'isotpologues rares du CO, nous avons observé des profils de raies à double pic qui ne pouvaient pas être attribués à des raies optiquement minces, conformément a ala faible abondance de ces molécules. Nous avons également étudié la morphologie des profils de raies à différents échelles de l'enveloppe et avons constaté qu'ils n'étaient pas en accord avec les modèles attendus d'effondrement en symétrie sphérique. Nous utilisons ces observations pour étudier la dynamique de l'effondrement sur la source et modéliser les profils de raies moléculaires pour obtenir les principaux paramètres, tels que la vitesse, la dispersion de vitesse et l'opacité. À partir de cela, nous avons constaté que l'émission observée était optiquement mince et que chaque composante du profil de raies à double pic avait une largeur de raie typique des vitesses d'effondrement. Cela nous a conduit à proposer que les deux pics provenaient de deux réservoirs de gaz différents avec une cinématique différente, c'est-à-dire que nous proposons que l'effondrement n'est pas symétrique et qu'il se produit le long de l'extérieur des parois de la cavité. Puisque les profils à double pic sont apparus dans d'autres dérivés du CO, tels que HCO+ et DCO+, nous avons gardé cette hypothèse des deux composantes de vitesse distinctes pour procéder à la dérivation de la deutération et de la fraction d'ionisation. Nos valeurs de la fraction d'ionisation montrent que B335 se situe dans la plage supérieure des valeurs observées dans la littérature pour les objets protostellaires. Grâce a nos cartes de la fraction d'ionisation, nous pouvons voir différentes tendances qui indiquent différents processus d'ionisation, c'est-à-dire l'ionisation due aux rayons cosmiques, probablement renforcée en raison de l'isolement de l'objet et de la présence d'un champ magnétique organisé, et l'ionisation due à la luminosité d'accrétion à proximité de la protoétoile. Nous comparons également la distribution de l'ionisation avec l'émission polarisée de poussière, ce qui est révélateur de la morphologie du champ magnétique. Une bonne corrélation est observée, où les plus grandes valeurs de la fraction d'ionisation sont corrélées avec l'intensité du continuum polarisé. Nous avons également tenté pour la première fois de calculer l'effet de la diffusion ambipolaire dans un objet de

Classe 0, c'est-à-dire la différence dans la cinématique des molécules neutres et ioniques. Nous avons pu observer que les deux types de molécules présentent des plages de dispersion de vitesse différentes, ce qui suggère que les ions sont couplés au champ magnétique. En résumé, une meilleure vision de l'interaction entre le gaz et le champ magnétique est obtenue, suggérant un bon couplage des deux et indiquant que l'effondrement dans B335 est fortement régulé magnétiquement.

Mots clés: *Formation stellaire; protoetoiles; interferometrie; effondrement stellaire; deuteration; ionisation; champ magnetique*

Contents

Acknowledgements

I believe that these acknowledgments should not only go to the people that has helped me during these three last years, the ones who supported me and the ones who guided me, but they should also be addressed to everyone that has accompanied me through my life, one way or another. So it is going to go like this:

To everyone who has believed in me. To the ones that stood through all the ups and downs that my path has taken me through. I hope I have make it good enough for them to know who they are. If not, I promise I will try to do better in the future. I could not have done it without you and I love you all.

To everyone who did not think I was good enough to make it here. Thank you because your doubt has been my strength. I hope that I have make it clear enough for them to know who they are as well. If not, I promise I will try to do better in the future. I could neither have done it without them.

A la meva mare,
l'única que sempre, sempre, ha estat al meu costat.
Sense importar quan, on o per què.
Això és per a tu,
perquè és gràcies a tu.
T'estimo més del què mai podré demostrar-te.

Chapter 1

Introduction

Stars have been an inextinguishable source of curiosity for humans since the first time we raised our heads up to look at the sky. Thousands of years of study allowed us not only to determine the position and movement of these little shiny dots, but also to understand what they are made of, how they evolve, how they tell us the story of the evolution of the universe and, last but not least, they give us a reference on the point of space and time we exist in. More technically speaking, the process by which stars form and evolve can tell us a lot about our universe. First, most of the elements that compose our universe are made in stars, particularly those required for the formation of life, such as Oxygen (O) and Carbon (C). It is when a star dies that those elements are spread into the neighboring area making them available to react and produce more complex chemistry. Second, the formation of planets is inevitably linked to the formation of stars, and therefore the study of Young Stellar Objects (YSOs) allows to construct the story of the planets that we see around most stars. Third, the star formation process is the responsible for the consumption and transformation of the gas content of a galaxy. Therefore, it also helps to unveil the evolution of matter in the universe.

This process raises many questions that cover all the scales at which it occurs and which are one of the main topics of modern astrophysics: Where do stars form and why they form there? Which is the chemical and physical influence of the environment of star forming regions (SFRs) in the outcome of the process? How do the collapse of gas clouds proceeds to form a star? Which are the characteristics of every SFR and why are they different among them? What is the exact influence of these processes in the formation of planets? And, as important as all of them, which is the best way to observe each of these processes? Since it is obviously impossible to find all the answers to these questions in one study, this work is centered in the initial phases of the star formation process and how to characterize some of its physical and chemical properties. In this chapter, a general description of the low-mass star formation process is given, with particular emphasis in the Class 0 protostellar phase and some of the problems that remain unsolved. A short review of the influence of magnetic fields in the process is also provided. Finally, a brief introduction to the object studied in this work, B335, is also given along with the framework and objectives of this thesis.

1.1 The low-mass star formation process

Generally speaking, stars form in clouds which are made of cold molecular gas and that inhabit the interstellar medium (ISM). These clouds are usually fragmented and present over-densities called clumps or dense cores, produced by mechanical processes such as gravity or compression. When these dense cores are perturbed or their mass is large enough they will undergo gravitational collapse, accreting most of their mass into a central object, which will become the future star, and a surrounding accretion disk, that might eventually give birth to a planetary system (Fig. 1.1). The first models of star formation appeared in the 60's (Larson 1969, Penston 1969) and were followed by many studies which tried to apply the models to observations (Shu 1977, Shu et al. 1987, Shu and Adams 1987), until the first protostars were found and the model could be constrained observationally (Lada 1987, André et al. 1993).

1.1.1 Molecular Clouds

Stars are mainly formed in molecular clouds, which are basically accumulations of gas on particular regions of the ISM (Blitz 1993, Bok 1948). They are big (1$\sim$15 pc) and cold enough

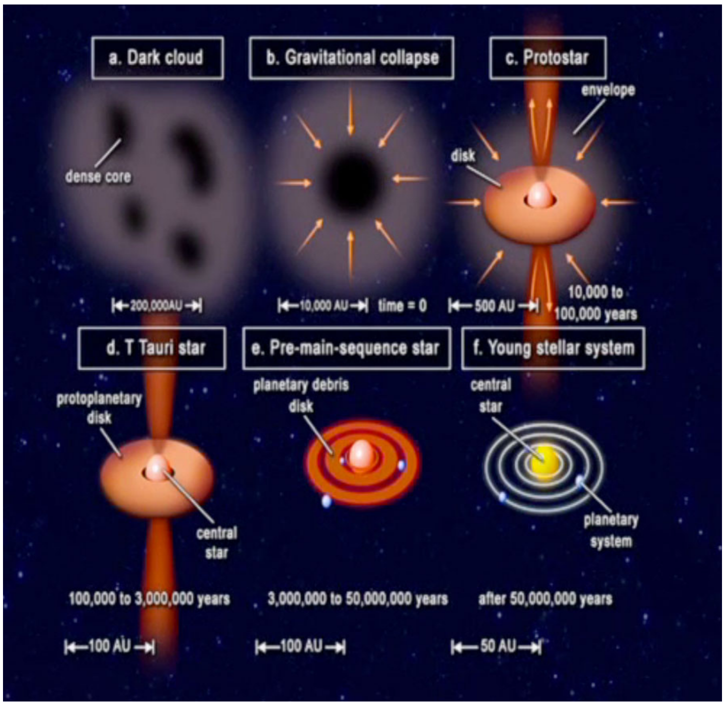

Figure 1.1: Schematic representation of the star formation process. Credit: PUC, Chile.

(10∼30 K) as to present the majority of the gas in molecular form, mainly molecular hydrogen (H_2, ∼63 %). The rest of the mass is mostly Helium (He, ∼36 %) and other simple molecules (∼1 %) such as CO (van Dishoeck and Black 1988, van Dishoeck et al. 1993). Molecular clouds also contain dust grains, which are little solid particles, composed mainly of silicates and carbonates, and which diameter varies from nanometers to a few tenths of micrometers (Mathis 1979, Draine and Lee 1984, Draine 2003). The presence of this dust makes molecular clouds opaque to radiation at short wavelengths (Draine 2003) and, therefore, they can not be observed at optical wavelengths, appearing as dark patches in the sky. Molecular clouds are, therefore, only observable at longer wavelengths: at infrared (IR) wavelengths, we observe the thermal emission from the dust; in the millimeter and submillimeter regime, the de-excitation of rotational transitions of molecules can be detected.

Depending on their size, mass and the type of star formation they present, molecular clouds can be classified in three different types (Mac Low 2004). The largest and more massive ones are Giant Molecular Clouds (GMC, left panel of Fig. 1.2). They extend for tens of parsecs and have masses from 10^4 up to 10^6 $M_{\odot}$. These giant clouds are the birth place of associations of massive stars (stars with mass >8 $M_{\odot}$). Smaller clouds can also be found, and are called simply Molecular Clouds (MC). They extend for a couple of parsecs and have lower masses ($10^2 \sim 10^4$ $M_{\odot}$). They generally form clusters of low-mass stars (stars with mass <8 $M_{\odot}$). Both have similar mean volume densities (∼ 50-500 cm^{-3}) and temperatures between 10 and 20 K (Bergin and Tafalla 2007). Finally, stars can also form in isolated cores, the so-called Bok Globules (Bok 1948, right panel of Fig. 1.2) which are smaller and less massive clumps that are not associated to a large-scale complex. They have typical sizes of less than a parsec and masses of the order of 10 $M_{\odot}$ or less (Clemens et al. 1991, Bergin and Tafalla 2007). Contrary to the other two types, they do not form associations of stars, forming only one or two objects in their interior.

Figure 1.2: *Left*: False color image of the Orion Nebulae as an example of GMC, observed with ESO Paranal Observatory in Chile using Z, J and K filters (credit: ESO/J. Emerson/VISTA). *Right*: NGC281/IC1590 as an example of Bok Globule (credit: NASA/ESA and the Hubble Heritage team).

Molecular clouds are stable against their own gravitational collapse, and can live for some tenths of Myr (see reviews by Bergin and Tafalla 2007 and Dobbs et al. 2014). The gravitational force produced by their mass is counteracted by different forces that include turbulence, thermal pressure, centrifugal forces or the magnetic field. However, perturbations of their structure caused by external forces, such as collisions or shock waves, can create over-densities called dense cores that are prone to gravitational collapse, and where stars will actually be formed.

1.1.2 Dense cores and the Pre-stellar phase

Dense cores are over-densities present in molecular clouds (about 10^2 to 10^4 times the density of the parent cloud) formed by fragmentation of the latter (Bergin and Tafalla 2007). These dense structures can or can not be gravitationally bound. If they are gravitationally bound (i.e., the gravitational energy of the system is more important than its kinetic energy) they are called pre-stellar cores. Pre-stellar cores are simple objects where star formation is expected to occur (Fig. 1.3). They usually appear in elongated shapes (Myers et al. 1991, Kauffmann et al. 2008), which indicates that they are not completely hydrostatic objects supported by isotropic pressure. Moreover, they are not completely homogeneous, as their density has been found to increase with radius with a factor of $\rho \propto r^{-2}$, which flattens towards the center at radii smaller than 2500-5000 au (André et al. 1996, Ward-Thompson et al. 1999). The whole cores are small, and have typical sizes of ~0.1 pc and masses from 0.1 to 10 $M_\odot$ (Bergin and Tafalla 2007). They are relatively long-lived, and can last up to 1 Myr. Since they are the first step of the star formation process, and because they are relatively simple objects with low and almost constant temperatures, they are ideal places to test the initial conditions of star formation models (Tafalla 2005).

Pre-stellar objects are key to study chemical evolution during the process of star formation. Their initial chemical composition is mostly inherited from the clouds where they formed. As the collapse proceeds, the larger densities ($n_{H_2} > 10^{-5}$ cm^{-3}) and smaller temperatures (T~10 K) found at the center will rapidly deplete neutral species (i.e., CO and N$_2$) from the gas phase and onto the dust grains. Since neutral species are major destroyers of molecular ions and deuterated molecules (Rawlings et al. 1992, Caselli et al. 1998, see Sec. 1.4.6 of this work), selective freeze-out will lead to chemical inhomogeneities, affecting properties of the gas such as the deuteration and ionization fraction (Bergin and Tafalla 2007) with respect to the parent cloud.

For the process of star formation to start, the dense core needs to become gravitationally unstable and start collapsing. There are various mechanisms by which this process can occur and which are similar to the ones for the formation of the dense cores themselves. First, and most straight forward, the core might become too massive and the mechanisms that stabilized it (thermal pressure, centrifugal forces or magnetic fields) can not longer counter balance gravity (e.g., "inside-out collapse", Shu et al. 1987). A system will become unstable when its gravitational energy is larger than its kinetic energy, i.e., E$_g$ > -2E$_k$. The mass at which this occurs is given by the Jeans mass:

$$M_J = \left(\frac{5k_bT}{G\mu m_H}\right)^{3/2}\left(\frac{3}{4\pi\rho}\right)^{1/2} \tag{1.1}$$

where k_b is the Boltzmann constant, T is the temperature of the gas, G is the gravitational constant, μ is the reduced mass of a gas molecule, m_H is the hydrogen mass and ρ is the density of the gas. Secondly, the system can be perturbed by a nearby event that compresses the core triggering its collapse, such as an exploding nearby supernova producing a shock-wave (Opik 1953, Hennebelle 2003). Additionally, diffusion processes, such as ambipolar diffusion, or dissipation of turbulence can also trigger the collapse (Nakano 1998).

At the beginning of the collapse, it is quasi-isothermal since the energy produced by the collapsing gas can be effectively absorbed and re-emitted by the dust in the form of thermal radiation. When the gas reaches a density large enough, close to ~10^{10} cm^{-3}, it becomes opaque to accretion radiation and the collapse becomes adiabatic. Temperature then rises and thermal pressure starts counter acting gravity reaching a quasi-hydrostatic equilibrium. The first hydro-static core (FHSC) is formed (Larson 1969). The first object has a radius of a few au, masses of approximately 0.01-0.1 $M_\odot$ and temperatures of 100 to 2000 K. At this time, the protostellar object has been formed and the pre-stellar phase ends.

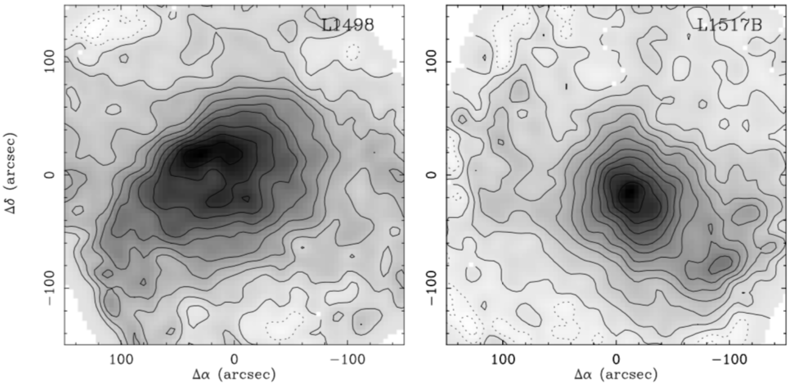

Figure 1.3: 1.2 mm continuum maps of the pre-stellar cores L1498 (left) and L1517B (right). The beam size is 11″ and contours are spaced every 2 mJy/beam. From Tafalla 2005.

1.1.3 Evolutionary stages of protostellar objects

The central object will continue accreting matter until the star gains most of its final mass. The remaining matter will continue to be accreted into larger objects and processed to finally form a new protoplanetary system. The different stages of protostellar evolution are separated in four different Classes, with two main accretion phases (0 and I) and the pre-main sequence phases (II and III). The four stages are briefly described in this section with a final description of the classification methods and two of the main problems that the models of star formation present: the angular momentum problem and the luminosity problem. In Section 1.4 the Class 0 stage, which is of foremost importance for this work, will be described with more details.

Class 0 phase

After the FHSC is formed, matter will still be accreted in the center and density and temperature of the object will keep increasing. When the central temperature reaches ∼2000 K, molecular hydrogen starts to dissociate in an endothermic reaction. Temperature decreases and thermal pressure is no longer able to support gravity, triggering a second collapse in a small region at the center of the FHSC. This leads to the formation of the second hydrostatic core (Larson 1969). The central object has a radius of a few solar radii and a mass of about 0.001-0.1 $M_\odot$. Since the FHSC are short-lived (10^3 - 10^4) the beginning of the protostellar phase is hard to pinpoint, the consensus is to use the appearance of the stellar embryo as $t = 0$ and the end of the pre-stellar phase.

During the Class 0 stage (André et al. 1993, André et al. 2000) most of the mass of the system is still contained in the envelope ($M_{env} >> M_*$) and it will keep being accreted onto the central object. Since the original molecular cloud, and hence the dense core, will have a non-zero angular momentum, conservation of this during the collapse might lead to the formation of a disk around the protostellar object (Terebey et al. 1984). From conservation of angular momentum, and with the influence of magnetic fields, bipolar outflows will develop, which will also help processing infallen material in the disk and will sweep away the surrounding envelope. This phase lasts for about 50.000 years, and it will be finished when the central protostar has obtained most of its final mass.

Class I phase

At this point, the central star has accumulated around 90 % of its final mass which will be similar to the remaining mass on the envelope. The matter that has not been accreted in the central object has been swept away by stellar winds and outflows. The protostar is mostly left with a disk of size between $\sim$ 10 and 100 au and a diffuse envelope with size of $\sim 10^4$ au and masses from $\sim$ 0.1 to 0.3 $M_\odot$.

During this phase, stellar winds and outflows will remove the rest of the envelope, until all the matter has been accreted or dispersed. In total, the accretion phase (Class 0 + Class I) will last a time of the order of the free-fall time:

$$t_{ff} = \sqrt{\frac{3\pi}{32G\rho}} \tag{1.2}$$

where typically $\rho \approx 10^{-7}$ g cm^{-3}. Estimations of the lifetime of the protostellar phase, derived from observations of Class 0 and I objects, give an estimated total lifetime of 0.5 Myr, where the lifetime of the Class 0 and I are 0.1 and 0.4 Myr, respectively (Evans et al. 2009).

Class II phase

After the main accretion phase (about 0.5 Myr after the collapse started), the object is not considered a protostar anymore but a young star or a YSO. Most of the envelope has disappeared and the young star is only surrounded by a rotationally supported and optically thick disk of a size $\sim$10 - 150 au and mass of 0.005-0.14 $M_\odot$ (André and Montmerle 1994, Andrews et al. 2009), what is called a T-Tauri star. The very diffuse envelope that remains will still be accreted, but the accretion rate will be around 10 times smaller than during the main accretion phase. The total lifetime of this phase has been estimated to be $\sim$2 Myr (Evans et al. 2009).

It is during this phase that the dust forming the disk will start to accrete and coagulate to form bigger objects (Carrera et al. 2017), such as asteroids, comets and planetesimals, although this vision is being questioned, pointing to a much earlier appearance of protoplanets (Booth and Clarke 2016, Nixon and Pringle 2019). Substructures are ubiquitously observed in disks (e.g., Andrews et al. 2018), the most common being bright rings, dark gaps and, in some cases, spiral structures (Fig. 1.4). Those substructures have two possible origins: they can be formed by dust trapped in axisymmetric gas pressure bumps which can trigger planet formation, but they can also form by the interaction of already formed protoplanets with the local material. If the second explanation is true, it implies that dust grains have already started to grow in previous phases and that protoplanetary objects might start forming very early in the star formation process.

Class III phase

After around 10 Myr, most of the material in the disk has been accreted and has been processed to finally form planets, becoming optically thin. Since the star has not reached radiative equilibrium, thermal pressure can not sustain the star against its own gravity, which will start a final collapse. The characteristic time for this contraction is the Kelvin-Helmholtz time:

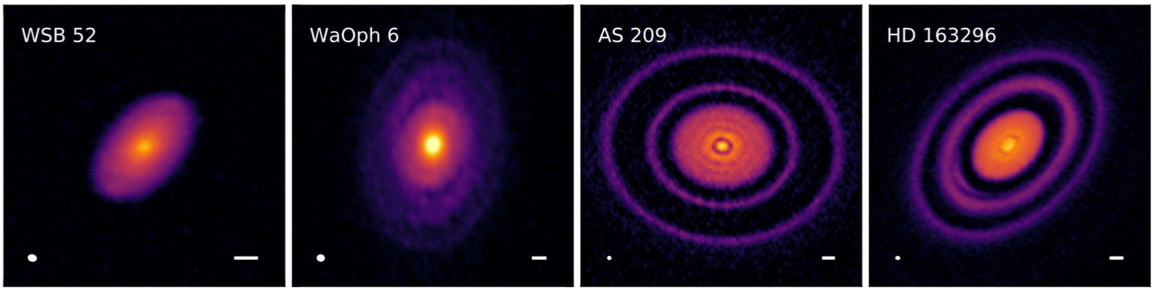

Figure 1.4: 1.25 mm continuum emission images for a subsample of disks in the DSHARP project. Beam sizes and 10 au scale bars are shown in the lower left and right corners of each panel. Obtained from Andrews et al. 2018.

$$t_{KH} = \frac{GM_*^2}{R_* L_*} \tag{1.3}$$

where M_*, R_* and L_* are the mass, the radius and the luminosity of the young star respectively. For low-mass stars, this time is of about 10^8 yr and much larger than the time of the accretion phase, while for high-mass stars this time is much smaller and the star will enter the main sequence before it has finished accreting all its mass.

The energy from this contraction will be used in increasing the central temperature of the star. When the temperature becomes high enough ($>10^7$ K) nuclear reactions will be ignited in the center of the object transforming hydrogen into helium. At this point the star enters the main sequence and becomes formally an adult star. Since all the material in the disk has accreted into larger objects, a new planetary system has been formed.

Methods of classification

When the envelope of the protostar is still present, the radiation coming from the stellar object is absorbed by the dust and re-emitted at longer wavelengths. During the Class 0 phase, most of the stellar radiation is re-emitted in the far-infrared and millimeter regime, and the spectral energy distribution (SED) corresponds to a black-body emitting at a very low temperature. As the object evolves to Class I, radiation is re-emitted in IR regime, until this emission disappears as the envelope dissipates for more evolved objects (see Fig. 1.5, Hughes et al. 2018). The different protostellar Classes are distinguished by their IR excess on the SED of the objects with respect to the radiation produced purely by a black-body (Lada 1987). The SED can be modeled as gray-body function of the form:

$$S_\lambda = B_\lambda(T_{dust})\,[1 - \exp(-\tau_\lambda)]\,\Delta\Omega \tag{1.4}$$

where S_λ is the flux density at a wavelength λ, $B_\lambda(T_{dust})$ is the Planck function for a dust temperature T_{dust}, τ_λ is the dust optical depth, and $\Delta\Omega$ is the source solid angle. The IR spectral index can be then defined as:

$$\alpha = \frac{d\log(\lambda S_\lambda)}{d\log\lambda} \tag{1.5}$$

The classification of the different evolutionary stages is as follows:

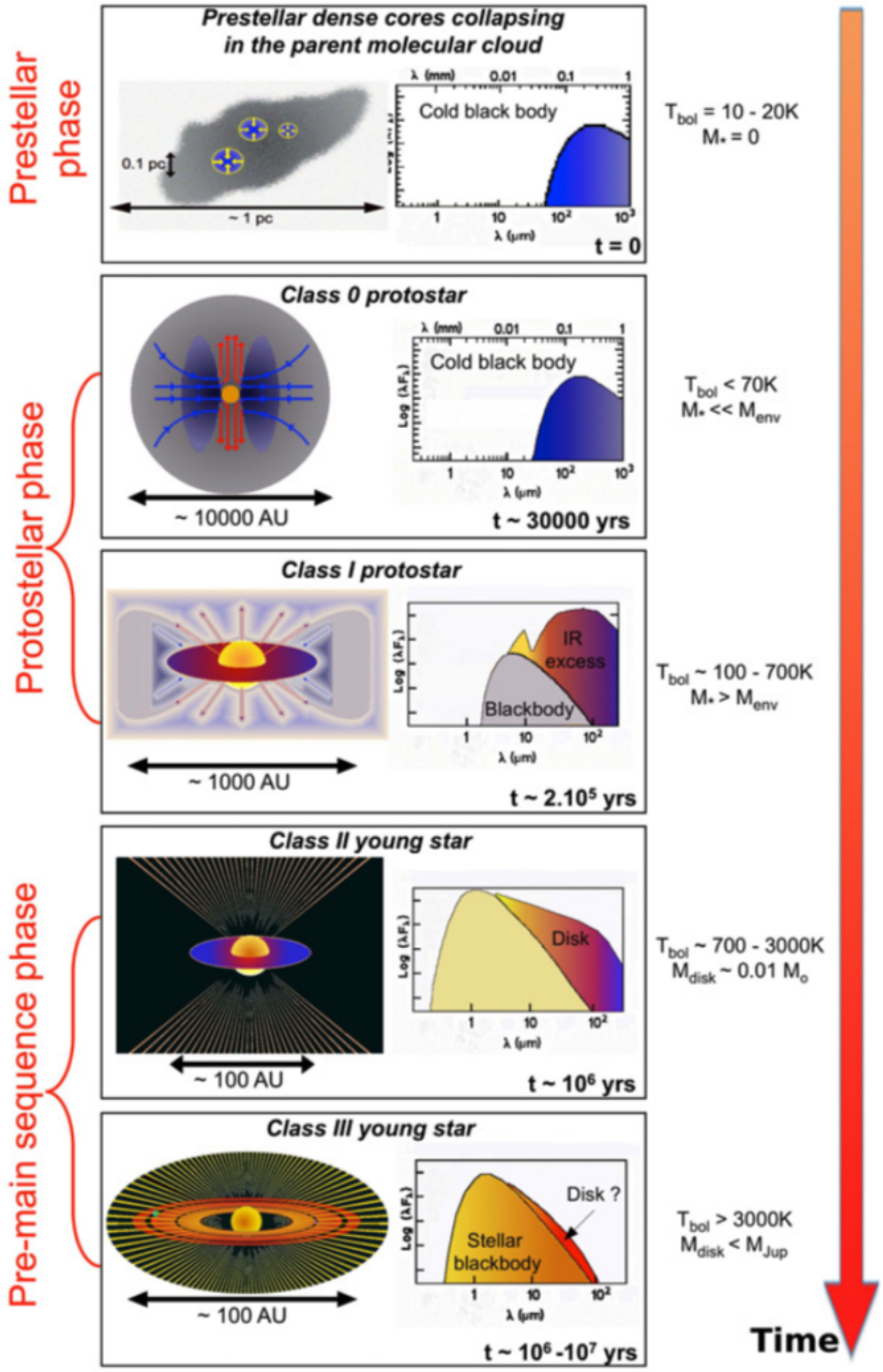

Figure 1.5: Empirical evolutionary sequence proposed to characterize the formation process of low-mass stars, showing the evolution of the SED, the envelope and the disk with time. Taken from Maury et al. 2011, proposed and adapted from André et al. 2000 and André 2002.

- Class I: $\alpha \geq 0.3$
- Flat-SED: $-0.3 \leq \alpha < 0.3$
- Class II: $-1.6 \leq \alpha < -0.3$
- Class III: $\alpha < -1.6$

Another form of classification of the different classes is done by the bolometric temperature, which corresponds to the effective temperature of a blackbody with the same flux-weighted mean frequency as the observed SED (Myers and Ladd 1993). T_{bol} begins at 20 K for deeply embedded protostars and eventually increases to the effective temperature of a low-mass star once all the surrounding envelope and disk material has dissipated (Launhardt et al. 2013, Dunham et al. 2014). The classification is as follows:

- Class 0: $T_{bol} < 70$ K
- Class I: 70 K $\leq T_{bol} \leq$ 650 K
- Class II: 650 K $\leq T_{bol} \leq$ 2800 K
- Class III: $T_{bol} >$ 2800 K

However, T_{bol} is a poor discriminator between different classes (Evans et al. 2009) since it is largely dependent on the inclination and geometry of the source, increasing by hundreds of K and crossing at least one class boundary (Young et al. 2003, Jørgensen et al. 2009 Fischer et al. 2013, Launhardt et al. 2013).

A more useful classification to distinguish between Class 0 and I objects is the ratio of sub-millimeter luminosity, L_{smm}, to the bolometric luminosity, L_{bol} (L_{smm}/L_{bol}), which is a better tracer of the underlying physical stage of a source (Young et al. 2003, Dunham et al. 2010, Launhardt et al. 2013). Figure 1.6 shows the comparison of the classification according to L_{smm}/L_{bol} and T_{bol} for protostars from different surveys. Protostars generally evolve from the upper right to the lower left. However, it should be noticed that the monotonic evolution breaks down if the accretion onto the protostar is episodic. This illustrates that a different number of Class 0 and Class I protostars will be found depending on the classification used.

1.1.4 Problems of the star formation models

The angular momentum problem

All structures in our universe have been found to be rotating (Spitzer and Arny 1978): From galaxies to individual stars and, of course, protostellar objects, such as Class 0 objects. Therefore, all of these objects possess a specific angular momentum, given by $j = \Omega R^2$, where j is the specific angular momentum, Ω is the angular velocity and R is the radii. By conservation of angular momentum, this implies that the gas forming a dense core of radius of about 0.1 pc ($\sim 3\times10^{13}$ km) which will collapse to a solar-type star of around 1 $R_\odot$ ($\sim 7\times10^{5}$ km) would have to increase its angular velocity as the collapse proceeds. If we take the observed typical angular momentum for dense cores, of $\sim 10^{21}$-10^{22} cm^2 s^{-1} (Goodman et al. 1993, Caselli 2002), and put it directly into the solar-type star, the acquired final

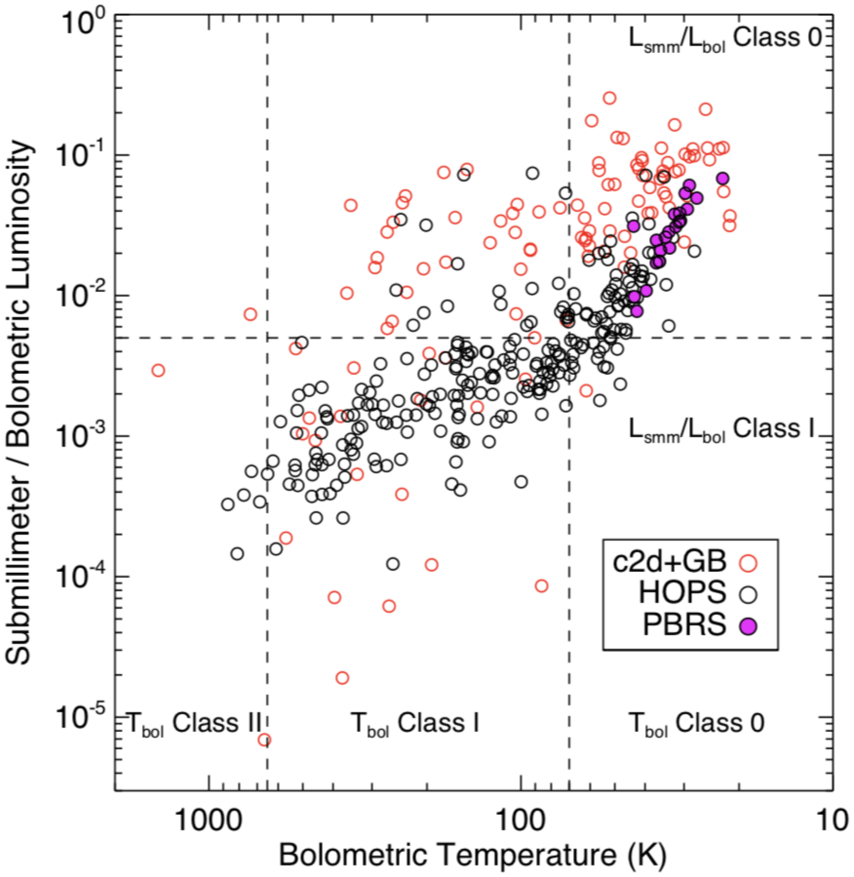

Figure 1.6: Comparison of L_{smm}/L_{bol} and T_{bol} for the protostars in the 'core to disk' survey (c2d), the 'Gould Belt' survey (GB), and the 'Herschel Orion Protostar Survey' (HOPS). The dashed lines show the Class boundaries in T_{bol} (Chen et al. 1995) and L_{smm}/L_{bol} (André et al. 1993). Adapted from Dunham et al. 2014.

velocity will be enough to disrupt it, fragment it, and prevent the formation of the star and the ignition of nuclear fission reactions. However, stars do form and therefore the angular momentum needs to be removed from the core before the collapse proceeds. This conundrum is called the "angular momentum problem" (Spitzer and Arny 1978, Bodenheimer 1995, Mathieu 2004), and it basically implies that there must be some other mechanisms at place to redistribute this angular momentum.

The specific angular momentum must then be reduced about 6 to 7 orders of magnitude from the dense core to the star but the question remains: when and how this process occurs? Observations have shown that angular momentum is progressively removed during the collapse (Table 1.1). By the time the protoplanetary disk is formed, the system has already reduced its specific angular momentum by 1 to 3 orders of magnitude from the initial angular momentum of the starless cloud. Clear signatures of rotation have been identified in Class 0 and I objects at different scales (5000 to 50 au) which have allowed to compute their specific angular momentum (Ohashi et al. 1997, Caselli 2002, Yen et al. 2011, Yen et al. 2015). These studies have shown that specific angular momentum values during the Class 0 stage are very similar to protoplanetary disks and, therefore, it has already decreased be-

Object	J/M ($cm^2\ s^{-1}$)
Starless dense cores	10^{21-22}
Star forming cores (Class 0 and I)	10^{19-21}
Protoplanetary disks	10^{19-21}
Pre-main sequence stars	10^{16-17}
Solar system (planets + Sun)	10^{17}
Sun	10^{15}

Table 1.1: Specific angular momenta from dense cores to the Sun. Adapted from Belloche 2013.

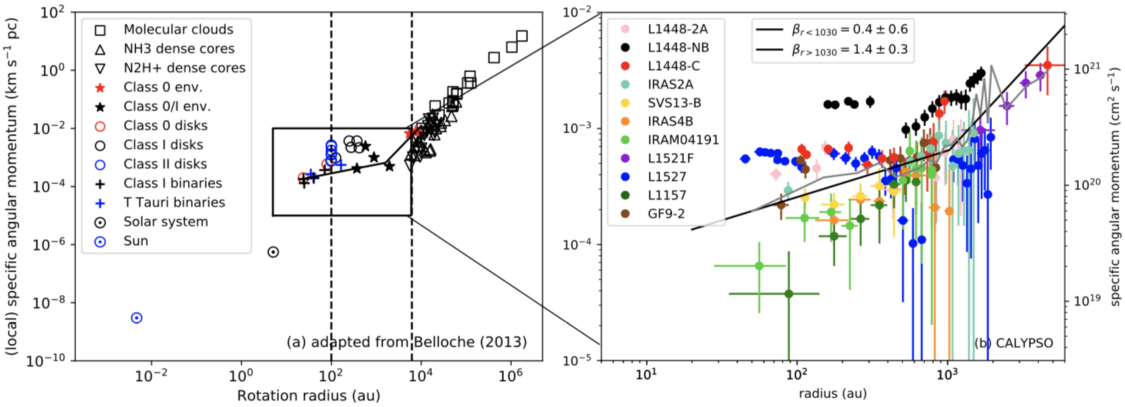

Figure 1.7: Radial distribution of specific angular momentum, from Gaudel et al. 2020. Left panel show values for different evolutionary stages, from molecular clouds to the Sun. Right panel shows a zoom on the region where the angular momentum profiles due to rotation of the CALYPSO sources lie. The gray curve shows the median profile of the angular momentum, and the black solid line shows the bes fit with a broken pwer-law model.

tween 1 to 3 orders of magnitude form the parental cores (Fig. 1.7, left panel) during the early stages.

While the velocity gradients from which the specific angular momentum values are obtained can be due to non-rotation motions, such as infall or turbulence (Caselli 2002, Tobin et al. 2012, Gaudel et al. 2020), it seems clear that protostellar objects, such as Class 0 and Class I, are key as to how angular momentum is removed during the first stages of the collapse. Gaudel et al. 2020 investigated how the specific angular momentum evolves radially and showed that it decreases $\propto r^{1.6}$ down to $\sim 10^3$ au where there is a break and then it becomes relatively constant at 6×10^{19} cm^2 s^{-1} (Fig. 1.7, right panel). This illustrates that the large scale angular momentum is probably not driven only by rotational motions but instead is caused by gravitationally-driven turbulence due to large-scale collapse.

Different mechanisms exist that could allow angular momentum to be transported or redistributed during the first stages of the collapse:

1. Fragmentation and formation of multiple systems:

Fragmentation of cores and formation of multiple stellar systems can be a way of transferring angular momentum into orbital motions of the different stellar components. Since the protostellar object is formed at the early stages of the collapse, it follows that this could be a good mechanism at the adequate stage to remove angular momentum. More than half of the sun-like stars (in terms of mass) are found in binary or multiple systems (Duquennoy and Mayor 1991, Raghavan et al. 2010), and while not all the systems that are born multiples remain in this configuration through all their life (Sadavoy and Stahler 2017), with some being ejected through dynamical interactions (Reipurth and Mikkola 2012) or become unbound after the dispersal of the envelope, the formation of multiples seems to be intrinsic to the star formation process. The VANDAM survey (Tobin et al. 2016a, Tobin et al. 2016b) showed a sample of at least 15 multiple systems in Class 0 and I low-mass protostellar objects. While the statistics are still reduced, it seems that the multiple configuration is indeed a common feature during the first stages of star formation, which might indicate the importance of fragmentation in the redistribution of angular momentum.

2. Redistribution of angular momentum from the envelope to the disk:

   By pure conservation of angular momentum during collapse, matter will accumulate in a disk beyond the centrifugal barrier. This is because in the mid plane, perpendicular to the rotation axis, centrifugal forces are more important and matter will tend to accumulate in this region. Therefore, it is expected that disks of $>$100 au will be formed around the central object (Hueso and Guillot 2005). Disks of these characteristics have been observed around T-Tauri stars (Andrews et al. 2018, for an example) and also around Class I objects (Jørgensen et al. 2009, Harsono et al. 2014), but they seem to be elusive in Class 0 objects. The CALYPSO project (Maury et al. 2019) showed that, for a sample of 26 Class 0 and Class I objects, $>$ 72 % of their Class 0 sources presented disks with radii of $<$60 au. This implies that while disks are ubiquitous and probably a way of removing some of the angular momentum, they can not account for the whole removal. Finally, once planets have been formed in the disk, storage of angular momentum can also occur in the orbital motions.

3. Matter ejection through jets and bipolar outflows:

   It is known that the first stages of protostellar collapse are accompanied by the ejection of matter in the form of outflows and jets. The launching of jets is related to the presence of a magnetic field and the magneto-centrifugal acceleration of particles close to the center of the object, due to the pinching of the magnetic field produced by its coupling with matter during the collapse (Blandford and Payne 1982, Pudritz et al. 2007, Cabrit et al. 2009). Outflows and jets have been largely observed in protostellar objects (Guilloteau et al. 1992, Cabrit et al. 1997, Hirano et al. 2006). While measurements of the angular momentum in Class 0 and I jets indicate that they are an important mechanism for the removal of significant angular momentum at small scale (Konigl and Pudritz 2000, Choi et al. 2011, Lee 2020, Tabone et al. 2020), the relative importance of the ejected matter to accreted matter is small ($M_{acreeted} \sim 1$ % $M_{ejected}$), and it is not clear if they can explain by themselves the total decrease in angular momentum.

4. Magnetic braking:

While all of the above mechanisms are more or less efficient in the redistribution of angular momentum, it appears that altogether their effects are not sufficient to explain the decrease in angular momentum during the Class 0 stage. The missing link might be the complex interaction between the gas and the magnetic field. The accumulation of magnetic field lines in the center of the object, due to the dragging of the field with the matter during the collapse, can be responsible of redistributing angular momentum at small scales, suppressing the formation of large disks due to magnetic braking (Gillis et al. 1974, Galli et al. 2006), and also preventing the fragmentation of cores and the formation of multiple systems for low- and high- mass cores (Añez-López et al. 2020, Palau et al. 2021). The morphology of the magnetic field has been characterized in a large number of Class 0 sources (Girart et al. 1999, Girart et al. 2006, Girart et al. 2008, Rao et al. 2009, Maury et al. 2018, Kwon et al. 2019). Although they are frequently observed, the dynamical role of the magnetic field during the collapse is still debated. More details on the influence of the magnetic field will be given in Section 1.2.

The luminosity problem

Another well-known problem of the theory of star formation is the so-called "luminosity problem" (Kenyon et al. 1990), and it is simple to state: Protostellar objects have luminosities between 10 and 100 times smaller than what it is predicted from the "inside-out" collapse model derived by Shu 1977, where accretion occurs at free-fall velocity. The total bolometric luminosity of an embedded protostellar object is given by the sum of two terms for internal and external luminosity ($L_b = L_{int} + L_{ext}$). The first term, L_{int}, is the internal or photospheric luminosity of the object and corresponds to the luminosity produced by deuterium burning (if it has started yet) and the luminosity produced by the Kelvin-Helmholtz contraction. The second term, L_{ext}, is the accretion luminosity and can be expressed as $L_{ext} = f_{acc}(GM_*\dot{M}/r)$, where f_{acc} is the fraction of accretion energy that is radiated in the form of light, $\dot{M}$ is the mass accretion rate and r is the protostellar radius (Dunham et al. 2008, Dunham et al. 2014). Initial constraints of the mass accretion considered that the protostellar phase had a lifetime of 0.1 Myr, this implied that for a 1 $M_\odot$ star the mass accretion rate had to be 10^{-5} $M_\odot$yr^{-1}, producing a luminosity of 10^2 $L_\odot$(considering that f_{acc} = 1). However, this value is far from the observed luminosities of young objects of $\sim$1.5 $L_\odot$ (Evans et al. 2003).

The problem was initially identified by Kenyon et al. 1990, and has been further investigated during the last years (Kenyon and Hartmann 1995, Young and Evans 2005, Evans et al. 2009, Dunham et al. 2008, Dunham and Vorobyov 2012, McKee et al. 2010,Dunham et al. 2014). This problem is of huge importance since observed bolometric luminosities are used to derive mass accretion rates and determine if those are in concordance with the different proposed models of star formation (McKee et al. 2010). Since it first appeared, several arguments have been given to conceal this discrepancy:

- The values to derive accretion luminosities are theoretically poorly constrained since the values of accretion rates are largely model dependent. Accretion is the infall of material from the outer envelope towards the circumstellar disk at free-fall velocities, but values might differ if other accretion regulators are considered, such as the magnetic field. Accretion also depends on the viscous transport of material through the circumstellar disk towards the central object, whose properties are, in turn, constrained by the core properties and the infall rate (Vorobyov and Basu 2009, Kratter et al. 2010). Theoretical consensus has not been achieved on which is the correct model and indeed this is a hard problem to overcome, since the model determination depends on measures of the infall rate and vice-versa. More certain determination of the infall models and accretion rates might help alleviate the luminosity problem.

- Another solution is that the observations used for deriving mass accretion rates have failed to grasp the complexity of gas motions in protostellar envelopes. If the typical line emission profiles that are used to derive these quantities contain unresolved velocity components coming from non-symmetric infall motions, mass accretion rates could be higher, as well as the protostellar luminosity. Recent observations of asymmetric collapse or accretion streamers (Tokuda et al. 2014, Maureira et al. 2017, Pineda et al. 2020, this work) seem to suggest that these features might be common and should be taken into account when constructing star formation models, as well as considered when deriving protostellar luminosities.

- Slow accretion scenario: This was one of the first solutions to the problem and it implied that the accretion rate was lower than initially thought ($\dot{M}$ $<$10^{-6} $M_{\odot}yr^{-1}$), which would mean that lifetimes of the different protostellar and prestellar phases was much longer (Kenyon et al. 1990). This was partially solved by Evans et al. 2009 who concluded that the lifetime of the protostellar phase was close to 0.5 Myr (contrary to the initial constraints of 0.1 Myr) and reducing the expected bolometric luminosity by 1 order of magnitude.

- Episodic accretion: Another one of the first solutions for this problem was episodic accretion from the circumstellar disk onto the protostar (Kenyon et al. 1990). This meant that most of the mass would be accreted in short periods of time with high luminosities and $\dot{M}$ $\sim$10^{-4} $M_{\odot}yr^{-1}$, followed by quiescent periods of $\dot{M}$ $\sim$10^{-6} $M_{\odot}yr^{-1}$ (Baraffe et al. 2009).

- Finally, an additional solution concerns the radiative efficiency of the accretion shock. If the accretion energy is not entirely thermally radiated and part of it is used, for example, to drive outflows, then $f_{acc} < 1$, and the theoretical bolometric of the star is reduced (Ostriker and Shu 1995).

1.2 Magnetic fields in the star formation process

Magnetic fields are ubiquitous in our universe at all different scales: from the ISM to the mechanisms governing stellar physics (Vallée 2004, Planck Collaboration), and they have also been observed repeatedly in SFRs. It seems then, that they might play an important role in regulating the formation of large-scale structures, dense cores and also the formation of stars. Additionally, magnetic fields are required at different points during star formation to explain some effects such as outflow and jets (Nixon and Pringle 2019). It is, therefore, important to understand how the matter interacts with the present magnetic field.

1.2.1 Ideal MHD and magnetic braking

Magnetic fields are able to redistribute angular momentum via magneto-hydrodynamic (MHD) interactions, and to cause other observed processes such as magnetocentrifugal winds which are able to launch jets and outflows from the circumstellar disks. Since matter in the envelope is at least partially ionized, charged particles will couple to the magnetic field lines and drag them to the center of the object as the collapse proceeds, producing the characteristic "hour-glass" shape (Galli and Shu 1993). Since the magnetic field tension increases towards the center, the removal of angular momentum at small scales is large, and will prevent the formation of large disks in a process called "magnetic braking" (Gillis et al. 1974, Galli et al. 2006). The importance of magnetic fields is usually measured with the mass-to-flux ratio, λ, given in units of critical value $(2\pi G^{1/2})^{-1}$ (Mellon and Li 2008). When $\lambda > 1$, the object is "supercritical" and gravity can overcome the magnetic field strength and subsequently collapse. On the contrary, if $\lambda < 1$, the object is "subcritical" and the gravitational collapse is prevented by the magnetic field. Derivations of these values in low-mass star forming cores have shown that those are indeed super critical ($\lambda > 1$, Li 2009). These results, added to the observed pinched magnetic fields in dense cores, and the lack of observations of large disks in Class 0 objects (Maury et al. 2019) suggest that magnetically regulated collapse is a common occurence during low-mass star formation.

The efficiency of the magnetic braking depends largely on the magnetic field geometry and strength (Allen et al. 2003). Simulations have shown that rotationally supported disks are not able to form in the ideal MHD limit: any disk forming would be magnetically linked to a slowly rotating envelope of much larger momentum of inertia and would lose angular momentum too quickly (Allen et al. 2003, Mellon and Li 2008). If the magnetic field is too strong and the magnetic braking is too efficient, the formation of the disk can be completely suppressed generating the so-called "magnetic braking catastrophe" (Galli et al. 2006). However, disks, if rather small, exist. Therefore, there must be a balance between enabling the removal of angular momentum and completely prevent the formation of disks (Nixon and Pringle 2019). Different explanations have been given to explain why the magnetic braking efficiency is lower, allowing the star formation process to take place:

1. Models have suggested that an initial misalignment of the magnetic field and the core rotational axis (measured with respect to the outflow axis) can reduce magnetic braking efficiency (Ciardi and Hennebelle 2010, Joos et al. 2012, Gray et al. 2018, Hennebelle et al. 2020, Wurster and Lewis 2020a, Wurster and Lewis 2020b). Simulations suggest that when the magnetic field is well aligned only small disks can form and accretion onto the central object can be completely stopped, compared to when the magnetic field is not aligned, which allows the formation of larger disks. Turbulence can diffuse the magnetic field out of the inner regions of the core, alleviating the magnetic field tension at small scales, and its non-zero angular momentum can cause the misalignment of the magnetic field and the rotation axis (Joos et al. 2013). Moreover, initial density perturbations on the core can also lead to the formation of disks not necessarily oriented with the magnetic field (Verliat et al. 2019).

2. Since matter in the envelope is not totally ionized, if the degree of ionization is low the coupling between matter and the magnetic field might not be efficient, and the magnetic braking effect is reduced. Non-ideal MHD processes can then be the key to explain the efficiency reduction of the magnetic braking.

1.2.2 Non-ideal MHD

In practice, ideal MHD conditions are not likely to be satisfied in the deep dense center of the collapsing cores (Mestel and Spitzer 1956). In those environments, not all the gas will be ionized, being the ionization fraction as low as 10^{-17} (Umebayashi and Nakano 1990, Caselli et al. 1998), so not all the matter will be coupled to the magnetic field. This effect makes the behavior of charged and neutral particles different from each other, allowing magnetic energy to be dissipated, for example by friction. Therefore, the efficiency of the magnetic field in regulating the collapse will not depend only on the intrinsic properties of the field, but also on the chemistry of the gas which, in turn, depends on the environment in which the core resides, for instance the amount of radiation that it receives that is able to ionize the medium.

Flux freezing, or the fact that ionized gas is coupled with the magnetic field is a direct consequence of the induction equation, which is the result of a convection and a diffusion term:

$$\frac{\partial B}{\partial t} = \nabla \times (v \times B) + \eta^2 B \tag{1.6}$$

where B is the magnetic field, v is the velocity of the gas and η is the magnetic diffusivity. The relative importance between the convection term (causing the flux-freezing) and the diffusion term, is given by the Reynolds number:

$$R_m = \frac{|\nabla \times (v \times B)|}{|\eta^2 B|} \sim \frac{VL}{\eta} \tag{1.7}$$

where L and V are the characteristic spatial and velocity scales for a given Reynolds number. When $R_m >> 1$, the flux-freezing approximation is warranted. Instead, when the gas is weakly ionized, as expected in protostellar cores, non-ideal MHD effects come into play. Now, the diffusivity is not only given by η and it will also depend on the velocity of neutrals:

$$E = -\frac{1}{c}\left(v_n \times B - \frac{4\pi}{c}\beta j_\perp\right) \tag{1.8}$$

where, c is the speed of light, v_n is the velocity of the neutral component of the gas, $j_\perp$ is the density component perpendicular to the magnetic field. Finally, β is the effective magnetic diffusivity:

$$\beta = \frac{B^2}{4\pi n_i \mu \nu_i} \tag{1.9}$$

where n_i is the ion density, ν_i and μ are the collision rates of ions with neutrals and the mean reduced mass of such collisions, respectively. The flux-freezing approximation will stop being valid when the magnetic diffusivity term dominates over the convective term in Eq. 1.8. A new Reynolds number can be define such as:

$$R_m = 4\pi n_i \mu \nu_i LV/B^2 \tag{1.10}$$

As the magnetic field gets stronger at smaller L, the convective term in Eq. 1.8 will lose importance and the charged particles will decouple more easily from the neutrals at the scales where the Reynolds number is 1 or smaller. This decoupling will generate friction forces between the charged and the neutral component of the gas and dissipate turbulent energy.

Non-ideal MHD processes allow the dissipation of magnetic flux at the center of the object avoiding the magnetic braking catastrophe and allowing the formation of disks and stellar systems. The induction equation is then governed by two terms, the ideal plus the non-ideal terms. Non-ideal terms can be of three different types, depending on their nature and the scale at which they act.

Ohmic resistivity

At high densities ($\rho > 10^{-9}$ g cm^{-3}), the collisional rates of charged particles (ions and electrons) with neutrals are high, the ionization fraction is low, and all the charged particles are decoupled from the magnetic field. Simulations with Ohmic resistivity enable the formation of small Keplerian disks ($\sim$10 au), but include too large resistivities (Shu et al. 2006, Krasnopolsky et al. 2010, Dapp and Basu 2010, Machida et al. 2011)

The Hall effect (ion-electron drift)

Massive particles (such as ions and charged grains) are decoupled from the magnetic field and get collisionally coupled to the neutral gas while electrons remain coupled to the magnetic field. The Hall effect is not a dissipative process. It dominates at intermediate density regime, where the electron diffusion becomes important (Braiding and Wardle 2012). Since electrons move perpendicularly to the magnetic field, its importance depends on the initial orientation of the magnetic field (Wurster et al. 2016) and it can introduce angular momentum due to the initial rotation of the cores affecting as well the morphology of the magnetic field (Krasnopolsky et al. 2011).

Ambipolar diffusion (ion-neutral drift)

At lower densities (10^{-13} - 10^{-10} g cm^{-3}), charged particles will be well coupled to the magnetic field. The friction between the flowing neutrals (which are not coupled to the magnetic field) and the charged particles reduces the radial velocity of neutrals, dissipating turbulent energy and allowing the formation of small disks (Mellon and Li 2009, Li et al. 2011, Dapp et al. 2012, Tsukamoto et al. 2015). However, if the ionization fraction is too high, the effect of ambipolar diffusion will be suppressed. Figure 1.8 illustrates that the effect of ambipolar diffusion starts to be important at densities larger than 10^{-12} cm^{-3}, where it reduces the strength of the magnetic field substantially compared to models with only Ohmic resistivity. When the density is larger than 10^{-9} cm^{-3}, the slope for the ambipolar diffusion model is the same as the one for the Ohmic dissipation, indicating that is the later effect that dominates.

Energy dissipation due to ambipolar diffusion will have two main consequences. First, ions and neutrals will have different infalling velocities, the so-called ambipolar drift. Simulations of protostellar collapse including ambipolar diffusion effects have shown that the ambipolar drift can be as low as 0.2 km s^{-1} at 100 au for a central mass star of 0.5 M$_{\odot}$, and increase towards smaller scales (Mellon and Li 2009, Li et al. 2011, Zhao et al. 2016, Zhao et al. 2018), being 0.3 km s^{-1} at 70 au and 1 km s^{-1} at 30 au (Li et al. 2011). For B335, Yen

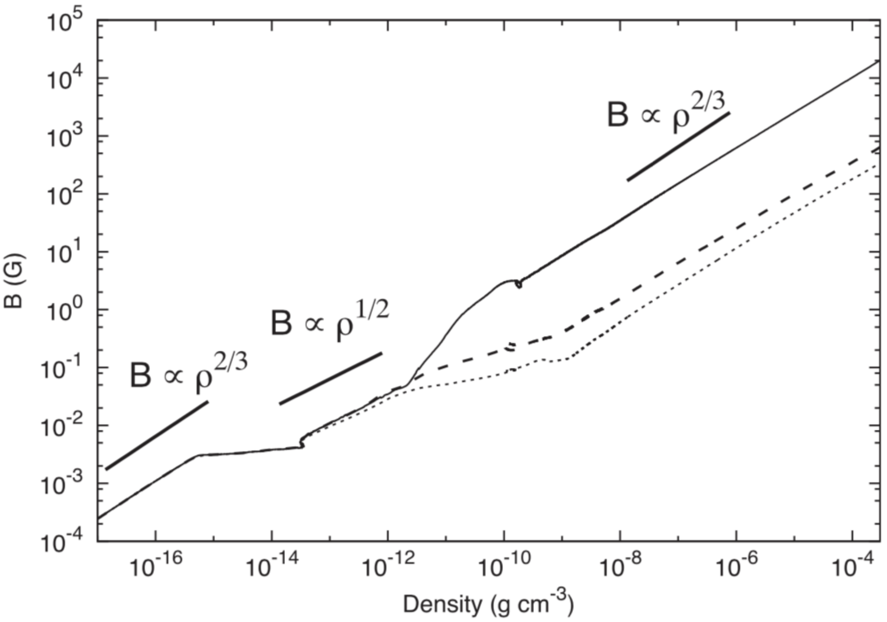

Figure 1.8: Evolution of the central magnetic field strength as a function of the density, for the different models in Tsukamoto et al. 2015. The solid line corresponds to an ideal MHD model, the dashed line corresponds to a model including Ohmic resistivity and the dotted line corresponds to the inclusion of ambipolar diffusion. The difference between models starts to be relevant at densities larger than 10^{-13} g cm^{-3}, where ambipolar diffusion becomes effective.

et al. 2020 derived a maximum drift of 0.30 km s^{-1} at 100 au. Some physical conditions of the medium, such as the mean size of the dust grains, can enhance this value up to 0.5 km s^{-1} at 100-300 au. Second, the velocity dispersion spectra of ions and neutrals will be different. Ions will present a narrower velocity dispersion spectra, and their minimum velocity dispersion will be smaller than for the neutrals (Fig. 1.9), in regions with magnetic fields with strengths of tenths of μG (Houde et al. 2000a, Houde et al. 2000b, Li and Houde 2008, Hezareh et al. 2010, Hezareh et al. 2014). The minimum value of the square of the minimum velocity dispersion will follow a Kolmogorov-type law. This hypothesis is valid only if the medium is dominated by turbulent motions, i.e., the ISM or molecular clouds. However, if the medium is dominated by gravitational motions, i.e., protostellar envelopes, this hypothesis might not hold. In this work, we will make use of this effect to investigate if this assumption is valid for protostellar envelopes, and attempt to search for this difference in the velocity dispersion to constraint the effect of the magnetic field in B335.

1.2.3 Ionization processes

The degree of ionization, or the ionization fraction (χ_e), is defined as χ_e=n$_e/n_H$, where n_e is the electron density and n_H is the hydrogen density. In a molecular core, it depends largely on the cosmic ray incidence from the ISM (Hayakawa et al. 1961, Tomasko and Spitzer 1968) and possible incident UV radiation, but also on the accretion radiation produced during collapse which is able to ionize the inner part of the envelope.

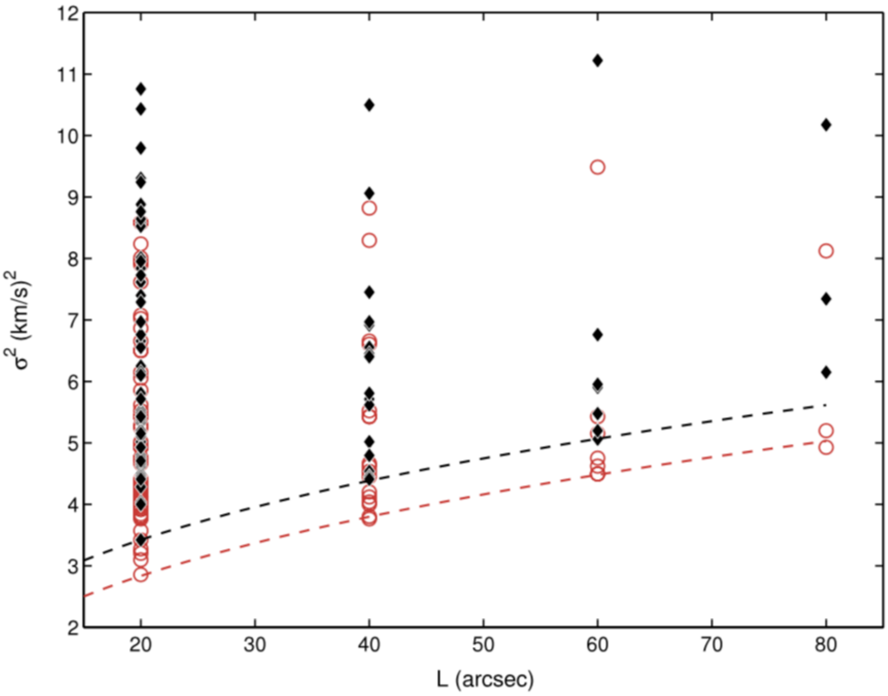

Figure 1.9: Square of the velocity dispersion (σ^2) at different lenghtscales (L), for ions (in red) and for neutrals (in black) derived from the observations of molecular clouds at scales of ∼30,000 au. The lowest envelopes are fitted by a Kolmogorov-type law. From Li and Houde 2008.

The ionization rate strongly influences the medium of dense clouds and the evolution of the core collapse. It determines the degree of ionization which, in turn, regulates the coupling of the gas to the magnetic field and hence the importance of the magnetic field in the collapse and of dissipative processes, such as ambipolar diffusion. Considering that ion-neutral reactions dominate at the cloud temperatures (Herbst and Klemperer 1973), the ionization rate also plays a huge role in determining the chemical composition of a core.

Observations of the ionization fraction in molecular clouds and dense cores vary widely and are subject to huge uncertainties. Deduction from molecular abundances give values that range from 10^{-5} (Evans et al. 1975) to 10^{-8} (Guelin et al. 1977) at the typical densities of these objects (ρ ∼10^4-10^5 cm^{-3}). More recent works, which derive the ionization fraction from the deuteration fraction, reduce the ranges for the ionization fraction 10^{-6} - 10^{-8} (Caselli et al. 1998, Chen et al. 2011). Such wide ranges might derive not only from observational and modeling uncertainties, but might reflect differences on the physical environments around different protostellar sources.

Cosmic Ray ionization

The dominant source of ionization for molecular clouds and cores are low-energy cosmic rays (CRs). They are not only the main ionization process needed to produce ions and allow the core to chemically evolve, but they also represent an important source of heating which supports clouds against gravitational collapse, since the energy produced during the ionization process is largely converted into heat (Gabici et al. 2007).

The first theoretical determinations of the CR ionization rate (ζ) was performed for clouds made of atomic hydrogen, deriving values of $\zeta^{H} \sim 10^{-18}$ - 10^{-15} s^{-1}, for gas in the diffuse interstellar clouds (Hayakawa et al. 1961 Spitzer and Arny 1978). More recent works have constrained these values to range from $\sim$ 10^{-17} - 10^{-16} s^{-1}, from measurements of abundance of chemical species (Black and Dalgarno 1977, Hartquist et al. 1978, Black 1978, van Dishoeck and Black 1986, Federman et al. 1996). In dense cores and protostellar envelopes, the determination of ζ is even more uncertain, since molecular abundances depend strongly on the level of depletion of C and O, and the role of dust grains during chemical evolution. However, values of χ^{H_2} derived from chemical modelling of molecular lines lay in the range of $\sim$ 10^{-17} - 10^{-14} s^{-1} (Caselli et al. 1998, Fontani et al. 2017, Redaelli et al. 2021).

Ionization processes from CRs involve a series of reactions occurring when a CR particle (electrons, protons and heavy nuclei) impact with atoms and molecules, mainly H_2 and He, producing ions and electrons (Padovani and Galli 2013). In molecular clouds, the process starts with the ionization reaction:

$$\mathrm{k_{CR} + H_2 \rightarrow k_{CR} + {H_2}^+ + e^-} \tag{1.11}$$

where k_{CR} is a CR particle of a species k, with k = electrons (e) or protons (p), and energy E_k. Low-energy CR protons can react with ambient H_2 by electron capture reactions:

$$\mathrm{{p_{CR}}^+ + H_2 \rightarrow H + {H_2}^+} \tag{1.12}$$

In addition, secondary electrons are sufficiently energetic to induce further ionization of H_2 molecules at a short spatial range:

$$\mathrm{{e_{CR}}^- + H_2 \rightarrow {e_{CR}}^- + {H_2}^+ + e^-} \tag{1.13}$$

These same reactions can occur as well for the interaction with He. The different values between ζ^{H_2} in the diffuse interstellar gas and the lower values in dense clouds and cores need to be reconciled by invoking mechanisms of CR suppression, such as the presence of a magnetic field. The relative importance of these processes depends on a number of variables related to the magnetic field, such as its geometry or its strength. In the absence of MHD fluctuations, CRs propagate closely following the magnetic field lines, performing an helicoidal motion with a characteristic radius called the Larmor radius (left panel of Fig. 1.10), which depends on the type of molecule and the strength of the magnetic field, and is of the order of $\sim 10^{-9}$ and $\sim 10^{-7}$ pc for protons and electrons respectively for B = 10 μG (Padovani et al. 2009). Perturbations of MHD waves with wavelengths of the order of the Larmor radius can affect the propagation of CRs and efficiently scatter them. These fluctuations are strongly dependent on the ionization fraction of the gas which is, in turn, mostly determined by the CRs themselves. Therefore, ζ^{H_2} in a magnetized core is always reduced with respect to the non-magnetized core, with a factor depending on the mass-to-flux ratio (Padovani and Galli 2011, Padovani and Galli 2013). Moreover, since CRs propagate through the magnetic field lines, χ_e should increase following the geometry of the magnetic field where the probability of collisions occurring is larger (right panel of Fig. 1.10).

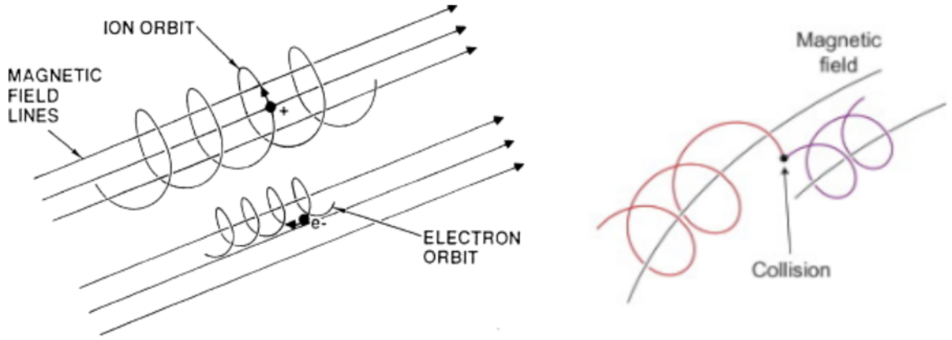

Figure 1.10: *Left*: Schematic representation of the propagation of different particles (ions and electrons) through the magnetic field. The radius of the helicoidal motion is the Larmor radius. *Right*: Schematic representation of a collision of two particles along the magnetic field lines. From McCracken and Stott 2013.

1.2.4 Magnetic fields in protostars

The study of the role of magnetic fields during protostellar formation has been increasing over the last two decades, but what is its exact role on regulating the collapse, and the initial conditions that affect the outcome of the process are still a matter of debate. Observations of the magnetic field morphology in protostellar objects help understanding the conditions at the onset of the collapse, and have also been increasing in the last years.

The main technique to observe the morphology of the magnetic field in protostellar cores has been polarization observations of the thermal dust continuum emission. Those rely on the fact that irregular dust grains present in the envelope will align with the magnetic field with their long axis perpendicular to the magnetic field direction (Dolginov and Mitrofanov 1976, Lazarian 2007). Grains tend to align with the magnetic field because they possess a magnetic moment, due to the presence of magnetic inclusions in their composition (Jones and Spitzer 1967). Additionally, grains are charged due to their collisions with charged particles and CRs (Padovani 2018) or their interaction with the present radiation field (Weingartner and Draine 2001, Weingartner et al. 2006). These alignment mechanisms are in constant competition with disaligning processes, for example grain-gas collisions (Weingartner 2006). In order for grains to be efficiently aligned with the magnetic field and produce a quantifiable amount of polarized light, other mechanisms are required. The main mechanisms for grain alignment are radiative alignment torques (RAT), produced by torques transfer when a grain interacts with a photon (Dolginov and Mitrofanov 1976) or mechanical alignment, produced by the interaction of grains with gas flows (Gold 1952). Which mechanism is more important and under which conditions, or if it is a combination of both, is still an open, and quite hot, debate. Whatever the case, grain emission is observed to be polarized, and this provides clues of the magnetic field morphology in the envelope of dense cores.

Structured magnetic fields are commonly observed in protostellar objects. Polarization observations at small scales, from 300 to 500 au, have been able to detect the "hour-glass" shape (Galli and Shu 1993) in an increasing number of sources, both in low-mass (Girart et al. 1999, Girart et al. 2006, Girart et al. 2008, Rao et al. 2009, Maury et al. 2018, Redaelli et al.

2019a, Kwon et al. 2019, Le Gouellec et al. 2019) and in the high-mass regimes (Schleuning 1998, Girart et al. 2009, Tang et al. 2010, Beuther et al. 2018, Dall'Olio et al. 2019). These observations confirm the presence of magnetic fields and suggest that the magnetic field might play a dynamical role during the collapse, although this is still to be confirmed.

Observations of the magnetic field morphology have also allowed to study the effect of the misalignment of the magnetic field and the rotational axis. Initial studies suggested that statistically there was no correlation between the magnetic field and the outflow axis (Hull et al. 2014). Recent observational studies question this view (Galametz et al. 2018, Galametz et al. 2020), and have shown a correlation between the misalignment and the observed velocity gradients (Fig. 1.11), which are indicative of the angular momentum of the gas. Their results show that sources with a small misalignment present smaller velocity gradients, and less angular momentum in the gas, indicating the importance of alignment regulating the efficiency of magnetic braking. Moreover, these studies show that objects with small misalignment, tend to be single objects or present low fragmentation.

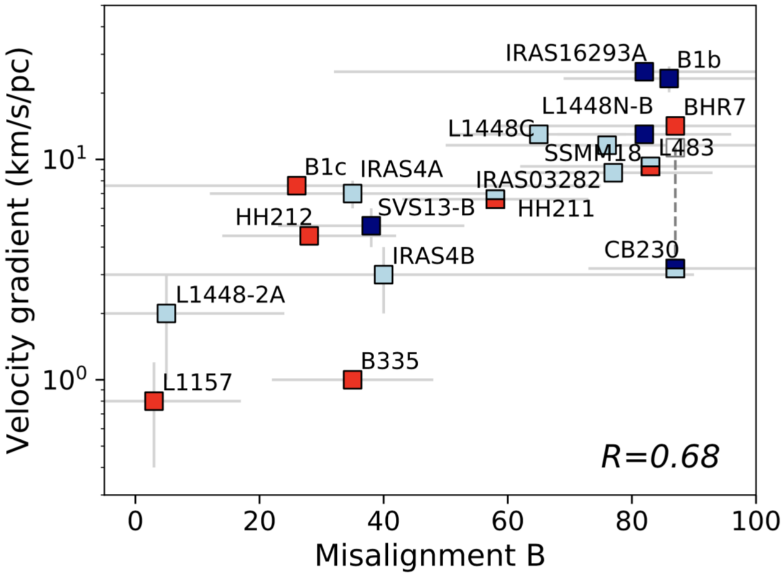

Figure 1.11: Velocity gradient of the source, obtained from line measurements, as a function of the projected angle between the mean magnetic field and the outflow direction. Sources are color coded as a function of their fragmentation: red/light-blue/dark-blue for sources with a detection of a single/double/3-4 peaks in the dust continuum. From Galametz et al. 2020.

1.3 Molecular line emission

The molecules present in dense cores allow to extract very important information about the chemical composition and evolution of the sources, but also about the physical conditions on the interior of protostellar envelopes. The analysis of molecules has been used to probe the physical conditions of different astrophysical processes since their discovery, and their study has been improved in the last years, as more lines were accessible due to the improvement of our telescopes.

The excited energy levels of a molecule can be populated by different processes. Collisions between molecules (or atoms) and radiation can excite and de-excite the different energy levels of a molecule (i.e., electronic, rotational or vibrational levels). When an excited level undergoes radiative decay, it emits a photon at the resonance frequency. A molecule decays radiatively if the timescale for this process is smaller than the timescale for collisional de-excitation. It is this radiation which can be observed and analyzed to obtain information on the conditions of the medium.

1.3.1 Radiative transfer

The intensity of the radiation field, $\bar{J}$, which propagates through a medium, is related to the specific intensity, I_ν, at a frequency ν, and is defined as the energy flowing through a surface per unit of time per steradian, such as:

$$I_\nu = \frac{dE}{d\nu dA dt d\Omega cos\Theta} \tag{1.14}$$

Propagation of radiation can be affected by absorption, emission and scattering processes, caused by the matter present in the medium. The radiative transfer equation then depends on the absorption and emission coefficients, but also the optical depth, τ_ν. It can be written as:

$$\frac{dI_\nu}{d\tau_\nu} = -I_\nu + S_\nu(\tau_\nu) \tag{1.15}$$

where $S_\nu(\tau_\nu)$ is the ratio of the emission and absorption coefficients. The intensity of the radiation field, independent of the direction, is obtained by integrating over all the solid angles:

$$J_\nu = \frac{1}{4\pi}\int I_\nu d\Omega \tag{1.16}$$

and the total integrated intensity, $\bar{J}$, is the intensity integrated over the line profile, $\phi(\nu)$.

1.3.2 Broadening of the molecular lines and opacity effects

When a molecule (or atom) is excited by a photon, it produces an absorption line in a spectral continuum. If the excited molecule decays radiatively, it will produce an emission line over the continuum. Ideally, the absorption and emission lines will have the same frequency, corresponding to the resonance frequency, and will be infinitely thin. However, there are many effects that can result in the broadening of the line, far from its resonance frequency. We describe here three of the main causes, and give some details on the effect of the line opacity.

- Natural broadening: This effect is a direct cause of the uncertainty principle. Without entering in any details, this relates the life-time of an excited state with the uncertainty in its energy: short life-timed excited states will have broader spectrum and vice-versa. In practice, this means that the emitted photon will not have the exact same energy as the absorbed one, resulting in a broadening following a Lorentzian distribution.

- Thermal broadening (Doppler broadening): This effect is due to the velocity distribution of a group of molecules. In a mass of gas at a given temperature, the molecules will have a random distribution of velocities following the Maxwell-Boltzmann distribution, which will only depend on the gas temperature (if the gas is homogeneously made of the same type of molecules). Following the Doppler effect, if a particular molecule is moving away from the observer, its emission will appear red-shifted with respect to its rest frequency, while if it is moving towards the observer, its emission will appear blue-shifted, resulting in the broadening of the spectral line. The shape of the line can be modeled with a Gaussian profile, and the linewidth (or the Full Width at Half Maximum, FWHM) can be expressed as:

  $$\Delta\nu = \sqrt{\frac{8k_bT\ln 2}{\mu c^2}}\nu_0 \tag{1.17}$$

  where T is the temperature of the gas, c is the speed of light, μ is the reduced mass of the system, and ν_0 is the rest frequency of the line.

- Opacity broadening and self-absorption: When a photon is emitted by a molecule, this photon can be re-absorbed by other molecules present in the medium. In a protostellar envelope, when the foreground of the cloud is colder than the inner region where photons are being emitted, it will absorb most of the radiation, and re-emit it at a slightly different frequency. As a consequence, the line will become broader. Because the re-absorption depends on wavelength, and the photons that have a frequency closer to rest frequency have a larger probability of being re-absorbed, if the cold layer is thick enough, a dip in intensity will be observed at the systemic velocity of the cloud.

  The total intensity observed will depend on the opacity of the medium. In order to properly analyze the properties of the line, such as the intensity or the linewidth, the opacity needs to be taken into account. The intensity of the line can be corrected by an opacity factor following:

  $$I_\nu = I_\nu(1 - e^{-\tau_\nu}) \tag{1.18}$$

  where the opacity is related to the level populations by:

  $$\tau_\nu = \frac{A_{lu}c^3}{8\pi\nu^3}\frac{N(mol)}{\Delta V}(x_1\frac{g_2}{g_1} - x_2) \tag{1.19}$$

  where A_{lu} is the Einstein coefficient for a given transition $l \rightarrow u$, ν is the frequency of the transition, $N(mol)$ is the column density of the molecule and ΔV is the linewidth.

1.3.3 Critical density and excitation temperature

The detection of a particular transition can provide information on the density and the temperature of the gas. The critical density, n_{crit} is traditionally used as a measure of the density at which a particular transition is excited and is observed. In the optically thin regime, this density can be defined such as:

$$n_{crit}^{thin} = \frac{A_{lu}}{\sum_{u \neq l} \gamma_{lu}} \tag{1.20}$$

where $\sum_{u \neq l} \gamma_{lu}$ is the sum over collision rates, and can be expressed as:

$$\gamma_{lu} = \gamma_{lu} \frac{g_u}{g_l} e^{-(E_u - E_l)/k_b T_k} \tag{1.21}$$

where g_u and g_l are the quantum degeneracy of the upper and lower levels, E_u and E_l are the energies for the upper and lower levels and T_k is the kinetic temperature.

Although the ISM is not in thermodynamic equilibrium, is often useful to define an excitation temperature, such as:

$$\frac{n_u}{n_l} = \frac{g_u}{g_l} \exp - \frac{h\nu_0}{k_b T_{ex}} \tag{1.22}$$

where n_u and n_l are the populations of the upper and lower levels of the transition, h is the Planck constant and T_{ex} is the excitation temperature. The excitation temperature is not a real temperature, it only measures the necessary temperature to obtain a given ratio of the population of the two states. Obtaining an accurate value of this temperature is not easy, and relies on the observation of multiple transitions to accurately measure the population of the different states. The excitation temperature and the critical densities are related because the the level population depends on the excitation temperature. Assuming that the transitions are thermally excited, T_{ex} can be used as a proxy for the gas kinetic temperature.

1.4 Class 0 objects in details

Since protostars were observed for the first time (André et al. 1993) several improvements have been made towards the detailed characterization of their evolutionary properties. During the last twenty years, different surveys have allowed the study of the first stages of protostellar evolution and, particularly, the differentiation of Class 0 and Class I objects. Since they were first detected in the sub-millimeter, the first surveys covered those wavelengths, searching for Class 0 candidates (e.g., Casali et al. 1993, Reipurth et al. 1992, Bontemps et al. 1995, Hurt and Barsony 1996). Later, they were surveyed by the *Spitzer* Space Telescope (e.g., 'From Molecular Cores to Planet-forming Disks', Evans et al. 2003, Evans et al. 2009), followed by the *Herschel* Space Observatory (e.g., the 'Gould Belt Survey', André et al. 2010) and now with the new era of interferometers, such as the Atacama Large Millimeter Array (ALMA, e.g., the 'CALYPSO' survey, Maury et al. 2014).

This section presents the identification and classification of Class 0 objects (Section 1.4.1), and the main physical properties observed (Sections 1.4.2, 1.4.3, 1.4.4 and 1.4.5). Finally, we present a description of the chemistry of these objects with an emphasis on the deuterium fractionation (Section 1.4.6).

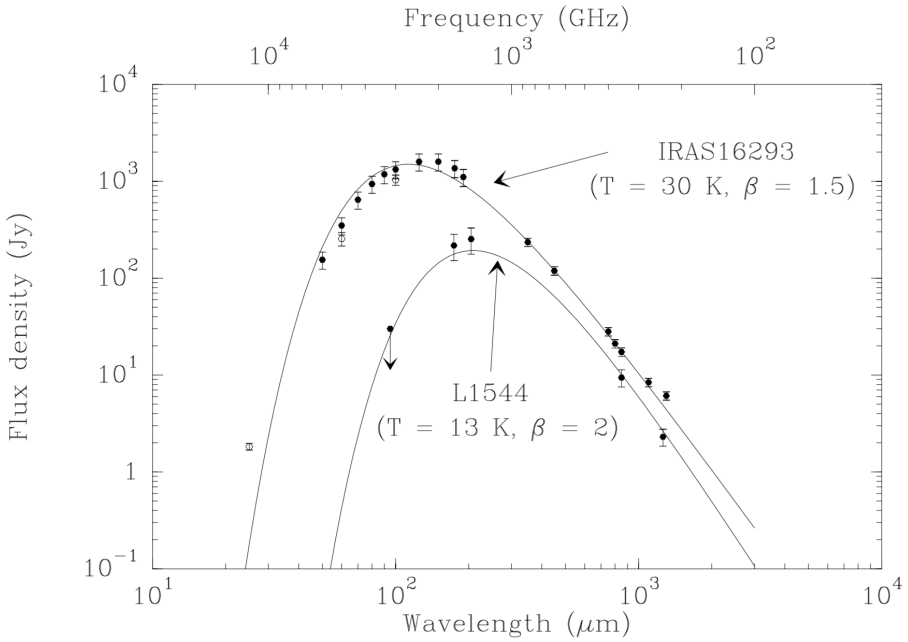

Figure 1.12: Spectral energy distributions of the pre-stellar core L1544 and the Class 0 protostar IRAS 16293, along with a grey-body fits. A simple gray-model can not account for the 25 μm emission of IRAS 16293, and a two-component model is required. From André et al. 2000.

1.4.1 Identification of Class 0 objects

The youngest stages of protostellar evolution are still deeply embedded in an envelope rich in dust. This dust absorbs light at short wavelengths and re-emits it at longer wavelengths. For this reason, the study of protostars is carried out at IR and radio wavelengths, which the aforementioned surveys covered.

The first Class 0 objects were detected thanks to an unusual high value of sub-millimeter luminosity, L_{smm}. André et al. 2000 used this high luminosity and other physical characteristics to define three criteria for the identification of Class 0 objects:

- Evidence for a central YSO, like, for example, the detection of a compact radio continuum source, a collimated CO outflow or an internal source of heating.
- Centrally peaked but extended sub-millimeter continuum emission tracing the presence of a spheroidal circumstellar dust envelope (as opposed to just a disk).
- High ratio of sub-millimeter to bolometric luminosity, $L_{smm}/L_{bol} > 0.5$ %, where L_{smm} is measured at $\lambda > 350$ μm. This means that the SED resembles a single temperature blackbody at T $\sim$ 15-30 K (Fig. 1.12). Moreover, this high ratio suggests that the envelope mass exceeds the central stellar mass ($M_{env} >> M_*$).

The first criterion allows to distinguish Class 0 from pre-stellar cores, that reveal no compact radio continuum sources and present no outflows. The second and third criteria distinguish Class 0 objects from more evolved ones.

1.4.2 Typical values of physical parameters

Class 0 protostars are the youngest objects and correspond to the initial stage of the process of star formation (André 1995). They are observed only $\sim 10^4$ yr after the formation of the central object. They are characterized by the fact that most of the mass is still in the envelope which has been characterized by different surveys, and ranges between 0.1 and 8.5 $M_{\odot}$ (Jørgensen et al. 2002, Enoch et al. 2009, Mottram et al. 2017). The mass is generally computed from the dust continuum integrated emission at millimeter wavelengths. The radius of the envelope is typically of the order of 10^4 au.

Models of an isothermal sphere (Larson 1969, Shu 1977) predict that the outer parts of the envelope follow a $\rho \propto r^{-2}$ density profile, while within the collapsing radius the density tends to flatten to $\rho \propto r^{-1.5}$. These values are in agreement with values derived by modeling the continuum emission on Class 0 envelopes (Jørgensen et al. 2002) which determined density profiles of $\rho \propto r^{-\alpha}$, where α varies from 1.3-1.9. Radial distribution of the temperature can also be described as a simple power-law of the type $\mathrm{T} \propto r^{-\alpha}$, where $\alpha =$ 0.4 (Shirley et al. 2000, Motte and André 2001, Jørgensen et al. 2002). These results, however, are based assuming that the emission is optically thick and under spherical symmetry.

1.4.3 Molecular outflows

A typical characteristic of Class 0 objects is the ubiquitous presence of bipolar molecular outflows. They are driven by accretion onto the protostars and allow to redistribute angular momentum from the central object to the envelope. However, their driving mechanism is still not well constrained and more observations are needed to test models (Arce et al. 2007, Machida and Hosokawa 2013, Frank et al. 2014).

The most important physical parameter to characterize outflows is their force, which measures the rate at which momentum is injected into the outflowing gas, and which is given by:

$$F_{outflow} = c_i \frac{M_{outflow} V_{max}^2}{R_{outflow}} \tag{1.23}$$

where c_i is an inclination correction (Cabrit and Bertout 1990), $M_{outflow}$ is the mass contained in the outflow (typically $\sim 10^{-3}$ - 10^{-2} $M_{\odot}$), $R_{outflow}$ is the the projected size of the outflow lobes as seen in intensity maps, generally probed by CO (typically $\sim 10^3$ - 10^4 au), and V_{max} is defined as $|V_{out}$ - $V_{LSR}|$ with V_{LSR} as the systemic velocity of the source and V_{out} is the maximum velocity detected in the outflow. Bontemps et al. 1996 found that while Class I objects have a direct relation between their L_{bol} and $F_{outflow}$, Class 0 objects lie an order of magnitude above this correlation (left panel of Fig. 1.13). Moreover, they found a good correlation between the $\mathrm{F}_{outflow}$ and M_{env} (left panel of Fig. 1.13). Their results, later supported by other works in different objects (Curtis et al. 2010, van der Marel et al. 2013), suggest an evolutionary trend, where the force of the outflow decreases as the mass on the envelope is accreted into the central object when passing from Class 0 to Class I. It supports the idea that outflows are driven and necessarily related to the mass accretion rate, as this is reduced for Class I objects when compared to Class 0. Additionally, it provides another way of distinguishing Class 0 and Class I objects, since the former are expected to have more powerful outflows.

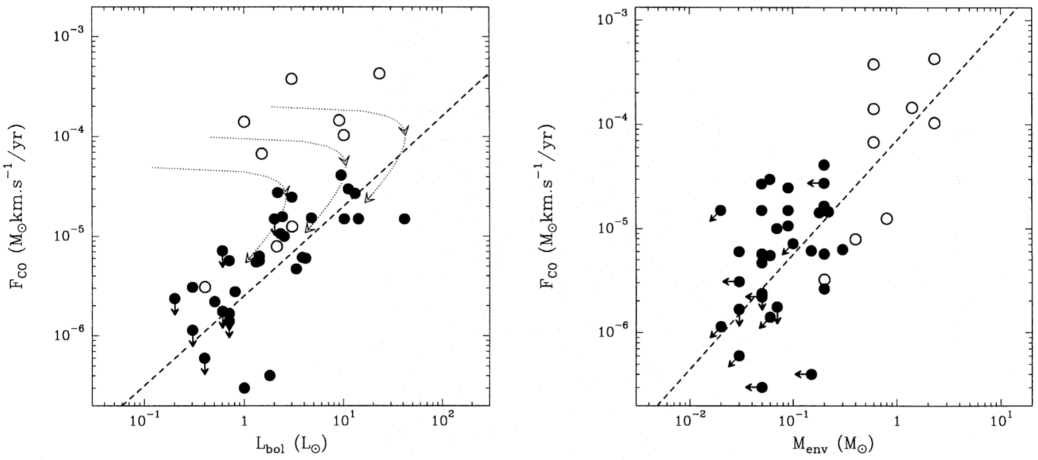

Figure 1.13: *Left*: $F_{outflow}$, measured in CO, versus L_{bol} for Class 0 objects (open circles) and Class I (filled circles). The dashed line represents the best fit for Class I sources. The dotted curves represent evolutionary tracks. *Right*: $F_{outflow}$ versus circumstellar mass for the same objects. The dashed line represents the best fit for both Class 0 and Class I. From Bontemps et al. 1996.

The outflow mass can also be used to determine the ratio of mass accretion vs. mass loss ($\dot{M}/M_{outflow}$), which in turn is useful to constrain how much mass ends up in the central object and the star formation efficiency. Mottram et al. 2017 found that this ratio is close to 1 $\%$, which reduces the star formation efficiency to $\sim$ 50 $\%$ (Machida and Hosokawa 2013). They also found that this value stays constant from Class 0 to Class I. Since the accretion rate decreases with time, so also does the mass that is ejected, maintaining this ratio constant.

Finally, since the processes of accretion and mass ejection are tightly related, any variability on the accretion (i.e., episodic accretion) will have a direct impact on the structure of the molecular outflow (Dunham et al. 2014). Clumpy structures observed in outflows can be linked to different ejection episodes. Although such structures can also be linked to the interaction between outflowing gas and a turbulent medium (Offner et al. 2011), many outflow structures present evidence of kinematic variability which allow to infer timescales for the episodicity of less than 100 to more than 1000 yr (Bachiller et al. 1991, Lee et al. 2009, Arce et al. 2013).

1.4.4 Accretion and infall kinematics

One of the most important problems to completely understand the star formation process is how stars accrete their mass. A variety of models has been proposed to regulate accretion at different scales of the dense core. First, core-regulated accretion assumes mass is channeled from scales of 0.1 pc to 0.1 au, and that the gas infall rate is the same as the mass accretion onto the central object (Krumholz and Thompson 2012). These models, based on the collapse of a simple isothermal sphere, predict $\dot{M} \sim 10^{-7}$ $M_\odot$yr^{-1}. Since most of accretion probably occurs through a disk, it is important to understand disk-regulated accretion. There are two main processes that can redistribute angular momentum to allow mass accretion: viscous torques due to turbulence triggered by magneto-rotational instabilities (MRI) or gravitational torques induced by gravitational instabilities (GI, Balbus and Hawley 1991, Lin and Pringle 1987). Finally, star formation in protostellar clusters is also affected by stellar feedback produced by other stars, such as ionizing radiation, winds and outflows which might disperse star-forming gas. In that case, accretion is regulated by the competition between infall and dispersal of gas (Norman and Silk 1980, Basu and Jones 2004).

Since most of the mass in the central object is accreted during the Class 0 phase, observations of the gas in the envelope should present evidence of infall. Molecular spectra can sometimes present double-peaked profiles, where the blue-shifted component is more intense than the red-shifted one. Those are attributed to optically thick lines tracing infall motions, and they can be used to derive the kinematics of the gas and infall properties (see Chapter 3 for details on infall line profiles).

Single-dish studies have detected these asymmetries in a variety of protostellar objects (Zhou et al. 1993, Gregersen et al. 1997). However, blue-asymmetries can be due to other motions, such as outflow, which the resolution of single-dish telescopes does not allow to distinguish. This was solved with interferometric observations, which allow to pinpoint the origin of the asymmetries (Mardones et al. 1997, Di Francesco et al. 2001, Evans et al. 2015) and to determine mass accretion rates of $\sim 10^{-7}$ - 10^{-4} $M_{\odot}\mathrm{yr}^{-1}$. This wide range of values arises from the fact that the derivation of those values is very model dependent, and models are not well constrained. Moreover, all of them are based on models of symmetric "inside-out" collapse (Shu 1977), which is not necessarily a perfect representation on how the collapse occurs.

1.4.5 Disks

The formation of disks is necessarily tied to the process of star formation, since large disks (radii $\geq$ 100 au) are ubiquitously observed in later evolutionary stages, such as Class I objects (Jørgensen et al. 2009, Wolf et al. 2008, Sakai et al. 2016) or Class II (Hernández et al. 2007, Andrews et al. 2009, Isella et al. 2009, Andrews et al. 2018). The formation of a circumstellar disk is a consequence of the conservation of angular momentum during the collapse of the protostellar envelope during the main accretion phase (Terebey et al. 1984, Shu et al. 1987). For low-mass protostars, if no magnetic field is present, Class 0 disks are expected to form at the radii at which they are observed in later stages, i.e., $\geq$ 100 au.

Observations of disks in protostellar objects are not easy, due to the difficulty of separating the disk and the envelope emission, particularly for the Class 0 phase, where the more massive envelope is responsible for more than 90 % of the emission in the millimeter wavelengths (Looney et al. 2000). Additionally, there is the need of molecular line emission to determine if those disks are rotationally supported and not "pseudo-disks" (small-scales flat structures resembling a disk which are not rotationally supported, Galli et al. 2006). However difficult, surveys have shown that circumstellar disks during the Class 0 phase are common, but rather small. Maury et al. 2019 showed with interferometric observations from the Plateau de Bure Interferometer (PdBI) that large disks, predicted by models, are rare. From their sample, the mean radius obtained for Class 0 was $<$ 50 au, while it increases up to 115 au for Class I (Fig. 1.14). Their results, added to other surveys such as the VANDAM survey (Segura-Cox et al. 2018), indicate that less than only 28 % of the observed Class 0 sources present disks which are larger than 60 au.

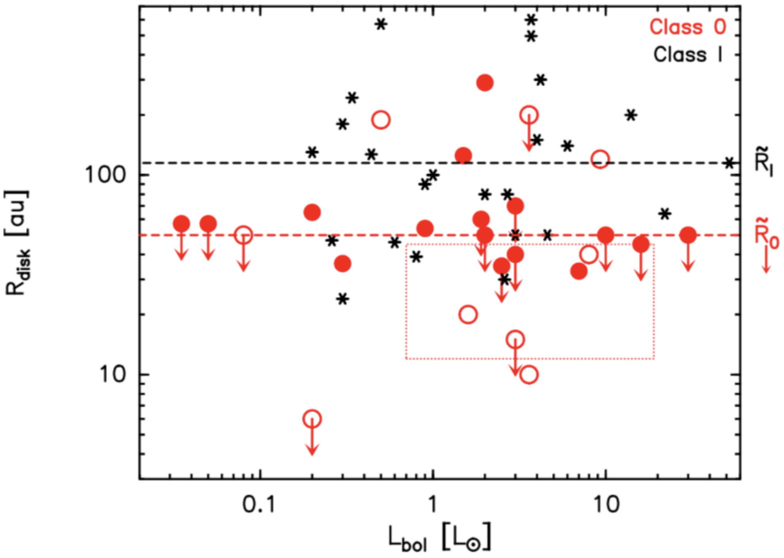

Figure 1.14: Protostellar disk radii as a function of the bolometric luminosity for all Class 0 (red circles) and Class I (black stars) observed in the CALYPSO survey (filled circles) and other works (contour circles). Red arrows show objects for which only an upper limit could be determined. The red box shows the location of the Class 0 disks from the VANDAM sample (Segura-Cox et al. 2018). The dashed lines show the median disk radii in red for the Class 0 and in black for Class I. From Maury et al. 2019.

The occurrence of such small disks can have different origins. First, objects can be too young as to have had time to form a disk. However, this is easily discarded by the presence of outflows, which indicate that accretion has been happening for a few thousands of years, of the same timescale for disk formation as a consequence of angular momentum conservation (Goodwin et al. 2004). The main explanation for this phenomenon is the presence of magnetic fields, and their regulation of the collapse. Models of protostellar collapse including magnetic field have shown that even weakly magnetized cases ($3 < \lambda < 10$) strong magnetic braking occurs, and no rotationally supported disks can form (Galli et al. 2006, Krasnopolsky et al. 2010, Hennebelle and Fromang 2008). This problem is alleviated when misalignment and non-ideal conditions (see Section 1.2.2) are implemented in models, which have shown that in those cases small disks can form (Joos et al. 2012, Hennebelle and Ciardi 2009, Li et al. 2014, Hennebelle et al. 2016). Therefore, the observed properties of disks in the Class 0 stage seem to point out that magnetic fields play an important role in regulating the envelope collapse.

1.4.6 Chemistry in protostellar objects

SFRs are cradles for important astrochemical processes to occur. The study of the chemistry of the initial phases of star formation is key. Initial chemistry on protostellar cores is mainly inherited from the ISM and the parent dense core where they formed (Visser et al. 2009, Visser et al. 2011, Aikawa et al. 2012, Hincelin et al. 2016). Additionally, they are the first step to the chemical evolution and composition of protoplanetary disks, where objects such as comets and planets are formed (Aikawa et al. 1999, Visser et al. 2009, Visser et al. 2011, Yoneda et al. 2016) and eventually life might appear.

Compounds often found in Class 0 objects range from simple molecules (di- and tri-atomic) and molecular radicals or ions, to larger molecules. The variety of more complex molecules might ultimately come from these simple molecules, which are most abundant in the gas-phase, e.g., H_2, N_2 and CO. Chemical processes take place in a wide range of environments with different properties, and the processes that occur for the formation and destruction of the different species is very dependent on those underlying conditions (i.e., density, temperature and/or irradiation) and their evolution during the collapse (Jørgensen et al. 2020). For low-mass protostellar objects there are two models of chemistry depending on the environment and the evolutionary stage of the source: hot corino and warm carbon-chain chemistry (WCCC). However, most YSOs lie in an intermediate state and have a relative content of both chemical products (Graninger et al. 2016, Oya et al. 2017, Higuchi et al. 2018, Law et al. 2018).

Hot corino chemistry is characterized by high abundances of the so-called Complex Organic Molecules (COM), which in an astrophysical context are organic compounds which contain 6 atoms or more (Herbst and van Dishoeck 2009, Ceccarelli et al. 2017), such as methanol (CH_3OH), acetaldehyde (CH_3CHO), formamide (NH_2CHO), and other important molecules for pre-biotic chemistry, e.g., amino acids. Since the observation of these molecules does not only give information on the chemical processes, but they are also used to derive physical quantities and processes (see Section 1.3), all of these molecules have been repeatedly observed in protostellar objects (e.g., Vasyunina et al. 2014, López-Sepulcre et al. 2015, Ceccarelli et al. 2017, Bianchi et al. 2019, van Gelder et al. 2020). Evidence indicates that the formation of COMs takes place on the surface of interstellar grains (Kress and Tielens 2001, Sekine et al. 2006, Garrod and Herbst 2006, Linnartz et al. 2015, Oberg 2016, Ferrante et al. 2000). Moreover, experiments suggest that it is the metallic inclusions present in the grains (e.g., Fe and Ni), which are primarily responsible for the chemical activity in environments such as the ISM or protostellar envelopes (Llorca and Casanova 1998, Ferrante et al. 2000, Cabedo et al. 2021a).

The other model, WCCC, is characterized by the the presence of molecules with long carbon-chains, such as C_2H, C_3H_2 or C_4H (Sakai et al. 2008). Multiple observations of these molecules have been obtained towards cold dark clouds (Kaifu et al. 2004, Sakai et al. 2010) but also towards warmer Class 0/I protostellar sources (Ohashi et al. 1997, Hirota et al. 2009, Sakai et al. 2009, Graninger et al. 2016, Araki et al. 2017, Higuchi et al. 2018). Long carbon-chain molecules are thought to be produced from the evaporation of CH_3OH from the ices surrounding the dust grains (Hassel et al. 2008, Aikawa et al. 2008). This can easily happen in the surroundings of protostellar cores where temperatures gets larger ($>$100 K), but more research is needed to understand how they formed in previous evolutionary stages, such as pre-stellar cores, where the temperatures are lower ($\sim$10 K).

The two different chemistries are thought to arise from differences on the timescale of the pre-stellar phase, when molecules freeze into the surfaces of dust grains (Sakai et al. 2009, Sakai et al. 2013). Short pre-stellar phases (t $\sim 10^5$ yr) will freeze onto grains the parent molecules (H_2, C and few CO), while longer pre-stellar phases (t $\sim 10^6$ yr) will lead to more CO frozen onto the grains. For short pre-stellar phases, CO hydrogenation will be restricted due to the lack of CO in the solid phase, and produce mainly CH_3OH, while for longer phases hydrogenation can proceed further forming COMs directly in the surface of dust grains. As the collapse proceeds and the temperature rises, evaporation of the ices will inject the formed molecules in the gas. For the first case, mainly only CH_3OH will be evaporated and gas-phase chemistry will form WCCC. In the second case, COMs will be directly evaporated into the gas-phase (Aikawa et al. 2020).

Additionally, there are other mechanisms that can induce different chemical processes and contribute to the chemical diversity of the source. Those include shocks or strong UV radiation from near OB stars (Higuchi et al. 2018, Girart et al. 2002).

Deuteration fraction

Deuteration fraction ([D]/[H]) is defined as the abundance (or column density) ratio between a deuterated molecule and its hydrogenated counterpart. In dense regions, such as star-forming dense cores, molecular deuterium enhancement starts with the following chemical reactions (Wootten 1987):

$$\mathrm{H_3}^+ + \mathrm{HD} \rightleftharpoons \mathrm{H_2D}^+ + \mathrm{H_2} + dE_1 \tag{1.24}$$

$$\mathrm{CH_3}^+ + \mathrm{HD} \rightleftharpoons \mathrm{CH_2D}^+ + \mathrm{H_2} + dE_2 \tag{1.25}$$

where $dE_1/k_b \sim 150$ K and $dE_2/k_b \sim 370$ K. It is accepted that the deuteration fraction is set during the early and colder (T $<$ 10 K) pre-stellar phases. The initial deuteration fraction of the core is inherited from the ISM gas (D/H $\sim 10^{-5}$) and it evolves during the pre-stellar phase, since it is affected by the selective freeze-out of neutral molecules, such as CO, N_2 or CS. Neutral molecules are a main destroyer of deuterated molecules, so their depletion from the gas phase allows H_2D^+ to react and form molecules such as DCO^+ or N_2D^+, enhancing the deuteration fraction with respect to the ISM values and reaching values of [D]/[H] > 0.1 (Pagani et al. 2007, Redaelli et al. 2019b). When the protostar is born, and during protostellar evolution, as the temperature of the gas starts to increase molecules that were frozen out will evaporate from the solid phase and deuterated molecules will be destroyed, reducing the deuteration fraction. The D/H ratios set during the pre-stellar phase can survive between 10^4-10^6 yr in the warm gas after the collapse has started (Rodgers and Millar 1996, Osamura et al. 2004), thus, analysis of the deuterium enhancement can provide information about the initial conditions of the gas, and might also be used as an evolutionary tracer (Emprechtinger 2009).

Derivations of the deuterium fraction in low-mass star forming cores can be done using different pairs of molecules which are indicative of different chemical processes taking place at different physical conditions. Single-dish observations of the $[DCO^+]/[H^{13}CO^+]$ have given values on the order of 0.005 to 0.05 (Caselli 2002, Roberts et al. 2002, Jørgensen et al. 2004). Similar values are found for other tracers, such as [DCN]/[HCN] (Roberts et al. 2002), which indicates similarities in the formation routes of DCO^+ and DCN, which form directly from H_2D^+. Other tracers, such as $[N_2D^+]/[N_2H^+]$, show values about one order of magnitude larger, $\sim$ 0.02 to 0.2 (Emprechtinger 2009, Caselli 2002). Since deuteration occurs in the colder envelope and because N_2 is more volatile than CO, molecules such as N_2D^+ and N_2H^+ are more abundant and the deuteration fraction of these molecules is enhanced with respect to CO derivatives.

Observations also support that deuterium enhancement decreases as the protostellar object evolves: as accretion radiation and the temperature increase during the collapse, molecules such as CO evaporate from the dust grains and react to destroy deuterated molecules.

Starless cores have been found to have similar deuteration values as Class 0 objects (Caselli 2002, Jørgensen et al. 2004). It is as the protostar evolves towards Class I that the deuterium fractionation seems to decrease to values one order of magnitude lower ([DCO$^+$]/[HCO$^+$] < 0.001, Jørgensen et al. 2004).

1.5 Class 0 protostellar object B335

This work focuses on the study of the protostellar object B335. The Class 0 protostellar object B335 is an isolated Bok globule (see Section 1.1.1 for the explanation of Bok globules). Since it is not affected by the interaction with any large-scale structure, B335 is an excellent source to test theories of star formation, such as kinematics or the interplay between matter and magnetic field. The globule contains in the center an embedded Class 0 protostar, IRAS 19347+0727, with a bolometric luminosity of $\sim$1.5 $L_\odot$ (Keene et al. 1983, Stutz et al. 2008, Watson 2020). It lies at a distance of 164.5 pc (Watson 2020) with centroid position at α = 19:37:00.9 and δ = +07:34:09.6 in the J2000 system, corresponding to the millimeter peak of dust continuum from high resolution maps (Maury et al. 2018). The extension of the core is $\sim$ 0.1 pc as observed at millimeter wavelengths (Saito et al. 1999, Yen et al. 2019) and of 0.05 pc as observed in IR bands (Launhardt et al. 2013). Figure 1.15 shows the extension of the core as observed in IR.

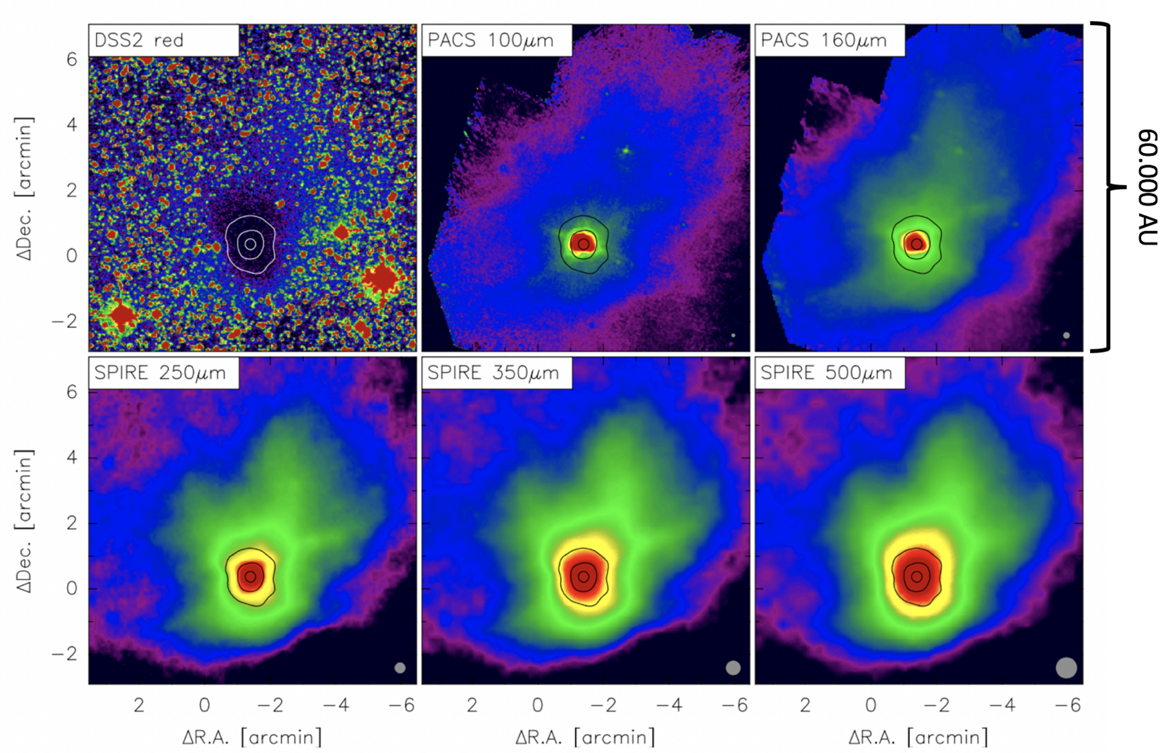

Figure 1.15: B335: Digitized Sky Survey 2 (DDS2) and Herschel FIR maps (color; log scale) at 100, 160, 250, 350 and 500 m with 850 μm contours overlaid (100, 300 and 900 mJy/20" beam). The Herschel beam is shown in gray (Launhardt et al. 2013). The scale is shown on the right considering a distance of 164.5 pc.

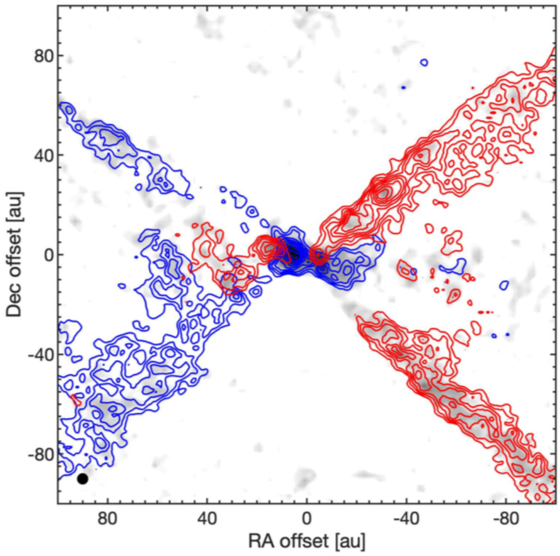

Figure 1.16: ^{12}CO (2-1) integrated intensity emission with a beam of 4 au, integrated from 2.0 km s^{-1}to 10.0 km s^{-1}. Contours are 3σ in steps of 1σ, where σ = 3.3 mJy/beam km s^{-1}. From Bjerkeli et al. 2019.

1.5.1 CO outflow

B335 is associated with an east-west outflow mainly detected in ^{12}CO of 0.02 pc in size, with an opening angle of 45° and an inclination on the plane of the sky of 10° (Hirano et al. 1988, Hirano et al. 1992, Yen et al. 2010, Bjerkeli et al. 2019). It is oriented so that the eastern lobe presents blue-shifted emission and the western lobe presents red-shifted emission. Very high angular resolution observations of the CO emission (Fig. 1.16, Bjerkeli et al. 2019), reveals an X-shaped morphology of the outflow, with most of the emission detected along the arms of the cavity walls.

The outflow is also associated with high-velocity (160 km s^{-1}) and compact ($\sim$1500 $\times$ 900 au) jets seen in ^{12}CO (2-1) emission (Yen et al. 2010), as well as Herbig-Haro objects (HH 119 A-F, Reipurth et al. 1992, Gâlfalk and Olofsson 2007).

1.5.2 Core's rotation

The kinematics of the core has been studied at very different scales: from 20,000 to $\sim$10 au. The large scale envelope ($>$ 2500 au) has been found to be slowly rotating (0.04 km s^{-1}, Frerking et al. 1987, Saito et al. 1999, Yen et al. 2010, Yen et al. 2011), with a flattening profile at $\sim$1000 au, suggesting no rotation is present at smaller scales (Kurono et al. 2013). However, signs of rotation at small scales (10 - 1000 au) have been detected from CH_3OH and SO emission (Yen et al. 2015, Imai et al. 2019, Bjerkeli et al. 2019), but no sign of rotation is detected at less than 10 au (Yen et al. 2015, Bjerkeli et al. 2019). When comparing the small scale rotation derived from velocity gradients with the expected protostellar mass, it is found that the rotation has not yet reached Keplerian velocity and that no signature of a disk is present at more than 10 au. The expected radius of the rotating Keplerian disk in B335 is estimated to be 1-3 au (Yen et al. 2015). Figure 1.17 shows the specific angular momentum of the envelope rotation for B335 at different scales compared to other sources.

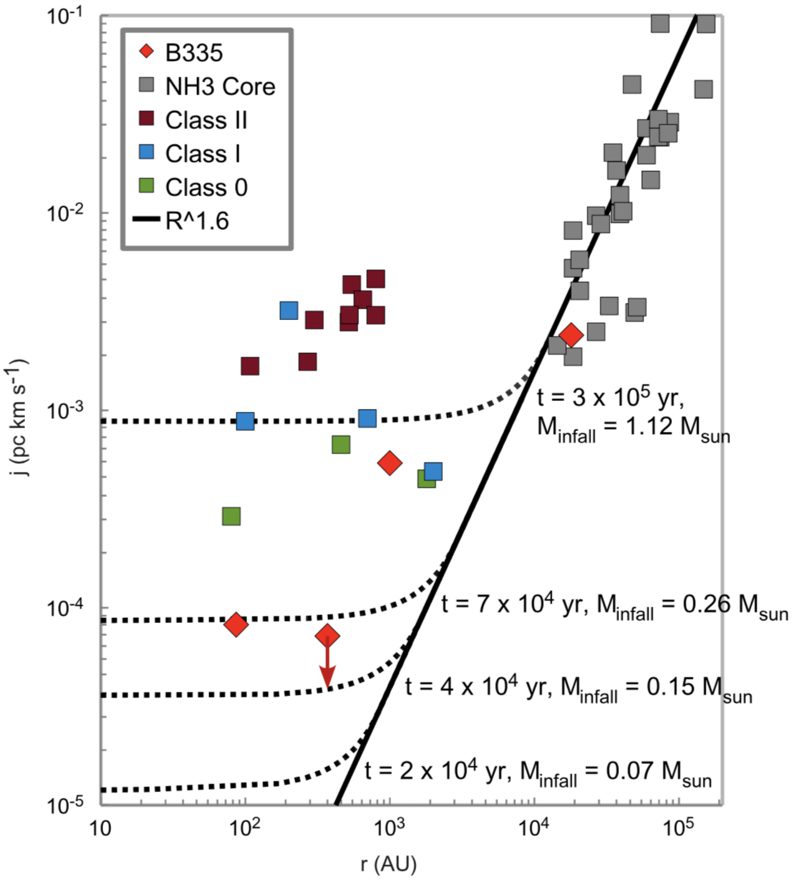

Figure 1.17: Diagram of the specific angular momentum of the envelope rotation plotted as a function of the radius. Red diamonds show values of the envelope rotation in B335 (Saito et al. 1999, Yen et al. 2010, Yen et al. 2011). The red arrow show the upper limit of the envelope rotation at 370 au. Gray squares represent specific angular momenta in NH_3 cores, and the black line is the power-law relation between the core size and the angular momenta (Goodman et al. 1993). Green, light blue, and dark red squares show values of specific angular momenta of disks or envelopes in Class 0, I and II respectively. Black dashed curves show the expected quantitative evolution of the profiles of specific angular momentum of infalling and rotating envelopes at t = 2, 4, 7 and 30 × 10^4 yr after the beginning of the collapse, and the masses within the infall radii are 0.07, 0.15, 0.36 and 1.12 $M_\odot$ at those times, respectively. From Yen et al. 2011.

1.5.3 Infall profiles in B335

Blue-asymetries were detected first in B335 in the work of Zhou et al. 1993 from H_2CO and CS emission. By modeling the lines with density and velocity profiles obtained from the inside-out collapse models, Shu 1977 they derived an infall radius of 30″ (0.036 pc at their considered distance of 250 pc) and a total mass in the center ($M_\star$ + M_{disk}) of 0.42 $M_\odot$. Since then, double-peaked profiles in this source have been attributed to infall motions and have been used to compute infall rates under the assumptions of symmetrical collapse and optically thick line emission (Yen et al. 2010, Evans et al. 2015, Yen et al. 2015), obtaining large uncertainties results that range from 10^{-7} $M_{\odot}$yr^{-1} to $3{\times}10^{-6}$ $M_{\odot}$yr^{-1} at radii of 150-2000 au, with infall velocities from 1.5 km s^{-1} to 0.8 km s^{-1} at radii of $\sim$100 au.

These common features are analyzed under the strong assumption that emission from these lines is optically thick, and that double-peaked profiles are caused by this effect (e.g., if the line is double-peaked, emission is optically thick). It should be noted that while most of these cited works are able to obtain results under these assumptions, they have very large errors associated, and this is because the models are not completely able to reproduce the observed line profiles (Zhou et al. 1993, Evans et al. 2005, Evans et al. 2015).

While complex velocity patterns on the line profiles across this source have also been observed (see Figs. 1, 2, and 3 in Zhou et al. 1993) the symmetrical inside-out collapse model has hardly been questioned in B335, since observations did not seem to require any additional explanation. Velusamy et al. 1995 also observed these characteristic line profiles in CCS single-dish observations and concluded that the line was coming from optically thin emission and, therefore, that the physical conditions in the source were not spherically symmetric.

1.5.4 Mass and Age

Probably the best estimation of the actual age of B335 comes from the study of the CO outflow. The dynamical time of the outflow has been found to be $\sim 3 \times 10^4$ yr (Stutz et al. 2008), which supports a young age for the object.

The mass on the central object can be derived from mass accretion rates, which are obtained from infall profiles observed in the spectra. Considering the derived accretion rates of 10^{-7} to $\sim 10^{-6}$ $M_{\odot}$yr^{-1}(Yen et al. 2010, Evans et al. 2015, Yen et al. 2015) and the age derived from the outflow, this implies an accreted mass into the central object of $\sim$0.04 - 0.15 $M_{\odot}$. The mass obtained from the integrated dust continuum emission inside 25 au is of the order of $\sim 10^{-3}$ $M_{\odot}$. Since the accreted mass is already larger than the remaining mass in the envelope, this points to a slightly larger age of the system.

Another point to consider B335 as a very young object is the non-detection of a Keplerian disk at more than 10 au (Yen et al. 2015). While this could be an effect caused by the presence of a strong an ordered magnetic field at small scales (Maury et al. 2018, see Chapter 4), it could also indicate that the system did not have time to accrete enough mass to form a large disk.

Finally, another estimation of B335 young age are the proper motions of the HH objects observed, which indicate dynamical timescales of a few hundred of years (Reipurth et al. 1992).

1.5.5 Magnetic field

Polarimetric observations of the dust continuum of B335 were obtained at large scales ($\sim 10^3$ - 10^5 au) at IR and sub-millimeter wavelengths with the Very Large Telescope (VLT) and the New Technology Telescope (NTT) by Bertrang et al. 2014. The polarization degree on the source was obtained to be large (2 % $<$ P $<$ 10 %) and extending from the inner part of the envelope ($\sim 10^3$ au) to the outer and less dense parts (10^5 au). Those observations allowed to derive the magnetic field strength, which they observed to vary from $\sim$ 12 μG to

40 μG, depending on the region. Polarization observations with Stratospheric Observatory For Infrared Astronomy (SOFIA), at $\sim$ 5000 au, show a similar morphology of the large scale field, but present a hole in the polarization maps at the center of the core (Zielinski et al. 2021). Those observations derived a magnetic field strength of $\sim$ 140 μG.

The magnetic field was mapped at smaller scales ($\sim$50-1000 au) using polarization observations of the 1.29 mm dust continuum obtained with ALMA (Maury et al. 2018). The high resolution and sensitivity of the data allowed to observe the details of the structure of the field, which presents a highly organized structure with the typical hour-glass shape. The pinching of the field lines around the center of the object, produced by infalling matter, is well observed. The field has two prevailing orientations, one tracing the equatorial plane align in the north to south direction, though it is only observed in the northern region, and another one tracing the outflow cavities, due to the efficient grain alignment on the cavity probably from strong irradiation in that region. Their results are supported by the observations at even smaller scales ($<$ 100 au) done by Yen et al. 2020, where the pinched structured of the magnetic field is also observed. Maury et al. 2018 observations also allowed to derive a value of the magnetic field strength, which is found to be 300-3,000 μG at scales from 50 to 500 au, which is much higher than model predictions ($\sim$130 μG at 100 au scales, Wolf et al. 2003), and also larger than what is found at larger scales (Bertrang et al. 2014).

Overall, the observations of the magnetic field in B335 show the evolution of the field morphology from large scales, 10^3 - 10^5 au, to a very pinched and organized morphology at smaller scales, 10^2 - 10^3 au (Fig. 1.18). This is an agreement with the magnetic field lines being strongly dragged inwards during the collapse, enhancing the magnetic field strength, suggesting a good coupling between the gas and the field.

Observations of the magnetic field alignment with the outflow axis, used as a proxy for the rotational axis (Galametz et al. 2018, Galametz et al. 2020) indicate the alignment is good, and that the angular momentum contained in the gas is small. However, only models of the magnetic field morphology with small misalignment, 15 °, are able to reproduce both the north-south component and the outflow component (Yen et al. 2020).

The magnetic field topology suggests there is little room for rotation at scales smaller than 500 au (Maury et al. 2018), which is supported by the slow rotation found at those scales and the fact that no rotationally supported disk has been observed at more than 10 au (Kurono et al. 2013, Yen et al. 2015). Overall, these results suggest that the effect of the magnetic field in B335 is large, and that magnetic braking might be very efficient in regulating the collapse in the source. This makes B335 an excellent candidate to study magnetically regulated collapse in a Class 0 object.

1.5.6 Chemistry

B335 is not only an excellent bed-test for physical models of star formation, but it is also a fantastic source to test astrochemical models. Molecular lines in the envelope of B335 have been observed with different telescopes and extensively studied. The CO molecule has been extensively reported to trace the outflow (Langer et al. 1986, Bjerkeli et al. 2019), whereas its less abundant isotopologues trace the colder envelope (Frerking et al. 1987, Chandler and Sargent 1993, Evans et al. 2005, this work). Derivatives of CO are also reported, such as H_2CO (Zhou et al. 1990, Zhou et al. 1993, Choi et al. 1995, Evans et al. 2005) and its ionized isotopologues, such as HCO^+ (Hasegawa et al. 1990, Evans et al. 2005, this work).

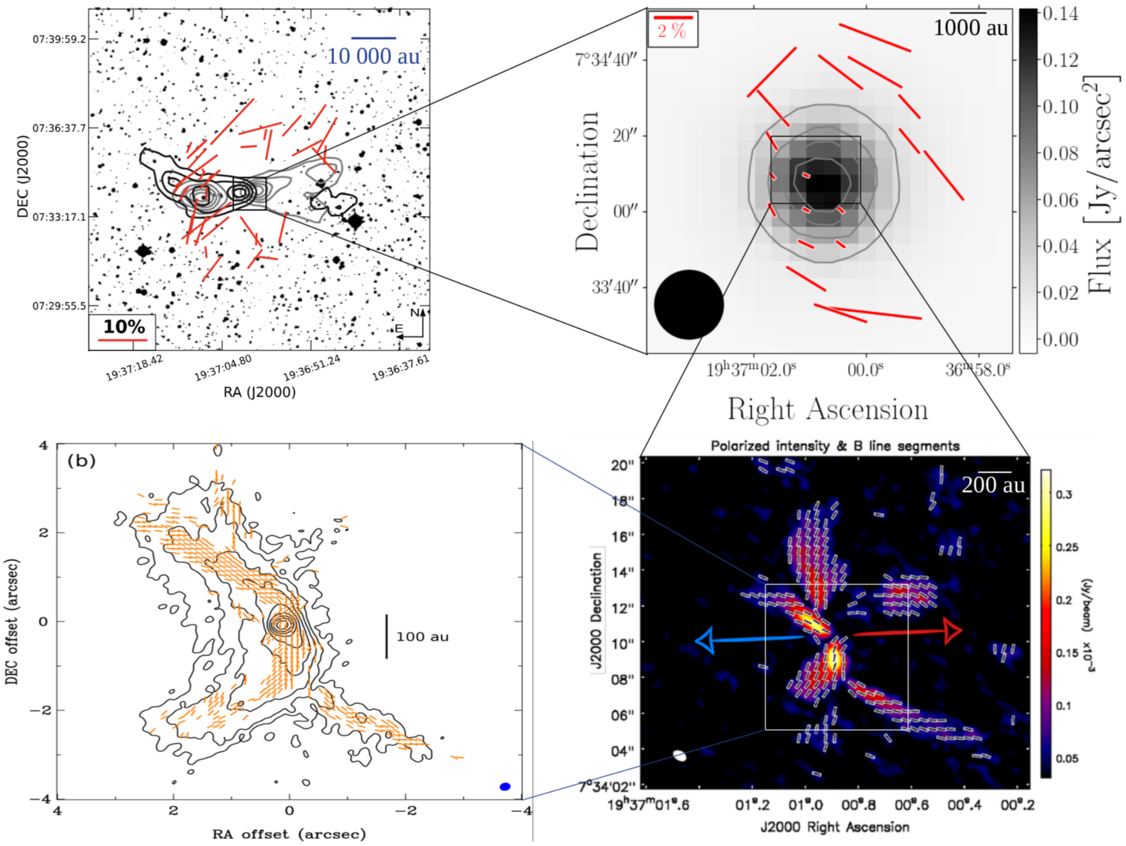

Figure 1.18: Dust polarization maps and corresponding magnetic field structure (in vectors) of B335 at different scales. Reproduced from Zielinski et al. 2021. *Top left*: Polarization map in the near-IR (1.24 μm with the DSS intensity map, from Bertrang et al. 2014). *Top right*: Polarization map of the far-IR (214 μm with SOFIA intensity map, from Zielinski et al. 2021). *Bottom right*: Polarization map in the mm regime (1300 μm with the ALMA polarized intensity map, from Maury et al. 2018). The arrows indicate the outflow direction. *Bottom left*: Polarization map in the mm regime (870 μm, with the ALMA continuum intensity map, from Yen et al. 2020).

Nitrogenated molecules and ions are also well studied, e.g., HCN and N_2H^+, and its isotopologues (Choi et al. 1999, Evans et al. 2005, Evans et al. 2015). Sulfur containing molecules are present in the envelope as well, such as CS (Zhou et al. 1993, Choi et al. 1995, Velusamy et al. 1995), or SO and SO_2, which is found at small scales at the center of the source, tracing either the accretion disk or the accretion shock (Bjerkeli et al. 2019, Ramsey et al. 2020, this work). Other molecules include, for example, SiO which traces the jet (Ziurys et al. 1989, Imai et al. 2019, Bjerkeli et al. 2019, Ramsey et al. 2020).

In addition, B335 also presents a hot-corino chemistry, it is rich in COMs and deficient in carbon-chains molecules (Imai et al. 2016). Compounds such as CH_3OH (Imai et al. 2019, Bjerkeli et al. 2019, Ramsey et al. 2020), have been clearly detected , along with other tentative detection of NH_2CHO, acetone (CH_3COCH_3), dimethyl ether (CH_3OCH_3), ethanol (C_2H_5OH), and ethyl cyanide (C_2H_5CN, Imai et al. 2016). The abundances of these molecules are $\sim10^{-9}$ (Imai et al. 2016), similar to what is found in other prototypical hot-corinos, such as IRAS 16293-2422 (Jaber et al. 2014) or NGC1333 IRAS 4A (Taquet et al. 2015). The emission of these molecules originates from a region between 10 to 55 au, where warmer temperatures are able to evaporate these molecules from the ices where they formed (Imai et al. 2016).

1.6 Thesis framework

As mentioned during this introduction, the isolation of B335 makes it an excellent object to study different kinematics and dynamical processes during the first stages of the star formation process without the influence of an external large-scale structure. Particularly, the fact that no disk has been observed at more than 10 au, and that it presents a very structured magnetic field, leads to think that magnetic braking is very efficient and that the collapse is being strongly regulated by the presence of the magnetic field. Additionally, B335 is a good source to study ionization processes and understand how the chemistry is linked to the coupling of matter and the magnetic field. In order to search for signatures of the magnetic field effect during the collapse, B335 was observed with ALMA to obtain a large interferometric data set with high angular resolution of both dust continuum and molecular line emission. The description of the observations will be given in Chapter 2.

The primary aim of this work was to understand how the chemical conditions, such as the deuteration and ionization fraction, relate the gas to the magnetic field. We wanted to use our observations to search for signatures of the magnetic field effect, constraining the coupling between the matter and the magnetic field, and how it affects the kinematics of the collapse (rotation, infall and redistribution of angular momentum) as well as the computation of the ambipolar diffusion lenghtscale and the magnetic field strength. However, science research is never as easy and straightforward as we would like, our observations proved to be more complex than we expected. Therefore, we were forced to perform a previous analysis of the data focusing on the characterization of infall motions, presented in Chapter 3. In Chapter 4 we discuss the deuteration and the ionization fraction of the gas in the source, with a brief discussion on how these are related to the coupling of the matter with the magnetic field and how it affects the collapse, according to our new vision of the infall mode. Finally, in Chapter 5 we present the conclusions of both studies, and provide some perspectives both for the use of the rest of our large data set and for further advancing in the investigation of the new properties we obtained in the source.

Chapter 2

Interferometric Observations

With the always evolving discovery of smaller and more distant objects in our universe, observational techniques and instruments have been developing to obtain each time better angular resolution observations at all possible wavelengths. Being the size of the telescope, and the unfeasibility of constructing infinitely large dishes the main limitation to obtain such high angular resolution images, interferometry has become the leading technique for such purpose, from the optical to the radio wavelength domains. At a given frequency, this technique allows to combine the signal received by various telescopes or antennas to obtain a single image of an object with an angular resolution corresponding to a single telescope as big as the largest separation between the antennas in the array.

The implementation of interferometry in astronomy has been blooming during the past 50 years or so, thanks to the evolution of radio interferometers, such as the Very Large Array (VLA, United States), the Plateau de Bure (PdB, France) interferometer and its renovation to create the NOrthern Extended Millimeter Array (NOEMA, France), the ALMA facility

(Chile) or the future Square Kilometer Array (SKA, Africa and Australia) and other bigger projects at global scale to allow very large baselines, and therefore exquisite resolution, such as the Very Large Baseline Array (VLBA, United States) or the Event Horizon Telescope (EHT).

This chapter presents a general explanation of the intereferometric principle, and its application in radio astronomy (Jackson 2008, Asayama et al. 2016). For a more complete explanation of the technique, the reader can consult Wilson et al. 2013. We provide a short description of the ALMA facility, from where our data was obtained. And finally, we present the ALMA project and the obtained data, along with the data reduction process.

2.1 Principles of Interferometry and radio astronomy

Generally speaking, interferometry is a technique which uses the phenomenon of waves interference to extract information from an object or a process. When two, or more, waves cross each other, be it light or mechanical waves, they will superimpose and interfere to create an alternate pattern of increased and decreased amplitude. For constructive interference to occur between them, the waves need to be coherent, meaning that their frequency and waveform are the same. This technique very useful in different areas of research, for example in the field of communication and optics, seismology, spectroscopy or astronomy.

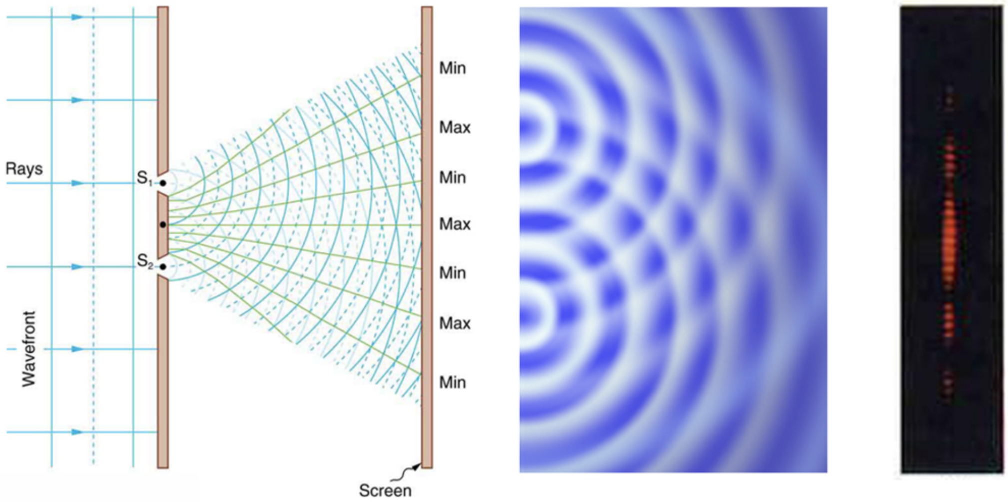

Figure 2.1: Principle of the Young experiment. *Left*: Set up of the experiment and the interference expected. *Center*: Interference pattern of the waves. *Right*: Pattern that would be observed in the second screen. Credit: PASCO.

2.1.1 Young's slits

Interferometry begins in 1801-1803, when the English scientist Thomas Young presented his work "On the Theory of Lights and Colours" and described his interference experiment which discarded the corpuscular vision of light in favor of an undulatory theory. In his experiment, a monochromatic source of light illuminates a screen with two holes, or slits, and is projected on a second surface, which intercepts the radiation (see left panel of Fig. 2.1).

Since the two secondary sources (i.e., the light traversing the two holes) are produced by the same monochromatic primary source, they will be coherent and interference fringes will be observed on the secondary screen. This is due to constructive and destructive interferences (see right panel of Fig. 2.1) which depend on the relative delay between the rays coming from the two new light point sources. The separation of the fringes is λ/d, where λ is the wavelength of the light and d is the separation between the slits.

Now, if the source is made wider, it can be interpreted as a sequence of point-like source, whose radiation will be incoherent. The total interference intensity pattern, $I(\Theta)$, is the sum of the individual patterns. Since the angular displacement of the source produces an angular displacement in the fringe pattern, as the source approaches λ/d, the fringe patterns adds to a constant. Then, the fringe visibility, $V(d)$, which is defined as the difference between the maximum and minimum intensity, drops to zero. On the contrary, for a source of size $<< \lambda/d$, the fringe visibility is 1. If the slit spacing is decreased, for the same size of the source, the disappearing of the fringes is lower because the same displacement of the source produces less displacement on the pattern. Figure 2.2 shows for a given source distribution, the variation of the visibility with the slit separation. The relation between $I(\Theta)$ and $V(d)$ is a Fourier Transform (FT), and it is the basis for the application in real interferometers.

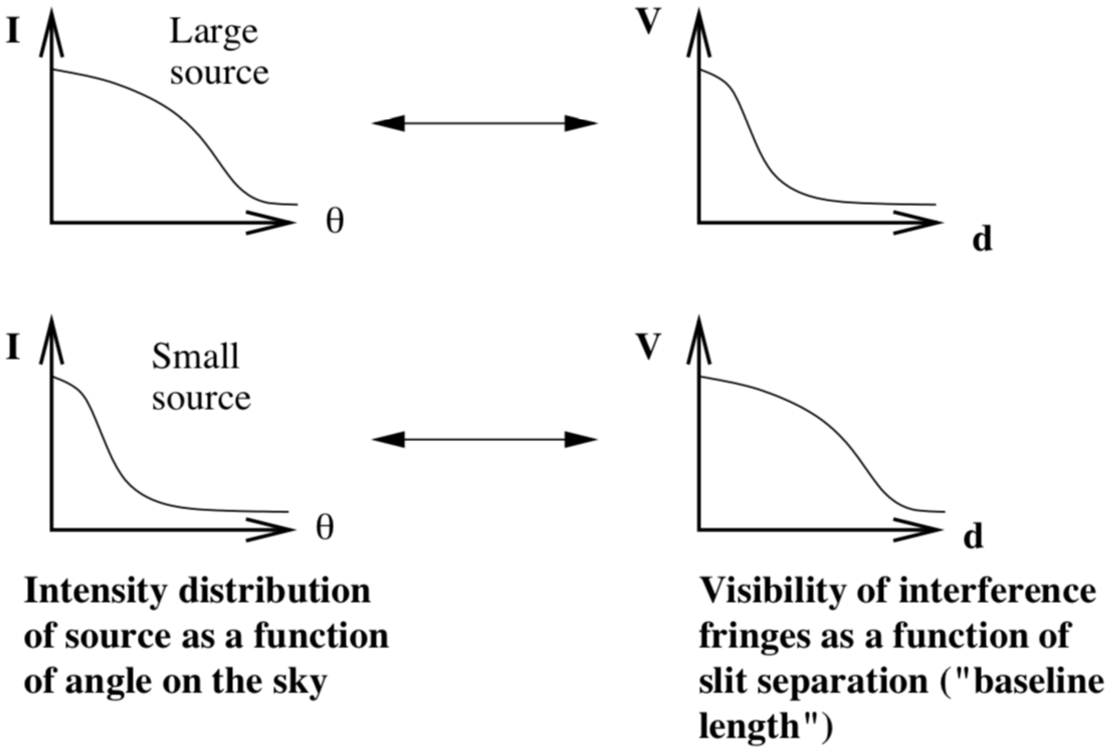

Figure 2.2: Relation between the source brightness as a function of angular distance and visibility interference fringes as a function of slit separation. From Jackson 2008.

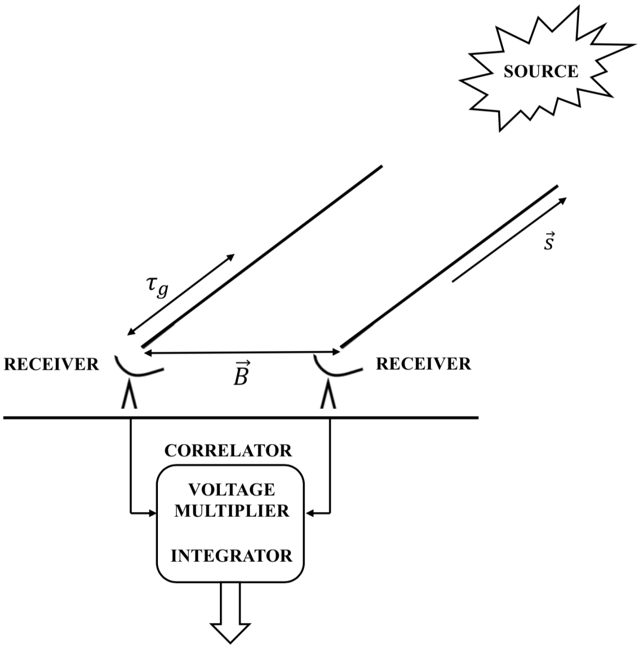

Figure 2.3: Schematic representation of a two antennae interferometer. b is the vector separating both antennas, or the baseline, $\vec{s}$ is the unit vector in the direction of the source. The phase delay between both antennas is given by τ_g. The signals of the antennas is transformed and amplified before sending it to the correlator.

2.1.2 Real interferometers

Interferometers in astronomy make use of the interferometric principle in order to obtain spatial information from an astronomical source. In practice, a plane wave coming from the source is sampled by two telescopes separated by a vector $\vec{B}$. The path delay between the waves reaching the two antennas is given by $\vec{B} \times \vec{s}$, where $\vec{s}$ is the unit vector in the direction of the source and the phase delay, τ_g, is given by $\frac{2\pi}{\lambda}\vec{B} \times \vec{s}$ (see Fig. 2.3).

The two antennas, A_1 and A_2, measure the incoming electric field. Due to the phase delay if A_1 measures an electric field such as $\vec{E_1} = \vec{E_0}$, then A_2 measures $\vec{E_2} = \vec{E_0} \times \exp(\frac{-2i\pi}{\lambda}\vec{B} \times \vec{s})$. If the source is point-like, the correlation function $R =< \vec{E_1}\vec{E_2}* >$ is written as:

$$R = I_0 \times \exp(\frac{-2i\pi}{\lambda}\vec{B} \times \vec{s}) \tag{2.1}$$

where I_0 is the brightness of the source. If the source is not point-like, which is usually the case in astronomy, Eq. 2.1 becomes the integral over the spatial extent of the source, such as:

$$R = \int_{source} I_0(\vec{s}) \times \exp(\frac{-2i\pi}{\lambda}\vec{B} \times \vec{s})\vec{ds} \tag{2.2}$$

Then, the interferometer response produces a series of fringes with a given visibility. The visibilities are complex quantities, which contain a real term, the amplitude, or the FT of the brightness distribution of the source, and an imaginary term, the phase.

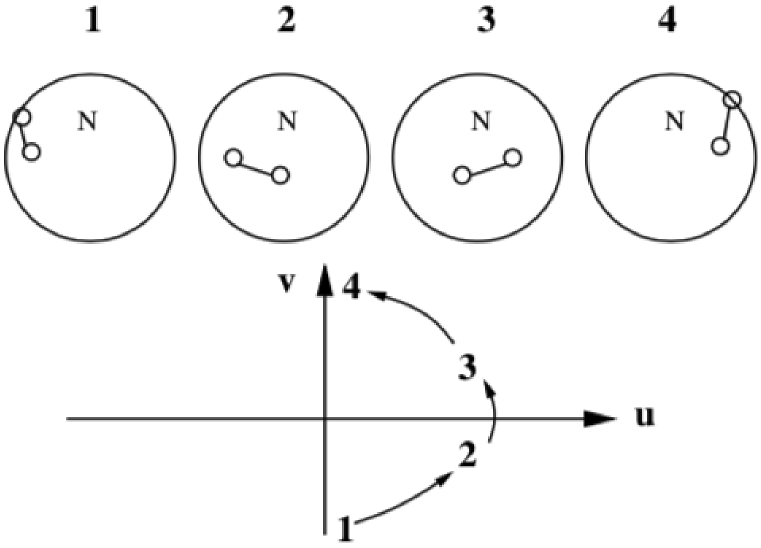

Figure 2.4: Schematic diagram showing the baselines between the two telescopes as the Earth rotates and its respective sampling of the *u,v*-plane. From Jackson 2008.

2.1.3 The *u,v*-plane

The next step is to decompose both $\vec{s}$ and $\vec{B}$ into Cartesian coordinates and transform the intensities to the spatial frequency plane (the Fourier plane or the *u,v*-plane). Considering that the source is at a very large distance, the decomposition of $\vec{s}$ and $\vec{B}$ is just a vector in the sky plane such as $\vec{s}$ = $s_x\mathbf{i}$ + $s_y\mathbf{j}$ and $\vec{B}$ = $b_1\mathbf{i}$ + $b_2\mathbf{j}$, where **i** and **j** are unit vectors in the east-west and north-south directions respectively. Then the response of the interferometer becomes:

$$R = \int\int_{source} I_0(s_x, s_y) \times \exp(\frac{-2i\pi}{\lambda}(b_1 s_x + b_2 s_y))ds_x ds_y \tag{2.3}$$

Which transformed into the *u,v*-plane, where $u=b_1/\lambda$ and $v=b_2/\lambda$, results in:

$$R = \int\int_{source} I_0(s_x, s_y) \times \exp(-2i\pi(us_x + vs_y))ds_x ds_y \tag{2.4}$$

For each pair of antennas we obtain R only at two points of the *u,v*-plane: *u,v* and *-u,v*. However, the projected baselines in the *u,v*-plane change with Earth's rotation, modifying as well the projected visibilities. Then, for each pair of antennas the *u,v*-plane is sampled in an ellipse, which depends on the baselines, the latitude of the telescope and the position of the source in the sky. Figure 2.4 shows the evolution of the *u,v*-plane sampling for two antennas. Studying the variation of the interferometer response R (amplitude and phase), over a period of time it is possible to retrieve the source structure by taking the FT of R.

2.1.4 Imaging interferometric data: Deconvolution and the CLEAN algorithm

The major problem, which differentiates interferometry from direct imaging, is that the interferometer response does not sample the full *u,v*-plane, and only provides a measure for the finite number of baselines. This means, that there is a large number of images that could fit the data.

The real intensity distribution of the source, the image plane, $I_0(s_x, s_y)$, resulting from the *u,v* response function $I(u, v)$ can be written as:

$$I(s_x, s_y) = \int\int I(u, v) \times \exp(-2i\pi(us_x + vs_y))dudv \tag{2.5}$$

but instead, the interferometer gives the "dirty image" which corresponds to the image in the *u,v*-plane convolved by the sampling function $S(u, v)$ that gives information of which baselines have been sampled: $S(u, v)$ is 1 for the sampled parts of the *u,v*-plane, and 0 where there is no measure. The dirty image can be expressed such as:

$$I_D(s_x, s_y) = \int\int I(u, v)S(u, v) \times \exp(-2i\pi(us_x + vs_y))dudv \tag{2.6}$$

Using the convolution theorem, the "dirty image" can be expressed as the convolution of the real intensity distribution convolved by the "dirty beam", $B(s_x, s_y)$, which is just the FT of the sampling function.

$$I_D(s_x, s_y) = I(s_x, s_y) * B(s_x, s_y) \tag{2.7}$$

$$B(s_x, s_y) = \int\int S(u, v) \times \exp(-2i\pi(us_x + vs_y))dudv \tag{2.8}$$

Since the sampling function and the "dirty beam" are known from the telescope position, recovering the real intensity distribution requires the deconvolution of the "dirty image". This can be done with the CLEAN algorithm (Högbom 1974). Basically, the algorithm finds the brightest point in the dirty map by shifting the dirty beam to this point and subtracting it off. This is done iteratively until the residual map (the map from which the beams have been subtracted), consists only of noise. The subtracted fluxes are convolved with a restoring Gaussian clean beam to give a final "clean map". An example of imaging procedure is given in Example 3.

Data weighting

Because the obtained data is not uniformly sampled across all the *u,v*-plane, an important parameter of the CLEAN algorithm is the relative weight of each data point in the sampling function $S(u, v)$. In addition to the sampling function obtained, a weighted visibility function can be defined, such as (Asayama et al. 2016):

$$S^W(u, v) = \sum_{k=1}^{N} R_k T_k D_k S_{u,v}, \tag{2.9}$$

where R_k, T_k and D_k are weights given to the data. R_k is a noise-variance weight derived from the sensitivity of the measure. It depends on factors such as the integration time, the system temperature (T_{sys}, see Section 2.1.5) and the bandwidth, which are in turn determined by the instrument and are not controlled by the imaging process. T_k is a "taper" weight that can be used to down-weight the longest baselines and to reduce small-scale side-lobes increasing the beam size and sensitivity. If not modified during the imaging process, T_k = 1. Finally, D_k is a *u,v* density parameter that can be used to to offset the usually high concentration of measurements near the center of the *u,v*-plane. The choice of D_k will determine the sensitivity and S/N of the produced map, as well as the angular resolution or the size of the beam. There are mainly three weighting options:

1. Natural weighting ($D_k = 1$): All data points are treated equally, with the same weight as they had in the observations. This provides the maximum sensitivity and S/N, however because most of the original weights are concentrated towards the center, the dirty beam is more extended and the final angular resolution of the map is worse.

2. Uniform weighting ($D_k = \frac{1}{N_s(k)}$): The weight of the data point is given by the original weight of the point divided by the total number of data points in a region centered on the k^{th} visibility ($N_s(k)$). This gives an increased resolution, however, because most of the central data points are weighting down (since they are more numerous), it degrades the sensitivity and the S/N.

3. Briggs weighting: It generates a distribution that varies smoothly between Natural and Uniform weighting, depending on the Robust parameter. The weight of a data point is computed according to this parameter, which can vary from -2 (uniform weighting) to +2 (natural weighting). Because it allows a customized weighting, it can reach different intermediate values between the sensitivity and the angular resolution.

2.1.5 Atmospheric problems and data calibration

Earth's atmosphere introduces alterations in the plane wave that arrives from the source. At radio frequencies, such as the ones used in this study, the main problem is water vapor, which introduces phase incoherence of few minutes for frequencies above 10 GHz, and successively shorter variations as the frequency goes up, producing phase variation of the orders of seconds in the mm regime. The amplitude is also affected with variations of the order of minutes. This problem can not be ignored, since it affects the interferometer response R and it can wipe up the observed fringes, and therefore the data needs to be calibrated to account for the atmospheric fluctuations.

The calibration procedure is complex and involves different stages. It includes *on-line* calibrations (i.e., when the observations are taking place), *off-line* calibration (i.e., after the data have been obtained) and optional further calibration, such as self-calibration. They are briefly described in this section, with their main features explained (Asayama et al. 2016).

On-line calibrations

There are three main procedures for the *in situ* calibration of the data. ALMA antennas and receivers are equipped with additional hardware that allows to account for atmospheric and temperature variations during the observation time.

Fluctuations on the line-of-sight (the straight line between the object and the observer, LOS) water vapor are measured by a Water Vapor Radiometer installed in all 12-m antennas. It measures the emission of the atmospheric water line in four spectral frequencies, and transforms this emission into appropriate delay changes.

At ALMA frequencies, additional random noise can be produced by (i) the noise associated with the receiving system, due to the temperature of the receivers, and (ii) the noise associated with atmospheric transmission, which acts as a black body emitter, and which depends on the frequency, elevation and the atmosphere composition and temperature. These noises are usually measured as temperatures (receivers temperature, T_{rx}, and sky temperature, T_{sky}). ALMA receivers are equipped with an Amplitude Calibration Device to measure these temperatures, and which give a combined measurement of the system temperature, T_{sys}.

Further corrections can be made during the observations using additional antenna pointing checks. This process is not a calibration *per se*, but the additional pointing compensate for errors on the antennas metrology systems or errors in the hardware, such as those caused by hardware changes with each system update.

Off-line calibrations: Bandpass, Gain and Flux calibrations

The main off-line calibrations consist in observing a source with a well known structure and properties, such as quasars or planets. They are observed periodically during the observation of the target. Afterwards, the structure of the source is removed from the interferometer response, leaving only structures produced by atmospheric contamination. The calibration parameters are obtained by interpolating the solutions at every scan of the calibrator. The artificial structures produced by the atmosphere are then removed from the observations of the target, ideally obtaining only the source structure. There are three main procedures: Bandpass (B), Gain (G) and Flux (T) calibrations.

The response of the receivers across each spectral window will not be flat in amplitude and phase. Most of these delay errors might have been removed during the initial calibrations, but a residual bandpass might be remaining. This is determined using a bright calibrator with a known radio spectral index. First, phase variations are removed and afterwards, phase an amplitude are determined for every antenna and spectral window (SPW) as a function of frequency.

Gain calibration are used mainly to correct for atmospheric variations on amplitude and phase. In order to be used as gain calibrators, the selected source needs to be a point compact source. It needs a good S/N per atmospheric coherence time (the time it takes the atmosphere to alter its properties). The calibrator needs to be close to the target, so the atmospheric perturbation is similar. Finally, the switching between the target and the calibrator must be done in a time shorter than the atmospheric coherence time, so it can be assumed that the same atmospheric effects are being subtracted.

Antennas measure temperatures that need to be transformed from K to Jy. The relationship between this conversion is called the *system equivalent flux density (SEFD)*, and depends on the antenna diameter and efficiency. This relationship is generally very stable, but a more accurate scale can be derived from the measurements of a source with known flux density.

In addition to the calibration, a flagging process can be used to eliminate bad data. Flagging is used during on-line calibration, as ALMA systems contain monitoring systems to indicate data that should be flagged. After the off-line calibration, flagging of data or antennas is also useful to detect faulty data that can only be noticed after the use of calibrators.

The application of these corrections can be done manually. However, ALMA provides an automated *python* script to carry out this procedure, *scriptForPI.py*.

Self-calibration

An additional solution to further refine the calibration process consists in self-calibrating the data, where the same data is used to compute the phase and amplitude corrections. In order to carry out this procedure, the data must have a continuum source which is bright enough, $>20\sigma$. Otherwise the model of the data is not good enough, it becomes noisy and can degrade the quality of the data.

A first model image is generated using the tCLEAN command in the Common Astronomy Software Applications (CASA) from the data visibilities (*.ms*, Measurement Set, CASA visibilities file format). The command *gaincal* is used to determine calibration gains as a function of time from the first model. The correction is derived for each antenna and for a specific time interval, determined by the parameter *solint*. The time interval is reduced at every cycle to correct for variation in shorter times. The new calibration parameters are applied to the data using the *applycal* command and a new image is generated using tCLEAN. The process is done iteratively until the calibration does not improve the S/N and the change between calibration cycles is negligible. Since amplitude variations occurs at longer times than phase variations, the usual procedure is to obtain first the phase calibration parameters at short intervals of time and, afterwards, obtain the amplitude parameters at longer times.

If the observed target contains a strong continuum source, which appears in all the channels, and line emission is peaking only in a small number channels, it is possible to calibrate the line emission data using the continuum model. In this case, once the best model of the continuum is found, it is possible to apply the obtained corrections to line emission data to correct its continuum emission. The continuum intensity depends on the frequency which, in turn, has a different dependence at different frequencies. A good approximation is to apply self-calibration only for line emission which frequency lies at less than 1 GHz from the central frequency of the continuum.

2.1.6 Other radio-astronomy concepts

Single antenna response

The response of a single parabolic antenna varies repeatedly at different scales. Figure 2.5 shows the power response of a typical 12 m antenna with changing angular offset. The central lobe can be approximated by a Gaussian, and corresponds to the primary beam or the antenna beam size, and its given by the Half Power Beam Width (HPBW) = 1.02 λ/D. The interference at larger scales gives the successive sidelobes. The first sidelobes have a relative response of 1.74 $\%$ of the primary beam.

The angular distance between the nulls of the response function is called the Full Width Between Nulls (FWBN) = 2.44 λ/D. Half the FWBN, $\sim$1.22 λ/D, is the resolution of the antenna or its capacity of distinguishing objects separated at a maximum angular distance.

Angular resolution

The angular resolution of the interferometer θ_{res} (i.e., the minimum scale distinguishable in an image) is typically approximated to the FWHM of a Gaussian fit of the central feature of the dirty beam. It depends ultimately on the spatial configuration of the interferometers

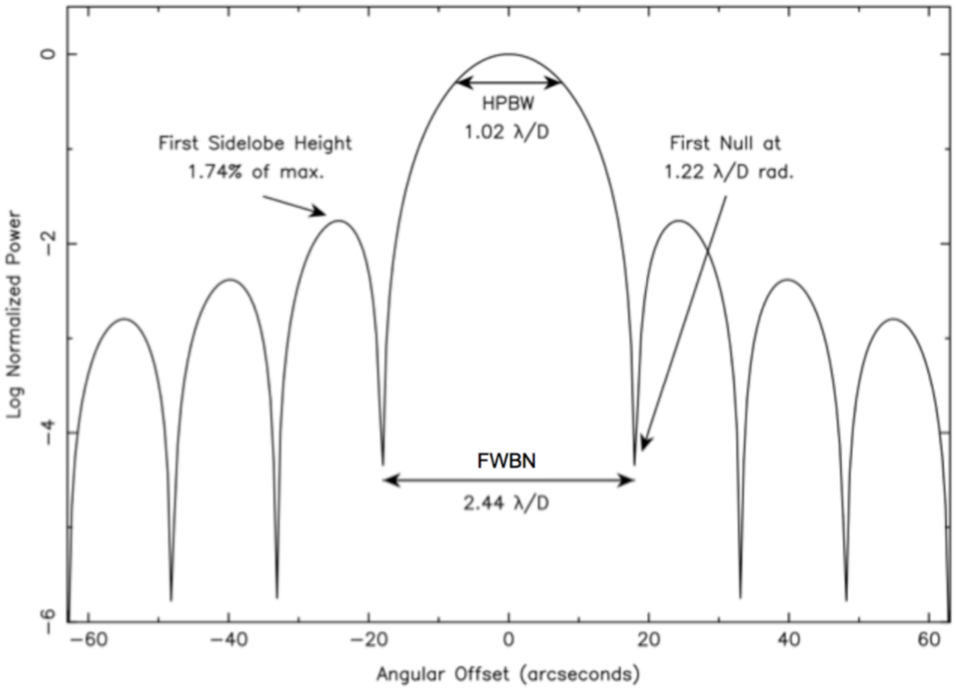

Figure 2.5: Normalized 1-D antenna power response for a 12 m antenna uniformly illuminated at 300 GHz. From the cycle-4 ALMA handbook (Asayama et al. 2016).

and the extent of the longest baseline in such configuration, such as $\theta_{res} \sim 1.2\lambda/\mathrm{B}_{max}$, where B_{max} is the longest baseline, with λ and B_{max} in m.

Largest recoverable scale

An important limitation of interferometry is its insensitivity to large scale emission. This is because the interferometer can not sample *u,v*-plane for baselines smaller than one antenna diameter, or in practice, the smallest baseline. This results on the zero-spacing problems, which is that the *u,v*-plane is not sampled near the center. The largest recoverable scale (LRS) is the maximum spatial scale that an interferometer can recover, such as LRS $\sim$0.6 λ/B_{min}, where B_{min} is the minimum baseline.

Sensitivity

The sensitivity of an interferometer, or its maximum S/N, is given by:

$$S = \frac{\sqrt{2}k_B T_{sys}}{A\eta\sqrt{n_b \Delta\nu t_{int}}} \tag{2.10}$$

where A is the area of each antenna, η is the aperture efficiency, n_b is the number of baselines, $\Delta\nu$ is the observing bandwith and t_{int} is the integration time. T_{sys} is defined as the temperature of a black body which provides the received power at the corresponding frequency. The main sources of thermal noise are: the receivers and the atmosphere (see Sec. 2.1.5) plus spillover emission from the ground and the Cosmic Microwave Background (CMB).

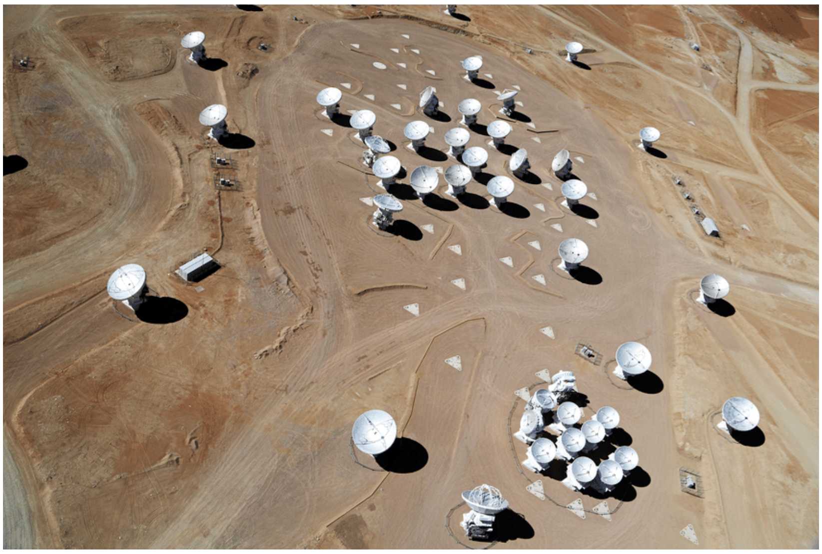

Figure 2.6: ALMA interferometer facilities showing the 12-m Array (top) and the ACA (bottom). Credit: Clem & Adri Bacri-Normier (wingsforscience.com)/ESO.

2.2 ALMA interferometer

ALMA is a state-of-the-art telescope situated at around 5000 m of altitude in the Chajnantor plateau, in the Chilean Andes, operated by an international collaboration (ALMA partnership, ESO, NRAO, NAOJ, Chile). ALMA is comprised of 66 high precision antennas (see Fig. 2.6) observing at millimeter/sub-millimeter wavelengths. Fifty of these antennas have a diameter of 12 m (12-m Array) and are movable, which allows to obtain different *u,v*-coverages. They are used for high-sensitivity and high-resolution imaging. Another twelve closely spaced antennas of 7 m in diameter compose the Atacama Compact Array (ACA) whose compact configuration allows to cover the spacings smaller than those covered by the 12-m array, from 9 to $\sim$30 m. The last four antennas of 12 m in diameter are used for single-dish observations (Total Power Array, TP) to cover the shortest spacing, from 0 to 12 m. The TP can allow wide-field imaging, but it can also be used for calibration of the 7-m array.

2.2.1 Multiconfiguration observations with ALMA

The 12-m array of the ALMA interferometer can be moved to different configurations, a given configuration with a baseline coverage from B_{min} to B_{max} is sensitive to angular scales from the LRS ($\sim \Theta_{LRS}$) to the one given by the angular resolution (Θ_{AR}), following $\Theta_i = k_j \lambda / L_m$, where (i, j, m) = (LRS, 0.6, min); (AR, 1.2, max). However, it is possible to extend this scale coverage by combining data obtained with different configurations. It is also possible to combine 12-m array with ACA or the TP antenna to cover a very large range of scales.

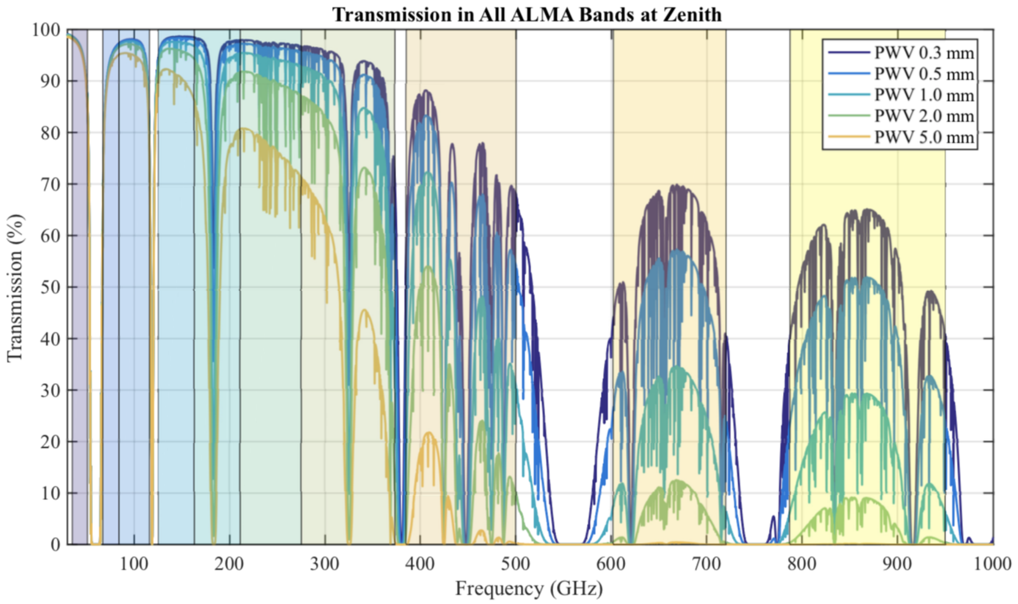

Figure 2.7: ALMA receiver bands plotted along with atmospheric transmission. The receiver coverage is shown shaded, superimposed on a zenith atmospheric transparency plot for 0.3, 0.5,1.0, 2.0 and 5.0 mm of Precipitable Water Vapour (PWV). From the Cycle 4 ALMA handbook (Asayama et al. 2016)

2.2.2 ALMA receivers

ALMA can accommodate up to 10 receiver bands covering most of the frequency range from 35 to 950 GHz, although at the present moment only Bands from 3 to 10 are available (84 to 950 GHz). Band 5 (163 to 211 GHz) was neither available during cycle 4, when the presented observations were taken. Every receiver is tuned to cover a range that is defined by the atmospheric transmissions windows available for millimeter and sub-millimeter observations, mostly due to the presence of H_2O in the lower part of the atmosphere, from the ALMA site. The coverage range of the ten different receivers is shown in Figure 2.7.

2.3 ALMA observations of B335 in this work

Observations of the Class 0 protostellar object B335 were carried out with the ALMA interferometer during the cycle 4 observation period from October 2016 to September 2017 as part of the project 2016.1.01552.S (P.I. A. Maury). The original goal of the ALMA proposal was to constrain the efficiency of magnetic braking during the early stages of star formation, by characterizing the magnetic field coupling and other diffusive processes using observations of molecular lines. Three main goals were envisioned:

1. Derivation of the ambipolar diffusion length-scale (L_{AD}): At small scales, where neutrals decouple from the flux-frozen ions and the magnetic field, the friction between the ions and the drifting neutrals causes the dissipation of turbulent energy (see Sec. 1.2.2, Li and Houde 2008). Under the effect of ambipolar diffusion, the velocity spectrum of ions drops below that of the neutrals, and this effect allows to obtain a mea-

surement of at which scales ambipolar diffusion is relevant on the collapse. This was tested originally in molecular clouds with HCN and HCO^+ (Li and Houde 2008, Li et al. 2014), but those can be optically thick under such conditions and therefore the method was further proved in molecular clouds and high-mass star forming cores using $H^{13}CN$ and $H^{13}CO^+$ (Hezareh et al. 2010, Hezareh et al. 2014), which are less abundant isotopologues and optically thin in most conditions. In this project all of these lines were targeted in order to derive this parameter for the first time in a low-mass core.

2. Deuteration and ionization fraction: Since the deuteration enhancement is limited by the rate at which electrons and neutrals destroy H_2D^+, the deuteration fraction is closely related to the ionization fraction. Following Caselli et al. 1998, the proposal aimed to obtain the deuteration fraction using DCO^+ and HCO^+ (or $H^{13}CO^+$ if the later is optically thick) abundance ratio.

3. Computation of the cosmic ray ionization rate (ζ_{H_2}): Following Hezareh et al. 2008, the proposal aimed at measuring abundances of HCO^+ and CO to provide an estimate of the H_3^+ abundance which can be used to compute the cosmic ray ionization rate.

4. Additionally, the derivation of the ambipolar diffusion length-scale and the ionization fraction might allow to compute the magnetic field strength. This might allow to constrain the importance of the magnetic field during the collapse in this particular object.

With these goals in mind, Band 3 and Band 6 observations were proposed, divided in 4 different spectral setups:

1. Band 3: The (1-0) transitions of CO isotopologues (^{12}CO, $C^{18}O$ and $C^{17}O$) for the computation of ζ_{H_2}.

2. Band 6: The DCO^+ (3-2) observations to obtain deuteration and ionization rates.

3. Band 3: The (1-0) transitions of HCO^+, $H^{13}CO^+$ and HCN to derive the ambipolar diffusion lengthscale and for the computation of ζ_{H_2}.

4. Band 6: The $H^{13}CO^+$ (3-2) for ζ_{H_2} estimation, plus $H^{13}CN$ (3-2) for the derivation of the ambipolar diffusion lengthscale.

Additionally, the full bandwidths were used to target additional lines, such as SO (5_5 - 4_4), HC_3N (12-11), HC_3N (27-26) and N_2D^+ (3-2). Those lines were used to obtain complementary information on the source on processes such as deuteration or disk accretion kinematics. Finally, we serendipitously detected other tracers, such as CH_3OH and HDCO. Those lines were not used during this work and their assignation should be considered tentative.

2.3.1 Technical details

In the project, a set of molecular lines and continuum emission were targeted using multiple ALMA configurations for each central frequency (spectral setup). The technical details of the different ALMA configurations are shown in Table 2.1. The details of the targeted transitions are shown in Table 2.2.

Table 2.1: Technical details of the ALMA observations.

Config.	Science Goal	Date (mm/dd/yy)	Center freq. (GHz)	Flux cal.	Gain cal.	Bandpass cal.
C40-1	2	19/03/2017	223.2	J1751+0939	J1851+0035	J1751+0939
C40-2	1	02/07/2017	110.0	J1751+0939	J1938+0448	J1751+0939
C40-3	3	12/06/2016	87.7	J1751+0939	J1938+0448	J1751+0939
C40-4	2	21/11/2016	223.2	J2148+0657	J1851+0035	J2148+0657
C40-5	1	10/22/2016 - 10/23/2016	110.0	J2148+0657	J1938+0448	J2025+3343
C40-6	3	10/10/2016	87.7	J1751+0939	J1938+0448	J1751+0939
		10/11/2016	87.7	J1751+0939	J1938+0448	J1751+0939
ACA	4	10/25/2016 - 10/26/2016	252.6	Mars	J1938+0448	J2232+1143

2.4 Data reduction

The following section describes the general procedure to obtain an interferometric map, using our data as a descriptive example. However, because of the size and the complex and heterogenous nature of the present data set, this section shows only a general presentation of the procedure to exemplify the methods followed, while the final images and maps for each line used in the different science cases will be presented in the corresponding chapter.

All data reduction, imaging and analysis has been done using the CASA version 5.6.1-8. In all the work it is assumed that the centroid position of B335 is at $\alpha =$ 19:37:00.9 and $\delta =$ +07:34:09.6, corresponding to the peak of dust continuum obtained from high resolution maps (Maury et al. 2018).

2.4.1 Raw data calibration

Calibration of the raw data (bandpass, gain and flux calibrations) was done using the standard script for cycle-4 ALMA data using CASA. The automated *ScriptForPI.py* ALMA script uses the different observed calibrators (listed in Table 2.1 for every configuration) to correct for variations in flux and phase. All the data used in this work were previously calibrated and, therefore, this part of the procedure is not described.

2.4.2 Continuum self-calibration

After obtaining the calibrated data, it is possible to refine the calibration process using self-calibration method as explained in Section 2.1.5.

We carried out this process for all the dust continuum data shown in Table 2.2. First, the phase was calibrated, reducing the time interval at each cycle, from 3000s to 30s, until the S/N did not improve substantially. Generally, an improvement of less than 10$\%$ with respect to the last cycle of calibration was considered enough to stop the phase calibration. The amplitude calibration was attempted, but no improvement on the S/N was observed with respect to the previous self-calibration cycle, so only the phase corrections were taken into account.

Once the best continuum phase model was obtained for each continuum *.ms*, it was applied to the corresponding line emission data when possible (self-calibrated lines are indicated for each science case in the corresponding chapters). A brief example of the self-calibration process is shown in Example 1.

Example 1. Continuum self-calibration of the 231 GHz data

Table 2.2: Targeted molecular line emission transitions information.

Molecule	Line	Rest Freq. (GHz)	LRS (″)	Spectral Res. (km/s)	ALMA config.
CO	J = 2-1	230.53800	10.9	0.15	C40-1/C40-4
$C^{18}O$	J = 1-0	109.78217	22.5	0.083	C40-2/C40-5
$C^{17}O$[a]	J = 1-0	112.35900	21.9	0.081	C40-2/C40-5
HDCO	J = 4-3	259.03491	16.1	0.071	ACA
HCO^+	J = 1-0	89.18852	27.5	0.205	C40-3/C40-6
$H^{13}CO^+$	J = 1-0	86.75428	28.3	0.105	C40-3/C40-6
$H^{13}CO^+$	J = 3-2	260.25534	16.0	0.070	ACA
DCO^+	J = 3-2	216.11258	11.3	0.085	C40-1/C40-4
HCN[a]	J = 1-0	88.63160	27.7	0.206	C40-3/C40-6
$H^{13}CN$	J = 3-2	259.01178	16.1	0.071	ACA
HC_3N	J = 12-11	109.17207	22.55	0.168	C40-2/C40-5
HC_3N	J = 27-26	245.60632	17.0	0.074	ACA
N_2D^+	J = 3-2	231.32182	10.64	0.158	C40-1/C40-4
SO	$J = 5_5 - 4_4$	215.22065	11.4	0.085	C40-1/C40-4
CH_3OH	J = 10-9	231.28115	10.6	0.085	C40-1/C40-4
CH_2DOH	J = 11-10	261.26392	15	0.070	ACA
Continuum		88.0	27.9	3.32	C40
		110.0	22.35	2.66	C40
		231.0	10.64	1.26	C40
		244.0	17.09	1.20	ACA

[a] Molecules that present Hyperfine structure

This example shows the improvement of the data due to continuum self-calibration. Figure 2.8 shows on top the two intensity maps obtained before (left) self-calibration and after 5 phase self-calibration iterations (right) for the continuum data at 231 GHz overlaid with intensity. The S/N is 98 and 421 respectively, and the improvement on the S/N is of 329 % with respect to the original image for the same imaging parameters. The bottom panels of Fig. 2.8 show the improvement of the phase-stability before (left) and after the 5 phase self-calibration cycles for the same continuum data. For the case after self-calibration, the scattering of the data over all the phase range is smaller, and more concentrated between $\pm$ 50 °, whereas before self-calibration the scattering is more disperse, between $\pm$ 100 °.

2.4.3 Continuum subtraction

Since B335 presents both a strong continuum source and line emission, in order to obtain precise measurements of the line parameters, such as the integrated intensity or the linewidth, it is necessary to remove the emission corresponding to the dust continuum from the observations.

This process can be done by using the best continuum model previously obtained from

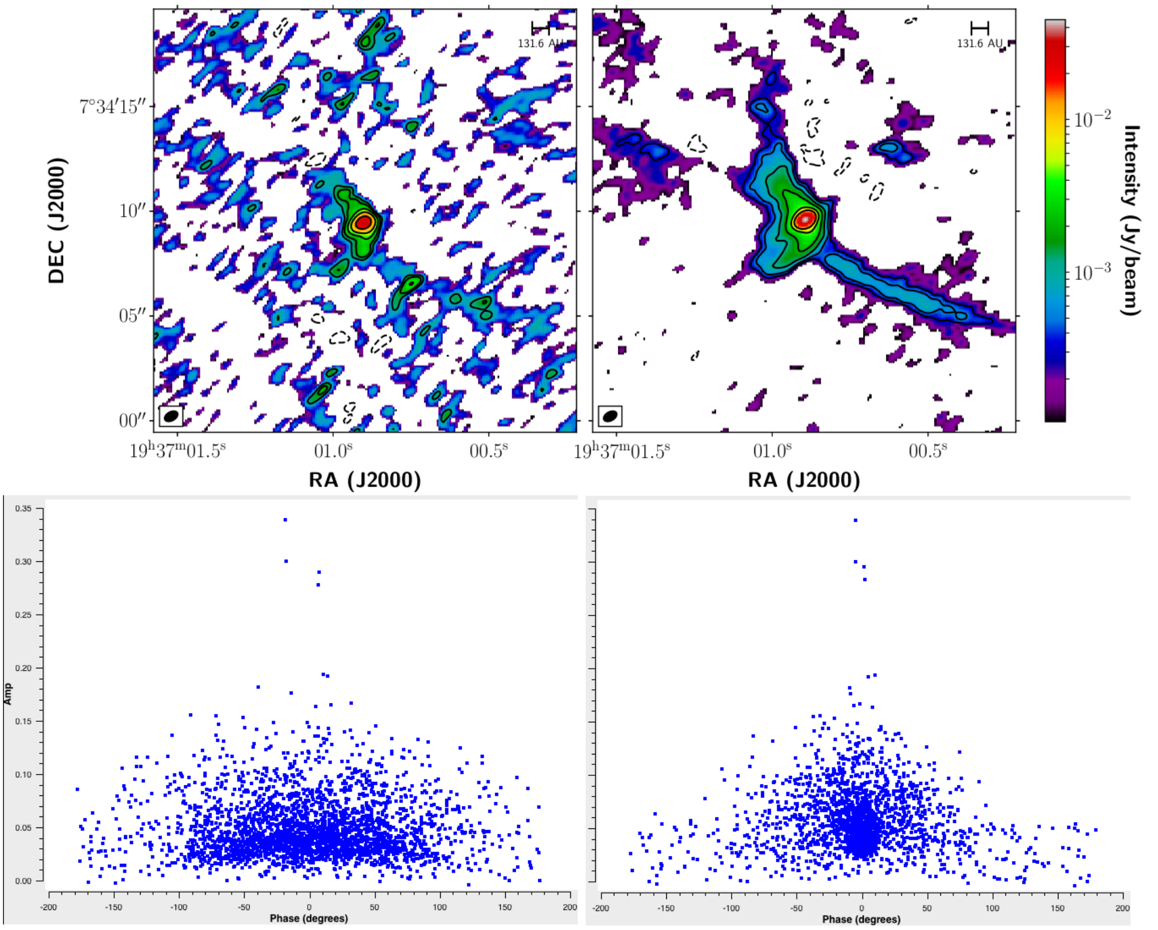

Figure 2.8: Continuum emission at 231 GHz before (left) and after continuum self-calibration. Top maps show in colors the continuum intensity overlaid with contours of the continuum intensity at -3, 3, 5, 10 and 30 σ, where σ is 0.10177 and 0.09411 mJy/beam respectively. Bottom panels show the phase difference before and after self-calibration.

the continuum dedicated spectral window during the continuum self-calibration. However, because some of our observed lines are too far away in frequency from the continuum central frequency, more than 1 GHz, applying the dedicated continuum model would result in an incorrect subtraction and therefore a poor spectrum. Since the continuum emission needs to be removed, a model of the continuum emission can also be created directly from the SPW where the line is observed. For our data, we used the second approach.

To do that, we made use of the CASA command *uvcontsub* which estimates the continuum emission by fitting polynomials on the visibility plane and subtracts the model from all the channels. The channels where there is no line emission are entered as input parameters, and the algorithm returns a *.ms* with the remaining emission, i.e., only molecular line emission, and another *.ms* with the continuum model. An example of the results from this procedure is shown in Example 2.

Example 2. Continuum subtraction from the DCO$^+$ (3-2) line emission data
Figure 2.9 shows the spectrum of the DCO$^+$ (3-2) transition averaged around 5″ in radius from the source center. It can be seen that the process has successfully subtracted the

continuum emission leaving only the intensity coming from the molecular line emission.

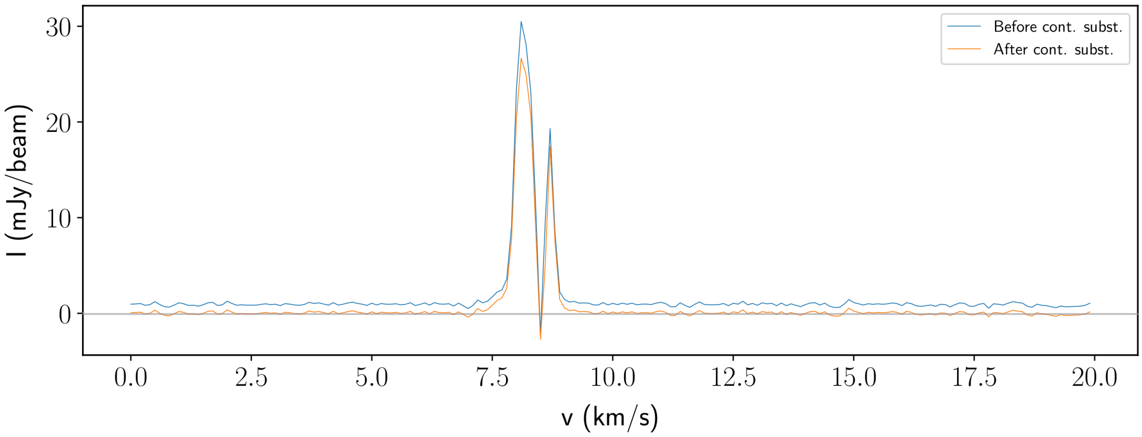

Figure 2.9: Comparison of the DCO^+ (3-2) spectra averaged around 5″ in radius from the source center before and after subtracting the continuum emission. The grey horizontal line indicates the zero intensity level.

2.4.4 Imaging the data

Imaging the continuum and line emission

After the data were calibrated, self-calibrated (when possible) and the continuum subtracted, the final images of the data were generated from the processed visibilities using again the *tCLEAN* algorithm. Since the data used and the imaging parameters are different for the different science cases presented in this work, the imaging parameters and the characteristics of the final images will be presented in every specific chapter.

The software CASA allows to do the cleaning automatically, until a certain rms is reached. It also allows to carry out this procedure interactively, in such a way that we could choose the regions with emission to be included in the model image. This allows to ignore regions where only noise is present or that include image artifacts due to, for example, large-scale emission filtering or lobes of the dirty beam.

Depending on the nature of the data we obtained different images. Imaging of the dust continuum emission dedicated SPW generate 2D maps showing the intensity of the emission. Imaging of the line emission generates 3D maps, or spectral cubes, showing the intensity of the emission at each observed frequency.

Integrated intensity maps

From the line emission data cubes we can obtain the moment 0 maps, or the integrated intensity images. To do this, the line intensity of the spectrum at each pixel, is integrated over the range of frequencies at which it is emitting over the noise level. This is done from the spectral cubes and on the image plane. We used the CASA command *immoments*. As inputs, the spectral data cube is given, along with the channels at which the line is emitting. An example of integrated intensity images is shown in Example 3, Fig. 2.10.

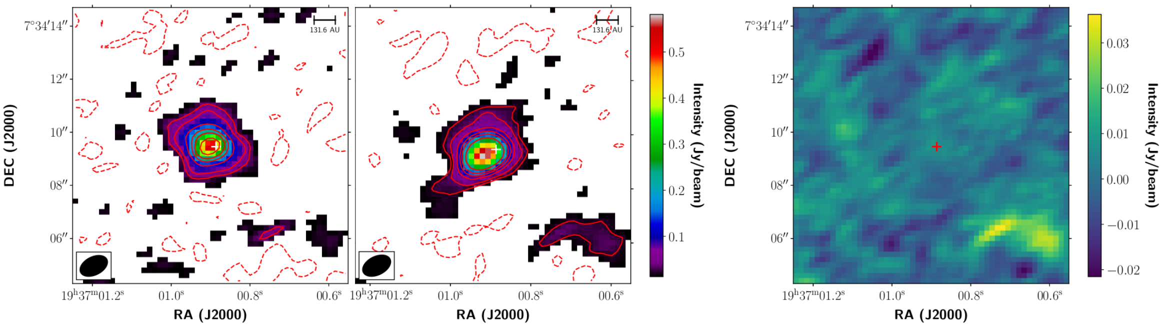

Figure 2.10: SO (5_5 - 4_4) integrated intensity image over the velocity range 7-9.4 km s^{-1}, with overlaid contours for -3, 3, 5, 10, 15, 20 and 30 σ before (left) and after cleaning (middle), where σ is 12.5 and 7.4 mJy/beam respectively. The residuals of the cleaning process are shown on the right panel.

Spectral maps

From the data cubes we also created spectral maps that present the spectrum (in frequency or velocity units) at each pixel of a determined region of the map, generally around the center of the source. These maps allow to evaluate the spectra at different offsets and detect any distinct line profiles or velocity patterns. An example of a spectral map is shown in Example 3, Fig. 2.11.

These maps are done with the purpose of analyzing the spectra at each pixel with the best angular resolution possible and without averaging the spectra. However, this only allows to print a small region of the data cubes. Nonetheless, this is usually enough to inspect the line profiles at different offsets and look for different velocity components or velocity patterns.

Example 3. Imaging of SO molecular line emission

Figure 2.10 illustrates the differences between before and after the cleaning process for the SO (5_5 - 4_4) molecular line emission. The left and middle panels show the integrated intensity images of the spectral cubes before cleaning (the dirty map), and after cleaning respectively. The intensity is integrated over the velocity range from 4.2 to 11 km s^{-1}. The residuals of the cleaning process are shown in the right panel.

After the cleaning process, more low signal emission is included in the image, as shown by the spatial extent of the 3 σ contour, as well as the increase in intensity of the central region. The residual map (right) shows that the remaining emission is only noise, and most of the emission of the line has been included in the model for the central region. However, the south-western region shows emission that has not been properly included in the model image. This indicates that the cleaning in that region has not been done properly and that there is still remaining emission that could be further cleaned. The S/N of the moment 0 images improves from 42 to 72 after the cleaning process (improvement of 83 %).

Figure 2.11 shows the spectral map obtained from a region of $2'' \times 2''$ around the center of the source for the SO (5_5 - 4_4) line emission. Each spectrum corresponds to a pixel of $0.2''$. Since the emission is very compact, most of it is visible in the spectral map. As an example, the SO emission presents very pronounced wings, the spectral map allows to study how this feature evolves with the offset, being more pronounced in the center and the north-west to south-east direction.

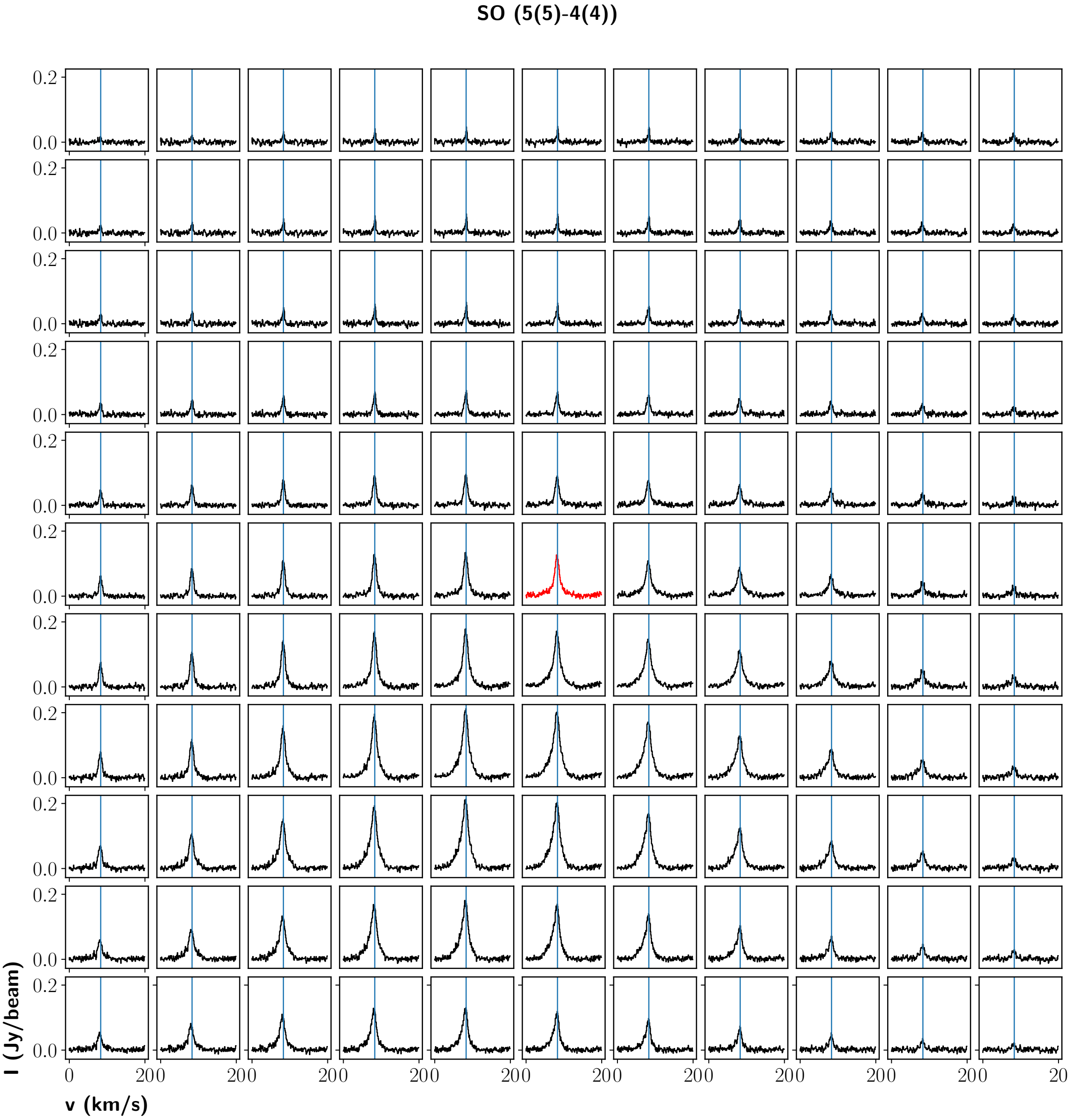

Figure 2.11: SO (5_5 - 4_4) spectral map showing spectra from a 2″× 2″ region around the center of the source. Each spectrum corresponds to one pixel on the intensity image of 0.2 ″. The red spectra shows the line profile at the centroid position of the source.

2.5 Modeling of the line profiles

In order to be able to extract crucial information, such as the velocity of the gas or the linewidth, we have modeled the spectra using a *fortrand* program which allows to fit the spectral line profiles using one or multiple velocity components (*HfS*, Estalella 2017). This software allows to derive the main line central velocity, peak intensity and the linewidth for each velocity component. If the transition presents a hyperfine structure, the code also allows to derive the optical depth of the main line from the intensity ratio of all the hyperfine components and for each velocity component.

For every velocity component the general *HfS* procedure fits simultaneously four independent parameters: the linewidth, assumed to be the same for each hyperfine component, and the main line central velocity, peak intensity and optical depth. The fitting procedure samples the space parameters to find the minimum value of the fit residual χ^2. Since the code does not output directly the values of the χ^2, we use the error values on the parameters to determine if the modeling is good enough to be used, generally we use values that are at least $2 \times$ uncertainty. From the procedure, we produced maps for the peak velocity, the linewidth and the opacity (whenever possible) of each transition.

Chapter 3

Characterization of Infall Profiles

The Class 0 phase corresponds to the main gas accretion phase (see Chapter 1). Hence, during this phase the matter on the envelope is infalling from the outer envelope to the more inner regions of the object. These motions can be generally traced by molecular line profiles, which present a characteristic double-peaked profile. While the study of infall motions was not the main goal of this work, our data show that an initial analysis of those motions was required in order to be able to proceed with the main goals.

This chapter aims to explain the infall gas kinematics of a collapsing object and how they can be traced with interferometric data. We will describe why our data needed such initial analysis and present our study of infall line profiles in observations of rare CO isotopologues, which has been already published in Cabedo et al. 2021b, and which is included in this chapter.

3.1 Introduction

Observations of molecular lines towards star forming cores have often found the presence of double-peaked line profiles, which are usually asymmetric, being the blue-shifted side more intense than the red-shifted one. Those profiles were early attributed to a contracting symmetric gas cloud, traced by optically thick lines and whose red-shifted side can be strongly absorbed against a continuum source (Leung and Brown 1977). Since then, asymmetric double-peaked line profiles observed towards dense clouds have been interpreted as a feature of infalling gas, and they have been used to characterize those infall motions in different pre-stellar and protostellar objects (Snell and Loren 1977, Zhou 1992, Zhou 1995, Mardones et al. 1997, Gregersen et al. 2000, Lee et al. 2001, Di Francesco et al. 2001, Attard et al. 2009, Mottram et al. 2013, Keown et al. 2016, Yang et al. 2020). Particularly, these profiles have also been observed multiple times towards B335, and have been attributed to optically thick lines being absorbed (Zhou et al. 1993, Evans et al. 2005, Evans et al. 2015, Yen et al. 2020). This has made of B335 a prototypical source to study infall motions.

During the preliminary analysis of our data, we encountered such profiles for different dense gas tracers, such as HCO^+, $H^{13}CO^+$, HCN, DCO^+, ^{12}CO, $C^{18}O$ and $C^{17}O$. While some of these can be attributed to optically thick lines being self-absorbed (HCO^+, $H^{13}CO^+$, $C^{18}O$) or can be attributed to other motions, such as outflowing gas (^{12}CO, Bjerkeli et al. 2019), it is not clear that other less abundant molecules (DCO^+ or $C^{17}O$) can present these peculiar line profiles. The main goal of this PhD work was not the characterization of these line profiles, but the characterization of other physical processes such as the deuterium fractionation, the ionization fraction or the ambipolar diffusion. However, these analyses required the use of optically thin lines and a precise determination of their line emission properties. Thus, the detection of such blue-asymmetries in our *a priori* optically thin emission, required further investigation as to their relation to infall motions, which is presented in this chapter.

3.1.1 Asymmetric profiles and characterization of infall motions

Studies of infall motions rely on the detection of blue-asymmetric line profiles produced by optically thick self-absorbed lines. If an object presents a static outer envelope which emits at the same velocity than the inner gas, an absorption of the emission at he rest frequency is produced and we can talk about P-Cygni profiles. The name, P-Cygni profile, comes from the observations of the Be star P-Cygni, which presented a strong absorption in the blue-shifted part of its molecular spectra. This characteristic profile is attributed to an expanding gas shell of material being ejected from the star. Conversely, when the absorption is observed on the red-shifted side of the spectra we talk about an inverse p-Cygni profile, which are attributed to the inverse motion: material infalling to the center of the object. The formalism of this effect is considered in the frame of spherically symmetric inside-out collapse. We explain here how this effect is produced considering spherical symmetry, and how it can be used to trace non-symmetric motions in protostellar envelopes.

Spherical collapse

At the center of a dense protostellar core, where gas densities become larger as the collapse proceeds ($> 10^5$ cm^{-3}, André 1995), the large abundance of some gas tracers in an outer static envelope produces a self-absorbed profile, with a dip in intensity centered at the systemic velocity. If the gas is infalling, as expected in a collapse, the line profile becomes asymmetric towards the blue-shifted side. In dense gas tracers, the typical signature consists on the appearance of two peaks in the spectral line profiles corresponding to the blue- and red-shifted components of the infalling shell, both observed in the same LOS and where the blue-shifted peak is stronger than the red-shifted (Fig. 3.1).

These profiles were first observed by Walker 1972. The formalism describing this spectral signature on infalling spherical cores was first presented in Anglada et al. 1987 during

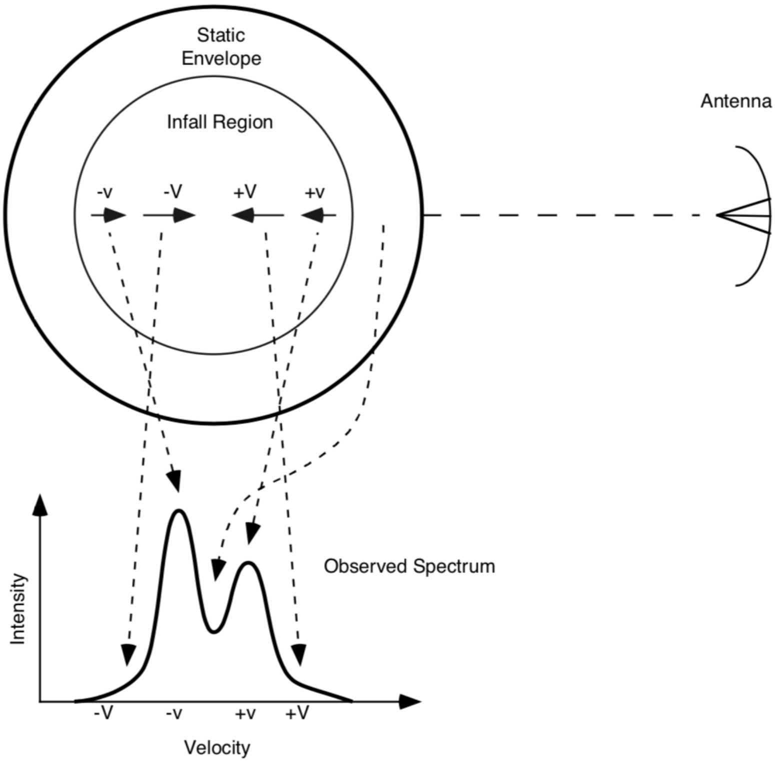

Figure 3.1: Line profile produced by a cloud undergoing inside-out collapse. The static envelope outside the infall region produces the central self-absorption dip, the blue peak comes from the back of the cloud which moves towards the observer at velocity $-v$, and the red peak comes from the from of the cloud which is moving away from the observer at velocity $+v$. The gradient in temperature inside the infalling region produces the intensity asymmetry and the faster collapse near the center produces the line wings. From Evans 1999.

the study of angularly unresolved infalling cores. Under the assumption of spherical symmetry and inside-out collapse, where infalling velocity increases towards the center, and considering that infall motions dominate the kinematics of the gas over turbulent and thermal motions, and therefore dominate the spectral line profile shapes, it can be shown that the points with same LOS velocity form closed surfaces. Those are surfaces with the same shape, decreasing in size with increasing velocity and converging into the core. The left panel of Fig. 3.2 shows the theoretical representation of these surfaces. A given LOS intersects two surfaces with the same isovelocity, one blue-shifted with respect to the rest frequency, and another one red-shifted. If the line is optically thick only the emission from the surface facing the observer is detected (thick lines in the left panel of Fig. 3.2).

Why the blue-shifted part of the line emission is more intense than the red-shifted one is a question of temperature gradients. Because the temperature increases towards the center, the channel maps of the blue- and red-shifted emission are different, and are in fact images of the temperature distribution of the isovelocity surfaces. For the blue-shifted channels, the observed emission peaks closer to the center of the core, a warmer region, while the red-shifted channels correspond to a region further away from the center and, therefore, colder (Smith et al. 2012, Mayen-Gijon et al. 2014, Calahan et al. 2018, Estalella et al. 2019).

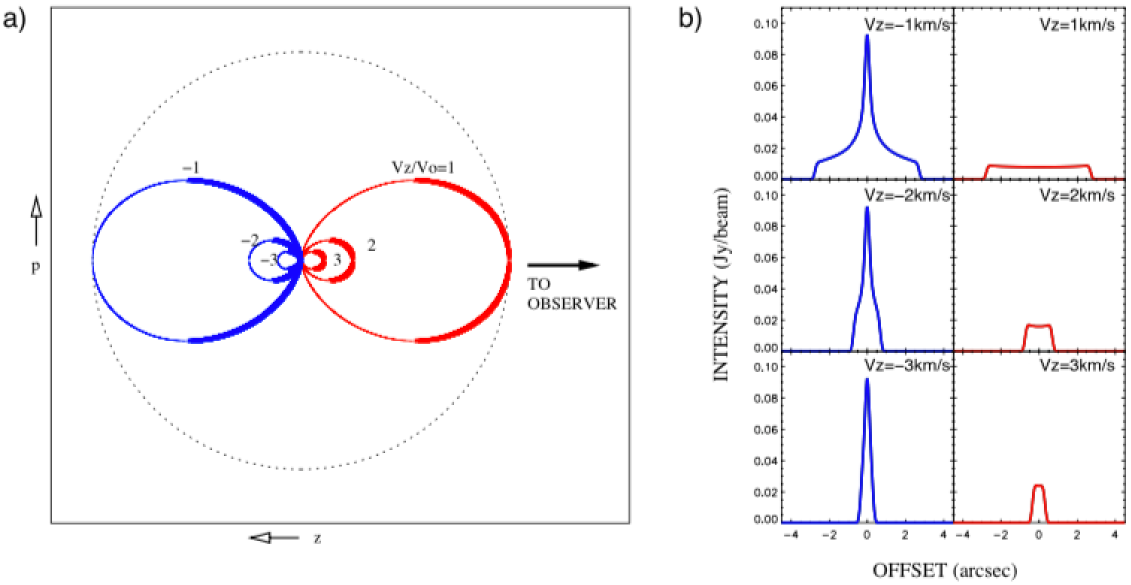

Figure 3.2: *Left*: Surface of equal LOS velocity for a collapsing protostellar envelope. *Right*: Intensity as a function of angular offset from the source centre for channel maps of different velocities. Adopted from Mayen-Gijon et al. 2014

This will produce a difference in intensity between the two velocity regimes, where the blue-shifted one is more intense than the red-shifted due to its larger temperature. The right panel of Fig. 3.2 shows how the intensity of both velocity components (blue- and red-shifted) would be observed as a function of angular offset from the center of the source.

Non-symmetric collapse

While symmetric collapse can partially explain some observations of double-peaked profiles, the hypothesis only applies to optically thick lines and the effect should not be observed for less abundant tracers, such as $C^{17}O$ or DCO^+. Such transitions should be optically thin and therefore present symmetric line profiles, if they are not affected by any other motion (Mayen-Gijon et al. 2014). Therefore, there is the need for other effects that match the line profiles of those molecules.

Blue-asymmetries in line profiles are not unique to symmetric infall motions, and therefore the effect of gas collapsing is hard to isolate from other dynamical processes. Abundant molecules that trace protostellar outflows, which are highly non-symmetrical motions, such as ^{12}CO, can present asymmetric line profiles (Bjerkeli et al. 2019). However, such tracers generally present a morphology that shows the outflow distribution, plus additional spectral signatures, such as very high velocity emission called "wings". Other asymmetric structures, such as close binaries could also produce asymmetries in the line profiles, but those would only be detected at sub-arcsecond scales (Tobin et al. 2010).

Observations of Class 0 protostars have revealed that non-axisymmetric signatures are widespread in the envelopes of protostellar envelopes and that those can not be attributed to any of the aforementioned motions (Tobin et al. 2010). Since then, symmetrical collapse has been debated and other non-isotropic gas kinematics have been proposed to explain these observations. Double-peaked profiles that are consistent with two separated velocity

#	Config.	Weight.	Rob.	Θ ($'' \times ''$)	P.A. (deg)	Pix. Size ($''$)	I_{max} ($\frac{mJy}{beam}$)	RMS ($\frac{mJy}{beam}$)	S/N
1	FullDS	Briggs	0.5	1.492×1.301	85.63	0.2	63.5	9.3	6.8
2	FullDS	Briggs	1	1.580×1.364	-86.73	0.2	66.7	8.9	7.4
3	FullDS	Natural	-	1.043×0.711	-70.27	0.3	44.9	6.1	7.3
4	C40-2	Briggs	0	2.527×1.712	-79.33	0.5	126.6	12.2	10.3
5	C40-2	Briggs	0.5	2.597×1.972	-88.56	0.2	129.9	10.6	12.2
6	C40-2	Briggs	0.5	2.599×1.926	-88.04	0.5	133.4	10.5	12.6
7	C40-2	Natural	-	2.728×2.173	80.19	0.3	250.7	13.4	18.7

Table 3.1: Sampling of the imaging parameters and resulting maps characteristics for $C^{17}O$.

components, rather than the product of self-absorption, have already been reported and are consistent with non-symmetrical collapse (Tobin et al. 2012, Maureira et al. 2017). Moreover, accretion streamers connecting the outer dense core with inner regions have also been reported (Pineda et al. 2020) and evidence the importance of local non-symmetric processes. In B335, indications of non-symmetric collapse have also been already reported in optically thin tracers which present double-peaked profiles at large scales (Velusamy et al. 1995).

All of these evidence seems to suggest that asymmetric infall motions are common during the main phase accretion. Tobin et al. 2010 already suggested that asymmetric structures might already be present during the pre-stellar phase and might be enhanced during the collapse. They suggested these asymmetries might also be the cause of other widespread features, such as the formation of binaries and multiple systems. The cause of the asymmetries is not clear, but they might be the effect of the presence of a non-symmetrical magnetic field or the evolutionary stage of the object (Maureira et al. 2017).

3.2 Infall profiles in the present observations: Imaging of CO isotopologues

In order to investigate the origin of the double-peaked profiles in our data, we decided to use the observations of $C^{17}O$ and compare them with the isotopologues ^{12}CO and $C^{18}O$. We made this choice, contrary to other molecules such as DCO^+, because the chemical network of $C^{17}O$ is much simpler and better constrained (Millar et al. 1989, Jørgensen et al. 2004), and therefore we do not expect to see sudden changes in its abundance, that could explain a very large optical thickness. This isotopologue, $C^{17}O$, was also chosen because it is expected to trace the gas in the inner core. This allows to characterize infall motions at smaller scales than previously studied with single-dish data.

3.2.1 Integrated intensity maps

In this section, the imaging results of the CO isotopologues are presented. The data were reduced following the general procedure detailed in Section 2.4, applying self-calibration only for ^{12}CO and $C^{18}O$, and later subtracting the continuum for all the tracers. During the preliminary analysis of the ALMA data, it was noticed that the $C^{17}O$ (1-0) transition

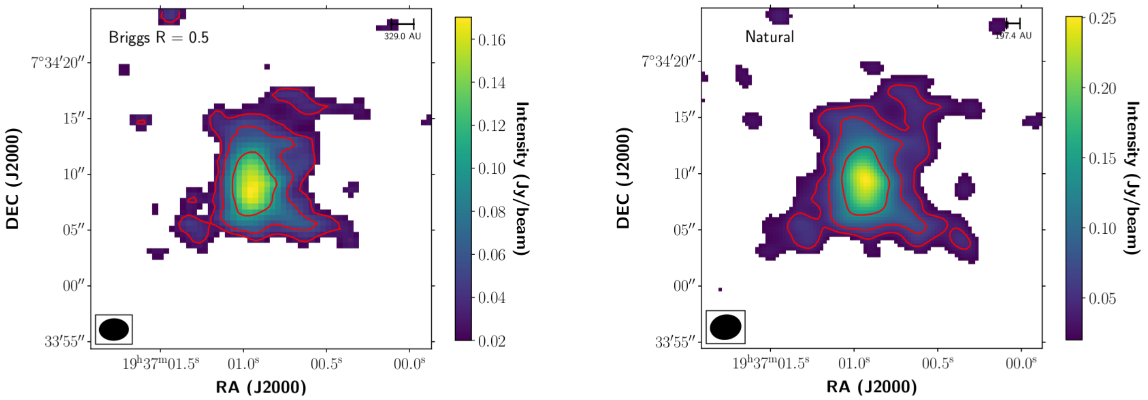

Figure 3.3: Integrated intensity images of C^{17}O (1-0) using different imaging parameters. Both images have been obtained by integrating in a velocity range 4.8-6.2 and 7.6-9.4 km s^{-1} accounting for the hyperfine structure of the line. Contours show integrated intensity at -3, 3, 5, 10 and 30 σ. *Left*: Briggs weighting with Robust parameter of 0.5 where σ = 10.6 mJy/beam (Map #6). *Right*: Natural weighting where σ = 13.4 mJy/beam (Map #7).

was only detected for the most compact configuration, C40-2. This could be expected since C^{17}O is a low abundance tracer, and observations at small scales might not be sensitive enough to pick up its emission. We imaged the data following the procedure described in Section 2.4.4. In order to obtain the image with the best compromise between S/N ratio and the angular resolution, we combined different imaging parameters and analyzed the characteristics of the different maps. We imaged the most compact configuration where emission is detected (C40-2) and the combination of the two configurations (C40-2 + C40-5, hereafter FullDS). We also applied different weighting algorithms, testing the 'natural' and the 'Briggs' weighting, the latter by sampling different robust parameters (0, 0.5 and 1).

From the spectral data cubes we produced the integrated intensity maps following the procedure on Section 2.4.4. The obtained parameters of the integrated intensity maps are shown in Table 3.1. We note that, as expected, the images with 'natural' weightings have a poorer angular resolution. We also note that changing the pixel size does not have a significant effect on the S/N, for the two values considered here (0.2 and 0.5 arcsec/pixel). The best S/N was obtained using only the most compact configuration, C40-2, with 'natural' weighting (map # 7). Nevertheless, the angular resolution of map #7 is worse than that of map #6 by $\sim$15 %. Figure 3.3 shows the comparison between the integrated intensity maps #6 and #7. The extension of the emission in both maps is very similar, thought it is slightly more compact for map #6, since we are giving more weight to larger baselines that pick up emission at smaller scales. Because of the better angular resolution, we decided to use map #6 for the following analysis.

To be sure that we were probing the same scales when comparing different gas tracers, and using the fact that the emission from both CO isotopologues is found at similar frequencies and that both observations were done with the same ALMA configuration, we produced the C^{18}O map in the same way as the C^{17}O one, by using only the C40-2 configuration data. To produce the CO images, emission from both datasets was used, and the resulting image was smoothed to the same resolution as the C^{17}O one.

Figure 3.4 shows the final integrated intensity maps for the three CO isotopologues. In

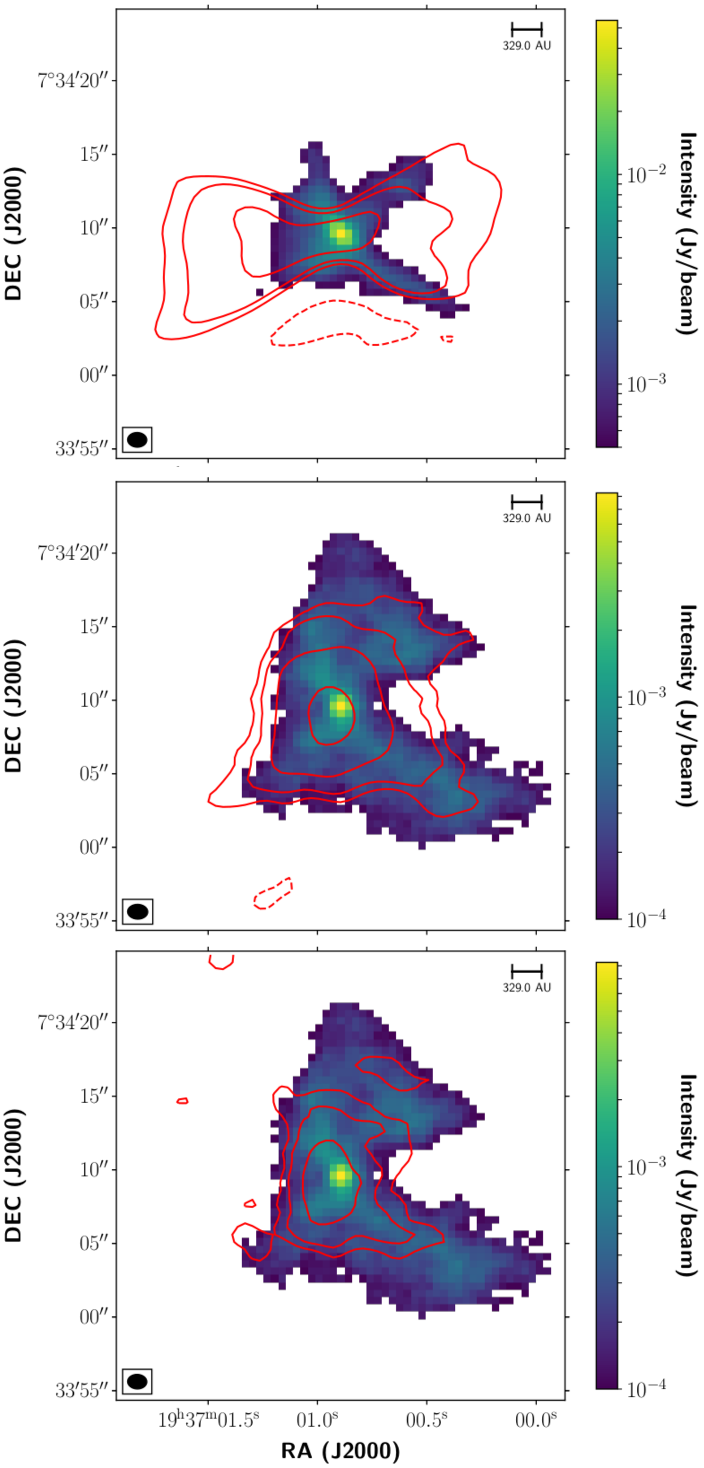

Figure 3.4: CO isotopologues moment 0 emission shown in red contours. Contours show emission at -3, 3, 5, 10 and 30 σ. The values for σ for each plot and the integrated velocities are shown in Table 3.2. Dust continuum emission at the correspondent frequencies is shown in colors. The beam size is shown in black on the left corner of each map, being the same for both the dust continuum and the molecular line emission. *Left*: ^{12}CO (2-1) with dust continuum at 231.0 GHz. *Middle*: C^{18}O (1-0) with dust continuum at 110.0 GHz. *Right*: C^{17}O (1-0) with dust continuum at 110.0 GHz.

Table 3.2: CO isotopologues imaging parameters and final maps characteristics. For lines for which more than one velocity range is indicated each range correspond to a different hyperfine component.

Transition	^{12}CO (2-1)	C^{18}O (1-0)	C^{17}O(1-0)
Robust parameter	1	0.5	0.5
F.O.V (arcsec)	26.9	56.7	55.2
Image size (arcsec)*	80.7	170.3	165.7
Pixel size (arcsec)	0.5	0.5	0.5
Θ_{maj} (arcsec)	2.61	2.73	2.60
Θ_{min} (arcsec)	1.99	2.01	1.93
P.A. (°)	88.55	88.68	88.00
Spectral res. (km s^{-1})	0.2	0.2	0.2
vel. range (km s^{-1})	1.4-16.2	7.6 - 9.4	4.8 - 6.2
			7.6 - 9.4
RMS (mJy/beam)	387	10	11

contours the integrated intensity emission is shown overplotted with the dust continuum emission at the appropriate frequency. The imaging parameters used and the resulting maps characteristics are shown in Table 3.2. All maps were produced with an image size of $3\times$F.O.V, but were later trimmed to $30''$ for convenience and appropriate comparison.

The left panel of Fig. 3.4 shows the ^{12}CO emission at the same scale as C^{18}O and C^{17}O. Emission of ^{12}CO presents a typical outflow morphology, and most likely probes outflowing gas. Since its F.O.V is ~ 50 % smaller than that of C^{17}O and C^{18}O its integrated emission picks up more compact emission from the outflow cavity and likely filters out most of the extended emission. The middle and right panels of Fig. 3.4 show the emission for C^{18}O and C^{17}O respectively, which do not present a biconical morphology typical from outflow emission and appear to probe the inner envelope material instead. Although the excitation conditions of the two transitions are different, i.e., ^{12}CO (2-1) vs. C^{17}O and C^{18}O (1-0), the same biconical structure of the outflow has been observed for the ^{12}CO (1-0) transition at larger scales (Hirano et al. 1988, Hirano et al. 1992), and there is no indication that suggests that higher transitions of C^{17}O and C^{18}O would trace the outflowing gas, due to their low abundance. This indicates that the different excitation conditions of the transitions do not affect our conclusion.

Focusing on the C^{17}O emission, the mean radius of the emission was computed by obtaining the FWHM of a Gaussian model fitted to the 3σ emission and was found to be 860 au. The extension of C^{17}O appears to be more compact than that of C^{18}O, which is agreement with the fact that C^{17}O is expected to be less abundant, and therefore its emission is confined to denser regions of the core.

3.2.2 Channel maps

From the spectral cubes of each CO isotopologue, the emission at every channel was plotted by averaging emission every 1 km s^{-1}, for velocities around the systemic velocity, 8.3 km s^{-1}, between 6 and 10 km s^{-1}.

From top to bottom, Fig. 3.5 shows the channel maps of ^{12}CO, C^{18}O and C^{17}O. The

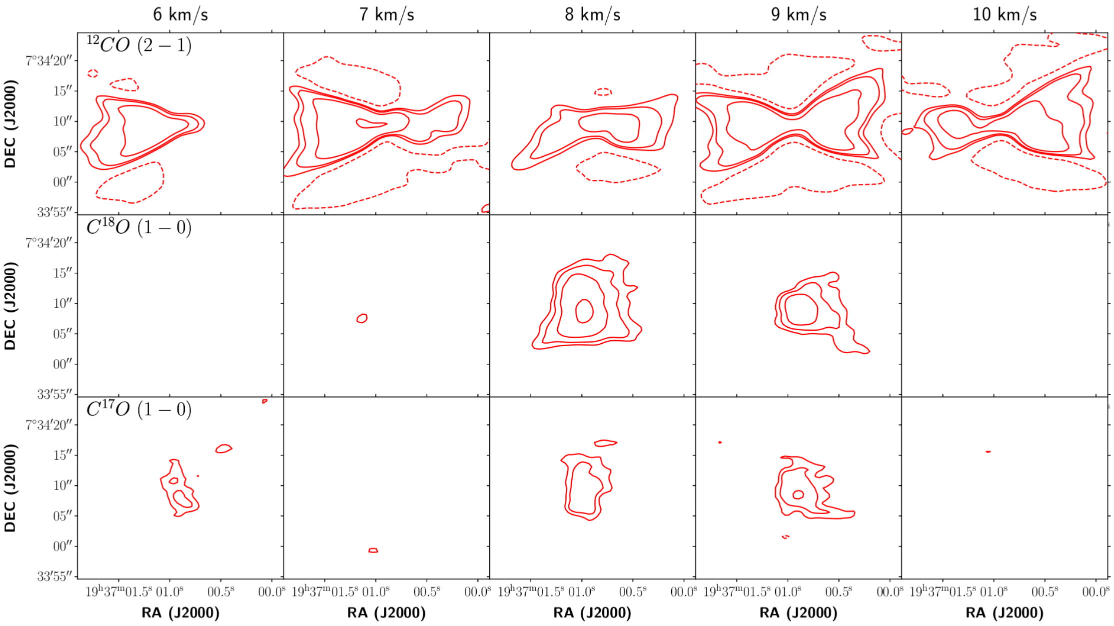

Figure 3.5: Channel maps for the three CO isotopologues. Emission from the spectral cubes is averaged every 1 km s^{-1} between 6 and 10 km s^{-1}. Contours show emission at -3, 3, 5, 10 and 30 σ. *Top*: ^{12}CO (2-1). *Middle*: C^{18}O (1-0). *Bottom*: C^{17}O (1-0).

^{12}CO emission extends to larger velocities from the systemic velocity, larger than ±2 km s^{-1}, while C^{18}O and C^{17}O are only confined to ± 1 km s^{-1} of the systemic velocity. At their emission peak, C^{18}O and C^{17}O show a similar morphology while the ^{12}CO is very different and in agreement with the biconical morphology of an outflow cavity tracer. These two effects clearly suggest that while ^{12}CO traces the outflow cavity, C^{18}O and C^{17}O are tracing a different structure, i.e., the envelope. The emission appearing at 6 km s^{-1} in the C^{17}O channel maps corresponds to the less intense hyperfine component of the transition.

3.2.3 Spectral maps

Spectral maps of the three isotopologues, ^{12}CO (2-1), C^{17}O (1-0) and C^{18}O (1-0) have been obtained following the procedure described in Section 2.4.4, and are shown in Figs. 3.6, and Figs. 2 and C.1 in the attached article, respectively. Each map shows the inner 900 au around the source, centered on the dust continuum emission peak. The whole maps are 5.5 ″ × 5.5 ″ and each pixel corresponds to 0.5 ″ (∼ 82 au). The red spectrum corresponds to the position of the peak of the continuum emission and the blue line indicates the systemic velocity (8.3 km s^{-1}). We note that in order to show the whole line profile of ^{12}CO the velocity range shown is much larger (0 to 16 km s^{-1}) than for C^{18}O and C^{17}O (6 to 10 km s^{-1}).

The ^{12}CO (2-1) spectral map (Fig. 3.6) shows the typical velocity pattern produced by outflowing gas, with very broad blue- and red-shifted wings, with the blue-shifted part being generally more intense. Filtering effects from large-scale emission are very important and can be observed, for example, in the south-east region of the source, producing multiple peaks and absorption below the continuum level.

In the C^{17}O (1-0) and C^{18}O (1-0) spectral maps (Figs. 2 and C.1 in the attached article), the double-peaked profiles can also be observed. In these cases the features can not be attributed to outflow because the morphology of the tracers does not appear to be tracing the outflow cavities (as discussed in Sections 3.2.1 and 3.2.2), and because they do not present broad spectral wings due to high velocity emission. Filtering effects from large scale emission does not seem to affect significantly our observations of $C^{18}O$ and $C^{17}O$. Since $C^{17}O$ is quite compact, even in single-dish data (Saito et al. 1999), we do not expect filtering to be important. However, since $C^{18}O$ is more abundant, it could potentially be more affected from large-scale filtering, although our spectral maps do not present any indication that this is the case. A more detailed study of the possible filtering effects is given in the included article (Section 3.3, Cabedo et al. 2021b). As it has been already stated, blue-asymmetries arise from infalling gas in dense regions, which presents optically thick emission which is self-absorbed. If that was the case, considering a spherically symmetric cloud, double-peaked profiles would be expected to be observed only in the more dense central regions, and the asymmetry would disappear as the offset from the center increases, and the gas becomes less dense. Instead, we observe two distinct velocity components which vary in intensity at different offsets from the center, being the blue-shifted component more intense on the eastern region, and the red-shifted on the western region. This suggests that the velocity pattern here observed does not match the expected velocity pattern from a symmetric cloud collapse. Finally, estimations of the line opacity (see Section 3.1 in the included article, Cabedo et al. 2021b) suggest that the line is optically thin, and even if the opacity effects could be non-negligible, they are not enough to explain the observed absorption or the velocity pattern across the source.

In the case of $C^{17}O$ a clear broadening of the line can be observed near the dust continuum emission peak and in the north-east region part of the core. The former can be due to thermal broadening of the two velocity components as the temperature rises near the center of the cloud, while the latter might be the consequence of the overlapping of the two components due to other dynamical processes.

3.2.4 Line profile modeling

We modeled the line profiles of the $C^{17}O$ emission using the procedure described in Section 2.5. The *HfS* program used is not able to successfully fit a strongly optically thick line which produces a double-peaked profile arising from a single velocity component. Since the spectral maps suggest that the two peaks are not related and because we do not expect opacity effects in the $C^{17}O$ line profiles due to its low abundance, we assume that we are observing two separated velocity components, and proceed with the modeling using this hypothesis. Hence, as an input to the *HfS* program, we use the velocity range of the two components. The results of this modeling are presented in the included article (Section 3.3, Cabedo et al. 2021b).

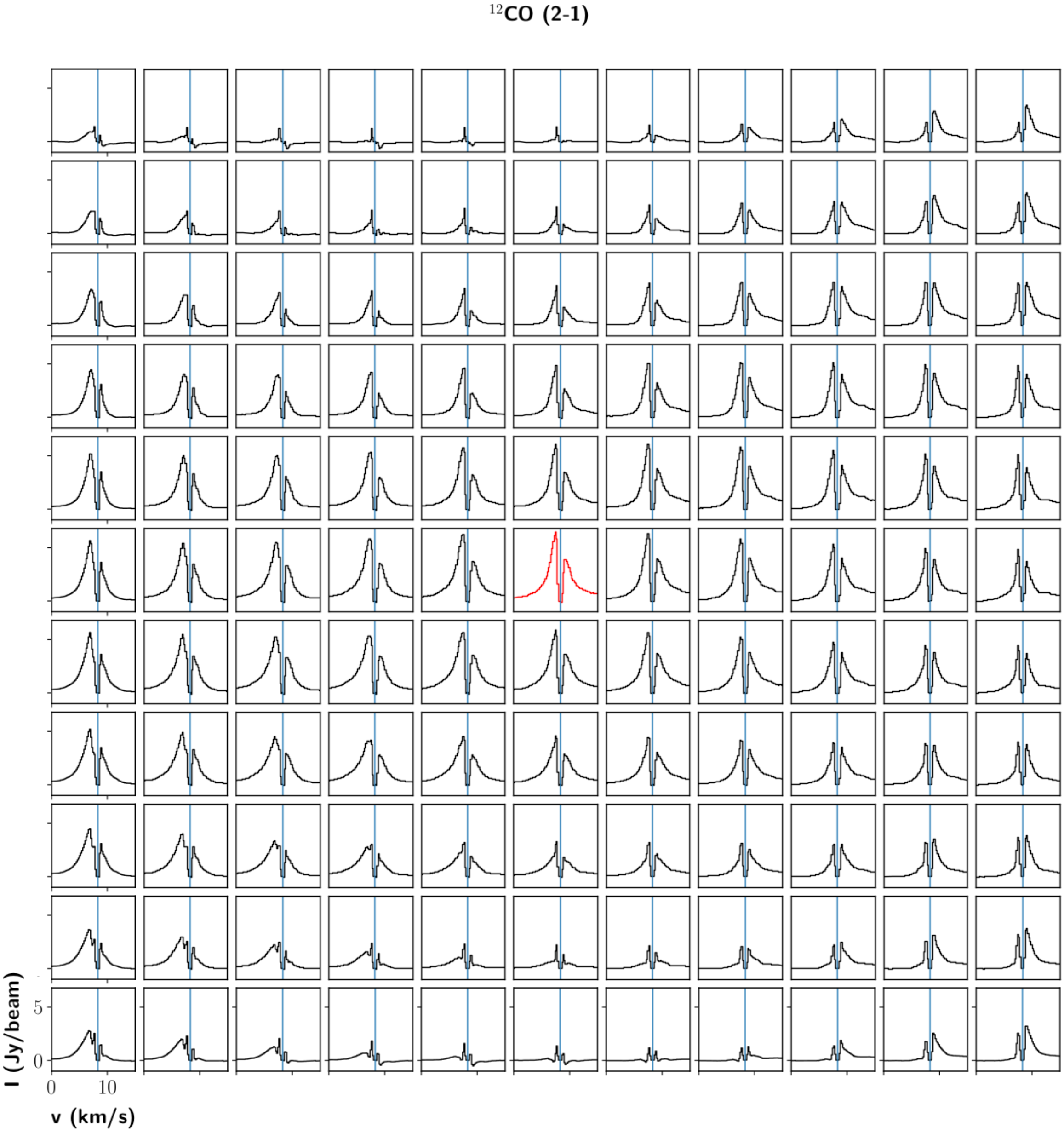

Figure 3.6: Spectral map of the ^{12}CO (2-1) emission in the inner 900 AU, centered on the dust continuum emission peak. The whole map is 5.5" × 5.5" and each pixel correspond to 0.5" ($\sim$ 82 au). The red spectrum refers to the peak of the continuum emission and the blue line indicates the systemic velocity (8.3 km s^{-1}).

3.3 Paper I: Structured velocity field in the inner envelope of B335: ALMA observations of rare CO isotopologues

In this section, we present the article already published, Cabedo et al. 2021b, where we discuss in more details the origins of the observed double-peaked profiles, and its implication in the models of star formation.

A&A 653, A166 (2021)
https://doi.org/10.1051/0004-6361/202140754
© V. Cabedo et al. 2021

Astronomy & Astrophysics

Structured velocity field in the inner envelope of B335: ALMA observations of rare CO isotopologues

Victoria Cabedo[1,3], Anaëlle Maury[1,2], Josep M. Girart[3,4], and Marco Padovani[5]

[1] Astrophysics department, CEA/DRF/IRFU/DAp, Université Paris Saclay, UMR AIM, 91191 Gif-sur-Yvette, France
e-mail: `victoria.cabedo@cea.fr`
[2] Harvard-Smithsonian Center for Astrophysics, 60 Garden street, Cambridge, MA 02138, USA
[3] Institut de Ciències de l'Espai (ICE), CSIC, Can Magrans s/n, Cerdanyola del Vallès, 08193 Catalonia, Spain
[4] Institut d'Estudis Espacials de Catalunya (IEEC), 08034 Barcelona, Catalonia, Spain
[5] INAF-Osservatorio Astrofisico di Arcetri, Largo E. Fermi 5, 50125 Firenze, Italy

Received 8 March 2021 / Accepted 30 June 2021

ABSTRACT

Context. Studies of Class 0 objects allow to characterize the dynamical processes taking place at the onset of the star formation process and to determine the physical mechanisms responsible for the outcome of the collapse. Observations of dense gas tracers allow for the characterization of key kinematics of the gas that are directly involved in the star formation process, such as infall, outflow, and rotation.

Aims. This work is aimed at investigating the molecular line velocity profiles of the Class 0 protostellar object B335 and attempts to place constraints on the infall motions happening in the circumstellar gas of the object.

Methods. We present observations of $C^{17}O$ (1–0), $C^{18}O$ (1–0), and ^{12}CO (2–1) transitions along with an analysis of spectral profiles at envelope radii between 100 and 860 au.

Results. $C^{17}O$ emission presents a double-peaked line profile distributed in a complex velocity field. Both peaks present an offset of 0.2–1 km s^{-1} from the systemic velocity of the source in the probed area. The optical depth of the $C^{17}O$ emission has been estimated and found to be less than 1, suggesting that the two velocity peaks trace two distinct velocity components of the gas in the inner envelope.

Conclusions. After discarding possible motions that could produce the complex velocity pattern, such as rotation and outflow, we conclude that infall motions are responsible for producing the velocity field. Because inside-out symmetric collapse cannot explain those observed profiles, it is suggested that these are produced by non-isotropic accretion from the envelope into the central source along the outflow cavity walls.

Key words. techniques: interferometric – techniques: spectroscopic – stars: formation – circumstellar matter – stars: protostars

1. Introduction

Low-mass stars are known to form in dense molecular gas clouds. Class 0 objects represent the first stage of the star formation process, when most of the mass is still contained in the envelope surrounding the protostar (André et al. 1993; André 1995). Models of protostellar collapse (Shu et al. 1987) suggest that it is during this phase that the circumstellar gas is transported to the central object thanks to accretion processes. During this stage, angular momentum needs to be removed from the envelope and stored in the central object or dissipated through viscous processes to allow for the formation of the star. Moreover, the accretion mode, the rate at which it happens, and the duration of possible accretion episodes during this phase will determine the final stellar mass (André 1995; Basu & Jones 2004; Bate & Bonnell 2005; Myers 2012). Therefore, studying this phase is crucial, as it allows us to understand what the kinematics and dynamics of the gas are at the onset of collapse and to determine how those affect the outcome of the star formation process.

The gas making up the majority of protostellar envelopes is typically probed using molecular gas line profiles, which trace the gas kinematics in the dense envelope and measure gas motions such as rotation or infall. Observations of the molecular line emission from embedded protostars have been reported to trace widespread infall signatures in the inner ~2000 au of some protostellar envelopes (Zhou et al. 1993; Rawlings 1996; Di Francesco et al. 2001; Mottram et al. 2013). Most of those studies rely on the detection and interpretation of the infall spectral signature known as blue asymmetry or inverse P Cygni profile. In the center of a dense protostellar core, where gas densities become larger as the collapse proceeds (>10^5 cm^{-3}, André 1995), the large optical depth of some molecular line emission produces a self-absorbed line profile, with the dip centered on the emission at systemic velocity, where most of the circumstellar gas emits. Because the core is collapsing under the effect of gravity, line emission from dense gas tracers will present the typical blue-asymmetry line profile. Most works that are focused on modeling these line profiles to put constraints on protostellar infall models rely on the assumption of a symmetrical cloud collapsing, which produces such a double-peaked profile on optically thick emission. From the models, key parameters can be extracted, such as central protostellar mass, infall velocities, and mass accretion rates (Zhou et al. 1993; Di Francesco et al. 2001; Evans et al. 2005, 2015). However, blue-asymmetries in line profiles are not unique to infall motions. Complex gas kinematics, such as asymmetric collapse (Tokuda et al. 2014; Maureira et al. 2017), accretion streamers

Open Access article, published by EDP Sciences, under the terms of the Creative Commons Attribution License (`https://creativecommons.org/licenses/by/4.0`),
which permits unrestricted use, distribution, and reproduction in any medium, provided the original work is properly cited.

(Pineda et al. 2020), or outflow-entrained gas, can produce separated velocity components along the same line-of-sight (LOS) that are observed as double-peaked line profiles that are not caused by optical thickness.

The isolated Bok globule B335, which contains an embedded Class 0 protostar (Keene et al. 1983), is located at a distance of 164.5 pc, (Watson 2020) and has been the prototypical object for testing symmetrical collapse infall models, since blue-asymmetries were first detected in the molecular emission of the source at core scales (Zhou et al. 1993; Choi et al. 1995; Evans et al. 2005). Double-peaked line profiles have also been observed with interferometric observations of the molecular emission from the inner envelope (Chandler & Sargent 1993; Saito et al. 1999; Yen et al. 2010; Kurono et al. 2013; Evans et al. 2015). Attempts have been made for infall models of an optically thick line emission to compute infall mass rates (Yen et al. 2010, 2015; Evans et al. 2015), obtaining values affected by large uncertainties ranging from 10^{-7} $M_\odot$ yr^{-1} to $\sim 3\times10^{-6}$ $M_\odot$ yr^{-1} at radii of 100–2000 au, as well as infall velocities from 1.5 km s^{-1} to $\approx$0.8 km s^{-1} at radii of $\sim$100 au. New models based on continuum emission, and using the revised distance of 164.5 pc, have determined an infall rate from the envelope to the disk of 6.2×10^{-6} $M_\odot$ yr^{-1} (Evans et al., in prep.). For the estimated age of 4×10^4 yr, this implies a total mass at the center (star + disk) of 0.26 $M_\odot$. However, the physical cause of these double-peaked line profiles has been debated. For example, Kurono et al. (2013) pointed out that despite expecting the $H^{13}CO^+$ emission to be optically thin, the inverse P Cygni profile and the position-velocity diagram they observe can be reproduced with models of moderately optically thick infalling gas. B335 is associated with an east-west outflow that is prominently detected in ^{12}CO with an inclination of 10° on the plane of the sky and an opening angle of 45° (Hirano et al. 1988; Hirano et al. 1992; Yen et al. 2010). The eastern lobe is slightly oriented on the near side (Stutz et al. 2008), producing blueshifted emission on the eastern side and redshifted emission on the western side. While the core has been found to be slowly rotating at large scales (>2500 au) (Frerking et al. 1987; Saito et al. 1999; Yen et al. 2010, 2011), no clear rotation was found at smaller radii (<1000 au) and no kinematic signature of a disk was reported down to $\sim$10 au (Yen et al. 2015, 2018). Recent observations of the hour-glass shaped magnetic field at small scales have suggested that B335 is an excellent candidate for magnetically regulated collapse (Maury et al. 2018).

In this work, observations of the molecular lines C^{17}O (1–0) and C^{18}O (1–0), which trace the dense circumstellar gas of the inner envelope of B335, are presented along with the ^{12}CO (2–1) line emission tracing the outflow cavity. The molecular line profiles are analyzed and interpreted, providing new constraints on the gas kinematics close to the protostar.

2. Observations and data reduction

Observations of the Class 0 protostellar object B335 were carried out with the ALMA interferometer during the cycle 4 observation period from October 2016 to September 2017, as part of the 2016.1.01552.S project (PI: A. Maury). In the entirety of the work, it is assumed that the centroid position of B335 is at α = 19:37:00.9 and δ = +07:34:09.6 in J2000 coordinates, corresponding to the peak of dust continuum obtained from high-resolution maps (Maury et al. 2018). All lines were targeted using a combination of ALMA configurations: C^{17}O (1–0) and C^{18}O (1–0) were targeted using two configurations, C40-2 and C40-5, and ^{12}CO (2–1) was targeted using C40-1 and C40-4. Technical details of the observations are shown in Table A.1.

Table 1. Characteristics of the applied maps.

Transition	^{12}CO (2–1)	C^{17}O (1–0)	C^{18}O(1–0)
Rest frequency (GHz)	230.53	112.359	109.782
Beam major (arcsec)	2.6	2.6	2.7
Beam minor (arcsec)	1.9	1.9	2.0
PA (°)	88	88	88
Spectral Res. (km s^{-1})	0.20	0.20	0.20
LRS $^{(*)}$ (arcsec)	10.6	21.9	22.4
RMS (mJy beam^{-1})	2016.9	10.0	10.7

Notes. $^{(*)}$Largest recoverable scale computed as $\Theta_{\rm LRS} = (0.6\lambda/B_{\rm min})206265$ in arcsec, where λ is the rest wavelength of the line, in m, and $B_{\rm min}$ is the minimum baseline of the configuration, in m (Asayama et al. 2016).

A preliminary analysis of the data was done with the product images delivered by ALMA to check if any emission was detected and to check the shape of the line profiles. The C^{17}O emission was only detected in the most compact configuration (C40-2), therefore, it is only this configuration that was used to produce C^{17}O and C^{18}O maps, while ^{12}CO was detected in both configurations; thus, a combination of the two data sets was used to produce the maps. Calibration of the raw data was done using the standard script for cycle-4 ALMA data using the Common Astronomy Software Applications (CASA) version 5.6.1–8. The continuum emission was self-calibrated with CASA. Line emission was calibrated using the self-calibrated model derived from the continuum data when it was possible. Final images of the data were generated from the calibrated visibilities using the tCLEAN algorithm within CASA, using Briggs weighting with robust parameter set to 2 for C^{17}O and C^{18}O and 1 for ^{12}CO. After imaging, the ^{12}CO maps were smoothed to reach the same angular resolution as C^{17}O and C^{18}O. The resulting map characteristics are shown in Table 1.

3. Results and analysis

Figure 1 shows the moment 0 of the C^{17}O (1–0) emission in red contours. The mean radius of the 3σ emission is 860 au, indicating that it traces the dense envelope. Top image shows in intensity the dust continuum map observed at 110 GHz, showing emission over 3σ. The bottom image shows in intensity the moment 0 of ^{12}CO (2–1) emission. The ^{12}CO emission probes the outflowing gas, therefore, it can be confirmed that the C^{17}O emission is tracing the envelope and it is not affected by the outflow.

In order to understand the dynamics of the gas that is being probed, the C^{17}O spectra were taken at every 0.5″ pixel of the emission cube, producing a spectral map, as shown in Fig. 2. The line profile patterns show two distinct velocity components with a dip centered around the systemic velocity (8.3 km s^{-1}). Their respective intensities vary depending on the direction of the offset from the continuum peak, with the blue component shown to be more intense in the eastern part of the core, while the red component is dominant in the western part. This behavior is true for all the hyperfine components detected. A clear broadening of the line can be observed near the dust continuum emission peak, and in the north-east region part of the core. The former can be due to natural thermal broadening of the two velocity

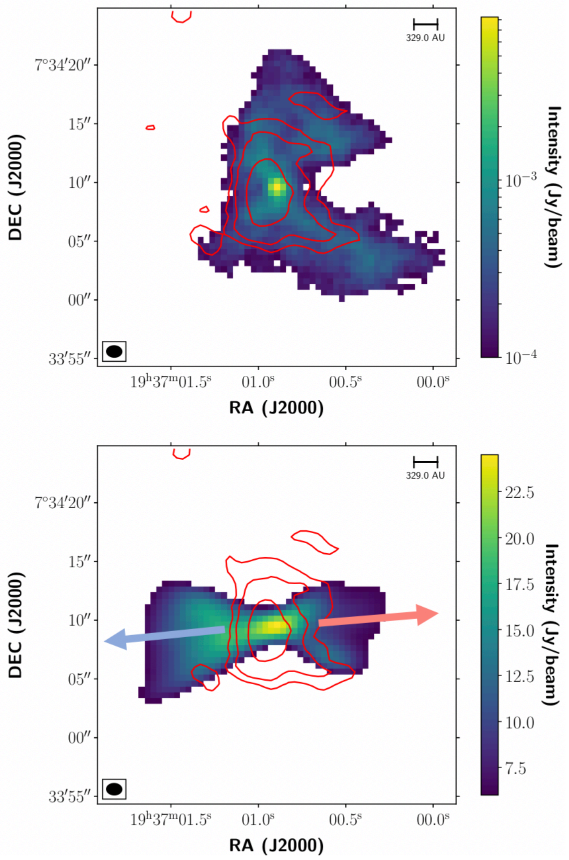

Fig. 1. Red contours showing moment 0 of $C^{17}O$ emission, integrated over the velocity range 4.8–6.2 km s^{-1} and 7.6–9.4 km s^{-1}. Contours show emission at −3, 3, 5, 10 and 30σ, where σ is 10.0 mJy $beam^{-1}$. *Top*: intensity shows dust continuum emission map at 110 GHz for emission over 3σ, where σ is 8.56×10^{-2} mJy $beam^{-1}$. *Bottom*: intensity shows ^{12}CO (2–1) moment 0 emission integrated over the velocity range 1.4–16.2 km s^{-1}, for emission over 3σ, where σ is 2016.9 mJy $beam^{-1}$. The two arrows show the direction of the E-W outflow.

components as the temperature rises in the center of the object, while the latter might be the consequence of the overlapping of the two components due to other dynamical processes. The possibility of the dip being caused by interferometric filtering is discarded since the recovered emission size is on the order of the largest recoverable scale (LRS, see Table 1). Moreover, because $C^{17}O$ is a rare isotopologue, it is not expected to be abundant at largest scales and, therefore, no emission can be filtered at the systemic velocity. Figure 3 shows the velocity channel maps of the $C^{17}O$ (1–0) emission, covering a velocity range from 7.7 to 9.1 km s^{-1} and only showing the main hyperfine component (Fig. B.1 shows a range covering from 5.0 to 9.6 km s^{-1}, showing the two observed hyperfine components). It can be seen that the blue- and red-shifted emission are confined to the east and west regions, respectively, suggesting that the two components are probing gas with different dynamics.

Three independent methods have been used to investigate the origins of the $C^{17}O$ spectral profiles and to examine whether the two distinct peaks could be produced by an optically thick line emission. In the following sections, the analysis of these methods and the modeling of the velocity field in the B335 inner envelope are presented.

3.1. Line opacity estimation

The maximum opacity at the center of the source has been estimated from the H_2 column density, and assuming a standard $C^{17}O$ abundance using Eq. (1) (Jansen 1995):

$$\tau_0 = \frac{A_{10}^{C^{17}O} c^3}{8\pi\nu^3}\frac{N_0^{H_2}[C^{17}O]}{\Delta V}, \tag{1}$$

where $A_{10}^{C^{17}O} = 6.695\times10^{-8}$ s^{-1} is the Einstein coefficient for the $C^{17}O$ J = 1–0 transition (Gordon et al. 2017; Müller et al. 2005), c is the speed of light, ν is the frequency of this transition, $N_0^{H_2} = 3.1\times10^{22}$ cm^{-2} is the peak column density of H_2 in B335 at a radius of 3600 au (Launhardt et al. 2013), $[C^{17}O] = 5\times10^{-8}$ is the $C^{17}O$ abundance relative to H_2 abundance (Thomas & Fuller 2008), and $\Delta V\approx1$ km s^{-1} is the average observed linewidth for the two components together. Using these values, the obtained opacity is $\tau_0 = 0.77$, which corresponds to an opacity typical from an optically thin line.

3.2. Intensity ratio

Because of their similar mass and molecular structure, $C^{17}O$ and $C^{18}O$ are expected to probe gas under similar physical conditions. The $[C^{17}O]/[C^{18}O]$ isotope ratio does not appear to be affected by fractionation and, in addition, if the emission from both $C^{17}O$ and $C^{18}O$ is associated with dense gas shielded from external ultraviolet radiation, selective photo-dissociation is not likely to affect the relative abundances (van Dishoeck & Black 1988). Thus, the only difference in the emission from these two isotopes would result from opacity effects because $C^{18}O$ is a factor of 3.6–3.9 more abundant than $C^{17}O$ (Penzias 1981; Jørgensen et al. 2002). The ratio of integrated intensities is much less sensitive to linewidth effects than the ratio of peak intensity; therefore, we use the latter to rule out any abundances effect on the $C^{17}O$ emission.

We produced beam-matching maps for $C^{17}O$ and $C^{18}O$ to compare the gas at similar scales in both isotopes. The obtained synthesized beams are given in Table 1. Intensities are integrated over the two velocity ranges of 4.8–6.2 km s^{-1} and 7.4–9.4 km s^{-1} for $C^{17}O$, taking into account the two observed hyperfine components and 7.4–9.4 km s^{-1} for $C^{18}O$. The fact that both lines emit in the same range of velocities and are spatially coincident indicates that they are probing the same reservoir of circumstellar gas.

The integrated intensity ratio was computed as $W_{C^{17}O}/W_{C^{18}O}$, where W_i is the integrated intensity of each $C^{17}O$ and $C^{18}O$ individual spectra. Figure 4 shows the obtained integrated intensity ratio map, with values ranging from 0.15 to 0.50 and a mean value centered at 0.28. We note that the intensity ratio is quite homogeneous in most of the extension of the emission, but gets larger at the north and south-west regions. This is attributed to a line broadening of the $C^{17}O$ in those regions when compared to the $C^{18}O$ emission (see $C^{18}O$ spectral map, Fig. C.1). The origin of this broadening is unknown, but we attribute it to complex dynamical processes that might be taking place in these regions.

The expected ratio if both transitions are optically thin is computed as $[C^{17}O]/[C^{18}O]\approx0.25$, where $[C^{17}O]$ and $[C^{18}O]$ are respectively the $C^{17}O$ and $C^{18}O$ abundance with respect to H_2 ($[C^{17}O] = 5\times10^{-8}$ and $[C^{18}O] = 2\times10^{-7}$, Thomas & Fuller 2008). Our observations are therefore in general agreement with the expected ratio if both transitions are optically thin. No increase of the intensity ratio is seen on the observations towards the center of the source, where opacity is expected to be

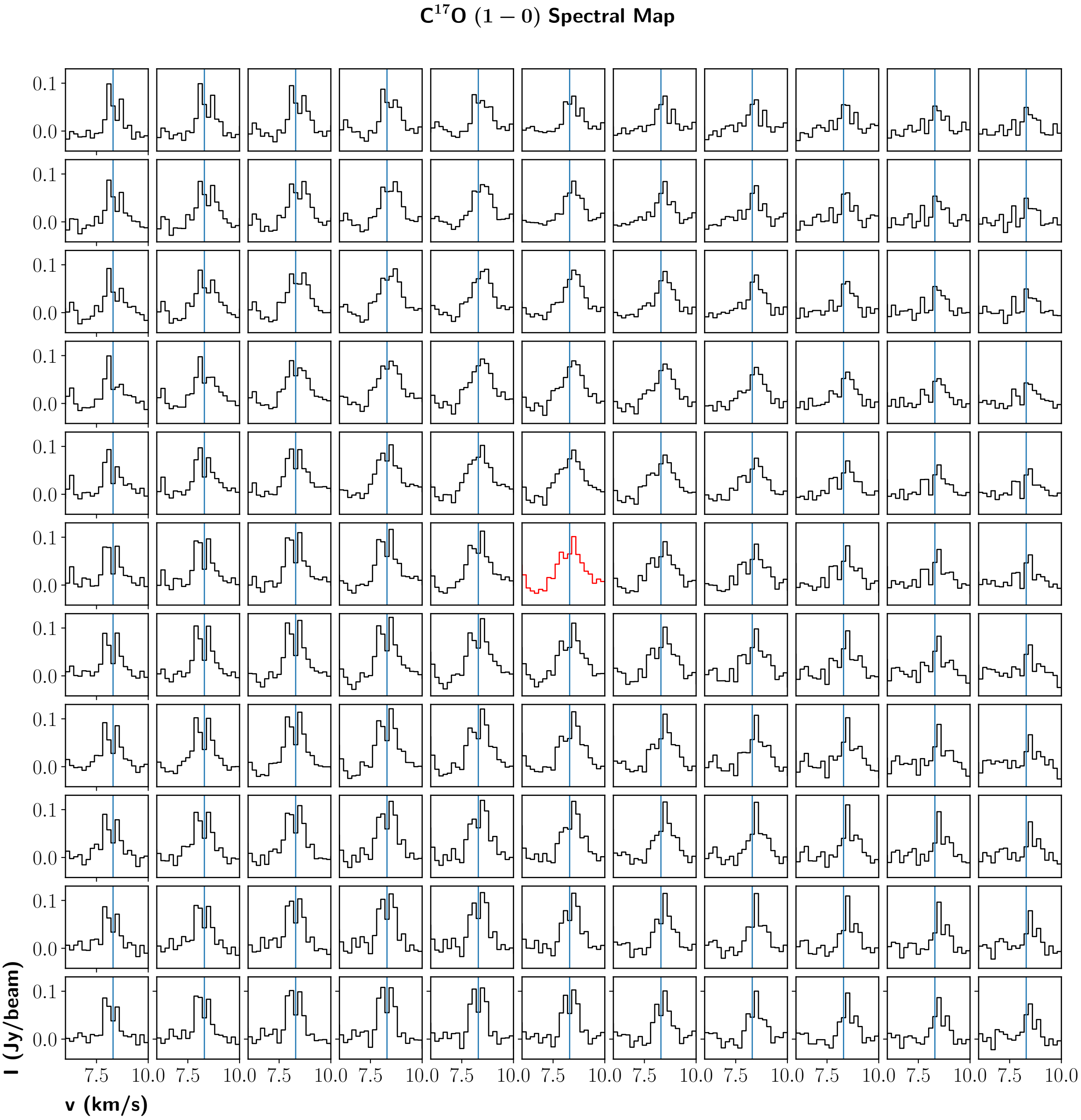

Fig. 2. Spectral map of the $C^{17}O$ (1–0) emission in the inner 900 au, centered on the dust continuum emission peak. The whole map is 5.5″ × 5.5″ and each pixel correspond to 0.5″ (~82 au). For clarity, the spectral range only shows the main hyperfine component. The green spectrum refers to the peak of the continuum emission and the blue line indicates the systemic velocity (8.3 km s^{-1}).

higher, further confirming the later hypothesis. We note that this is also in agreement with the conclusions reached by the analysis of single-dish observations of the $C^{18}O$ (2–1) and $C^{17}O$ (2–1) ($\tau_{C^{18}O\ (2-1)} \sim 0.8$, Evans et al. 2005).

3.3. Modeling of the molecular line profiles

The spectrum at each pixel has been modeled using a program that allows to fit the hyperfine structure of spectral lines with multiple velocity components (*HfS*, Estalella 2017). It also allows to compute the opacity of the line from the relative intensity of the different hyperfine components of the given transition. For every velocity component, the general *HfS* procedure fits four independent parameters simultaneously: the linewidth assumed to be the same for each hyperfine component; the main line central velocity; the main line peak intensity; and the optical depth. The fitting procedure samples the space parameters to find the minimum value of the fit residual χ^2. Because the $C^{17}O$ (1–0)

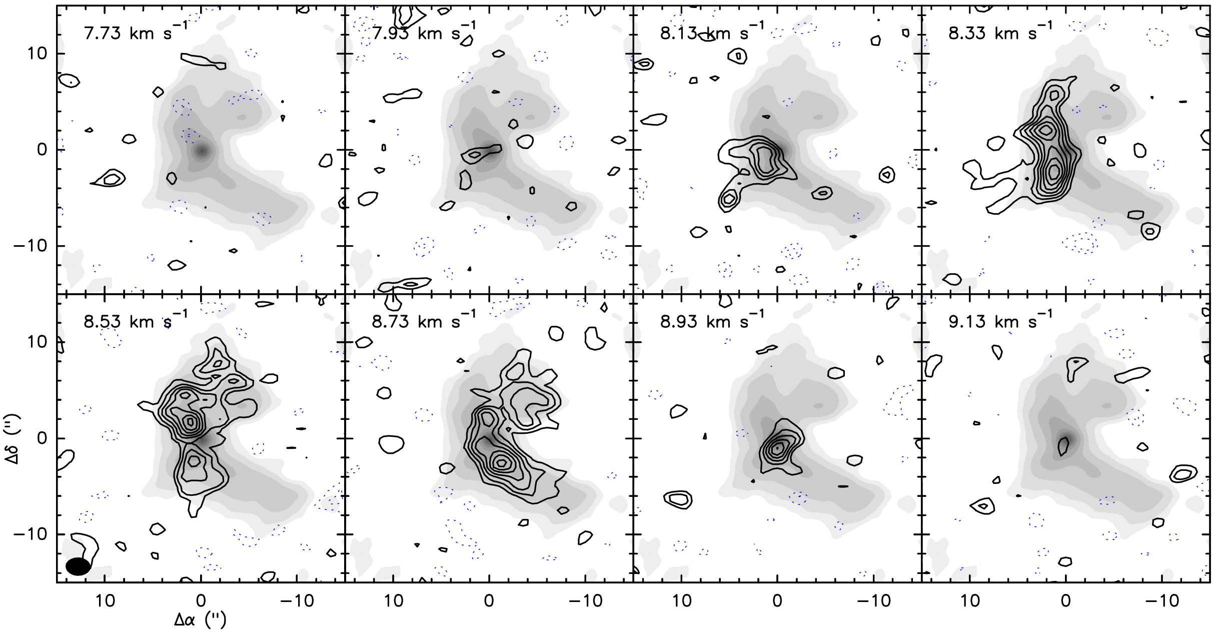

Fig. 3. Contour channel maps of the emission of the $F = 5/2$–$(-5/2)$ hyperfine component of the C^{17}O $J = 1$–0 transition, overlapped with the gray scale image of the 1.3 mm dust emission. Contours are −4, −2, and from 2 to 18 by steps of 2σ, where σ is 10 mJy beam^{-1}. The synthesized beam is shown in the *bottom left panel* as a filled ellipse. The $v_{\rm LSR}$ channel velocities are shown in the *top left part of the panels*.

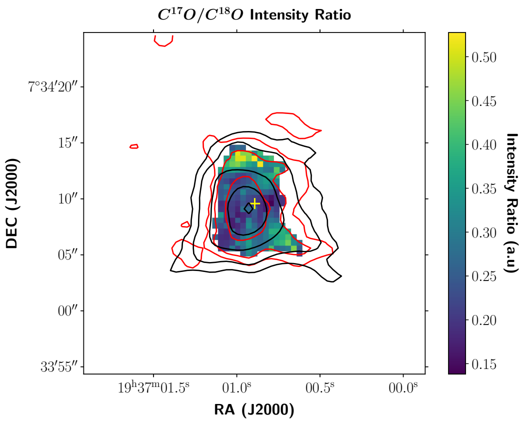

Fig. 4. C^{17}O to C^{18}O integrated intensity ratio. Red contours show integrated intensity for C^{17}O at −3, 3, 5, 10 and 30σ, where σ is 10.0 mJy beam^{-1}. Black contours show integrated intensity for C^{18}O at −3, 3, 5, 10 and 30σ, where σ is 10.7 mJy beam^{-1}. The yellow cross indicates the centroid position of B335.

emission is expected to be optically thin, we attempted to model the double-peaked profiles with two velocity components: one blue- and another red-shifted. Initial expected values were introduced and the program was allowed to proceed to fit emission with a minimum signal-to-noise ratio (S/N) of 3σ. The peak velocity, the linewidth, and the opacity maps obtained from the fitting are shown in Fig. 5.

The velocity maps (top images of Fig. 5) show that the two different components, blue and red-shifted, occupy two separated regions, at east and west offsets from the center of the source respectively, with some regions overlapping, where the double peak can be observed in the spectra. The mean average, velocity for the two components are 8.1 and 8.6 km s^{-1} respectively. The velocity dispersion maps (middle images of Fig. 5) show a mean velocity dispersion for the two components of 0.7 and 0.5 km s^{-1}, which get broader, up to 0.9 ∼ 1, closer to the center of the object where the two components overlap (see central spectra in Fig. 2). The opacity maps (bottom images of Fig. 5) show that the opacity is generally less than 1, and only goes up to 3 in some specific pixels. These larger values are also associated with a very large error (on the order of the value itself) so, they are not significant and are not shown in the plots. Figure 6 shows the histograms for the opacity values for both fitted components. The average opacity has been estimated from the *HfS* modeling and is found to be $\tau_{\rm bs} = 0.464$ and $\tau_{\rm rs} = 0.474$, for the blue- and red-shifted components, respectively, which is in concordance with the upper limit estimated before.

4. Discussion

4.1. Linewidths and kinetic temperature

The main radius probed with the C^{17}O emission was computed from the 3σ contour and found to be 860 au. A region enclosing radii from 100 (about half of the FWHM beam) to 860 au was chosen for the gas kinematics analysis. The kinetic temperature of the gas has been estimated from the formula for dust temperature in an optically thin regime assuming only central heating by the B335 protostar derived by Shirley et al. (2011). The underlying assumption is that dust and gas are expected to be in thermal equilibrium, being coupled via collisions at the densities probed here ($>10^5$ cm^{-3}). We use Eq. (2) (Evans et al. 2015) which we adapted to the new distance of 164.5 pc:

$$T_{\rm k}(r) = 67\left[\frac{r}{41\ {\rm au}}\right]^{-0.4}\ {\rm K}. \quad (2)$$

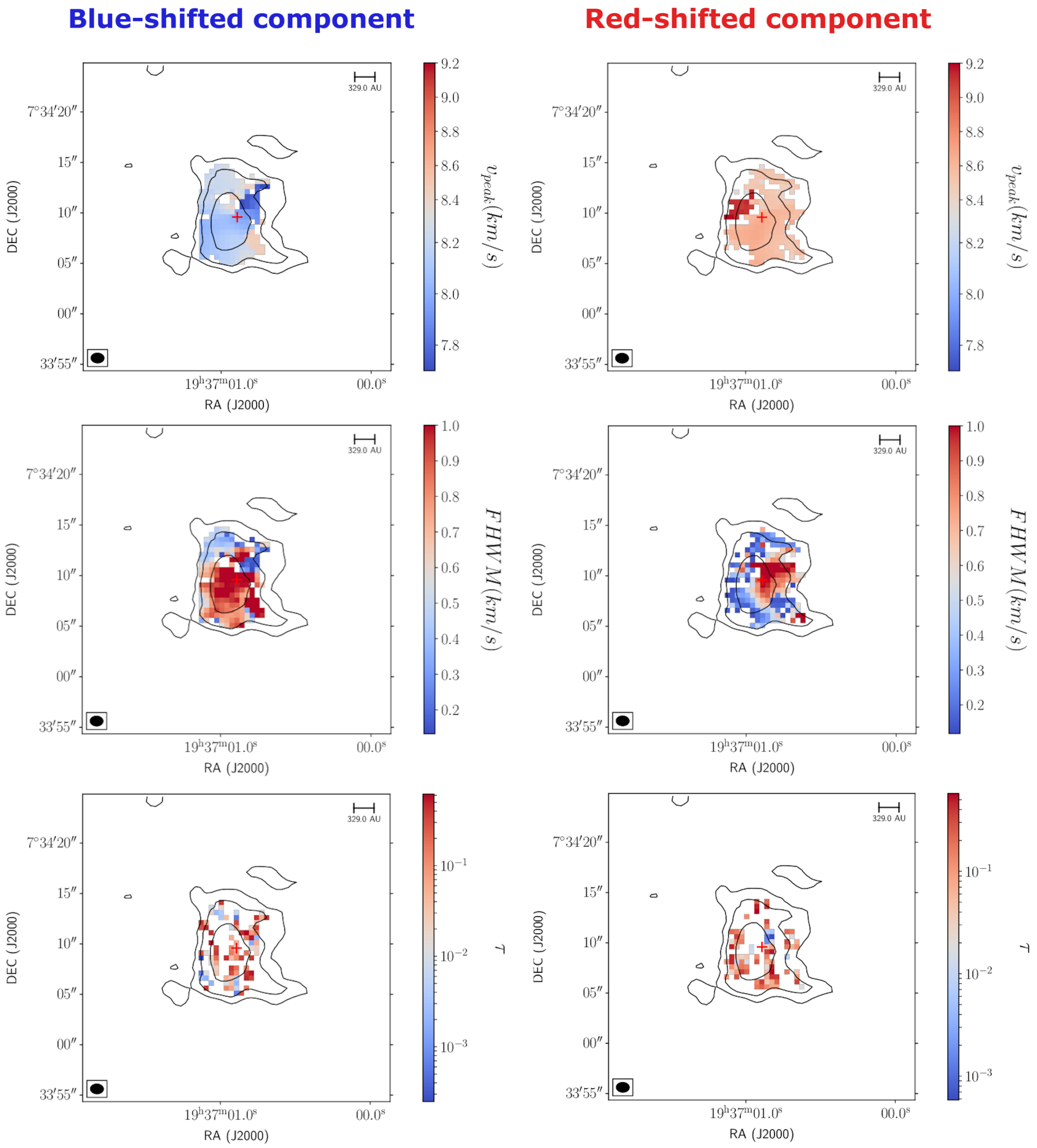

Fig. 5. $C^{17}O$ (1–0) maps obtained from modeling the line profiles with two velocity components. Overlaid contours show the integrated intensity at 5, 10, 20 and 30σ, where σ is 10.0 mJy beam^{-1}. *Top*: peak velocity. *Middle*: linewidt. *Bottom*: opacity. *Each column* shows one of the two velocity components. Red crosses indicate the centroid position of B335.

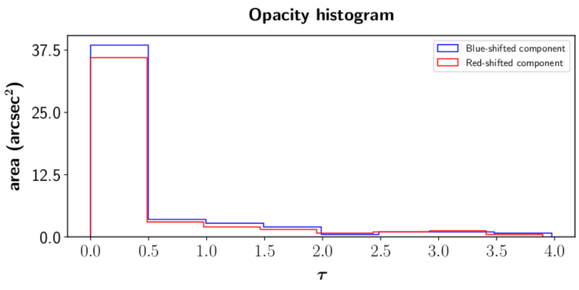

Fig. 6. Opacity histograms from the fitting of the two individual velocity components.

The gas kinetic temperature was computed for the two radii probed, with values in the range of $T_k(100\text{ au}) = 46$ K and $T_k(860\text{ au}) = 20$ K. The observed linewidths obtained in the previous section have been compared with the expected thermal linewidth, given by:

$$\Delta v_{\rm th} = \sqrt{\frac{8\ \ln 2\, k_{\rm b}\, T_{\rm k}}{m}}\ \text{km s}^{-1}, \tag{3}$$

where T_k is the gas kinetic temperature, m is the molecular mass (29.01 amu for $C^{17}O$) and k_b is the Boltzmann constant. The expected thermal linewidth for $C^{17}O$ has been computed for the temperatures at the two different radii: $\Delta v_{\rm th}(100\text{ au}) = 0.27$ km s^{-1} and $\Delta v_{\rm th}$ (860 au) = 0.17 km s^{-1}. The observed linewidths are

Table 2. $C^{17}O$ (1–0) observed linewidth and non-thermal contributions at different radii.

	Blue-shifted *FWHM* (km s^{-1})	Red-shifted *FWHM* (km s^{-1})
Observed total	0.78	0.56
Non-thermal (100 au)	0.73	0.48
Non-thermal (860 au)	0.76	0.52

larger than the thermal ones for both velocity components. This indicates that the observed linewidth is the result of the thermal component plus a non-thermal contribution (e.g., turbulence and large-scale motions such as infall and outflow, $v_{\rm obs}^2 = v_{\rm th}^2 + v_{\rm non-th}^2$). The non-thermal contribution of the line has been computed for both velocity components and the results are shown in Table 2. The non-thermal component at the inner and outer radius are indistinguishable because of the limited spectral resolution (0.2 km s^{-1}).

The sound speed, c_s, is in the 0.2–0.3 km s^{-1} range for temperatures between 20 and 46 K and $\gamma \sim 7/5$. This means that the non-thermal contribution to the linewidth is supersonic.

Simulations have shown that in star forming cores systematic large-scale motions (such as infall) can contribute significantly (∼50%) to the non-thermal component of the linewidth (Guerrero-Gamboa & Vázquez-Semadeni 2020). We can do a rough estimation of the contribution from infall, by measuring the infall velocity difference from two different radii, $\Delta\sigma = v_{\rm ff}(r1) - v_{\rm ff}(r2)$, where $v_{\rm ff}(r) = \sqrt{\frac{2GM_{B335}(r)}{r}}$, G is the gravitational constant and M_{B335}(r) is the mass enclosed at the considered radius r. To compute the mass, we consider that the total mass at different radii is the sum of the mass in the envelope plus the mass of the central object. The mass of the gas in the envelope contained up to a certain radius is computed by integrating the 110 GHz dust continuum emission and using standard assumptions (see Eq. (4) in Jørgensen et al. 2007). The maximum velocity difference along the LOS would occur at the core's center. For the two adopted radius, 860 and 100 au, the envelope mass, $M_{\rm env}$, is ∼0.16 $M_\odot$ and ∼0.012 $M_\odot$, respectively. We also adopt a mass for the central object between 0.05 and 0.26 $M_\odot$, which are the predicted values from infall models (see Yen et al. 2015; Evans et al. 2015, and in prep.). Therefore, the total mass enclosed within a 100 and 860 au radii are in the 0.06–0.16 $M_\odot$ and 0.27–0.41 $M_\odot$ ranges, respectively. The estimated range of $\Delta v_{\rm ff}$ is 0.46–1.01 km s^{-1}. Given the errors coming from the computation of all the previous parameters, the non-thermal contribution of the linewidth is of the same order as the broadening due to free-fall motions along the line of sight: it is, hence, possible that the observed velocity pattern is due to infall.

4.2. Possible origins of the observed gas motions

Our ALMA observations of the $C^{17}O$ (1–0) emission suggest an optically thin emission at all scales probed by the observations (100–860 au). Overall, the spatial extent of the $C^{17}O$ emission is similar to the one of the dust continuum emission, but $C^{17}O$ is less peaked and decreases more smoothly with decreasing density outwards; this suggests that the gas traced with $C^{17}O$ is not entirely related to the outflow cavity. The $C^{17}O$ emission maximum is not coincident with the dust continuum peak position, which might suggest slight abundance variations of the $C^{17}O$ at high densities close to the protostar. Nevertheless, the prominence of the double-peaked velocity pattern is not correlated with the intensity of the dust continuum emission, demonstrating that those profiles are not due to red-shifted absorption against a strong continuum or a source of $C^{17}O$. Thus, these two velocity components trace distinguished gas motions. A simple isotropic inside-out envelope collapse can not easily reproduce the gas motions we observe in the B335 envelope. In this section, we discuss various hypothesis for the physical origin of the gas motions observed.

Despite being isolated, B335 is embedded in an extended molecular gas cloud of density $\sim 10^3$ cm^{-3} (Frerking et al. 1987). However, $C^{17}O$ is a rare isotopologue which is mostly confined to a high-density central region and its low abundance at large-scales would prevent observing such a tenuous layer, suggesting there is no missing flux coming from large-scale $C^{17}O$ emission. To confirm that this is the case, we estimated the missing flux from the $C^{18}O$ (1–0) ALMA observations by comparing it with the 45 m Nobeyama data of the same transition presented in Saito et al. (1999). Our $C^{18}O$ map was smoothed to match the beam size of the Nobeyama telescope, which at the frequency of this transition (109.782 GHz) is 16″. We obtained the spectra on a region of one beam size around the center of B335 and transformed the flux density to brightness temperature using the Rayleigh-Jeans law. We obtained a peak temperature of $T_{\rm MB} = 0.79 \pm 0.08$ K and an integrated temperature of $\int T_{\rm MB} {\rm d}v = 0.53$ K km s^{-1}. This means that our ALMA observations are recovering around 14% of the total flux detected with single-dish data. However, because $C^{17}O$ is expected to be much more compact than $C^{18}O$ we expect the missing flux to be much less for the former. Frerking et al. (1987) presented single-dish data of the $C^{17}O$ (1–0) transition and concluded that all their emission is coming from the center of the source in a region smaller than the beam of their telescope (1′.6 for the $C^{17}O$ (1–0) transition). This extension is much smaller than the one observed for $C^{18}O$ (1–0) detected in both works, which is about 4′. This is consistent with the fact that $C^{17}O$ is much less abundant than $C^{18}O$, especially at large scales, and that it is mainly tracing the core and not the envelope. Therefore, we expect the missing flux of $C^{17}O$ in our ALMA data to be much less and, in addition, to be recovering at least twice the recovered flux of $C^{18}O$, namely, around 30%. We also note that while our observation might be missing flux, this should not be enough to produce the huge dip in our data and it cannot explain the structured velocity pattern we observe in the spectral maps, since the missing flux will be at the systemic velocity and would not be able to completely absorb only one of the two components at different offsets.

A possible cause for the blueshifted and redshifted gas motions observed in protostellar envelopes could be organized core rotation. Our observations do not support this hypothesis as they do not show a clear velocity gradient in the equatorial plane, where rotation motions would mostly contribute to the observed velocity field. Instead, both redshifted and blueshifted velocities are observed in both the northern and southern regions (see Fig. 5). While rotation motions have only been detected at larger envelope radii in B335 (>2500 au, Saito et al. 1999; Yen et al. 2011), we stress that the conclusion regarding the absence of small-scale rotation (e.g., Yen et al. 2010) should be further investigated using the new insights on gas motions in the envelope that our observations have uncovered.

B335 has a well-studied outflow, with its axis close to the plane of the sky and with a well-defined X-shaped biconical shape in ^{12}CO (Bjerkeli et al. 2019). Although some contamination by the gas from the outflow cannot be completely ruled out, we present here arguments supporting the hypothesis that our $C^{17}O$ maps can be used to study the envelope gas kinematics.

$C^{17}O$ is a rare isotopologue which is known to trace dense envelope gas and is not expected to be detected in more tenuous outflow cavities. The morphology of $C^{17}O$ emission is very different from the one observed in typical outflow cavities tracers, such as C_2H (Imai et al. 2016) or ^{12}CO (see bottom image in Fig. 1 and Bjerkeli et al. 2019). Moreover, no spectral signature of outflow is observed, such as large wings observed in ^{12}CO (Bjerkeli et al. 2019), and the maximum velocity shift from the rest velocity remains quite small (±1 km s^{-1}). Therefore, the kinematic pattern observed in our $C^{17}O$ maps cannot be produced by outflow alone, and it does provide a strong evidence of distinguished velocity contributions from the gas in the inner region of the B335 protostellar envelope.

The $C^{17}O$ velocity maps in Fig. 5 show that the largest gas velocities are found ∼1″ from the center along the two northern outflow cavity walls, tracing gas at reverse velocities with respect to the outflow velocities. Considering the 10° inclination of the system, the spatial distribution of $C^{17}O$ emission following closely that of the dust and other typical dense gas tracers; and the fact that the linewidths of the two velocity components are in general agreement with the expected linewidths from infall motions, the most likely hypothesis is that these high-velocity (±1 km s^{-1}) features trace, accreting gas flowing along the outflow cavity walls and onto the central protostar. The peak velocities tentatively increase towards the central protostellar objects, for the features along the eastern outflow cavity walls, but no clear velocity gradient could be resolved in the current observations: additional observations with better spatial resolution may allow to test further this hypothesis. Finally, we note that the strongly redshifted emission at the north-east was already detected in ALMA $C^{18}O$ observations reported by Yen et al. 2015 (see Fig. 2 in their work).

Dust continuum emission observed with ALMA at various millimeter and sub-millimeter wavelengths all show a striking excess of dust emission associated to the outflow cavity walls. While this could be a temperature effect due to increased heating from the central protostar of these walls, it could also be a true density increase in compact features easily picked up by interferometric observations. Magnetized models of protostellar formation (for a review see Zhao et al. 2020) suggest cavity walls could be preferential sites to develop accretion streamers, as observed in the non-ideal magneto-hydrodynamic (MHD) models of protostellar accretion and outflow launching (Machida 2014; Figs 8 and 9 in Tomida et al. 2012). Indeed, these are locations where the poloidal magnetic field is mostly parallel to the inflow direction and, therefore, would exert less magnetic braking for material infalling along the walls. This hypothesis is also in agreement with the dust polarization observations of magnetic field lines in B335 (the redshifted gas feature we observe along the north-eastern cavity wall is associated to highly organized B-field lines aligned with the tentative gas flow) and the scenario of magnetically-regulated infall proposed in Maury et al. (2018).

We note that the observed non-thermal components of the linewidths are found to be supersonic. If the observed gas motions we detect indeed trace localized accretion motions, these could be supersonic. While the development of supersonic filamentary accretion features were reported in numerical models of protostellar formation (Padoan et al. 2005; Banerjee et al. 2006; Kuffmeier et al. 2019) and the observations suggested supersonic infall is occurring in a few protostellar envelopes at larger scales (>1000 au, Tobin et al. 2010; Mottram et al. 2013), it is the first time such anisotropic supersonic infall motions have been tentatively reported in the B335 inner envelope.

4.3. Impact on the characterization of protostellar mass accretion rates

In the following, we briefly discuss the implications of our work and whether the localized accretion features detected in B335 are common, all the while remaining mostly unresolved in many observations of accreting protostars.

Self-similar solutions for analytical models of the collapse of an isothermal sphere, including only thermal pressure and gravity, predict typical mass accretion rates on the order of $\sim 10^{-4}\,M_\odot\,\mathrm{yr}^{-1}$ (Larson 1969; Penston 1969; Shu 1977). Turbulent models and MHD numerical models have produced slightly lower mass accretion rates of $\sim 10^{-6}$–$10^{-5}\,M_\odot\,\mathrm{yr}^{-1}$. Episodic accretion with highly variable rates (from a $\dot{M} \sim 10^{-5}\,M_\odot\,\mathrm{yr}^{-1}$ down to $\dot{M} < 10^{-6}\,M_\odot\,\mathrm{yr}^{-1}$) is often observed in both hydro and MHD numerical models of protostellar formation, in the accretion of envelope material onto the disk and the protostar itself (Lee et al. 2021), and of disk material to the central growing protostar (Dunham & Vorobyov 2012; Vorobyov & Basu 2015). Robust observational estimates of protostellar accretion rates are crucial to distinguish between models, but also to shed light on several open questions on star formation, since they are key quantities for our interpretation of the protostellar luminosities and of the typical duration of the main protostellar accretion phase (Evans et al. 2009; Maury et al. 2011). Indeed, observations may have revealed a discrepancy between the observed protostellar bolometric luminosities, and the protostellar accretions rates: this is the so-called "luminosity problem" (Kenyon et al. 1990). Protostellar accretion rates derived from molecular line emission – and more particularly from the modeling of inverse P Cygni profiles with analytical infall models – should produce luminosities 10–100 times larger than the typically observed bolometric luminosities (for a review, see Dunham et al. 2014). Observations of the molecular line profiles in B335 (Evans et al. 2005, 2015) have been used to fit models of protostellar infall suggesting $\dot{M} \sim 6.2 \times 10^{-6}\,M_\odot\,\mathrm{yr}^{-1}$ (assuming an effective sound speed of $0.3\,\mathrm{km\,s^{-1}}$, Evans et al., in prep.), although arguably these estimates are associated to large error bars. The observed bolometric luminosity of B335 lies an order of magnitude below the accretion luminositym L_{acc}, that such accretion rates should produce (Evans et al. 2015); despite being a prototype for protostellar infall models, B335 also suffers from the luminosity problem.

If the "actual" protostellar mass accretion rates stem from localized collapsing gas at small scales, potentially affected by unresolved multiple velocity components, the true linewidths associated with infalling gas feeding the growth of the protostar would be quadratically smaller than the ones measured at larger scales where these components would be entangled (or if the individual velocity components are interpreted as being part of a single velocity component with a central dip due to optically thickness). Smaller intrinsic linewidths of the infalling gas, at small radii, may result in smaller effective sound speed and, hence, lower mass accretion rate derived from the analytical infall models, since $\dot{M} \propto c_s^3/G$. It is, therefore, possible that the observed bolometric luminosity of B335 is, ultimately, compatible with its accretion luminosity L_{acc}. In the revised B335 scenario we propose here, the mass accretion rate on the protostar could be dictated by localized supersonic infall rather than by the large scale infall rate of the envelope: this may open a window to partially solving the "luminosity problem", although episodic vigorous accretion would probably continue to be necessary to explain the relatively short statistical lifetimes for the Class 0 phase. Future observations should be used to carry out a more detailed characterization of whether a significant fraction of the final stellar mass could be fed to the central object through highly localized anisotropic infall. Recently, Pineda et al. (2020) reported the detection of an "accretion streamer" connecting the dense core to disk scales and found a streamer infall rate $\sim 10^{-6}\,M_{\odot}\,\mathrm{yr}^{-1}$, of the same order of magnitude as the global mass accretion rate inferred from molecular line observations in B335. Hence, it is possible that many previous studies have failed to grasp the full complexity of the gas motions making up the accretion onto the central protostars. It is the large angular and spectral resolution, along with the great sensitivity of the presented ALMA observations which allowed to detect the two distinct velocity components on the line emission profiles in B335. More observations at the same small-scales and spectral resolution of optically thin emission in different protostars are needed in order to determine if these localized gas motions are common. Moreover, more refined protostellar infall models will have to be carried out in the future to take this new small scales into account and include more complex geometries with, for instance, asymmetric structures and preferential accretion along outflow cavities.

5. Summary

In this work, we describe ALMA observations of the $C^{17}O$ emission tracing gas kinematics in the B335 envelope and we show that the line emission exhibits widespread double-peaked profiles. Based on the analysis, we present the following conclusions:

- Derivations of the line opacity have shown that the emission of the line is optically thin and, therefore, the observed double-peaked profiles cannot be produced by self-absorption. Thus, inverse P Cygni profiles coming from symmetrical inside-out collapse cannot fully explain the observed complex velocity field.
- After discarding filtering of large-scale emission or other types of motions, such as rotation or outflow, we determined that only distinct gas motions contributing to the same line-of-sight (LOS) could explain the observed line profile pattern.
- The linewidth analysis determined that the two velocity components are compatible with infall motions and could be due to localized infall in preferential directions. The main hypothesis presented here is that the collapse of the envelope onto the protostar is occurring along the equatorial plane, but also along the outflow cavity walls, where the magnetic field topology is more favorable.

More observations at similar scales and spectral resolution are needed to determine whether these double-peaked profiles are common in protostellar objects at similar evolutionary states. Moreover, further modeling of the B335 envelope with more complex collapse models, such as anisotropic collapse, are needed to determine the exact physical origin of the observed velocity field.

Acknowledgments. The authors acknowledge the very useful discussions with N. Evans and Y. Yang. This project has received funding from the European Research Council (ERC) under the European Union Horizon 2020 research and innovation program (MagneticYSOs project, grant agreement N° 679937). J.M.G. is supported by the grant AYA2017-84390-C2-R (AEI/FEDER, UE). This publication is based on data of ALMA data from the project 2016.1.01552.S (PI: A. Maury).

References

André, P. 1995, Astrophys. Space Sci., 224, 29
André, P., Ward-Thompson, D., & Barsony, M. 1993, ApJ, 406, 122
Asayama, S., Biggs, A., de Gregorio, I., et al. 2016, ALMA Partnership
Banerjee, R., Pudritz, R. E., & Anderson, D. W. 2006, MNRAS, 373, 1091
Basu, S., & Jones, C. E. 2004, MNRAS, 347, L47
Bate, M. R., & Bonnell, I. A. 2005, MNRAS, 356, 1201
Bjerkeli, P., Ramsey, J. P., Harsono, D., et al. 2019, A&A, 631, A64
Chandler, C. J., & Sargent, A. I. 1993, ApJ, 414, L29
Choi, M., Evans, N. J., Gregersen, E. M., & Wang, Y. 1995, ApJ, 448, 742
Di Francesco, J., Myers, P. C., Wilner, D. J., Ohashi, N., & Mardones, D. 2001, ApJ, 562, 770
Dunham, M. M., & Vorobyov, E. I. 2012, ApJ, 747, 52
Dunham, M. M., Stutz, A. M., Allen, L. E., et al. 2014, in Protostars and Planets VI (Tucson: University of Arizona)
Estalella, R. 2017, PASP, 129, 21
Evans, N. J., Lee, J., Rawlings, J. M. C., & Choi, M. 2005, ApJ, 626, 919
Evans, N. J., Dunham, M. M., Jørgensen, J. K., et al. 2009, ApJ, 181, 321
Evans, N. J., Di Francesco, J., Lee, J., et al. 2015, ApJ, 814, 22
Frerking, M. A., Langer, W. D., & Wilson, R. W. 1987, ApJ, 313, 320
Gordon, I. E., Rothman, L. S., Hill, C., et al. 2017, J. Quant. Spectr. Rad. Transf., 203, 3
Guerrero-Gamboa, R., & Vázquez-Semadeni, E. 2020, ApJ, 903, 136
Hirano, N., Kameya, O., Nakayama, M., & Takakuro, K. 1988, ApJ, 327, L69
Hirano, N., Kameya, O., Kasuga, T., & Umemoto, T. 1992, ApJ, 390, L85
Imai, M., Sakai, N., Oya, Y., et al. 2016, ApJ, 830, L37
Jansen, D. 1995, PhD thesis, Leiden University, The Netherlands
Jørgensen, J. K., Schöier, F. L., & van Dishoeck, E. F. 2002, A&A, 389, 908
Jørgensen, J. K., Bourke, T. L., Myers, P. C., et al. 2007, ApJ, 659, 479
Keene, J., Davidson, J. A., Harper, D. A., et al. 1983, ApJ, 274, 43
Kenyon, S. J., Hartmann, L. W., Strom, K. M., & Strom, S. E. 1990, AJ, 99, 869
Kuffmeier, M., Calcutt, H., & Kristensen, L. E. 2019, A&A, 628, A112
Kurono, Y., Saito, M., Kamazaki, T., Morita, K., & Kawabe, R. 2013, ApJ, 765, 85
Larson, R. B. 1969, MNRAS, 145, 271
Launhardt, R., Stutz, A. M., Scmiedeke, A., et al. 2013, A&A, 551, A98
Lee, Y.-N., Charnoz, S., & Hennebelle, P. 2021, A&A, 648, A101
Machida, M. N. 2014, ApJ, 796, L17
Maureira, M. J., Arce, H. G., Offner, S. S. R., et al. 2017, ApJ, 849, 89
Maury, A. J., André, P., Men'shchikov, A., Könyves, V., & Bontemps, S. 2011, A&A, 535, A77
Maury, A. J., Girart, J. M., Zhang, Q., et al. 2018, MNRAS, 477, 2760
Mottram, J. C., van Dishoeck, E. F., Schmalzl, M., et al. 2013, A&A, 558, A126
Müller, H. S. P., Schlöder, F., Stutzki, J., & Winewisser, G. 2005, J. Mol. Struct., 215
Murillo, N. M., van Dishoeck, E. F., van der Wiel, M. H. D., et al. 2018, A&A, 617, A120
Myers, P. C. 2012, ApJ, 752, 9
Padoan, P., Kritsuk, A., Norman, M., & Nordlund, Å. 2005, ApJ, 622, L61
Penston, M. V. 1969, MNRAS, 144, 425
Penzias, A. A. 1981, ApJ, 249, 518
Pineda, J. E., D., S., Caselli, P., et al. 2020, Nat. Astron., 4, 1158
Rawlings, J. M. C. 1996, Astrophys. Space Sci, 237, 299
Saito, M., Sunada, K., Kitamura, Y., & Hirano, N. 1999, ApJ, 518, 234
Shirley, Y. L., Mason, B. S., Magnum, J. G., et al. 2011, ApJ, 141, 39
Shu, F. H. 1977, ApJ, 214, 488
Shu, F. H., Adams, F. C., & Lizano, S. 1987, ARA&A, 25, 23
Stutz, M. A., Rubin, M., Werner, M. W., et al. 2008, ApJ, 687, 389
Thomas, H. S., & Fuller, G. A. 2008, A&A, 479, 751
Tobin, J. J., Hartmann, L., Looney, L. W., & Chang, H. F. 2010, ApJ, 712, 1010
Tokuda, K., Onishi, T., Saigo, K., et al. 2014, ApJ, 789, L4
Tomida, K., Okuzumi, S., & Machida, M. N. 2012, ApJ, 801, 117
van Dishoeck, E. F., & Black, J. H. 1988, ApJ, 334, 771
Vorobyov, E. I., & Basu, S. 2015, ApJ, 805, 115
Watson, D. M. 2020, Res. Notes AAS, 4, 88
Yen, H. W., Takakuwa, S., & Ohashi, N. 2010, ApJ, 710, 1786
Yen, H. W., Takakuwa, S., & Ohashi, N. 2011, ApJ, 742, 57
Yen, H. W., Takakuwa, S., Koch, P. M., et al. 2015, ApJ, 812, 22
Yen, H. W., Zhao, B., Koch, P. M., et al. 2018, A&A, 615, A58
Zhao, B., Caselli, P., Li, Z., et al. 2020, MNRAS, 492, 3375
Zhou, S., Evans, N. J., Kömpe, C., & Walmsley, C. M. 1993, ApJ, 404, 232

Appendix A: Technical details of the ALMA observations

Table A.1. Technical details of the ALMA observations.

Config.	Date (mm/dd/yy)	Timerange (hh:min:s.ms)	Center freq. (GHz)	Spec. Res. (km s^{-1})	Flux cal.	Phase cal.	Bandpass cal.
C40-1	19/03/2017	10:40:52.8 - 10:53:42.8	231.0	0.09	J1751+0939	J1851+0035	J1751+0939
C40-2	02/07/2017	15:30:38.9 - 15:49:59.2	110.0	0.08	J1751+0939	J1938+0448	J1751+0939
C40-4	21/11/2016	22:41:22.0 - 23:28:19.8	231.0	0.09	J2148+0657	J1851+0035	J2148+0657
C40-5	10/22/2016 - 10/23/2016	23:34:05.4 - 00:02:51.3	110.0	0.08	J2148+0657	J1938+0448	J2025+3343

Appendix B: C^{17}O full channel maps

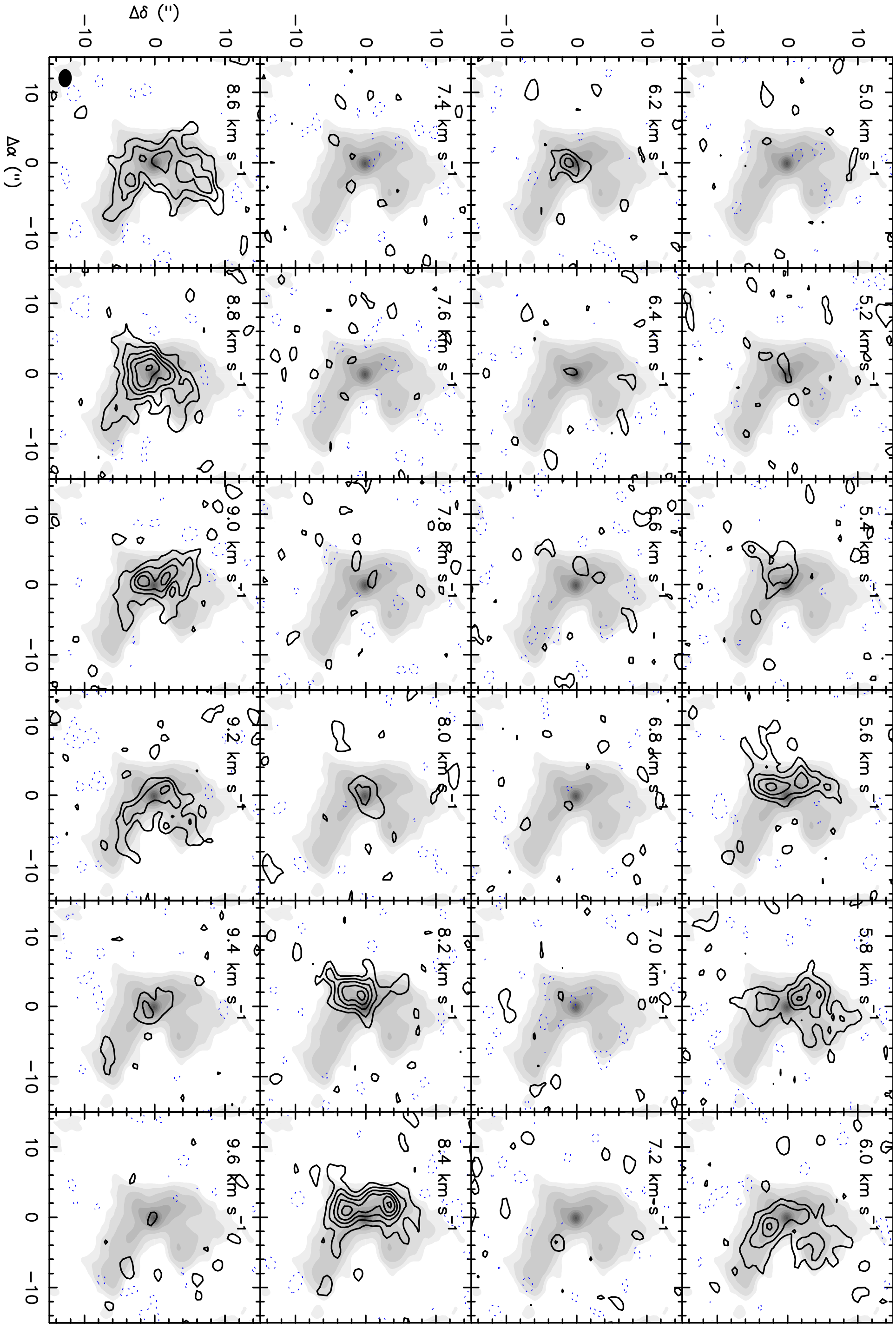

Fig. B.1. Contour channel maps of the C^{17}O (1-0) emission showing the two main hyperfine components, overlapped with the gray scale image of the 1.3 mm dust emission. Contours are −4, −2, and from 2 to 18 by steps of **2σ, where σ is** 10 mJy Beam^{-1}. The synthesized beam is shown in the bottom left panel as a filled ellipse. The $v_{\rm LSR}$ channel velocities are shown in the top-left part of the panels.

Appendix C: C^{18}O spectral map

Fig. C.1. Spectral map of the C^{18}O (1-0) emission in the inner 900 au, centered on the dust continuum emission peak. The whole map is 5.5″ × 5.5″ and each pixel correspond to 0.5″ (∼ 82 au). The green **refers to the** peak of the continuum emission and the blue line indicates the systemic velocity (8.3 km s^{-1}).

Chapter 4

Ionization and Magnetic Field

Studying the chemical composition of active star forming cores is an important step towards the understanding of the chemical evolution of the universe. Moreover, a deep knowledge of the chemical species that populate those regions is an important asset to understand and study key aspects of the star formation process. Understanding how the chemistry and the physics of an object are related is a complicated issue which relies not only in astronomical observations, but also in laboratory studies and complex chemical modeling which help unveiling the processes that promote the formation of the different species.

As stated in Sections 1.2.3 and 1.4.6, deuteration and ionization fraction of some of the present species are particularly important processes which relate the chemistry and the physics of a particular object. Since deuterium is the most abundant rare isotopologue, its presence and incorporation into other molecules can trace the fate of the species that formed the gas in the interstellar medium and collapsed to form the protostellar envelopes. Ionization, on the other hand, can give clues about energetic processes that might occur in the source, such as CR incidence or UV radiation.

As described in Section 1.2, magnetic fields might play a significant role in regulating the collapse on the first stages of protostellar formation. Since the gas in a protostellar object is not completely ionized and not all the matter is coupled to the magnetic field, the behavior of neutral and charged particles will be different and non-ideal MHD processes become then important. The importance of these effects depends not only on the strength of the magnetic but also on the ionization degree of the source.

In this chapter, we will describe how the deuteration and ionization fraction are related, and derive both quantities in our source, B335. We will also describe how to compute an important quantity characterized by the coupling of the magnetic field and directly related to the ionization fraction, the ambipolar diffusion lengthscale, and how all these together can be used to determine the strength of the magnetic field present in the source.

4.1 Introduction

4.1.1 Derivation of χ_e from [D]/[H]

Direct measure of electron abundances can be done by observing ionized molecules and comparing them to their neutral counterparts. However, the more abundant charge carriers, such as H_3^+ or atomic carbon and metals (e.g., C^+, Mg^+ or Fe^+), are difficult to observe, or are highly depleted (Graedel et al. 1982, Caselli et al. 1998). Instead, indirect determination of χ_e can be done through the estimation of molecular column densities and chemical models (Caselli 2002). One way to do that is to observe the deuterium abundance.

Simple models have been developed for the estimate of the ionization fraction and the cosmic ray ionization rate in molecular clouds (Dalgarno and Lepp 1984). In a simple steady-state model, the deuteration fraction (here R_D) and the hydrogenation fraction (R_H = $[HCO^+]/[CO]$) are given by (Wootten et al. 1979, Guelin et al. 1982):

$$R_D = \frac{1}{3}\frac{k_f x(HD)}{k_e \chi_e + \delta} \tag{4.1}$$

$$R_H = \frac{[\zeta/n(H_2)]k_{H_3^+}}{[\beta\chi_e + \delta]\beta'\chi_e} \tag{4.2}$$

where k_f is the forward rate coefficient for reaction 1.24, k_e is the dissociative recombination rate of H_2D^+, β is the dissociative recombination rate coefficient of H_3^+, β' is the dissociative recombination rate coefficient of HCO^+, $k_{H_3^+}$ is the rate coefficient for the reaction $H_3^+ + CO \rightarrow HCO^+ + H_2$, $x(HD)$ is the fractional abundance of HD relative to H_2, ζ is the cosmic-ray ionization rate and $\delta = \delta + H_2D^+ \sim \delta_{H_3^+}$ is the destruction rate of H_2D^+ and H_3^+ due to reactions with neutral species such as CO and O.

The computation of R_D and R_H from Eqs. 4.1 and 4.2 rely on the derivation of δ which, in turn, depends on the depletion fraction of O and C. When only a fraction of O and C remains in the gas-phase, $1/f_D$, the destruction rate at 10 K is $\delta = 6.5 \times 10^{-13}/f_D$ cm^{3}s^{-1}. Then χ_e and ζ, can be estimated at 10 K as:

$$\chi_e = \frac{2.7 \times 10^{-8}}{R_D} - \frac{1.2 \times 10^{-6}}{f_D} \tag{4.3}$$

$$\zeta = \left[7.5 \times 10^{-4}\chi_e + \frac{4.6 \times 10^{-10}}{f_D}\right] \chi_e n(H_2) R_H \tag{4.4}$$

This is a good approximation for molecular clouds, but it does not necessarily hold in denser environments. Mainly, it is based on the strong assumption that the depletion of C and O are equal (x(O) $\sim$ x(C) $\sim$ x(CO), where x(i) are the fractional abundances). While there is evidence that a large fraction of both atoms is still contained in the solid-phase in dense regions at temperatures of around 10 K, there is no good evidence that the depletion value is the same for both (Caselli et al. 1998). Moreover, it only takes into account the presence of CO as a neutral species in the gas for the destruction of H_2D^+.

For highly depleted cores, observations of DCO^+ and HCO^+ can not be used alone to estimate χ_e. One solution is to use other molecules, such as N_2D^+ and N_2H^+. The greater volatility of N_2 allows it to remain in the gas-phase even when CO is very depleted, making the ratio $[N_2D^+]/[N_2H^+]$ a good estimate of R_D and, subsequently, of χ_e (Caselli 2002).

4.1.2 Formation and destruction pathways of DCO^+

Another strong assumption included in the derivation of R_D from equation 4.1 is that rate coefficients are computed at 10 K, but it could be different at larger temperatures. At these temperatures, Eq. 1.24 is very favorable (Pagani et al. 1992), and the evolution of the deuteration fraction will be mainly dependent of the abundance of H_2D^+. In the particular case of DCO^+ and HCO^+, these species will be formed following the reactions (Wootten 1987):

$$\mathrm{H_2D^+ + CO \rightarrow DCO^+ + H_2}, \tag{4.5}$$

$$\mathrm{H_2D^+ + CO \rightarrow HCO^+ + HD} \tag{4.6}$$

However, at warmer temperatures (T > 50 K) Eq. 1.25 becomes more favorable than Eq. 1.24, and DCO^+ can also form from the following reaction:

$$\mathrm{CH_2D^+ + O \rightarrow DCO^+ + H_2} \tag{4.7}$$

Thus, the deuteration fraction at such temperatures will not only depend on the destruction rate of H_2D^+, but also on reactions involving CH_2D^+, which are not contemplated in Eq. 4.1.

Additionally, in regions with high irradiation and as temperatures become larger, the depletion of neutrals decreases and the presence of those species, i.e., CO or N_2, in the gas phase will increase the destruction rate coefficients of H_2D^+ and H_3^+ which, in turn, will decrease the rate at which reaction 4.6 occurs, and diminishing the presence of DCO^+ and other deuterated molecules in the gas phase.

4.1.3 The ambipolar diffusion lengthscale

Assuming that the medium is dominated by turbulence, and that the turbulent flow is not aligned with the magnetic field, the velocity of neutrals at a scale L depends on the energy density at that given scale, and can be represented by a Kolmogorov-type power law for the smallest turbulent energy of the following form (Li and Houde 2008):

$$V_{AD}^2(L_{AD}) = a + bL_{AD} \tag{4.8}$$

The ambipolar diffusion lengthscale, L_{AD} corresponds to the scale at which the magnetic diffusion overcomes the flux-freezing ($R_m < 1$) and ions decouple from neutrals. It can be derived as:

$$L_{AD}^n = -a/[b(1-0.37n)] \tag{4.9}$$

where n is the spectral index, and a and b are the fitting parameters of the power law for the velocity dispersion of neutrals and ions, respectively:

$$\sigma_{neutrals}^2(L) = bL^n \tag{4.10}$$

$$\sigma_{ions}^2(L) = bL^n + a \tag{4.11}$$

4.1.4 Estimation of the magnetic field strength

From Eq. 1.10, and knowing V and L, the strength of the magnetic field can be computed. Following Li and Houde 2008 and Hezareh et al. 2014 we assume that the decoupling scale $L = L_{AD}$ corresponds to $R_m = 1$. Substituting $n_i = n_n\chi_e$, where χ_e is the ionization fraction and n_n is the neutral volume density, $\nu_i = 1.5 \times 10^{-9}\ n_n$ and mean ion and neutral atomic mass numbers $A_i = 29$ and $A_n = 2.3$, the field strength can be derived as (Hezareh et al. 2014):

$$B = \left(\frac{L_{AD}}{10^6 au}\right)^{1/2} \left(\frac{V_{AD}}{1kms^{-1}}\right)^{1/2} \left(\frac{n_n}{10^6 cm^{-3}}\right) \times \left(\frac{\chi_e}{10^{-7}}\right)^{1/2} mG \tag{4.12}$$

4.2 Observations of H^{13}CO$^+$ (1-0), (3-2) and DCO$^+$ (3-2)

In order to obtain maps of the ionization fraction following the method presented in Section 1.2.3 we have to produce first maps of the deuteration fraction. For this we use our observations of the DCO$^+$ (3-2) and H^{13}CO$^+$ (3-2) molecular line emission. The preliminary analysis of the product images given by ALMA reported that the line profiles of both molecules present double-peaked profiles, similar to the ones observed in C^{17}O and presented in Chapter 3. The preliminary analysis also shows that DCO$^+$ (3-2) emission is detected in both ALMA configurations (C40-1 and C40-4), therefore, we combined the two datasets to obtain the spectral cubes. For the H^{13}CO$^+$ (3-2) emission, since our datasets only include ACA observations, we obtained small scale data for the same transition from

Table 4.1: Imaging parameters and final maps characteristics. For lines where more than one velocity range is indicated each range correspond to the multiple hyperfine components.

	DCO^+ (3-2)	$H^{13}CO^+$ (3-2)	^{12}CO (2-1)	N_2D^+ (3-2)	$H^{13}CO^+$ (1-0)	$C^{17}O$ (1-0)
Robust parameter	1	1	1	1	1	1
L.R.S (arcsec)	11.3	16.0	10.6	10.6		
Pixel size (arcsec)	0.5	0.5	0.5	0.5	0.25	0.25
Θ_{maj} (arcsec)	1.5	1.5	1.5	1.5	2.6	2.6
Θ_{min} (arcsec)	1.5	1.5	1.5	1.5	2.6	2.6
P.A. (°)	0	0	0	0	0	0
Spectral res. (km s^{-1})	0.2	0.2	0.2	0.2	0.15	0.15
vel. range (km s^{-1})			7.6 - 9.4		7.4-9.2	4.7-6.5 7.7-9.3
RMS (mJy/beam)	11.17	21.28	634.6	5.23	17.17	17.58

the ALMA Project 2015.1.01188.S (P.I. H. Yen), and combined them with our own data. Additionally, we will make use of the ^{12}CO (2-1) and N_2D^+ (3-2) line emission data obtained from our data set, both presenting emission in the same two ALMA configurations.

To be able to compute the AD length-scale following the method in Section 4.1.3, we need to find among our sample two molecules (one neutral and one ionic) that probe gas at similar conditions and similar scales, and whose emission is optically thin. The first approach was to use $H^{13}CO^+$ (3-2) and $H^{13}CN$ (3-2) line emission (following Hezareh et al. 2010). However, our dataset only contained $H^{13}CN$ emission from the ACA configuration. We obtained data for $H^{13}CN$ (4-3) from the ALMA project 2012.1.00346.S (P.I. N. Evans). This presented two problems, (i) line profiles of the $H^{13}CN$ emissions were very broad (Fig. 4 in Evans et al. 2015), suggesting that both molecules do not trace the same gas or trace different kinematics (e.g., outflow contamination in $H^{13}CN$ emission), and (ii) $H^{13}CO^+$ (3-2) line profiles are double-peaked, and the two velocity components were indistinguishable in the $H^{13}CN$ emission. Since the only neutral molecules left in our dataset are CO isotopologues, we chose $C^{17}O$ (1-0), and compare them to our $H^{13}CO^+$ (1-0) observations. This presents the advantage that $C^{17}O$ emission was found to be optically thin. Moreover, both molecules present the two velocity components well distinguished in frequency, which allows a direct comparison of the two tracers.

Since the scales of the DCO^+ and $H^{13}CO^+$ observations are similar to the ones observed in the $C^{17}O$ (1-0) emission presented in Chapter 3, we assume the presence of the two distinct velocity components through all of our data. To ensure that we are tracing similar scales as the $C^{17}O$ (1-0), so that this hypothesis is valid, and allow for comparison among all the tracers, we adjust our imaging to obtain maps with similar angular and spectral resolution as the ones presented in Chapter 3. For DCO^+ (3-2) and $H^{13}CO^+$ (3-2) we restricted the baselines to a common *u,v*-range, between 9 and 140 $k\lambda$, and finally smoothed them to the same angular resolution. The preliminary analysis shows that both, $C^{17}O$ (1-0) and $H^{13}CO^+$ (1-0), emission is barely detected in the most extended configurations. We proceed by applying a common *uv-tapering* of 1.5″ to both lines. This procedure allows to weight down the largest baselines, giving more weight to the smaller baselines and allowing to obtain a better S/N. Furthermore, we smoothed the data to obtain exactly the same angular resolution. The imaging parameters used to obtain all the spectral cubes are shown in Table 4.1. Even though the characteristics and properties of the $C^{17}O$ (1-0) maps are slightly different than the ones present in Chapter 3, due to the differences in the imaging process, the intensity, the line profiles and the velocity patterns show the same characteristics, i.e., line profiles are double-peaked, present a blue-asymmetry and present the same velocity pattern at different offsets. In Fig. 4.1 we present the spectra of both maps of $C^{17}O$ (1-0) averaged in the central 5″ in radius around the center of the source. Both spectra show the same distribution over the velocity range, confirming that the imaging process has no large effect on the shape of the line profile, and that the two velocity components can still be observed.

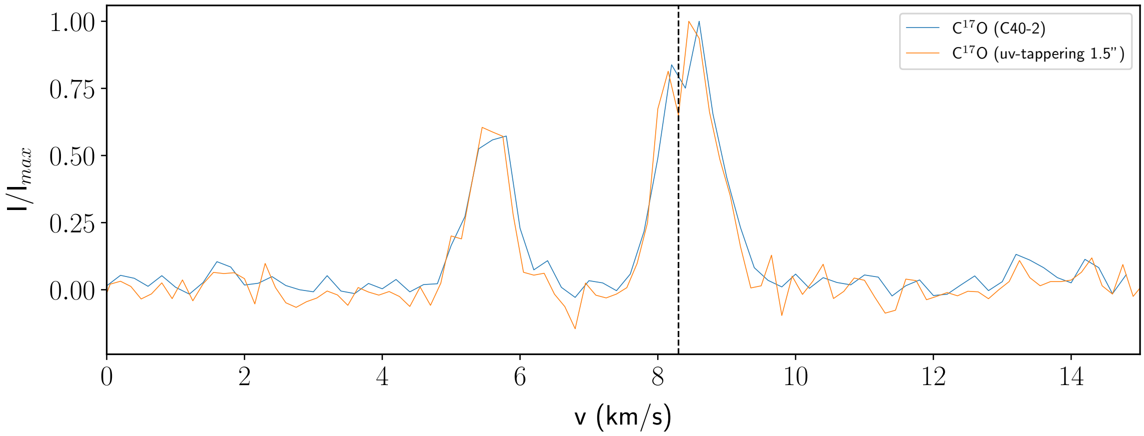

Figure 4.1: Comparison of the $C^{17}O$ (1-0) spectra averaged around 5″ in radius from the source center for the map presented in Chapter 3, obtained only used the C40-2 ALMA configuration (in blue), and for the map presented in this Chapter, obtained with both configurations and a *uv-tappering* at 1.5″.

To be able to carry the ambipolar diffusion length scale analysis, we produced 6 additional smoothed maps of $C^{17}O$ (1-0) and $H^{13}CO^+$ (1-0), increasing the beam size by 0.5 ″ each time. The obtained resolutions of each map are shown in Table 4.2. Since the results for $C^{17}O$ are similar to the ones presented in Chapter 3, only the results from the $H^{13}CO^+$ (1-0) observations are presented in this section, and only for the first length scale (L_1).

We note that for all of the lines and prior to the imaging process, (i) only N_2D^+ (3-2) was self-calibrated following the procedure described in Section 2.1.5, and (ii) we subtracted the continuum emission from all the lines following the procedure described in Section 2.4.3.

Table 4.2: Angular resolution values for the different lengths-scales used in the AD analysis.

	L_1	L_2	L_3	L_4	L_5	L_6
Θ_{maj} (″)	2.6	3.1	3.6	4.1	4.6	5.1
Θ_{min} (″)	2.6	3.1	3.6	4.1	4.6	5.1

4.2.1 Integrated intensity images

The integrated intensity images for all the lines were obtained from the spectral data cubes following the general procedure detailed in Section 2.4.4. All maps presented in this section have a size of 30″× 30″. The integrated velocity ranges and the resulting RMS noise are shown in Table 4.1.

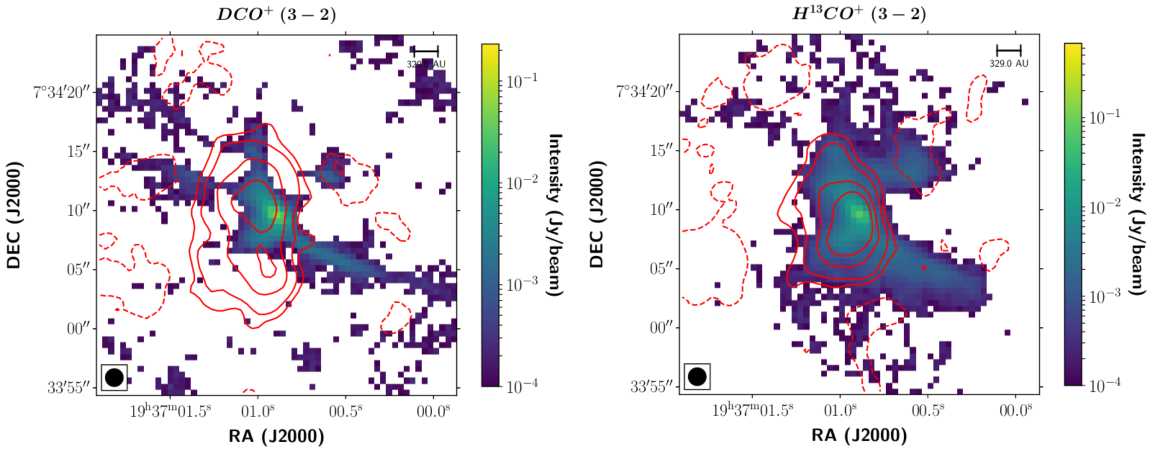

Figure 4.2: In contours, integrated intensity maps for DCO$^+$ (3-2) and H^{13}CO$^+$ (3-2), left and right respectively, overplotted with intensity maps of the continuum at the appropriate frequency, 231 GHz and 247 GHz. The beam size is indicated with a black circle on the bottom left part of the images, where the beam size is the same for the dust continuum and for the line emission observations.

Figure 4.2 shows in contours the integrated intensity emission of DCO$^+$ (3-2) and H^{13}CO$^+$ (3-2) overplotted with the dust continuum emission at the appropriate frequencies. The morphology of both lines is similar and slightly asymmetric towards the blue-shifted side of the core. Their extension is also similar, however, H^{13}CO$^+$ emission is slightly more compact, extending only ∼7″ (1,151 au) from north to south, while DCO$^+$ extends to ∼11″ (1,809 au). This indicates that DCO$^+$ traces colder gas. Both emission seems mostly uncorrelated from the dust continuum emission. Emission from H^{13}CO$^+$ peaks close to the dust continuum peak, while it is not the case for the DCO$^+$. The displacement of the DCO$^+$ intensity peak respect to the H^{13}CO$^+$ one suggests that they are not probing exactly the same gas at the peak continuum, even if the scales are similar. This might be a local effect due to the large T and irradiation conditions destroying DCO$^+$. Additionally, DCO$^+$ emission presents a little arm extension towards the south-west region which coincides with the arm of the dust continuum emission. However, this could also be an effect of the outflow. In general, their emission is coincident at the same projected scales, and while this is not an absolute indicative that they trace the same gas, we assume that the conditions traced by both molecules are similar enough as to proceed with the deuteration analysis.

Left panel of Fig. 4.3 shows in contours the integrated intensity of H^{13}CO$^+$ (1-0) overplotted with the corresponding continuum emission. The morphology of the line emission does not coincide with the one observed for the dust continuum, being the former more extended and suggesting that they are not correlated. Similar to the DCO$^+$ (3-2) emission, H^{13}CO$^+$ (1-0) also presents an extension towards the south-west region, but again this can be an effect of the outflow. The right panel of Fig. 4.3 shows the same integrated intensity emission overplotted to the C^{17}O (1-0) integrated intensity. The morphology of both lines is similar, however, H^{13}CO$^+$ (1-0) is more asymmetric towards the east region, similar to DCO$^+$ (3-2) and H^{13}CO$^+$ (3-2). The extension of the H^{13}CO$^+$ (1-0) is also larger than for

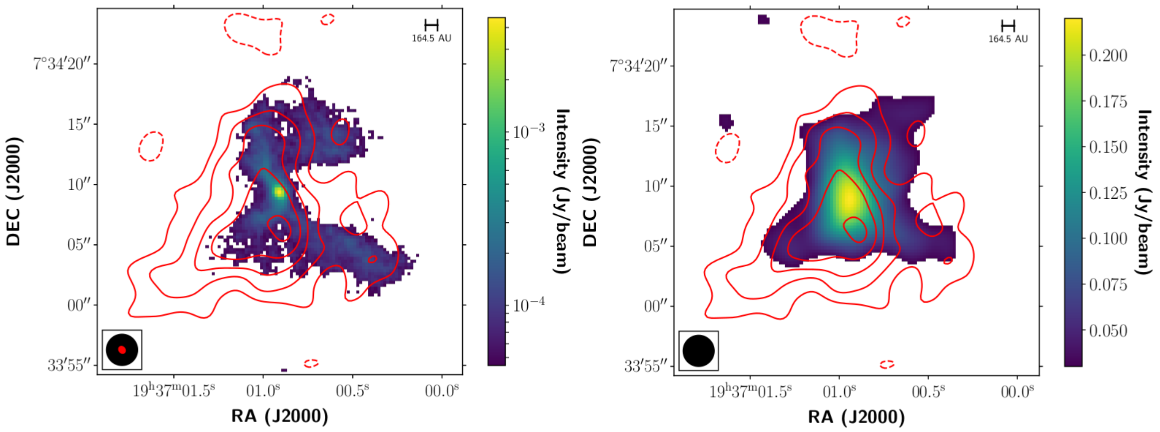

Figure 4.3: In contours, $H^{13}CO^+$ (1-0) integrated intensity emission at -2, 3, 5, 7, 9 and 11σ. In colors, dust continuum intensity at 88 GHz(left), showing emission over 3σ, where σ = 1.501$\times$10^{-2} mJy/beam and $C^{17}O$ (1-0) integrated intensity emission (right), showing values over 3σ. The size of the beam is shown in the bottom left part of the images. The black circles correspond to the beam of the molecular line observations while the red circle indicates the beam of the dust continuum observations.

$C^{17}O$(1-0), indicating that $H^{13}CO^+$ is tracing colder gas at larger radii from the protostar. The extension of $H^{13}CO^+$ (1-0) is also larger than for $H^{13}CO^+$ (3-2). This is expected since the excitation temperature and the critical density of the J=1-0 is lower than the J=3-2 (T_{ex} $\sim$ 5 K vs. $\sim$ 15 K, Houde et al. 2000a, Hezareh et al. 2008), the former tracing colder gas. The intensity peak of both $H^{13}CO^+$ (1-0) and $C^{17}O$ (1-0) is also not coincident. It is then, not completely clear that both species are tracing the same gas at the dust peak.

None of the lines show a morphology which indicates that they are tracing the outflow cavity. To make sure this is the case, Fig. 4.4 shows in contours the integrated intensity emission of the three tracers overplotted with the integrated intensity emission of ^{12}CO (2-1). All of the lines seem to present some outflow contamination, which appears to be more important in the southern region, where the intensity contours present arms which coincide with the emission of the outflow walls. This effect seems to be particularly important for $H^{13}CO^+$ (1-0), however, we will restrict our ambipolar diffusion analysis to the equatorial region where contamination from the outflow should be less important. The presence of outflow contamination will also be addressed by analyzing the spectral maps presented in the next section.

4.2.2 Spectral maps

The spectral maps for the DCO^+ (3-2), $H^{13}CO^+$ (3-2) and $H^{13}CO^+$ (1-0) were produced following the procedure on Section 2.4.4 and are shown in Figs. 4.5, 4.6 and 4.7 respectively. The DCO^+ (3-2) and $H^{13}CO^+$ (3-2) show the emission in a region of 5.5″ × 5.5″(900 au) around the center of the source and each spectrum corresponds to one pixel on the image of 0.5″ (82 au). The $H^{13}CO^+$ (1-0) shows only a region of 4″ × 4″ (658 au) and each spectrum corresponds to a pixel of 0.25″ (41 au). We choose the extension of each spectral map considering the pixel size of the original images and for readability of the plots.

The three lines present the same double-peaked line profiles already observed for the

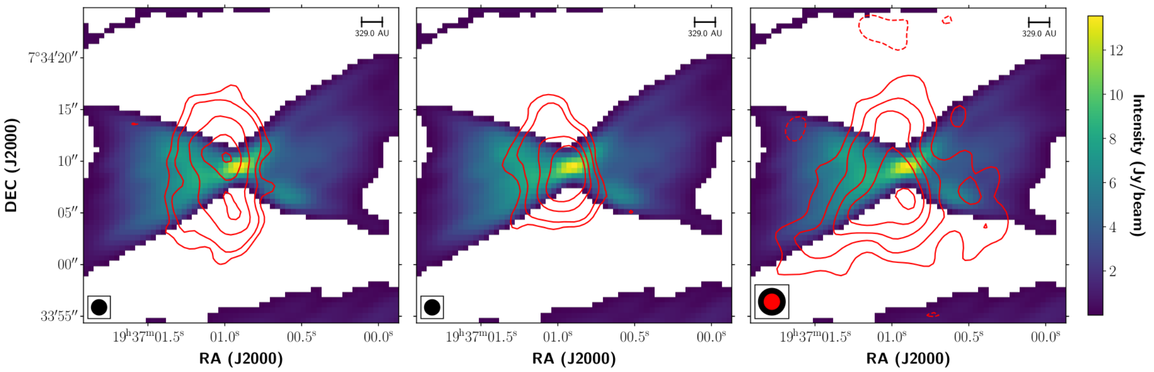

Figure 4.4: In intensity, ^{12}CO (2-1) integrated intensity, showing values $>3\sigma$ for convenience. In contours, left panel shows DCO^{+} (3-2) emission, middle panel shows H^{13}CO^{+} (3-2) and right panel shows (1-0). For DCO^{+} (3-2) and H^{13}CO^{+} (3-2) contours show intensity for 3, 5, 10, 15, 20 and 30σ, for H^{13}CO^{+} (1-0) contours show intensity for -2, 3, 5, 7, 9 and 11σ, where σ values are indicated in Table 4.1. The beam size of the DCO^{+} (3-2), H^{13}CO^{+} (3-2) and (1-0) is indicated in black in the bottom left part of the image. The beam size for the ^{12}CO (2-1) emission is only different for the H^{13}CO^{+} (1-0) map, where it is indicated in red.

C^{17}O (1-0) line and presented in Chapter 3. The same pattern repeats where one of the two velocity components progressively disappears at different offsets from the center of the object, being the blue-shifted component predominant in the eastern region of the source and the red-shifted component in the western region. For the three transitions, the blue-shifted component presents always a larger intensity than the red-shifted one, which produces the asymmetric morphology observed in the integrated intensity images (Figs. 4.2 and 4.3). Since none of the lines present a morphology typical from outflow tracers (see Fig. 4.4), we assume that the observed double-peaked profiles are not tracing the outflow cavity and tracing the inner envelope instead. However, the H^{13}CO^{+} (3-2) spectral map presents an additional third component, or a "*shoulder*", situated in the south-east region of the emission. This additional component appears to be broad and at velocities of $\sim$7.6 - 7.7 km s^{-1}. We do attribute this component to outflow contamination. The additional component is not observed in H^{13}CO^{+} (1-0), which traces colder gas, neither in DCO^{+} (3-2) which is not expected to be present in the outflow cavity, since it is destroyed by high irradiation. Considering the morphology of the integrated intensity images, and the general lack of outflow signatures in the line profiles, we assume that the outflow has a a negligible effect in our observations and that we can proceed with the analysis.

Contrary to the case of the C^{17}O (1-0) line, we can not rule out the presence of effects produced by large-scale filtering in the other tracers. This is particularly visible in the DCO^{+} (3-2) and H^{13}CO^{+} (3-2) spectral maps, where negative emission is observed in the center and west regions of the emission (Figs. 4.5 and 4.6). To asses the filtering effect in the data, we produced channel maps of the DCO^{+} (3-2) and the H^{13}CO^{+} (3-2) emission, which are shown in Figs. 4.8 and 4.9. Channels between 8.0 and 8.4 km s^{-1} show an important amount of negative emission, indicating that the filtering effect is large and has an important effect on the west region of the source, and will be important for the shape of the two components in that area. The east region of the source does not suffer such a

Figure 4.5: Spectral map of the DCO^+ (3-2) emission in the inner 900 AU, centered on the dust continuum emission peak. The whole map is 5.5" × 5.5" and each pixel correspond to 0.5" (∼ 82 au). The red spectrum refers to the peak of the continuum emission and the blue line indicates the systemic velocity (8.3 km s^{-1}).

contamination. We can conclude that the effect of filtering is large.

To further prove if the spectral features of the lines are similar, and assess if they are tracing the same gas, we present the averaged spectra over 5″ in radius around the source for DCO^+, $C^{17}O$ and both transitions of $H^{13}CO^+$ in Fig. 4.10. The spectra of DCO^+, $H^{13}CO^+$ (1-0) and (3-2) present a similar morphology, with the same relative intensities for both velocity components, being the blue-shifted component more intense than the red-shifted and indicating that they are tracing gas which is subject to the same physical processes. This is not true for $C^{17}O$ (1-0), which presents a much more intense red-shifted profile, being even more intense than the blue-shifted component. The intensity of both components agree with the asymmetry observed in the integrated intensity images, being $C^{17}O$ (1-0) much less asymmetric than DCO^+ (3-2) and $H^{13}CO^+$(1-0) and (3-2). This represents another indication that the gas traced by $C^{17}O$ and $H^{13}CO^+$ is not the same, and it is not subject to

Figure 4.6: Spectral map of the H^{13}CO^{+} (3-2) emission in the inner 900 au, centered on the dust continuum emission peak. The whole map is 5.5" × 5.5" and each pixel correspond to 0.5" ($\sim$ 82 au). The red spectrum refers to the peak of the continuum emission and the blue line indicates the systemic velocity (8.3 km s^{-1}).

the same kinematics.

While both outflow contamination and filtering effects can present a source of uncertainty in our measurements, we understand that they alone can not produce the observed line profiles and the velocity pattern observed through the source. Therefore, we keep our hypothesis for the presence of two distinct velocity components tracing different kinematics and proceed with the modeling under this assumption.

4.2.3 Line profile modeling

The spectrum at each pixel was modeled using the *HfS* fitting program, following the procedure described in Section 2.5. Since none of the lines presents a resolved hyperfine structure, the opacity can not be derived, and only peak velocity and velocity dispersion maps

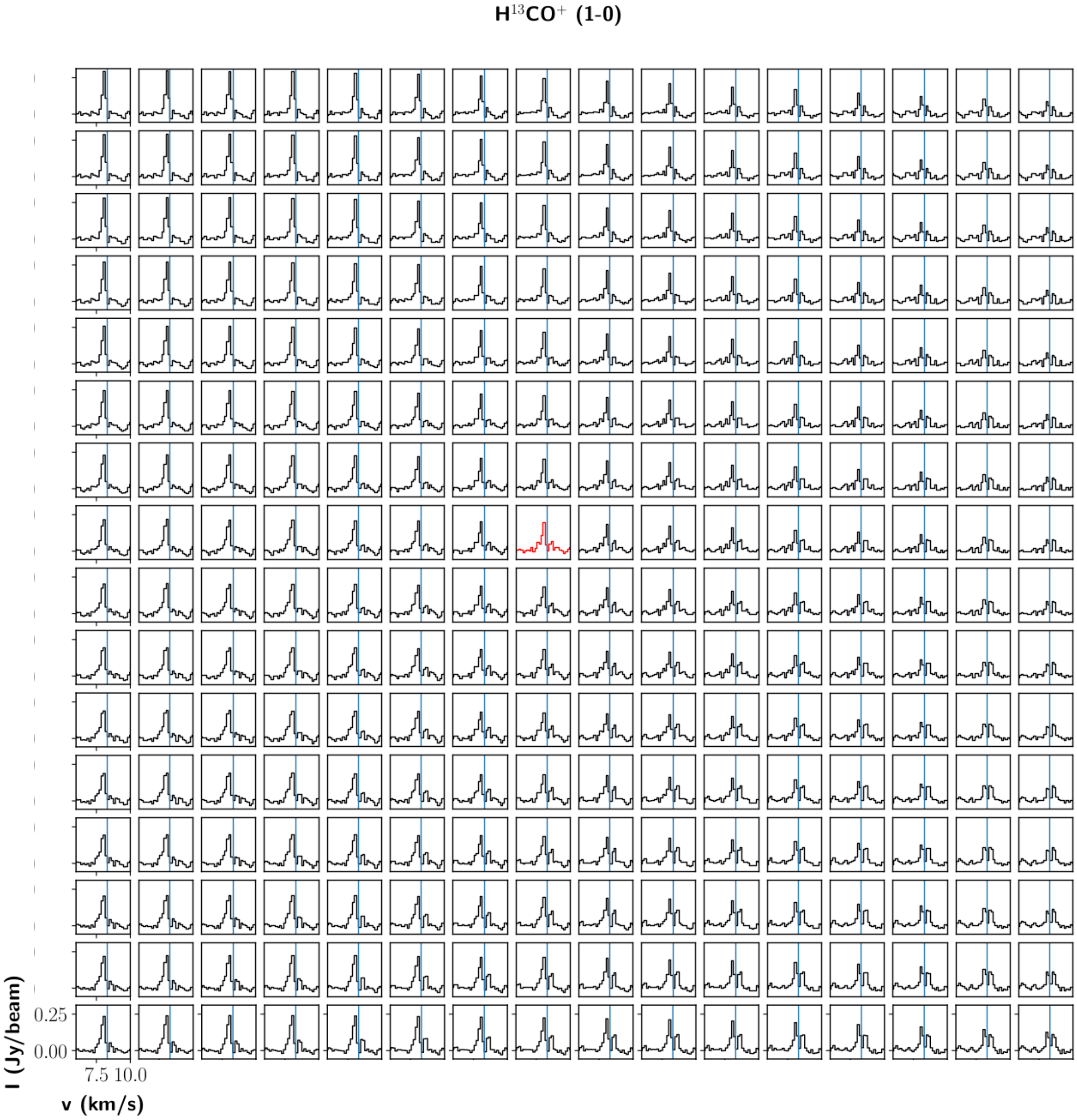

Figure 4.7: Spectral map of the H^{13}CO^{+} (1-0) emission in the inner 658 au, centered on the dust continuum emission peak. The whole map is 4" × 4" and each pixel correspond to 0.25" ($\sim$ 41 au). The red spectrum refers to the peak of the continuum emission and the blue line indicates the systemic velocity (8.3 km s^{-1}).

are obtained.

Figures 4.11, 4.12 and 4.13 show the peak velocity and the velocity dispersion for the blue- and the red-shifted velocity components of DCO^{+} (3-2) and H^{13}CO^{+} (1-0) and (3-2), respectively. In all three cases, the two separated velocity components occupy different regions of the source, indicating that they are probing different motions of the gas and with the same behavior as the C^{17}O (1-0) emission shown in Chapter 3. The extension of the two components is different, being the blue-shifted component observed in all the integrated emission, while the red-shifted component is only observed towards the west region.

Peak velocity values (top panels of Figs. 4.11, 4.12 and 4.13) ranges are similar for all

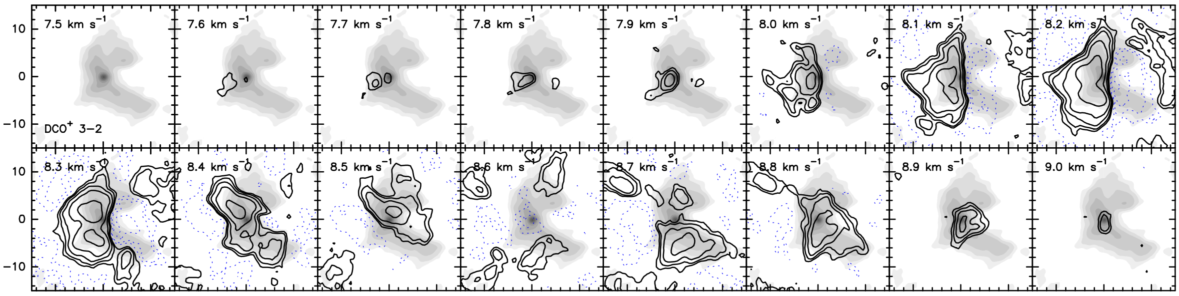

Figure 4.8: Integrated intensity emission of DCO$^+$ (3-2) shown in intensity, overplotted with intensity contours for the velocities where emission is present and every 0.1 km s^{-1}. Contours show emission at -4, 4, 8, 16, 32, 64 and 128 σ, where σ = 5 mJy/beam.

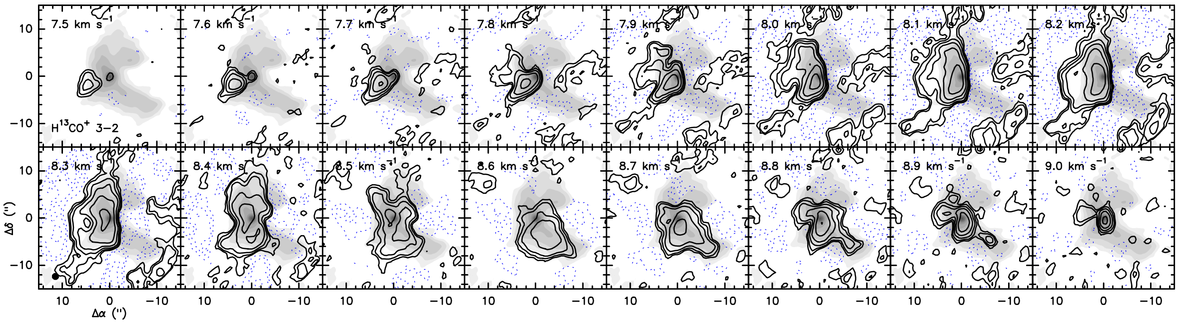

Figure 4.9: Same as Fig. 4.8 for H^{13}CO$^+$ (3-2).

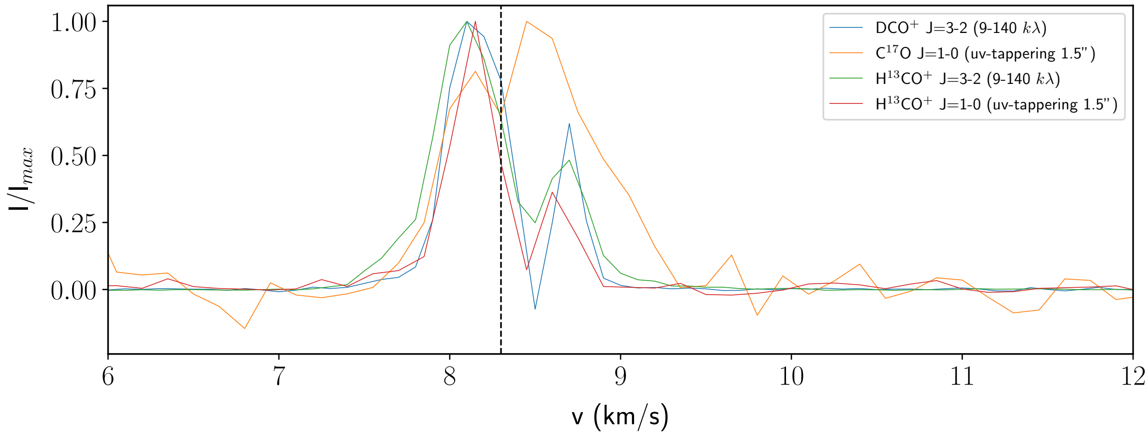

Figure 4.10: Comparison of the DCO$^+$ (3-2), C^{17}O (1-0), H^{13}CO$^+$ (1-0) and H^{13}CO$^+$ (3-2) spectra averaged at 5″ in radius around the source center.

molecules (from ∼8 to ∼9 km s^{-1}), but the blue-shifted component goes to slightly lower velocities for H^{13}CO$^+$(3-2, top-left panel of Fig. 4.13), being the lowest velocities ∼7.8 km s^{-1}. The decrease in velocity occurs towards the south-eastern side region of the core, at ∼5″ from the center of the source. This is due to the presence of a third velocity component produced by outflow contamination, as observed in the spectral map in Fig. 4.6. Because of the presence of a third velocity component, the fitting procedure can not produce a good model of the line profile. No gradient indicating rotation is observed for any tracer.

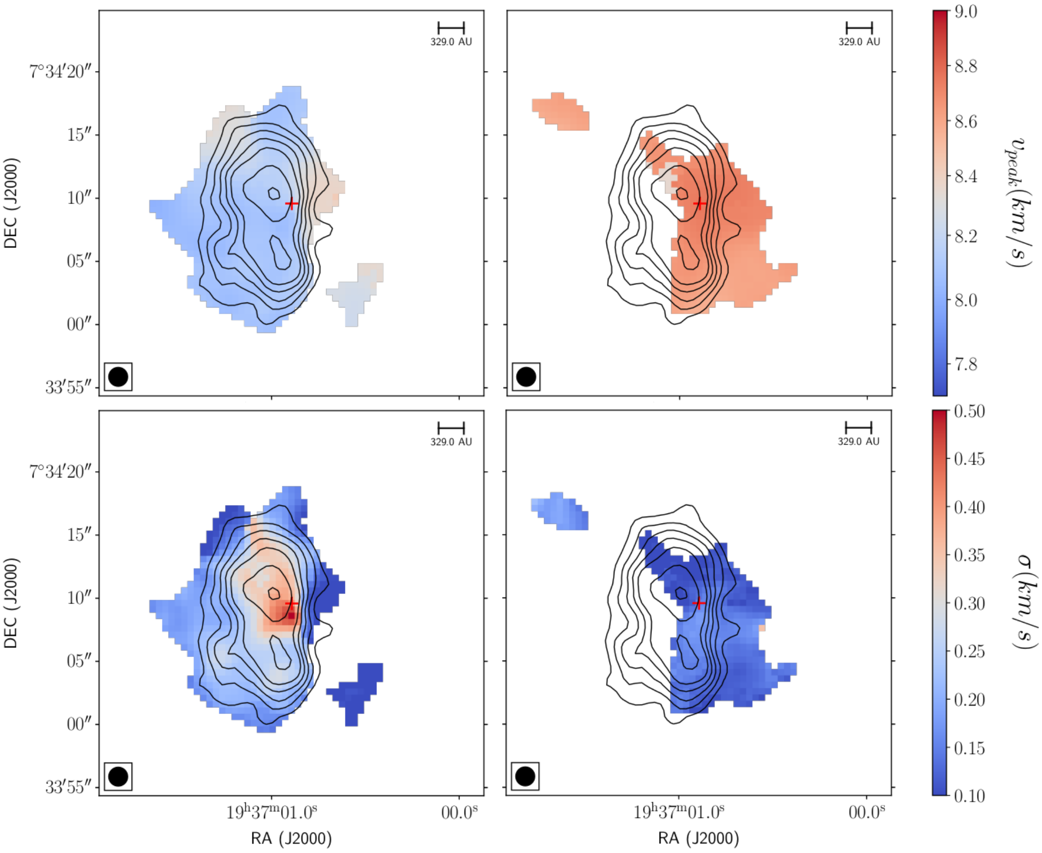

Figure 4.11: DCO^+ (3-2) maps obtained from modeling the line profiles with two velocity components. Overlaid contours show the integrated intensity at -3, 3, 5, 10 and 20 σ. Top map shows values for the peak velocity and bottom show values for the linewidth (given as σ). Left and right show the blue- and red-shifted component respectively.

For DCO^+ (top panels of Fig. 4.11), a similar trend to the one detected in $C^{17}O$ (1-0) is observed, where some regions present a more blue- or red-shifted region (±0.3 km s^{-1} from the average value for each component).

Velocity dispersion ranges (bottom panels of Figs. 4.11, 4.12 and 4.13) are also similar for all molecules (from 0.1 to 0.5 km s^{-1}). However, there are some differences: velocity dispersion is generally larger for $H^{13}CO^+$ (3-2), where average values are $\sim$0.4 km s^{-1}, whereas for DCO^+ (3-2) and $H^{13}CO^+$ (1-0) mean values are $\sim$ 0.25 km s^{-1}. Very large values of the velocity dispersion (>0.5 km s^{-1}) are observed in the same south-eastern region of the blue-shifted component of $H^{13}CO^+$ (3-2, bottom-left panel of Fig. 4.13), consequence of the poor fitting due to the presence of the third velocity component. Values of the velocity dispersion are larger for the blue- than for the red-shifted velocity component for both tracers, which supports the fact that they are tracing different gas reservoirs which are subjected to different kinematics, i.e., they can present different infall velocities or are affected differently by turbulence due to their non-symmetric morphology. For all tracers and both velocity components, the velocity dispersion increases towards the center as temperature rises closer to the protostar, although this increase is not so large for $H^{13}CO^+$ (1-0), being the velocity dispersion larger than 0.5 km s^{-1} for DCO^+ (3-2) and $H^{13}CO^+$ (3-2), whereas $H^{13}CO^+$ (1-0) is only around 0.35 km s^{-1}. This indicates that for $H^{13}CO^+$ (1-0) we are probably tracing gas at larger scales and colder temperatures. The increase is always larger for the blue-shifted component. In the red-shifted component of $H^{13}CO^+$ (1-0) and $H^{13}CO^+$ (3-2), there is a region west to the center position presenting a larger velocity dispersion (>0.5 km s^{-1}). This pattern is also observed for $C^{17}O$ (1-0) but not for DCO^+ (3-2).

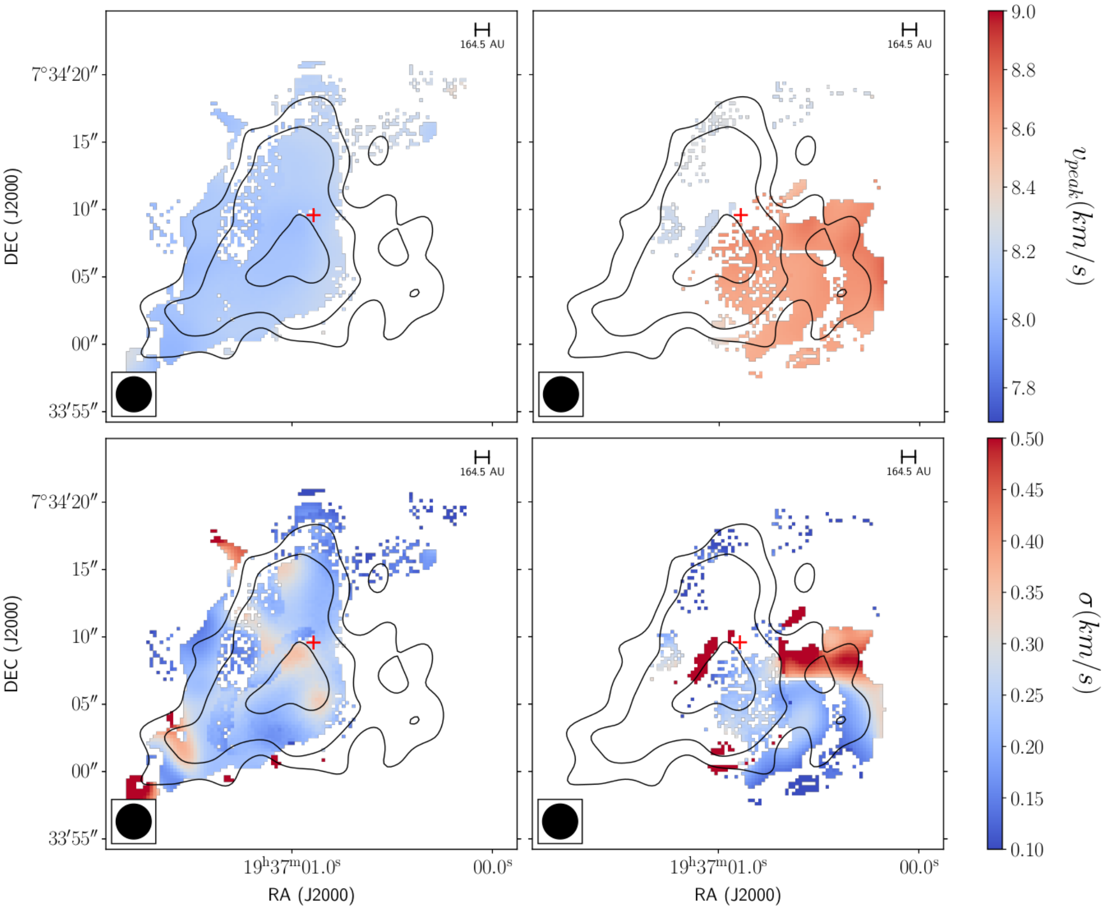

Figure 4.12: $H^{13}CO^+$ (1-0) maps obtained from modeling the line profiles with two velocity components. Overlaid contours show the integrated intensity at -3, 3, 5 and 10 σ. Top map shows values for the peak velocity and bottom show values for the linewidth (given as σ). Left and right show the blue- and red-shifted component respectively.

In general, there is a good agreement between the values obtained for DCO^+ (3-2) and $H^{13}CO^+$ (3-2), both for peak velocity and velocity dispersion of each velocity component. Considering we are observing similar scales, this confirms that both velocity components are tracing gas reservoirs with different kinematics, and it is safe to assume that they are suffering differently from physical processes. However, $C^{17}O$ presents some differences, mainly the blue asymmetry is not so prominent, which could be an indication of $C^{17}O$ tracing slightly different conditions, such as warmer and densest gas closer to the protostar.

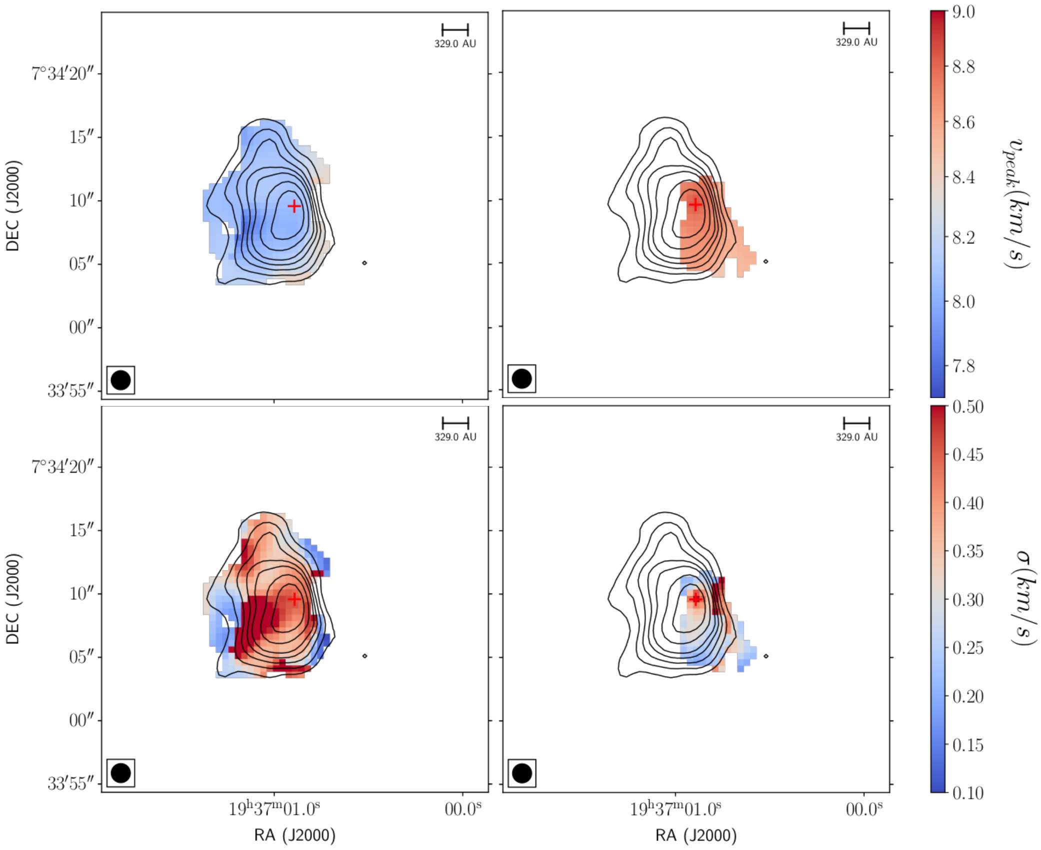

Figure 4.13: $H^{13}CO^+$ (3-2) maps obtained from modeling the line profiles with two velocity components. Overlaid contours show the integrated intensity at -3, 3, 5, 10 and 20 σ. Top map shows values for the peak velocity and bottom show values for the linewidth (given as σ). Left and right show the blue- and red-shifted component respectively.

4.3 Derivation of the deuteration fraction

In the following section, the deuteration fraction of the HCO^+ molecule is computed. We derive [D]/[H] from the column density using the maps of DCO^+ (3-2) and $H^{13}CO^+$ (3-2), considering that the deuteration fraction can be measured as the column density ratio and accounting for the abundance ratio of ^{12}C to ^{13}C ($f_{12/13_C}$):

$$\frac{\chi\left(DCO^+\right)}{\chi\left(HCO^+\right)} = \frac{1}{f_{12/13_C}} \times \frac{\chi\left(DCO^+\right)}{\chi\left(H^{13}CO^+\right)} \tag{4.13}$$

$$\frac{\chi\left(DCO^+\right)}{\chi\left(H^{13}CO^+\right)} = \frac{N(DCO^+)/N(H_2)}{N(H^{13}CO^+)/N(H_2)} = \frac{N(DCO^+)}{N(H^{13}CO^+)} \tag{4.14}$$

Since $f_{12/13_C}$ is subjected to high uncertainties depending on the observed system, we considered a medium value of $f_{12/13_C}$ = 43 (Frerking et al. 1987, Langer and Penzias 1993, Smith et al. 2009). Although we are choosing a relatively low value, it lies within the error bar of the observational derived values, and should not affect largely our derivation of the deuteration fraction. Ideally, we could use the abundance ratio instead to derive the deuteration fraction, but this would require detailed chemical modeling, which is out of the scope of this work. Since we assume that both molecules are probing similar gas, and knowing that the extension of both molecules is similar, we can use the column density instead. The column density was computed from the integrated intensity following:

$$N_{tot} = \frac{8\pi}{\lambda^3 A}\frac{1}{J_v(T_{ex}) - J_v(T_{bg})}\frac{1}{1 - exp(-h\nu/k_b T_{ex})}\frac{Q_{rot}(T_{ex})}{g_u exp(-E_l/k_b T_{ex})}\int I_0 d\nu \quad (4.15)$$

where λ is the wavelength of the transition, A is the Einstein coefficient, g_u is the upper state degeneracy, $J_v(T)$ is the Planck function at the background (2.7 K) and excitation temperature of the line (assumed to be 25 K), $Q_{rot}(T_{ex})$ is the partition function, E_l is the energy of the lower level and $\int I_0$ is the line integrated intensity. Values of these parameters for each molecule can be found in Table 4.3.

Transition	λ (mm)	A (log)	g_u	Q_{rot} (25 K)	E_l (cm^{-1})	J_v (2.7 K)	J_v (25 K)
DCO$^+$ (3-2)	1.388	-3.1159	7	25.22	7.2089	2.7	24.99
H^{13}CO$^+$ (3-2)	1.152	-2.8737	7	22.91	8.6814	2.7	24.99

Table 4.3: Parameters for the computation of column density

For DCO$^+$ (3-2) we found column density values ranging from 5.1×10^{10} to 1.1×10^{12} cm^{-2}, with mean values of 3.1×10^{11} cm^{-2} and 1.9×10^{11} cm^{-2}, for the blue- and red-shifted component respectively. For H^{13}CO$^+$ (3-2) the column density values range from 2.3×10^{11} to 1.7×10^{12} cm^{-2}, with mean values of 7.2×10^{11} cm^{-2} and 5.6×10^{11} cm^{-2}, for the blue- and red-shifted component respectively. Figure 4.14 shows on the top panels the deuteration fraction, derived as the column density ratio, and in the bottom panels the associated error for the blue- (left) and the red-shifted (right) velocity components. The errors, which are mainly associated to the modeling of the line profiles, are of the order of $\sim$ 10^{-4} - 10^{-3} and in general more than one order of magnitude smaller than the derived values, allowing to obtain values of the [D]/[H]with a precision of $\pm$10 %. Figure 4.15 shows the histogram for the [D]/[H] values, for the blue- (left) and the red-shifted (right) velocity components. Mean values for both components are $\sim$0.010-0.015. The deuteration fraction is lower in the center of the object, mostly coinciding with the position of the protostar though the peak is slightly displaced with respect to the assumed centroid position. The deuteration values increase towards the outer region, where the gas gets colder. The maximum values for [D]/[H] are found for the blue-shifted component (top-left panel of Fig. 4.14), increasing up to 0.045. However, these values have associated the largest errors, due to the presence of the third velocity component observed in the H^{13}CO$^+$ (3-2) spectral maps (see Fig. 4.6) and should not be trusted. While the average values for both velocity components are similar, the dispersion for the red-shifted is more restricted, with values ranging from $\sim$ 0.006 to 0.020. For the blue-shifted component, the dispersion is larger with values ranging from $\sim$0.002 to 0.03 (without taking into account the largest values, $\sim$0.045, which have large errors associated due to the poor modeling of the lines).

4.3.1 T_k and assumption of T_{ex}

One important factor in the derivation of the deuteration fraction from Eq. 4.1 is that DCO$^+$ is only formed from H$_2$D$^+$ (Eq. 4.6. This is expected in the source since the estimated kinetic

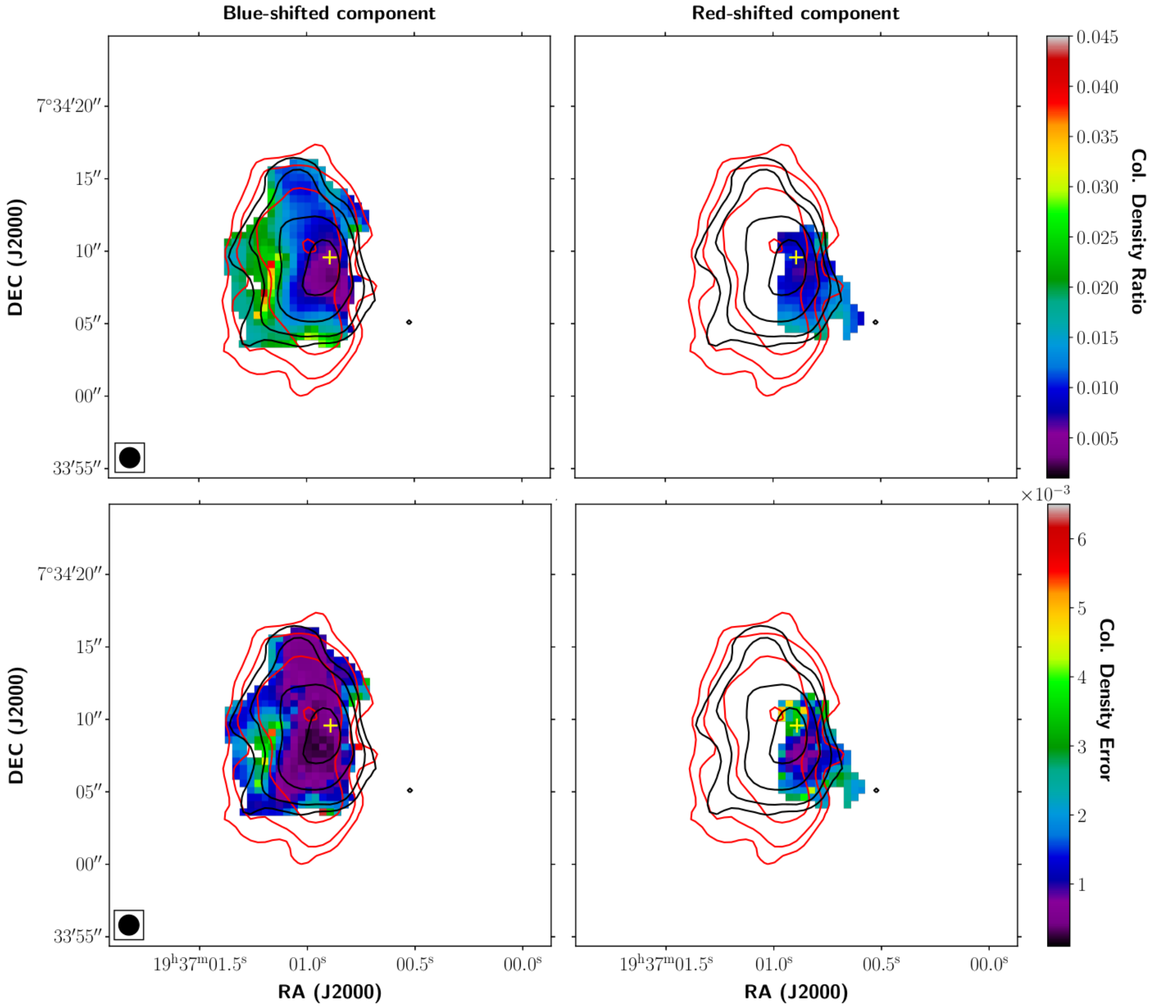

Figure 4.14: In contours, DCO$^+$ (3-2), in red, and H^{13}CO$^+$ (3-2) emission, in black, at 3, 5, 10 and 30σ (values of σ for each molecule are indicated in Table 4.1). In intensity scale, deuteration fraction maps computed as the column density ratio following Eq. 4.13 (top) and deuteration fraction uncertainties (bottom), for the blue- (left) and red-shifted (right) velocity components. The yellow cross indicates the centroid position of the source.

temperature at these scales lies between 20 and 40 K (Frerking et al. 1987, Evans et al. 2015, Cabedo et al. 2021b) and this reaction is only important at temperatures larger than 50 K.

Another one of the main uncertainties of the deuteration analysis is the assumption that both DCO$^+$ (3-2) and H^{13}CO$^+$ (3-2) have the same T_{ex}. This assumption should be accurate enough since both molecules present a similar geometry and dipolar moment. However, to check the effect that the variation of T_{ex} would produce in our values, we obtained the column densities of both DCO$^+$ (3-2) and H^{13}CO$^+$ (3-2) at two additional temperatures, 20 and 30 K. While we observe that the DCO$^+$ column densities do not present a change appreciable within our error margin produced by the model, the column density of H^{13}CO$^+$ has an increase of ~30 % from 20 to 30 K. After computing the deuteration fraction values for the three different temperatures, we find an associated uncertainty on the [D]/[H] at T_{ex} = 25 K of ±11 %. Nevertheless, the new values are still in concordance with the derived

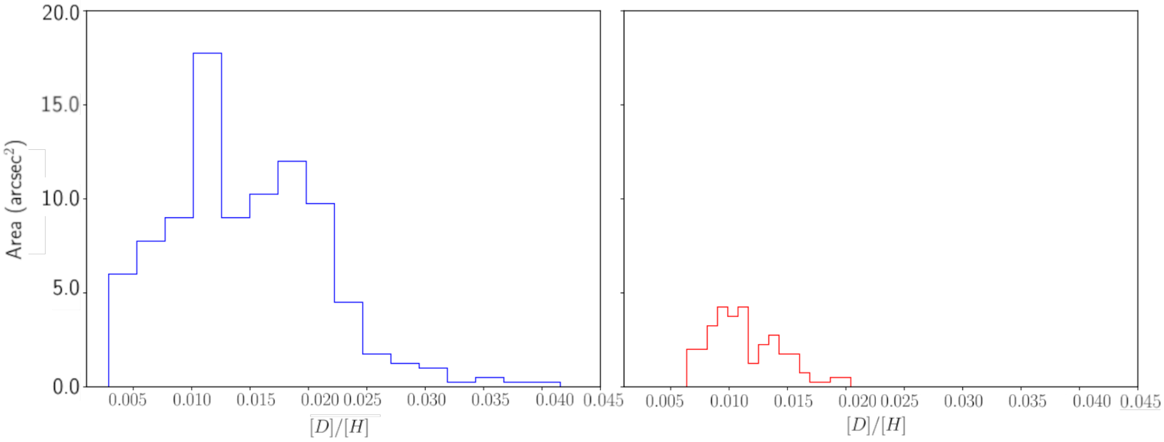

Figure 4.15: Histograms for the values of the deuteration fraction for the blue- (left) and red-shifted (right) velocity components.

values of [D]/[H] of DCO^+ reported in the literature.

4.4 Computation of the ionization fraction

We computed the ionization fraction from our deuteration maps following the method explained in 4.1.1, and assuming f_D = 3 (Caselli et al. 1998). Figure 4.16 shows on the top panels the derived ionization fraction and in the bottom panels the associated error for the blue- (left) and red-shifted (right) velocity components. Figure 4.17 shows the histograms of χ_e for the blue- (left) and red-shifted (right) velocity components. We obtain mean values of $\chi_e = 2 \times 10^{-6}$ for both components. Generally, these values are subjects to errors of $\sim$0.1 - 0.2 $\times$ 10^{-6}, but they get larger in the central regions, where they go up to $\sim$1.5 $\times$ 10^{-6}. This allows a minimum precision on the derivation of χ_e of $\pm$25 %. Values of χ_e increase towards the center, as expected since radiation increases towards the center of the protostar. This effect is more important for the blue-shifted component, where values increase up to $\sim$9 $\times$ 10^{-6}, while for the red-shifted component the increase only goes up to $\sim$5 $\times$ 10^{-6}. These values have large associated errors, however, the tendency is still valid. The range of values is also different for both velocity components, being larger for the blue-shifted ($\sim$2 $\times$ 10^{-7} - 9 $\times$ 10^{-6}) than for the red-shifted one ($\sim$9 $\times$ 10^{-7} - 4 $\times$ 10^{-6}).

4.4.1 Effect of the depletion fraction on the derivation of χ_e

The main uncertainty in our derivation of the ionization fraction relies in the assumed CO depletion fraction. While we use the depletion fraction of f_D = 3, as obtained in Caselli et al. 1998 and confirmed by Emprechtinger 2009, these values are obtained from single-dish data probing larger scales. Since our observations probe smaller scales, the temperature of the gas we are observing will be larger, $\sim$25 K, allowing the CO to sublimate from the solid phase and into the gas phase, decreasing the depletion factor. From Eq. 4.3, this decrease will in turn transform into a lower ionization fraction.

To explore the effect caused by this process, we computed the ionization fraction for different values of the depletion fraction, f_D = 0.5, 1, 2 and 4. For values between 1 and 4,

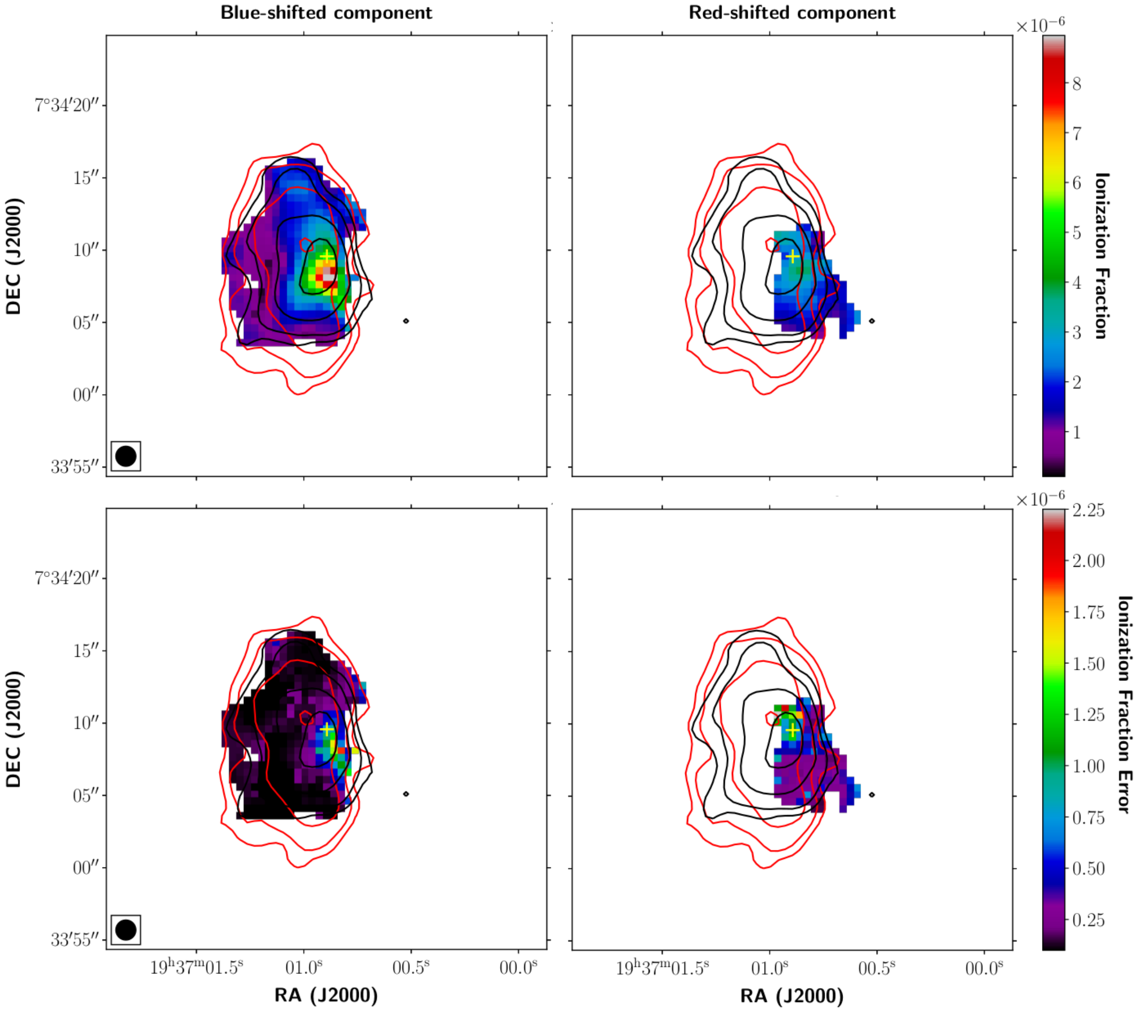

Figure 4.16: In contours, DCO^+ (3-2), in red, and $H^{13}CO^+$ (3-2) emission, in black, at 3, 5, 10 and 30σ (values of σ for each molecule are indicated in Table 4.1). In intensity scale, ionization fraction maps (top) and ionization fraction error (bottom), both in arbitrary units, for the blue- (left) and red-shifted (right) velocity components. The yellow cross indicates the centroid position of the source.

all results give values ~1-2 $\times 10^{-6}$, which our uncertainties would not allow to distinguish. All of them lay in the mentioned upper range of values for protostellar cores. Only for f_D as low as 0.5 can the ionization fraction start to go down to values between 10^{-7} and 10^{-9}. The CO depletion fraction is in general observationally poorly constrained but we note that there is no observational evidence of such low depletion fractions in Class 0 protostars, which would indicate that the desorption mechanisms are highly efficient. Such values of f_D might only be found for the very inner regions where temperatures are larger than 100 K (Alonso-Albi et al. 2010).

Since the depletion factor used in this work is a standard value used found for Class 0 objects, and there is no indication that temperatures are as large as to produce very small depletion fractions, we regard our χ_e as real, and conclude that efficient ionization processes might be occurring in B335.

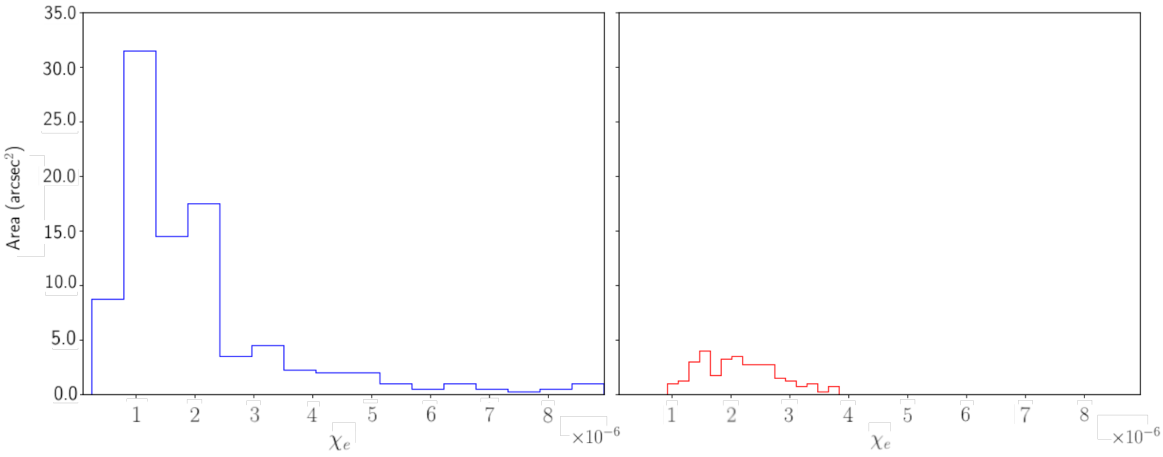

Figure 4.17: Histograms for the values of the ionization fraction for the blue- (left) and red-shifted (right) velocity components.

4.5 Derivation of the ambipolar diffusion lengthscale

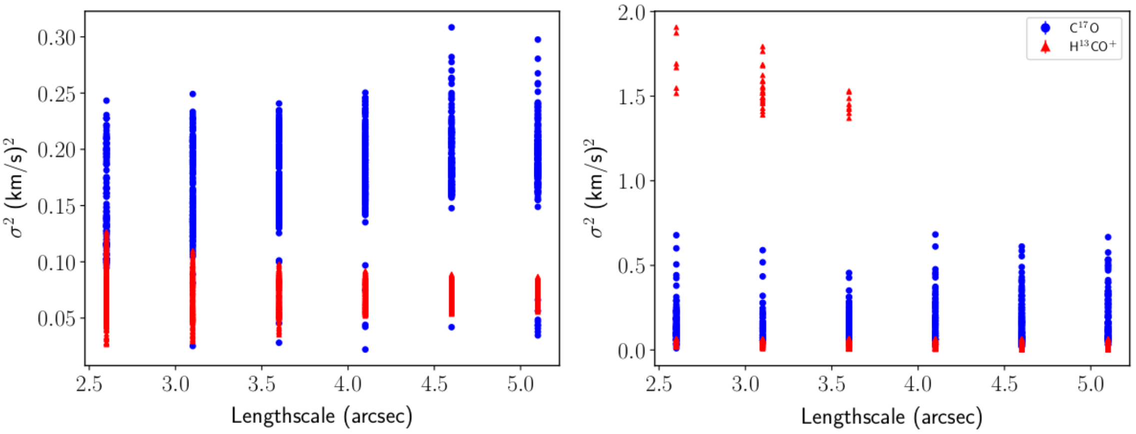

Figure 4.18: Values of σ^2 for each pixel in the analyzed region, for C^{17}O and H^{13}CO$^+$, and for the blue- (left) and red-shifted (right) velocity components.

We attempted the computation of L_{AD} following the procedure described in Section 4.1.3. We obtained the σ values for C^{17}O (1-0) and H^{13}CO$^+$ (1-0) from a region around the center position of the source of 2.5$''$ in width and 10$''$ in height. This ensures that we are using gas that is more possibly spatially coexistent, and avoids large outflow contamination effects in the linewidth. Figure 4.18 shows the obtained values of σ^2 for each pixel and both components. As observed in the σ maps, the range of values for the H^{13}CO$^+$ (1-0) is smaller, extending only between 0.05 and 0.15 (km s^{-1})^2, contrary to C^{17}O which extends to larger values, from 0.05 to 0.30 (km s^{-1})^2. This is true for both components, however, the red-shifted component presents values up to 2.0 (km s^{-1})^2. Those are associated to the large σ values close to the center of the source in the east direction (see bottom left panel in Fig. 4.12).

From the region we obtained the minimum values of σ^2 which are shown in Fig. 4.19.

Uncertainties in the values are only displayed in Fig. 4.19 for clarity. For the blue-shifted component, the minimum σ^2 values are larger for $H^{13}CO^+$ (1-0) than for $C^{17}O$ (1-0) for scales between L_3 and L_6, however, the uncertainties on the values are too large to properly distinguish if this trend is true. In the case of the red-shifted component, uncertainties on the values are small enough to distinguish a trend between the two tracers. Except for the smallest scale, L_1, the σ^2 values for $H^{13}CO^+$ (1-0) are significantly smaller than for $C^{17}O$ (1-0) by a factor ∼3, suggesting there is indeed a difference in the kinematics of the gas. Equations 4.10 and 4.11 indicate that we should expect an increase of the minimum velocity dispersion with lengthscale. However, this trend is not obeved in none of the velocity components and prevents us to derive a value for L_{AD} at the probed lengthscales.

Since we can not derive the value for L_{AD}, we can not use the ionization fraction derived in Section 4.4 to approximate the value of the magnetic field from Eq. 4.12. In Section 4.6.3, we will discuss possible caveats of the method and of the presented analysis.

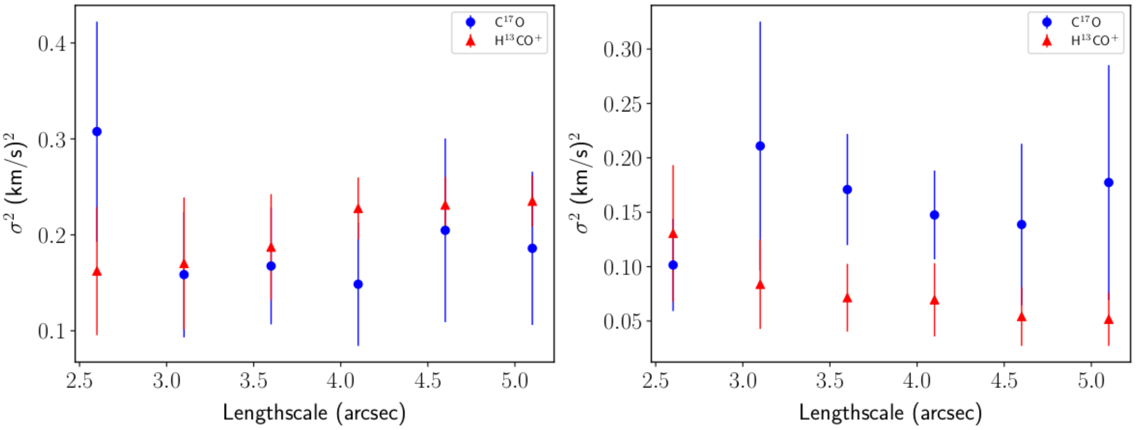

Figure 4.19: Minimum σ^2 value at each lengthscale and for the blue- (left) and red-shifted (right) velocity components.

4.6 Discussion

4.6.1 Deuteration in B335

Our obtained values for [D]/[H] are in agreement with other values for the [DCO$^+$]/[H^{13}CO$^+$] ratio found in the literature for Class 0 protostellar objects ([D]/[H]= 0.005-0.05, Caselli 2002, Roberts et al. 2002, Jørgensen et al. 2004). These values are larger than the typical values observed on the ISM of [D]/[H]$\sim 10^{-5}$. On the most external part of the envelope we observe values of the deuteration fraction which are in agreement with the ones found for pre-stellar cores ([D]/[H]>0.01, Redaelli et al. 2019a). Deuterium enhancement is determined at the first stages, during the pre-stellar phase. Once the temperature starts to rise, this enhancement can last for 10^4-10^6 yr (Rodgers and Millar 1996). The presence of pre-stellar values of the deuterium fractionation indicates that the source is still young enough to maintain the original enhancement set in the previous phases. Our values are therefore in agreement with the age derived from the molecular outflow of $\sim 3 \times 10^4$ yr (Stutz et al. 2008).

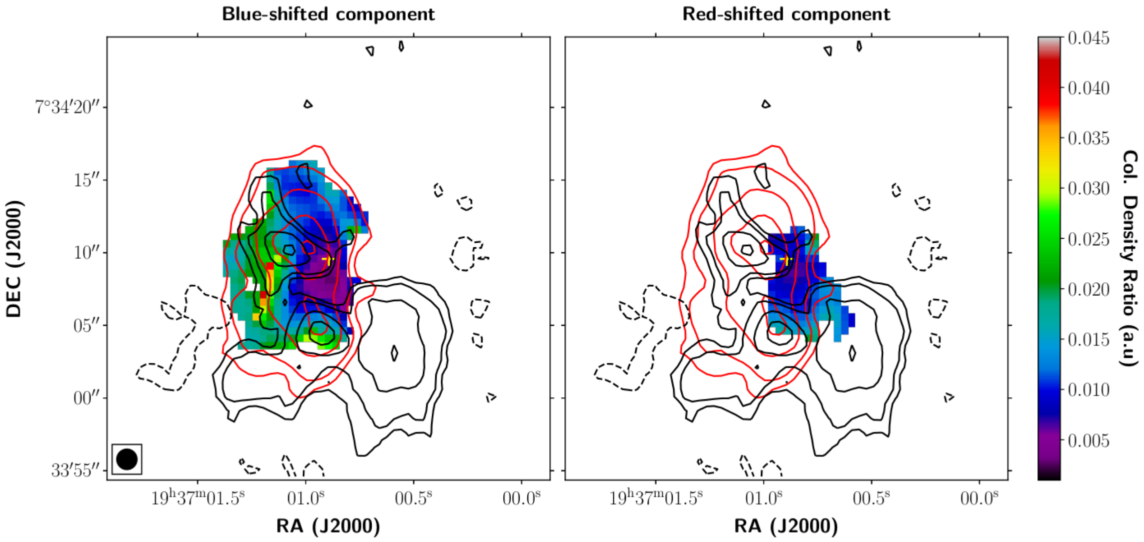

Figure 4.20: In intensity scale, deuteration fraction maps computed as the column density ratio following Eq. 4.13 for the blue- (left) and red-shifted (right) velocity components (in arbitrary units). In contours, DCO^+ (3-2) in red, and N_2D^+ (3-2) emission in black, at 3, 5, 10, 15 and 20σ (values of σ for each molecule are indicated in Table 4.1). The yellow cross indicates the centroid position of the source.

Although pre-stellar values of the deuteration fraction are seen in the source, a clear decrease ([D]/[H]<0.1) is observed towards the center and the northern regions. This decrease might be due to local radiation processes which destroy deuterated molecules, particularly towards the center where accretion radiation might be very strong. In Fig. 4.20 we show the deuteration overplotted with the DCO^+ (3-2) and N_2D^+ (3-2) integrated emission. While most of the emission coincides, a clear absence of N_2D^+ is observed in the regions where the deuteration fraction is lower, indicating that there are local processes effectively reducing the abundance of deuterated molecules. These processes will be explored in Section 4.6.2.

Effects of the line optical depth

To asses the effect of the opacity of the lines, we estimated the optical depth of both transitions using Eq. 1 in Cabedo et al. 2021b, considering abundances of $[DCO^+] \sim 10^{-11}$ and $[H^{13}CO^+] \sim 10^{-10}$, and assuming a total linewidth (considering only one velocity component) of 1 km s^{-1}. We obtained expected opacities of $\sim$ 0.2 and $\sim$ 2, for DCO^+(3-2) and $H^{13}CO^+$ (3-2) respectively. This indicates that the DCO^+ (3-2) is indeed optically thin, and further confirms that the observed double-peaked profiles can not come from opacity effects. However, the large estimated opacity for $H^{13}CO^+$ could have an effect in the line profiles and the presence of the two separated velocity components, directly impacting the values of the deuteration fraction, which could decrease down to ~50 %. Nevertheless, we note that this opacity has been estimated considering only one velocity component. Given the similarities in the line profiles between DCO^+ (3-2) and $H^{13}CO^+$ (3-2) we assume that the double-peaked profiles in $H^{13}CO^+$ are not mainly produced by opacity effects, although they might not be completely unaffected. We conclude then, that the opacity here estimated is only an upper limit of the real opacity, and that its effect on the deuteration fraction is necessarily smaller.

4.6.2 Origin of the ionization in B335

Values of ionization for protostellar objects lie in the range between 10^{-8} to 10^{-6} (Caselli et al. 1998). These values are derived from single-dish observations of a sample of molecular clouds, tracing the large-scale envelope (Butner et al. 1995). The values obtained from our observations, which probe smaller scales on the inner envelope, are in the most upper values of this range, around 2×10^{-6}, with the larger values being $\sim8\times10^{-6}$. The ionization fraction might depend on many factors related to the physical processes in the object, such as the penetration of cosmic rays, or the presence of an organized magnetic field.

To test which is the relation between the ionization fraction and the magnetic field, we compare our ionization maps (Fig. 4.16) with the polarized dust continuum emission obtained at 1.29 mm presented by Maury et al. 2018. The obtained maps are shown in Fig. 4.21. The regions of high ionization show a good correlation with the regions of highly polarized emission, particularly for the blue-shifted component. The regions of high ionization also follow the magnetic field direction, shown in segments. This result suggests that regions with larger ionization are correlated with a more organized magnetic field.

The distribution of the ionization fraction around the source seems to suggest that the ionization levels on the source have two different origins: (i) enhanced ionization around the magnetic field lines due to CR acceleration, and (ii) ionization of the central region by accretion radiation onto the protostar. We explore these two origins in the following sections and explore the differences between the two velocity components. We note that we can explore local ionization processes occurring during the Class 0 phase using the Caselli et al. 1998 method because those processes destroy deuterated molecules and decrease their abundances with respect to the abundance settled during the pre-stellar phase. If that was not the case, the ionization fraction obtained through this method will correspond to the one determined during the pre-stellar phase.

CR acceleration by the magnetic field

Propagation of cosmic rays gets damped as the column density of the medium gets larger, diminishing the CR ionization rate. At column densities between 10^{20} and 10^{25} cm^{-2}, the ζ is characterized by a power-law such as (Padovani and Galli 2013):

$$\zeta_k^{H_2} \approx \zeta_{0,k} \left[\frac{N(H_2)}{10^{20} cm^{-2}} \right]^{-a} \tag{4.16}$$

where $\zeta_{0,k}$ is the incident radiation of a given particle (protons and electrons) and a is the power-law index, which also depends on the type of particle. When the column density becomes higher than 10^{25} cm^{-2} the CRs ionization spectra changes to an exponential decrease. At the column density protostellar envelopes ($\sim 10^{22}$-10^{23} cm^{-2}), these models suggest that ζ will range from $\sim10^{-17}$ to 10^{-16} s^{-1}. From our data, we could not derive the CR ionization rate, however, Caselli et al. 1998 found that for values of χ_e of $\sim10^{-6}$, similar to the ones we obtain, correspond to ζ close to 10^{-16} s^{-1}, which would be in agreement with the models. The fact that we observe an enhancement of the ionization fraction following the magnetic field lines also agrees with the magnetized models of CR propagation,

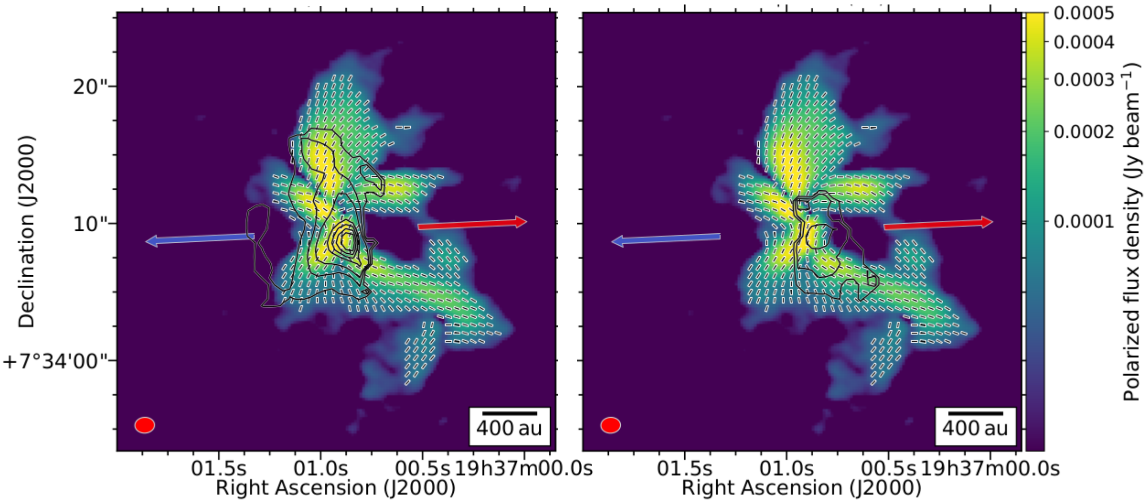

Figure 4.21: Polarized flux density (in color scale), overplotted with the segments showing the magnetic field direction (polarization angle rotated by 90 °). Contours show the values of χ_e for 1, 2, 3, 5, 6, 7, and 8 $\times 10^{-6}$ for the blue-shifted (left) and red-shifted (right) velocity components. The beam size of the polarized emission is shown in the bottom left in red (1.43″× 1.15″). The arrows represent the position and direction of the outflow.

where charged particles propagate along the field lines and enhance the ionization in those regions.

Being B335 an isolated object, a larger ionization degree could be expected, since there is no shielding from external radiation due to the presence of a large-scale structure. Since our observations probe a much more embedded region than the ones used in Caselli et al. 1998, CR ionization would be expected to be dumped reducing the ionization fraction. However, our values of χ_e are not only not smaller than those observed at large scales, but lie in the upper range derived for protostellar objects. Dumping of the CR due to a strong pinching of the magnetic field will be expected at scales smaller than 300-400 au (Padovani and Galli 2013), therefore our values of the ionization fraction, on the northern region of the source can still be explained by acceleration of interstellar CR along the magnetic field lines, since we are probing scales larger than 400 au.

Ionization due to the protostar

Our maps also present an enhancement in the ionization fraction around the center of the source, which is observed for both velocity components. This large enhancement can not be a consequence of the aforementioned acceleration of cosmic rays along the magnetic field and down to the center of the object, since, at those gas densities and with the strong pinching of the magnetic field oberved with polarization maps, the ionization fraction will be expected to be reduced (Padovani and Galli 2013). However, the values close to the protostar are very large, reaching almost 10^{-5}, which are not predicted by the models.

An additional source of ionization in this very inner regions is radiation produced by accretion processes onto the protostar (Padovani et al. 2016, Padovani et al. 2021), where a ionization fraction of 10^{-4}-10^{-5} can be expected. Such a high ionization of the medium around the protostar will favor the coupling between the gas and the magnetic field, helping to produce an organize morphology of the magnetic field around the source as the collapse proceeds and matter falls inwards, dragging the magnetic field lines, and creating the observed "hour-glass" shape, which, in turn, will help producing the large ionization observed around regions with highly polarized emission.

Other sources of ionization

Other sources of ionization include high-velocity and high-energy processes, such as shock waves produced by the presence of jets (Padovani et al. 2016) and outflows, or high-irradiation along the cavity walls. However, our maps do not show any sign of enhancement along the outflow cavity, or along the jet axis. Although these mechanisms might be contributing significantly to the ionization degree of the source, since deuterated molecules are not expected to be present inside the outflow cavity, due to the destruction by radiation, our analysis can not show their influence on the ionization fraction.

4.6.3 Ion-neutral velocity drift: can we observe ambipolar diffusion effects?

In Fig. 4.18, a clear difference is observed between the velocity dispersion values of $C^{17}O$ (1-0) and $H^{13}CO^+$ (1-0). While the range of values for $C^{17}O$ (1-0) is large (∼0.01 - 0.30 (km $s^{-1})^2$), the range of values for $H^{13}CO^+$ (1-0) is much smaller, and only goes up to ∼0.15 (km $s^{-1})^2$. This is expected in an scenario where ions are well coupled to the magnetic field, and are less affected by turbulence during the collapse. Even considering that the errors on σ of our analysis are large ($\pm$0.1 (km $s^{-1})^2$), this trend will hold. This is in agreement with the results shown in the previous section, where the larger values of the ionization fraction are found preferentially where the magnetic field is more organized (see Fig. 4.21), and supports the theory of a magnetically regulated collapse in B335. However, the method used to derive the AD lenghtscale did not provide the expected results. We did not observe the expected increasing slope for the minimum velocity dispersion (Fig. 4.19), as compared to the results obtained by Li and Houde 2008 and Hezareh et al. 2014. Since it is the fitting of this slope which allows to derive the ambipolar diffusion lengthscale, we were not able to derive this quantity by following their method.

Because of the difference in the velocity dispersion range for ions and for neutrals, we can safely assume that ions are well coupled to the magnetic field, and we discard the idea that ambipolar diffusion is not taking place at the lengthscales that we are probing. Hence, we propose two main hypothesis as to why we are not able to observe the expected increasing trend in our data:

1. The effect of ambipolar diffusion is equal at all the probed scales: It is possible that for all the scales we are probing, from 410 to 820 au, we are observing a region that is equally affected by ambipolar diffusion. This implies that for every lengthscale, the minimum turbulent velocity dispersion has a similar value. In their original work, Li and Houde 2008, applied this method in a molecular cloud using a difference of ∼32,000 au for each lengthscale with a total range of ∼190,000 au and obtaining a L_{AD} of 1.8 mpc. In their following work, Hezareh et al. 2014 used this method in two other molecular clouds with a difference in lengthscales of ∼850 au and a total range of ∼5,000 au, obtaining of 8.5 and 21 mpc. In our work, we are using a difference of

$\sim$82 au with a total range of 410 au. If the influence of ambipolar diffusion over all our lengthscale range is similar, it is plausible that we can not observe a difference in the minimum turbulent velocity dispersion at different scales.

2. The medium is dominated by gravitational motions: As it has been stated in Section 1.2.2, the validity of the assumption that the minimum velocity dispersion of ions and neutrals follows a Kolmogorov-type law strongly depends on the medium. The derivation of this method assumes that the gas motions are dominated by turbulence, which is a good assumption for regions such as the ISM and molecular clouds. However, this is not true for gas that is strongly subject to gravitational motions during the collapse, as it is the case of SFRs. Moreover, in our case the gas flow is parallel to the magnetic field. The presence of turbulent motions in protostellar envelopes is evidenced by the observation of linewidths in molecular line profiles which are larger than the expected thermal linewidth (Caselli and Myers 1995). Ward-Thompson et al. 2005, derived a model to relate the separation of the peaks in double-peaked line profiles with the level of turbulence for a sample of Class 0 and Class I protostars. Although they showed that Class 0 objects can present both high and low levels of turbulence, they concluded that B335 contained low level of turbulence. This emphasizes the fact that B335 is not dominated by turbulent motions but by infalling motions, which would support the hypothesis that the Li and Houde 2008 is not applicable, at least in this source. This is a probable explanation since infall analysis do assume that turbulence is not the dominant motion in collapsing envelopes (see Sec. 3.1.1).

Both these hypothesis would produce the results we have obtained in this work: (i) smaller velocity dispersion range for ions than for neutrals, since the ions are coupled to the magnetic field (Fig. 4.18), and (ii) the non-detection of an increasing trend for the minimum turbulent velocity dispersion, either because all the lengthscales are equally affected by turbulence, or because such trend does not exist in the medium we are probing. Unfortunately, our data does not allow to distinguish between the two hypothesis. There are two main problems that prevent us from doing so:

1. Large uncertainties in the modeling: In their previous work, Li and Houde 2008 found a difference in σ^2 of $\sim$1 (km s^{-1})^2 between ions and neutrals. In their following work, Hezareh et al. 2014 found differences between 0.1 and 0.5 (km s^{-1})^2 for their two objects. Our results suggest that the difference in the minimum σ^2 between ions and neutrals, if there is any, should lie between 0.1 and 0.2 (km s^{-1})^2. However, our derived uncertainties are of a similar order of the values, between $\pm$0.05 and $\pm$0.15 (km s^{-1})^2. Since our uncertainties are all derived from the modeling, we conclude that the modeling is not accurate enough to provide the uncertainties needed to properly conclude the lack of a trend, < 0.05 (km s^{-1})^2. We attribute those large uncertainties mainly to the presence of the two velocity components, which have a very variable S/N over the spatial extent of the source, and which are blended, particularly in the center of the source, preventing us to obtain accurate enough values of the velocity dispersion.

2. The choice of $C^{17}O$ and $H^{13}CO^+$ as tracers: We can not discard that the two molecules are not tracing the same gas reservoirs. While the morphology of their emission is

similar (see right panel of Fig. 4.3), $H^{13}CO^+$ is more extended, suggesting that it traces colder gas, and it presents a larger asymmetry towards the blue-shifted region that is not observed in $C^{17}O$. More importantly, while the two velocity components are present in the emission of both molecules, the extension of the two is very different (see Chapter 3 for $C^{17}O$, Fig. 4.12 for $H^{13}CO^+$ and Fig. 4.10 for the comparison of their averaged spectra). Particularly, the red-shifted component in $H^{13}CO^+$ is only present in the south-west region of the emission while in $C^{17}O$, though it is as well more intense in the western region, it extends through all the integrated emission. While this could, in principle, produce the observed effect in the range of velocity dispersion, since $H^{13}CO^+$ would still be coupled to the magnetic field while $C^{17}O$ would not, if they do not trace the same gas the minimum velocity dispersion would not be necessarily correlated, and will not present any increasing trend at different lengthscales.

Nonetheless, we suggest that further observations could help disentangle which of the two presented hypothesis is really at play in Class 0 objects. Our observations do not allow to reach scales of $\sim$4000 au, where our emission becomes unresolved. However, the combination of our data with large scale data, such as ACA observations, probing scales between 400 and $\sim$4000 au, could overcome this problem.

4.6.4 Magnetically regulated collapse in B335?

This chapter provides very interesting results about the studied object, B335, giving a new observational perspective of the interplay between matter and magnetic field. For the first time, we derived deuteration and ionization fraction values at scales of the inner envelope. We also attempted for the first time the derivation of the ambipolar diffusion lengthscale in a protostellar envelope of a Class 0 object. We summarize here the three main results of our analysis:

- We obtained maps of the ionization fraction of B335, showing that the source presents large values of ionization (between 1×10^{-6} and 8×10^{-6}), lying in the upper range of values found for protostellar objects. The large ionization suggests that there is a good coupling between the magnetic field and the gas.

- We showed that the large values of ionization correlate well with the magnetic field morphology, corroborating the enhanced gas-field coupling. We show that the ionization is mainly due to two processes: (i) the ionization from the protostar and (ii) cosmic ray acceleration through the magnetic field lines.

- While we could not derive the ambipolar diffusion lengthscale, we showed that ionic and neutral species present two different kinematic behaviors. Those are probably determined by the presence of a structured magnetic field and further corroborate that the gas is well coupled to the magnetic field.

All of these results present additional hints for the hypothesis of a large magnetic braking effect in B335, together with the observed magnetic field morphology (Maury et al. 2018) and the non-detection of a circumstellar disk larger than 10 au (Yen et al. 2015). We suggest that all these results are naturally correlated to one another: the isolation of B335 enhances the ionization of the medium, which enhances the magnetic field coupling creating an important difference in the kinematics of ions and neutrals. However, since the ionization fraction is very large, ambipolar diffusion alone can not prevent magnetic braking and a large disk can not be formed.

We also suggest that this correlation should further be confirmed by carrying out similar analysis in other objects, both isolated and embedded in large-scale structures. If our hypothesis are correct, non-isolated sources will present lower values of ionization. Additionally, the correlation between the magnetic field structure and the ionization fraction should also be determined for other sources for which the magnetic field morphology has already been obtained. Both the ionization fraction and its correlation with the magnetic field should also be compared with identifications of circumstellar disks in other protostellar sources to determine if there is any relation between them and the size of the disk.

Finally, we conclude that this study brings us a step closer to confirm that magnetic braking has a large effect in B335, whose collapse seems to be regulated by the presence of the magnetic field.

Chapter 5

Conclusions and Perspectives

In this work we have presented and analyzed our obtained data set, mainly the molecular line emission, of the protostellar Class 0 object B335. Our object of study, B335, is an excellent source for the study of gas kinematics and dynamical processes, and to test theories of gravitational collapse during low-mass star formation. It has been extensively studied to test the classical inside-out collapse models from Shu 1977 and to provide observational confirmation of this model by comparing it to molecular line profiles characteristic of infall motions (Frerking et al. 1987, Zhou et al. 1993, Velusamy et al. 1995, Yen et al. 2010, Evans et al. 2015, Yen et al. 2015). It has also been suggested that B335 is an excellent source to test models of magnetized collapse, since its magnetic field has been studied at very different scales (Bertrang et al. 2014, Zielinski et al. 2021, Maury et al. 2018, Yen et al. 2020) and has been observed to present the 'hour-glass' shape morphology expected from the dragging of the magnetic field lines to the center of the object (Galli and Shu 1993). It is also a good source to test astrochemical models, presenting a rich chemistry in the envelope, and a hot corino in its interior (Imai et al. 2019).

For this phD thesis, we used high resolution observations in Band 3 and Band 6 obtained with ALMA, combining the 12-m and the ACA array. We obtained dust continuum and molecular line emission observations which probed scales from $\sim$100 to $\sim$ 4000 au. The main goal of this thesis was to use our observations to constrain some of the aforementioned processes, mainly to determine how chemical conditions, such as the deuteration and ionization of the gas, relate to the coupling of the gas and the magnetic field, and how it affects the collapse during the first stages of the star formation process. However, this analysis needed to be preceded by an additional analysis to disentangle the gas kinematics that the observations revealed and to be able to use the molecular line emission to probe the physico-chemical conditions in B335. In this chapter, we present a summary of the main conclusions obtained from our analysis and their implications on the field of star formation. We also present the perspectives and possible future work, both for the study of the properties of protostars and possible projects that could be pursued with our data set.

5.1 Conclusions

This work made use of a large data set of molecular line emission of the object B335. We detected emission for common molecules tracing scales of the envelope. The use of ALMA multiconfiguration observations and the additional ACA data allowed us to probe scales from $\sim$ 450 to 4000 au. The molecules detected at those scales include CO, HCO^+, HCN and their isotopologues, $C^{17}O$, $C^{18}O$, $H^{13}CO^+$ and $H^{13}CN$, plus species such as HC_3N . We also obtained emission from deuterated species, such as DCO^+ and N_2D^+. Although they have not been presented in this manuscript, we also detected emission at smaller scales, $\sim$ 430 au, such as SO. Additionally, we detected species at even smaller scales, between $\sim$ 150 and 250 au, such as CH_3OH and CH_3CHO, which probe the hot corino chemistry at the center of the object. All these observations make from our data set a complete sample of the chemistry on the inner envelope of B335.

Our data set has proven to be very heteregoneous in nature, due to the characteristics of the ALMA observations, but also very complex. The detection of double-peaked line profiles was unexpected, especially for molecules which are not expected to be very abundant and which emission under the core conditions should be optically thin, such as $C^{17}O$ and DCO^+. This result is puzzling by itself, and has driven an important part of the work presented. However, it has proven very useful to obtain other constraints on the physical properties of the source, as we summarize in the following sections.

5.1.1 On the infall kinematics of B335

After the realization of the presence of such double-peaked line profiles in optically thin lines, we decided to use them to study the characteristics of the infall motions in our source. Such line profiles did not only presented an unexpected double-peaked morphology, but the velocity pattern of those across different offsets of the source did not match expectations of the pattern if the line was optically thick, meaning that double-peaked profiles would be expected at the center of the source, where densities are larger, and to progressively disappear towards the edges of the emission, where the density decreases and where single-peaked lines would be expected to be observed. As presented in Chapter 3, this was not the case, presenting instead the absorption of only one component, the blue- or the red-shifted at different offsets of the source.

Following the hypothesis that the observations corresponded to two different components tracing different gas motions, we analyzed the line emission of $C^{17}O$. We obtained spectral maps showing the velocity pattern of the source, and modeled the spectra to obtain the main properties of the gas, i.e., the peak velocity, the velocity dispersion and the opacity. From this analysis we obtained the following conclusions:

- We computed the expected opacity of the emission and determined it to be $\tau = 0.77$, typical from an optically thin line. We derived the opacity of the emission from the modeling of the hyperfine structure of the line profiles and found it to be ~ 0.4 for each velocity component present on the spectra. After discarding other possible effects, such as large-scale filtering or deviations from the expected abundance of C^{17}O, we concluded that the observed line profiles were not due to opacity effects. A simple spherically symmetric model of collapse could not reproduce our observations, since such a configuration of isotropic motions should produce single-peaked velocity profiles.

- From the modeling of each component of the spectral lines, we obtained values of the velocity dispersion of $\Delta v_{bs} \sim 0.7$ km s^{-1} and $\Delta v_{rs} \sim 0.5$ km s^{-1} for the blue- and red-shifted components respectively. We first compared these values to the linewidth expected just from thermal motions, which was obtained to be ~ 0.2 km s^{-1}, at all the lengthscales probed with our data. We then, compared the derived velocity dispersion values to the expected velocity dispersion coming from infall motions with free-fall velocities onto the center of the object, which were found to range between 0.4 and 1 km s^{-1}, for an enclosed mass in the analyzed radius between 0.06 and 0.4 $M_{\odot}$. From our linewidth analysis we conclude that observed line profiles were not compatible with pure thermal broadening, and that instead were in good agreement with values expected from infall motions.

- We discarded that our observations are tracing other kind of motions. We discarded rotation motions, since no velocity gradient is detected across the continuum peak. We also discarded that the two velocity components are not produced by outflowing gas, because the morphology of the C^{17}O emission does not correspond to the typical morphology of outflow tracers nor with the spatial distribution observed for the outflow in B335 (Imai et al. 2016, Bjerkeli et al. 2019), and because no spectral signature of outflowing motions is observed, such as large spectral wings.

- Finally, we conclude that a simple inside-out symmetric profile can not reproduce our observations of C^{17}O and we corroborated the initial hypothesis that the two velocity components are tracing two different gas reservoirs with different infall motions. We suggest that infall is anisotropic and it is occurring along the outflow cavity walls. This hypothesis is an agreement with the observed excess of dust continuum emission towards the cavity walls, but also with the observed morphology of the magnetic field at the probed scales (Maury et al. 2018, Yen et al. 2020).

Our results can have direct implications on the derivation of infall velocities and mass accretion rates. Derivation of these quantities is largely model dependent, and at this point, it is not clear weather the derived accretion rates in protostars are realistic. The simplified modeling of gas kinematics, which seems to break down at the scales probed in this work, could be an underlying cause of the discrepancy between the observed and the derived protostellar luminosities, the former lying one order of magnitude below the later (Kenyon et al. 1990, Dunham et al. 2014, Evans et al. 2015). The potential accretion rates derived from models with localized anisotropic collapse might produce values of the luminosity closer to the observed ones, opening a door to reconcile accretion models and observations.

5.1.2 On the deuteration and ionization processes on B335

Once we determined the origin of the double-peaked profiles in our data, we could use our observations of DCO^+ (3-2) and $H^{13}CO^+$ (3-2) to derive the deuteration fraction and further derive the ionization fraction (Chapter 4). Since both transitions presented the double-peaked profiles and followed the same velocity pattern as the observations of $C^{17}O$ we assumed that these species are tracing two distinct gas reservoirs with different kinematics as well. We followed the same procedure as for $C^{17}O$, we obtained the spectral maps for the DCO^+ (3-2) and $H^{13}CO^+$ (3-2) transitions at similar scales and further modeled the line profiles to obtain the peak velocity and the velocity dispersion maps. We obtained the following conclusions:

- In this case, we could not discard that filtering effects are affecting our data, since we observed absorption below the continuum in some regions of the spectral map (Figs. 4.5 and 4.6). This is also clear from the obtained channel maps (Figs. 4.8 and 4.9), which show large amounts of negative emission at velocities between 8.1 and 8.4 km s^{-1}, coinciding with the region where the red-shifted component is more intense, and also coinciding with the same region observed in the spectral map. In this case we also detected outflow contamination, seen in the south-east region of the spectral map of $H^{13}CO^+$ (3-2, Fig. 4.6) appearing as an additional component at very blue-shifted velocities ($\sim$ 7.5 km s^{-1}). However, we concluded that these two effects are not the main cause for the presence of the two velocity components.

- We derived the deuteration fraction of DCO^+ by computing the column density ratio of DCO^+ to $H^{13}CO^+$ for each velocity component and obtained the corresponding maps (Fig. 4.14). In the outer regions of the emission we observe deuteration fraction values in agreement with pre-stellar cores ($[D]/[H] > 0.1$). However, we do observe a decreasing of the deuteration fraction ($[D]/[H] < 0.1$) towards the center and the northern region of the source, probably due to local destruction of deuterated molecules. This idea is confirmed by the decreased observed in N_2D^+ in the regions where the deuteration fraction is lower. We obtained mean values of $[D]/[H] \sim 0.01$ for both velocity components. We note that, while mean values are similar for both components, their ranges differ, with the blue-shifted component showing a wider range of [D]/[H] than the red-shifted one, indicating that different evolutionary processes are taking place for the two gas reservoirs.

- Our deuteration values are in agreement with single-dish values obtained in the literature for B335 (Jørgensen et al. 2002). The observation of pre-stellar values is in agreement with the idea that pristine deuteration ratios can survive for 10^4 - 10^6 yr in warm gas and agrees with the age of the source derived from the outflow (3×10^4 yr).

- Since our results are in agreement with the large-scale observations in the literature, we confirm that neither filtering effects nor the contamination from the outflow have a strong influence in our analysis. We also tested our assumption of T_{ex} and found that a change of ± 20 % in the temperature has an impact of ± 15 % in the derived values of the deuteration fraction. However, these values are still in agreement with the values in the literature.

- We computed the ionization fraction from the obtained deuteration fraction following the method in Caselli et al. 1998, and obtained the corresponding χ_e maps (Fig. 4.16) for the two velocity components. We obtained mean values of $\chi_e \sim 2 \times 10^{-6}$ for both velocity components, with the largest values ($\sim$8 $\times$ 10^{-6}) found in the center of the source for the blue-shifted component. Our values lie on the most upper range of the derived values for protostellar objects (Caselli et al. 1998). We suggest that high irradiation levels are modifying the pristine deuteration values, causing the decrease in the abundance of deuterated molecules in the central and norhtern regions.

- We compared our maps with the polarized dust continuum emission obtained in Maury et al. 2018 (Fig. 4.21). The regions with the largest ionization fraction are coincident with the polarized continuum intensity, particularly the northern lobe of the emission. This suggests that external radiation, i.e., cosmic rays, are being channeled through the magnetic field lines producing a larger ionization in this area. Since the ionization fraction values in this area are still on the upper range of values derived for Class 0 objects, we conclude that the fact that B335 is isolated might indeed allow a larger incidence of CRs, increasing the ionization fraction. We concluded that cosmic rays should not penetrate down to the center of the source where the values of the ionization fraction are even larger. We therefore suggest that those very large values are produced by accretion shocks close to the protostar.

5.1.3 On the computation of the ambipolar diffusion lengthscale and the magnetic field strength

Following the method in Hezareh et al. 2014, we attempted to study the ambipolar diffusion mechanisms, since it is expected to be the dominant effect at our probed lengthscales, and derive the ambipolar diffusion lengthscale. Since we could not use the $H^{13}CN$ (4-3) observations obtained from the ALMA archive, and our $H^{13}CN$ (3-2) observations were only obtained using the ACA configuration and therefore only comparable with the $H^{13}CO^+$ (3-2) at ACA scales, we decided to use our observations of $H^{13}CO^+$ (1-0) with the $C^{17}O$ (1-0) data. We made this choice because both tracers are detected at similar scales and with similar angular resolution. Moreover, they present the advantage of being the same transition which have similar excitation temperatures. However, we were not able to derive the value for the ambipolar diffusion lengthscale. The reasons behind this result are discussed in details in Chapter 4 and summarized in the following paragraphs:

- A clear difference was observed between the distribution in velocity dispersion of $C^{17}O$ and $H^{13}CO^+$, where the range of values for $C^{17}O$ is larger than for $H^{13}CO^+$ (Fig. 4.18) at all the probed lengthscales. This is expected in an scenario where ions are well coupled to the magnetic field and are less affected by other motions, i.e., turbulence or infall, than the neutrals. This is an agreement with our results of the ionization fraction distribution around the source, where larger values of χ_e are found preferentially where the polarization fraction is larger, and supports an scenario of magnetically regulated collapse for B335.

- We were unable to detect the increasing trend of the minimum velocity dispersion with increasing lengthscale, as presented in the works of Li and Houde 2008 and

Hezareh et al. 2014, therefore we could not compute the ambipolar diffusion lengthscale and neither the magnetic field strength. We propose two hypothesis to explain this result: (i) our lengthscale range (from 410 to 820 au) is very restricted and is only tracing a region where ambipolar diffusion has a similar effect in the minimum linewidth. Additionally, our differences between every lengthscales might not large enough (82 au) as to detect any change in the velocity dispersion as a function of lengthscale due to ambipolar diffusion. (ii) The assumption used to derive the method in previous works, where turbulent motions dominate the gas kinematics is not valid in B335. In our case, gravitational motions are causing the velocity dispersion observed and not turbulence, and hence the dependence of the linewidth with lengthscale does not follow a Kolmogorov scaling relationship. This would be in agreement with the fact that B335 has been suggested to present a low level of turbulence (Ward-Thompson et al. 2005).

- Our data does not allow to distinguish between the two scenarios proposed above for two main reasons: (i) our modeling of the line profiles do not allow the necessary accuracy (between 0.05 and 0.15 (km s^{-1})^2) to distinguish very small changes in the velocity dispersion of the line, which are approximated to be 0.1 - 0.2 (km s^{-1})^2, and (ii) the two tracers used, $C^{17}O$ and $H^{13}CO^+$ are not tracing the same gas and therefore their minimum velocity dispersion is not necessarily correlated.

5.1.4 On the coupling of gas and matter in B335

As a summary we can say that, while we have not achieved some of the goals initially presented, we have obtained a better view of the interplay between matter and magnetic field in the source. All of our results already mentioned, are added hints to the previous literature that the magnetic field plays an important role in the collapse in B335. The two main projects presented show a good agreement, since a good coupling of the gas with the magnetic (Chapter 4) might result in an asymmetric collapse of the gas along the external cavity walls, where the magnetic field has a more favorable morphology (Chapter 3). We believe we are in a position to say that magnetically regulated collapse is occurring in the source.

5.2 Perspectives and future work

5.2.1 On the properties of protostars

One of the most important results of this work is the detection of double-peaked profiles in optically thin tracers with characteristic velocity patterns and that we interpreted as a sign of non-isotropic collapse. It is, therefore, important to investigate this characteristic and understand if it is a common feature among protostellar objects, and thus intrinsic to the star formation process. For this purpose, we consider three flanks to approach:

- On the observational aspect, more observations are needed at similar scales, particularly of optically thin tracers that could present these particular double-peaked profiles. Since infall profiles are not expected to be observed in optically thin tracers the observation of double-peaked profiles in them would be a good indication of the non-isotropic collapse being intrinsic to the star formation process. Double-peaked profiles have been observed in B335 many times, but always interpreted as symmetric infall in optically thick tracers at large scales (e.g., Zhou et al. 1993, Evans et al. 2005). However, they have also been observed in optically thin tracers and already interpreted as non-symmetric collapse (Velusamy et al. 1995). Additionally, the same velocity patterns that we have observed have already been detected (Zhou et al. 1993), but not interpreted in the same way. It is thus important to obtain more observations of optically thin tracers, both at large scale and at our same scales, to further investigate this effect and confirm our results. Furthermore, to understand if it is common to the star formation process, it is important to try to detect this effect in other low-mass protostars, both isolated and clustered, and in high-mass protostars to detect any difference.

- Another important observational aspect is to derive the values of the deuteration and ionization fraction for other sources known to present an organized magnetic field to determine if there is a correlation for these sources. It would be necessary to determine if this correlation is also related to the environment in which the source lies, either an isolated source, like B335, or embedded in a large-scale structure, and if it has any relation with the disk size.

- The ambipolar diffusion effects and the potential derivation of the ambipolar diffusion lengthscale could be further investigated by gathering observations of B335 with a larger scale range. Assuming that for this object one could obtain two tracers coexisting at the same scales and a very precise modeling with an accuracy of $<$0.05 (km s^{-1})^2, the larger lengthscale range could potentially reveal the increasing trend for the minimum turbulent velocity dispersion. If these observations were not to reveal this trend, a more clear view of the effect of gravitational motions could be obtained, and potentially discard the validity of the used method for Class 0 objects. Additionally, as it has been mentioned, B335 presents a low level of turbulence, comparing the observations of B335 with other more turbulent sources (see Table 1 in Ward-Thompson et al. 2005 for potential sources), could reveal the potential applicability of the method for turbulent Class 0 sources.

- It is important to reconcile observations with theoretical models of star formation, therefore, non-symmetric collapse should be included in those models. Some models have already started to include asymmetric features by including density fluctuations and have shown that disks can form under those conditions (Verliat et al. 2020). Their results agree with the observational derivations of angular momentum. However, these models are scarce, and should be developed to match the already described molecular line observations.

5.2.2 On the data set

Our data set on B335 is very complete and presents a good representation of the chemistry from large scales of the envelope ($\sim$ 4000 au) to small disk scales ($\sim$ 150 au). The time to produce this work was short, and we could not explore all the different aspects that our data set can offer. We present here some of the possible studies that could be explored with these data on B335:

- By obtaining observations of N_2H^+ at similar scales, already existing in the archive, the N_2D^+ deuteration fraction could also be derived, to observe any possible differences with the DCO^+. Following Caselli 2002, this method will help constraining better the ionization fraction to compare them with our results. Additionally, we tentatively detected the presence of HDCO in our ACA observations. Those could be used to derive the deuteration fraction at larger scales ($\sim$ 3000 au).

- A very interesting observation was the SO molecular line emission. Its integrated intensity image presents two wings on the north-west and south-east regions. The spectra also presents very asymmetric wings towards the blue-shifted side. Since SO is a tracer of accretion shocks in the disk around the centrifugal barrier (Sakai et al. 2016, Oya et al. 2017), it is possible that these features are an effect produced by non-isotropic infall into the disk, and should be explored. Additionally, SO shows a clump in the south-west region, which appears to be rich in COMs, with very broad line profiles, this could also be caused by accretion shocks producing a rich chemistry in that region.

- We tentatively detected multiple lines of CH_3CHO at small scales of the disk. The production of excitation diagrams could be use to derive exact temperatures of the accretion disk region and help constraining chemical models.

Bibliography

N. Añez-López, G. Busquet, P. M. Koch, J. M. Girart, H. B. Liu, F. Santos, N. L. Chapman, G. Novak, A. Palau, P. T. P. Ho, and Q. Zhang. Role of the magnetic field in the fragmentation process: the case of G14.225-0.506. , 644:A52, Dec. 2020. doi: 10.1051/0004-6361/202039152.

Y. Aikawa, T. Umebayashi, T. Nakano, and S. M. Miyama. Evolution of Molecular Abundances in Protoplanetary Disks with Accretion Flow. *ApJ*, 519(2):705–725, July 1999. doi: 10.1086/307400.

Y. Aikawa, V. Wakelam, R. T. Garrod, and E. Herbst. Molecular Evolution and Star Formation: From Prestellar Cores to Protostellar Cores. *ApJ*, 674(2):984–996, Feb. 2008. doi: 10.1086/524096.

Y. Aikawa, V. Wakelam, F. Hersant, R. T. Garrod, and E. Herbst. From Prestellar to Protostellar Cores. II. Time Dependence and Deuterium Fractionation. *ApJ*, 760(1):40, Nov. 2012. doi: 10.1088/0004-637X/760/1/40.

Y. Aikawa, K. Furuya, S. Yamamoto, and N. Sakai. Chemical Variation among Protostellar Cores: Dependence on Prestellar Core Conditions. *ApJ*, 897(2):110, July 2020. doi: 10.3847/1538-4357/ab994a.

A. Allen, Z.-Y. Li, and F. H. Shu. Collapse of Magnetized Singular Isothermal Toroids. II. Rotation and Magnetic Braking. , 599(1):363–379, Dec. 2003. doi: 10.1086/379243.

T. Alonso-Albi, A. Fuente, N. Crimier, P. Caselli, C. Ceccarelli, D. Johnstone, P. Planesas, J. R. Rizzo, F. Wyrowski, M. Tafalla, B. Lefloch, S. Maret, and C. Dominik. Chemical study of intermediate-mass (IM) Class 0 protostars. CO depletion and N_2H^+ deuteration. , 518:A52, July 2010. doi: 10.1051/0004-6361/201014317.

P. André. Low-Mass Protostars and Protostellar Stages. , 224(1-2):29–42, Feb. 1995. doi: 10.1007/BF00667817.

P. André. The Initial Conditions for Protostellar Collapse: Observational Constraints. In J. Bouvier and J.-P. Zahn, editors, *EAS Publications Series*, volume 3 of *EAS Publications Series*, pages 1–38, Jan. 2002. doi: 10.1051/eas:2002043.

P. André and T. Montmerle. From T Tauri Stars to Protostars: Circumstellar Material and Young Stellar Objects in the rho Ophiuchi Cloud. , 420:837, Jan. 1994. doi: 10.1086/173608.

P. André, D. Ward-Thompson, and M. Barsony. Submillimeter Continuum Observations of rho Ophiuchi A: The Candidate Protostar VLA 1623 and Prestellar Clumps. , 406:122, Mar. 1993. doi: 10.1086/172425.

P. André, D. Ward-Thompson, and F. Motte. Probing the initial conditions of star formation: the structure of the prestellar core L 1689B. , 314:625–635, Oct. 1996.

P. André, D. Ward-Thompson, and M. Barsony. From Prestellar Cores to Protostars: the Initial Conditions of Star Formation. In V. Mannings, A. P. Boss, and S. S. Russell, editors, *Protostars and Planets IV*, page 59, May 2000.

P. André, A. Men'shchikov, S. Bontemps, V. Könyves, F. Motte, N. Schneider, P. Didelon, V. Minier, P. Saraceno, D. Ward-Thompson, J. di Francesco, G. White, S. Molinari, L. Testi, A. Abergel, M. Griffin, T. Henning, P. Royer, B. Merín, R. Vavrek, M. Attard, D. Arzoumanian, C. D. Wilson, P. Ade, H. Aussel, J. P. Baluteau, M. Benedettini, J. P. Bernard, J. A. D. L. Blommaert, L. Cambrésy, P. Cox, A. di Giorgio, P. Hargrave, M. Hennemann, M. Huang, J. Kirk, O. Krause, R. Launhardt, S. Leeks, J. Le Pennec, J. Z. Li, P. G. Martin, A. Maury, G. Olofsson, A. Omont, N. Peretto, S. Pezzuto, T. Prusti, H. Roussel, D. Russeil, M. Sauvage, B. Sibthorpe, A. Sicilia-Aguilar, L. Spinoglio, C. Waelkens, A. Woodcraft, and A. Zavagno. From filamentary clouds to prestellar cores to the stellar IMF: Initial highlights from the Herschel Gould Belt Survey. *A&A*, 518:L102, July 2010. doi: 10.1051/0004-6361/201014666.

S. M. Andrews, D. J. Wilner, A. M. Hughes, C. Qi, and C. P. Dullemond. Protoplanetary Disk Structures in Ophiuchus. *ApJ*, 700(2):1502–1523, Aug. 2009. doi: 10.1088/0004-637X/700/2/1502.

S. M. Andrews, J. Huang, L. M. Pérez, A. Isella, C. P. Dullemond, N. T. Kurtovic, V. V. Guzmán, J. M. Carpenter, D. J. Wilner, S. Zhang, Z. Zhu, T. Birnstiel, X.-N. Bai, M. Benisty, A. M. Hughes, K. I. Öberg, and L. Ricci. The Disk Substructures at High Angular Resolution Project (DSHARP). I. Motivation, Sample, Calibration, and Overview. , 869(2):L41, Dec. 2018. doi: 10.3847/2041-8213/aaf741.

G. Anglada, L. F. Rodriguez, J. Canto, R. Estalella, and R. Lopez. The spectral hallmark of a contracting protostellar fragment. , 186(1-2):280–286, Nov. 1987.

M. Araki, S. Takano, N. Sakai, S. Yamamoto, T. Oyama, N. Kuze, and K. Tsukiyama. Long Carbon Chains in the Warm Carbon-chain-chemistry Source L1527: First Detection of C_7H in Molecular Clouds. *ApJ*, 847(1):51, Sept. 2017. doi: 10.3847/1538-4357/aa8637.

H. G. Arce, D. Shepherd, F. Gueth, C. F. Lee, R. Bachiller, A. Rosen, and H. Beuther. Molecular Outflows in Low- and High-Mass Star-forming Regions. In B. Reipurth, D. Jewitt, and K. Keil, editors, *Protostars and Planets V*, page 245, Jan. 2007.

H. G. Arce, D. Mardones, S. A. Corder, G. Garay, A. Noriega-Crespo, and A. C. Raga. ALMA Observations of the HH 46/47 Molecular Outflow. *ApJ*, 774(1):39, Sept. 2013. doi: 10.1088/0004-637X/774/1/39.

S. Asayama, A. Biggs, I. de Gregorio, W. Dent, J. Di Francesco, E. Fomalont, A. Hales, E. Humphries, S. Kameno, E. Müller, B. Vila Vilaro, and F. Stoehr. *ALMA Partnership*. 2016. ISBN 978-3-923524-66-2.

M. Attard, M. Houde, G. Novak, H.-b. Li, J. E. Vaillancourt, C. D. Dowell, J. Davidson, and H. Shinnaga. Magnetic Fields and Infall Motions in NGC 1333 IRAS 4. , 702(2):1584–1592, Sept. 2009. doi: 10.1088/0004-637X/702/2/1584.

R. Bachiller, J. Martin-Pintado, and A. Fuente. High-velocity SiO emission in the L1448 outflow. Evidence for dense shocked gas in the molecular bullets. *A&A*, 243:L21, Mar. 1991.

S. A. Balbus and J. F. Hawley. A Powerful Local Shear Instability in Weakly Magnetized Disks. I. Linear Analysis. *ApJ*, 376:214, July 1991. doi: 10.1086/170270.

I. Baraffe, G. Chabrier, and J. Gallardo. Episodic Accretion at Early Stages of Evolution of Low-Mass Stars and Brown Dwarfs: A Solution for the Observed Luminosity Spread in H-R Diagrams? , 702(1):L27–L31, Sept. 2009. doi: 10.1088/0004-637X/702/1/L27.

S. Basu and C. E. Jones. On the power-law tail in the mass function of protostellar condensations and stars. , 347(3):L47–L51, Jan. 2004. doi: 10.1111/j.1365-2966.2004.07405.x.

A. Belloche. Observation of rotation in star forming regions: clouds, cores, disks, and jets. In P. Hennebelle and C. Charbonnel, editors, *EAS Publications Series*, volume 62 of *EAS Publications Series*, pages 25–66, Sept. 2013. doi: 10.1051/eas/1362002.

E. A. Bergin and M. Tafalla. Cold Dark Clouds: The Initial Conditions for Star Formation. , 45(1):339–396, Sept. 2007. doi: 10.1146/annurev.astro.45.071206.100404.

G. Bertrang, S. Wolf, and H. S. Das. Large-scale magnetic fields in Bok globules. *A&A*, 565: A94, May 2014. doi: 10.1051/0004-6361/201323091.

H. Beuther, J. D. Soler, W. Vlemmings, H. Linz, T. Henning, R. Kuiper, R. Rao, R. Smith, T. Sakai, K. Johnston, A. Walsh, and S. Feng. Magnetic fields at the onset of high-mass star formation. , 614:A64, June 2018. doi: 10.1051/0004-6361/201732378.

E. Bianchi, C. Codella, C. Ceccarelli, F. Vazart, R. Bachiller, N. Balucani, M. Bouvier, M. De Simone, J. Enrique-Romero, C. Kahane, B. Lefloch, A. López-Sepulcre, J. Ospina-Zamudio, L. Podio, and V. Taquet. The census of interstellar complex organic molecules in the Class I hot corino of SVS13-A. , 483(2):1850–1861, Feb. 2019. doi: 10.1093/mnras/sty2915.

P. Bjerkeli, J. P. Ramsey, D. Harsono, H. Calcutt, L. E. Kristensen, M. H. D. van der Wiel, J. K. Jørgensen, S. Muller, and M. V. Persson. Kinematics around the B335 protostar down to au scales. , 631:A64, Nov. 2019. doi: 10.1051/0004-6361/201935948.

J. H. Black. Molecules in planetary nebulae. *ApJ*, 222:125–131, May 1978. doi: 10.1086/156128.

J. H. Black and A. Dalgarno. Models of interstellar clouds. I. The Zeta Ophiuchi cloud. *ApJS*, 34:405–423, July 1977. doi: 10.1086/190455.

R. D. Blandford and D. G. Payne. Hydromagnetic flows from accretion disks and the production of radio jets. , 199:883–903, June 1982. doi: 10.1093/mnras/199.4.883.

L. Blitz. Giant Molecular Clouds. In E. H. Levy and J. I. Lunine, editors, *Protostars and Planets III*, page 125, Jan. 1993.

P. Bodenheimer. Angular Momentum Evolution of Young Stars and Disks. , 33:199–238, Jan. 1995. doi: 10.1146/annurev.aa.33.090195.001215.

B. J. Bok. *Dimensions and Masses of Dark Nebulae*, volume 7, page 53. 1948.

S. Bontemps, P. Andre, and D. Ward-Thompson. Deep VLA search for the youngest protostars: a Class 0 source in the HH 24-26 region. *A&A*, 297:98–102, May 1995.

S. Bontemps, P. Andre, S. Terebey, and S. Cabrit. Evolution of outflow activity around low-mass embedded young stellar objects. *A&A*, 311:858–872, July 1996.

R. A. Booth and C. J. Clarke. Collision velocity of dust grains in self-gravitating protoplanetary discs. , 458(3):2676–2693, May 2016. doi: 10.1093/mnras/stw488.

C. R. Braiding and M. Wardle. The Hall effect in star formation. *MNRAS*, 422(1):261–281, May 2012. doi: 10.1111/j.1365-2966.2012.20601.x.

H. M. Butner, E. A. Lada, and R. B. Loren. Physical Properties of Dense Cores: DCO + Observations. , 448:207, July 1995. doi: 10.1086/175953.

V. Cabedo, J. Llorca, J. M. Trigo-Rodriguez, and A. Rimola. Study of Fischer-Tropsch-type reactions on chondritic meteorites. , 650:A160, June 2021a. doi: 10.1051/0004-6361/202039991.

V. Cabedo, A. Maury, J. M. Girart, and M. Padovani. Structured velocity field in the inner envelope of B335: ALMA observations of rare CO isotopologues. *A&A*, 653:A166, Sept. 2021b. doi: 10.1051/0004-6361/202140754.

S. Cabrit and C. Bertout. CO Line Formation in Bipolar Flows. II. Decelerated Outflow Case and Summary of Results. *ApJ*, 348:530, Jan. 1990. doi: 10.1086/168261.

S. Cabrit, P. O. Lagage, M. McCaughrean, and G. Olofsson. Origin of the mid-infrared emission and supersonic jet toward LkHα 234. , 321:523–530, May 1997.

S. Cabrit, M. Bocchi, M. Camenzind, A. Ciardi, F. de Colle, T. Downes, J. Ferreira, A. Frank, J. Gracia, S. Lebedev, A. Marrochino, S. Massaglia, T. Matsakos, J. O'Sullivan, C. Stehlé, M. Stute, F. Suzuki-Vidal, O. Tesileanu, K. Tsinganos, and C. Zanni. Dynamics of magnetized YSO jets: Examples of results from the JETSET network. In *Revista Mexicana de Astronomia y Astrofisica Conference Series*, volume 36 of *Revista Mexicana de Astronomia y Astrofisica Conference Series*, pages 171–178, Aug. 2009.

J. K. Calahan, Y. L. Shirley, B. E. Svoboda, E. A. Ivanov, J. R. Schmid, A. Pulley, J. Lautenbach, N. Zawadzki, C. Bullivant, C. W. Cook, L. Gray, A. Henrici, M. Pascale, C. Bosse, Q. Chance, S. Choi, M. Dunn, R. Jaime-Frias, I. Kearsley, J. Kelledy, C. Lewin, Q. Mahmood, S. McKinley, A. M. Mitchell, and D. R. Robinson. Searching for Inflow toward

Massive Starless Clump Candidates Identified in the Bolocam Galactic Plane Survey. , 862(1):63, July 2018. doi: 10.3847/1538-4357/aabfea.

D. Carrera, U. Gorti, A. Johansen, and M. B. Davies. Planetesimal Formation by the Streaming Instability in a Photoevaporating Disk. , 839(1):16, Apr. 2017. doi: 10.3847/1538-4357/aa6932.

M. M. Casali, C. Eiroa, and W. D. Duncan. A second phase of star formation in the Serpens core. *A&A*, 275:195–200, Aug. 1993.

P. Caselli. Deuterated molecules as a probe of ionization fraction in dense interstellar clouds. , 50(12-13):1133–1144, Oct. 2002. doi: 10.1016/S0032-0633(02)00074-0.

P. Caselli and P. C. Myers. The Line Width–Size Relation in Massive Cloud Cores. , 446: 665, June 1995. doi: 10.1086/175825.

P. Caselli, C. M. Walmsley, R. Terzieva, and E. Herbst. The Ionization Fraction in Dense Cloud Cores. , 499(1):234–249, May 1998. doi: 10.1086/305624.

C. Ceccarelli, P. Caselli, F. Fontani, R. Neri, A. López-Sepulcre, C. Codella, S. Feng, I. Jiménez-Serra, B. Lefloch, J. E. Pineda, C. Vastel, F. Alves, R. Bachiller, N. Balucani, E. Bianchi, L. Bizzocchi, S. Bottinelli, E. Caux, A. Chacón-Tanarro, R. Choudhury, A. Coutens, F. Dulieu, C. Favre, P. Hily-Blant, J. Holdship, C. Kahane, A. Jaber Al-Edhari, J. Laas, J. Ospina, Y. Oya, L. Podio, A. Pon, A. Punanova, D. Quenard, A. Rimola, N. Sakai, I. R. Sims, S. Spezzano, V. Taquet, L. Testi, P. Theulé, P. Ugliengo, A. I. Vasyunin, S. Viti, L. Wiesenfeld, and S. Yamamoto. Seeds Of Life In Space (SOLIS): The Organic Composition Diversity at 300-1000 au Scale in Solar-type Star-forming Regions. *ApJ*, 850(2):176, Dec. 2017. doi: 10.3847/1538-4357/aa961d.

C. J. Chandler and A. I. Sargent. The Small-Scale Structure and Kinematics of B335. , 414: L29, Sept. 1993. doi: 10.1086/186988.

H. Chen, P. C. Myers, E. F. Ladd, and D. O. S. Wood. Bolometric Temperature and Young Stars in the Taurus and Ophiuchus Complexes. , 445:377, May 1995. doi: 10.1086/175703.

H.-R. Chen, S.-Y. Liu, Y.-N. Su, and M.-Y. Wang. Deuterium Fractionation as an Evolutionary Probe in Massive Protostellar/Cluster Cores. *ApJ*, 743(2):196, Dec. 2011. doi: 10.1088/0004-637X/743/2/196.

M. Choi, I. Evans, Neal J., E. M. Gregersen, and Y. Wang. Modeling Line Profiles of Protostellar Collapse in B335 with the Monte Carlo Method. , 448:742, Aug. 1995. doi: 10.1086/176002.

M. Choi, J.-F. Panis, and I. Evans, Neal J. Berkeley-Illinois-Maryland Association Survey of Protostellar Collapse Candidates in HCO^+ and HCN Lines. *ApJS*, 122(2):519–556, June 1999. doi: 10.1086/313222.

M. Choi, M. Kang, and K. Tatematsu. Rotation of the NGC 1333 IRAS 4A2 Protostellar Jet. , 728(2):L34, Feb. 2011. doi: 10.1088/2041-8205/728/2/L34.

A. Ciardi and P. Hennebelle. Outflows and mass accretion in collapsing dense cores with misaligned rotation axis and magnetic field. *MNRAS*, 409(1):L39–L43, Nov. 2010. doi: 10.1111/j.1745-3933.2010.00942.x.

D. P. Clemens, J. L. Yun, and M. H. Heyer. BOK Globules and Small Molecular Clouds: Deep IRAS Photometry and 12CO Spectroscopy. , 75:877, Mar. 1991. doi: 10.1086/191552.

E. I. Curtis, J. S. Richer, J. J. Swift, and J. P. Williams. A submillimetre survey of the kinematics of the Perseus molecular cloud - II. Molecular outflows. *MNRAS*, 408(3):1516–1539, Nov. 2010. doi: 10.1111/j.1365-2966.2010.17214.x.

A. Dalgarno and S. Lepp. Deuterium fractionation mechanisms in interstellar clouds. , 287: L47–L50, Dec. 1984. doi: 10.1086/184395.

D. Dall'Olio, W. H. T. Vlemmings, M. V. Persson, F. O. Alves, H. Beuther, J. M. Girart, G. Surcis, J. M. Torrelles, and H. J. Van Langevelde. ALMA reveals the magnetic field evolution in the high-mass star forming complex G9.62+0.19. , 626:A36, June 2019. doi: 10.1051/0004-6361/201834100.

W. B. Dapp and S. Basu. Averting the magnetic braking catastrophe on small scales: disk formation due to Ohmic dissipation. *A&A*, 521:L56, Oct. 2010. doi: 10.1051/0004-6361/201015700.

W. B. Dapp, S. Basu, and M. W. Kunz. Bridging the gap: disk formation in the Class 0 phase with ambipolar diffusion and Ohmic dissipation. *A&A*, 541:A35, May 2012. doi: 10.1051/0004-6361/201117876.

J. Di Francesco, P. C. Myers, D. J. Wilner, N. Ohashi, and D. Mardones. Infall, Outflow, Rotation, and Turbulent Motions of Dense Gas within NGC 1333 IRAS 4. , 562(2): 770–789, Dec. 2001. doi: 10.1086/323854.

C. L. Dobbs, M. R. Krumholz, J. Ballesteros-Paredes, A. D. Bolatto, Y. Fukui, M. Heyer, M. M. M. Low, E. C. Ostriker, and E. Vázquez-Semadeni. Formation of Molecular Clouds and Global Conditions for Star Formation. In H. Beuther, R. S. Klessen, C. P. Dullemond, and T. Henning, editors, *Protostars and Planets VI*, page 3, Jan. 2014. doi: 10.2458/azu_uapress_9780816531240-ch001.

A. Z. Dolginov and I. G. Mitrofanov. Orientation of Cosmic Dust Grains. *A&SS*, 43(2): 291–317, Sept. 1976. doi: 10.1007/BF00640010.

B. T. Draine. Interstellar Dust Grains. , 41:241–289, Jan. 2003. doi: 10.1146/annurev.astro.41.011802.094840.

B. T. Draine and H. M. Lee. Optical Properties of Interstellar Graphite and Silicate Grains. , 285:89, Oct. 1984. doi: 10.1086/162480.

M. M. Dunham and E. I. Vorobyov. Resolving the Luminosity Problem in Low-mass Star Formation. , 747(1):52, Mar. 2012. doi: 10.1088/0004-637X/747/1/52.

M. M. Dunham, A. Crapsi, I. Evans, Neal J., T. L. Bourke, T. L. Huard, P. C. Myers, and J. Kauffmann. Identifying the Low-Luminosity Population of Embedded Protostars in the c2d Observations of Clouds and Cores. , 179(1):249–282, Nov. 2008. doi: 10.1086/591085.

M. M. Dunham, I. Evans, Neal J., S. Terebey, C. P. Dullemond, and C. H. Young. Evolutionary Signatures in the Formation of Low-Mass Protostars. II. Toward Reconciling Models and Observations. , 710(1):470–502, Feb. 2010. doi: 10.1088/0004-637X/710/1/470.

M. M. Dunham, A. M. Stutz, L. E. Allen, I. Evans, N. J., W. J. Fischer, S. T. Megeath, P. C. Myers, S. S. R. Offner, C. A. Poteet, J. J. Tobin, and E. I. Vorobyov. The Evolution of Protostars: Insights from Ten Years of Infrared Surveys with Spitzer and Herschel. In H. Beuther, R. S. Klessen, C. P. Dullemond, and T. Henning, editors, *Protostars and Planets VI*, page 195, Jan. 2014. doi: 10.2458/azu_uapress_9780816531240-ch009.

A. Duquennoy and M. Mayor. *How Many Single Stars Among Solar Type Stars?*, volume 390, pages 39–43. 1991. doi: 10.1007/3-540-54752-5_186.

M. Emprechtinger. Deuterium Fractionation As Evolutionary Tracer Of Class 0 Protostars. In *American Astronomical Society Meeting Abstracts #214*, volume 214 of *American Astronomical Society Meeting Abstracts*, page 315.02, May 2009.

M. L. Enoch, I. Evans, Neal J., A. I. Sargent, and J. Glenn. Properties of the Youngest Protostars in Perseus, Serpens, and Ophiuchus. , 692(2):973–997, Feb. 2009. doi: 10.1088/0004-637X/692/2/973.

R. Estalella. HfS, Hyperfine Structure Fitting Tool. , 129(972):025003, Feb. 2017. doi: 10.1088/1538-3873/129/972/025003.

R. Estalella, G. Anglada, A. K. Díaz-Rodríguez, and J. M. Mayen-Gijon. Analysis and test of the central-blue-spot infall hallmark. , 626:A84, June 2019. doi: 10.1051/0004-6361/201834998.

I. Evans, N. J., B. Zuckerman, G. Morris, and T. Sato. Interstellar H_2CO. I. Absorption studies, dark clouds, and the cosmic background radiation. *ApJ*, 196:433–456, Mar. 1975. doi: 10.1086/153424.

I. Evans, Neal J. Physical Conditions in Regions of Star Formation. , 37:311–362, Jan. 1999. doi: 10.1146/annurev.astro.37.1.311.

I. Evans, Neal J., L. E. Allen, G. A. Blake, A. C. A. Boogert, T. Bourke, P. M. Harvey, J. E. Kessler, D. W. Koerner, C. W. Lee, L. G. Mundy, P. C. Myers, D. L. Padgett, K. Pontoppidan, A. I. Sargent, K. R. Stapelfeldt, E. F. van Dishoeck, C. H. Young, and K. E. Young. From Molecular Cores to Planet-forming Disks: An SIRTF Legacy Program. , 115(810):965–980, Aug. 2003. doi: 10.1086/376697.

I. Evans, Neal J., J.-E. Lee, J. M. C. Rawlings, and M. Choi. B335: A Laboratory for Astrochemistry in a Collapsing Cloud. , 626(2):919–932, June 2005. doi: 10.1086/430295.

I. Evans, Neal J., M. M. Dunham, J. K. Jørgensen, M. L. Enoch, B. Merín, E. F. van Dishoeck, J. M. Alcalá, P. C. Myers, K. R. Stapelfeldt, T. L. Huard, L. E. Allen, P. M. Harvey, T. van Kempen, G. A. Blake, D. W. Koerner, L. G. Mundy, D. L. Padgett, and A. I. Sargent. The Spitzer c2d Legacy Results: Star-Formation Rates and Efficiencies; Evolution and Lifetimes. , 181(2):321–350, Apr. 2009. doi: 10.1088/0067-0049/181/2/321.

I. Evans, Neal J., J. Di Francesco, J.-E. Lee, J. K. Jørgensen, M. Choi, P. C. Myers, and D. Mardones. Detection of Infall in the Protostar B335 with ALMA. , 814(1):22, Nov. 2015. doi: 10.1088/0004-637X/814/1/22.

S. R. Federman, J. Weber, and D. L. Lambert. Cosmic Ray–induced Chemistry toward Perseus OB2. *ApJ*, 463:181, May 1996. doi: 10.1086/177233.

R. F. Ferrante, M. H. Moore, J. A. Nuth, and T. Smith. NOTE: Laboratory Studies of Catalysis of CO to Organics on Grain Analogs. , 145(1):297–300, May 2000. doi: 10.1006/icar.2000.6350.

W. J. Fischer, S. T. Megeath, A. M. Stutz, J. J. Tobin, B. Ali, T. Stanke, M. Osorio, E. Furlan, HOPS Team, and Orion Protostar Survey. Results from HOPS: A multiwavelength census of Orion protostars. *Astronomische Nachrichten*, 334(1-2):53, Feb. 2013. doi: 10.1002/asna.201211761.

F. Fontani, C. Ceccarelli, C. Favre, P. Caselli, R. Neri, I. R. Sims, C. Kahane, F. O. Alves, N. Balucani, E. Bianchi, E. Caux, A. Jaber Al-Edhari, A. Lopez-Sepulcre, J. E. Pineda, R. Bachiller, L. Bizzocchi, S. Bottinelli, A. Chacon-Tanarro, R. Choudhury, C. Codella, A. Coutens, F. Dulieu, S. Feng, A. Rimola, P. Hily-Blant, J. Holdship, I. Jimenez-Serra, J. Laas, B. Lefloch, Y. Oya, L. Podio, A. Pon, A. Punanova, D. Quenard, N. Sakai, S. Spezzano, V. Taquet, L. Testi, P. Theulé, P. Ugliengo, C. Vastel, A. I. Vasyunin, S. Viti, S. Yamamoto, and L. Wiesenfeld. Seeds of Life in Space (SOLIS). I. Carbon-chain growth in the Solar-type protocluster OMC2-FIR4. , 605:A57, Sept. 2017. doi: 10.1051/0004-6361/201730527.

A. Frank, T. P. Ray, S. Cabrit, P. Hartigan, H. G. Arce, F. Bacciotti, J. Bally, M. Benisty, J. Eislöffel, M. Güdel, S. Lebedev, B. Nisini, and A. Raga. Jets and Outflows from Star to Cloud: Observations Confront Theory. In H. Beuther, R. S. Klessen, C. P. Dullemond, and T. Henning, editors, *Protostars and Planets VI*, page 451, Jan. 2014. doi: 10.2458/azu_uapress_9780816531240-ch020.

M. A. Frerking, W. D. Langer, and R. W. Wilson. The Structure and Dynamics of BOK Globule B335. , 313:320, Feb. 1987. doi: 10.1086/164970.

S. Gabici, F. A. Aharonian, and P. Blasi. Gamma rays from molecular clouds. *A&SS*, 309 (1-4):365–371, June 2007. doi: 10.1007/s10509-007-9427-6.

M. Galametz, A. Maury, J. M. Girart, R. Rao, Q. Zhang, M. Gaudel, V. Valdivia, E. Keto, and S.-P. Lai. SMA observations of polarized dust emission in solar-type Class 0 protostars: Magnetic field properties at envelope scales. *A&A*, 616:A139, Aug. 2018. doi: 10.1051/0004-6361/201833004.

M. Galametz, A. Maury, J. M. Girart, R. Rao, Q. Zhang, M. Gaudel, V. Valdivia, P. Hennebelle, V. Cabedo-Soto, E. Keto, and S.-P. Lai. An observational correlation between magnetic field, angular momentum and fragmentation in the envelopes of Class 0 protostars? , 644:A47, Dec. 2020. doi: 10.1051/0004-6361/202038854.

M. Gâlfalk and G. Olofsson. Herbig-Haro flows in B335. *A&A*, 475(1):281–300, Nov. 2007. doi: 10.1051/0004-6361:20077889.

D. Galli and F. H. Shu. Collapse of Magnetized Molecular Cloud Cores. I. Semianalytical Solution. , 417:220, Nov. 1993. doi: 10.1086/173305.

D. Galli, S. Lizano, F. H. Shu, and A. Allen. Gravitational Collapse of Magnetized Clouds. I. Ideal Magnetohydrodynamic Accretion Flow. , 647(1):374–381, Aug. 2006. doi: 10.1086/505257.

R. T. Garrod and E. Herbst. Formation of methyl formate and other organic species in the warm-up phase of hot molecular cores. *A&A*, 457(3):927–936, Oct. 2006. doi: 10.1051/0004-6361:20065560.

M. Gaudel, A. J. Maury, A. Belloche, S. Maret, P. André, P. Hennebelle, M. Galametz, L. Testi, S. Cabrit, P. Palmeirim, B. Ladjelate, C. Codella, and L. Podio. Angular momentum profiles of Class 0 protostellar envelopes. *A&A*, 637:A92, May 2020. doi: 10.1051/0004-6361/201936364.

J. Gillis, L. Mestel, and R. B. Paris. Magnetic Braking During Star Formation, I. , 27(1): 167–194, Mar. 1974. doi: 10.1007/BF00641596.

J. M. Girart, R. M. Crutcher, and R. Rao. Detection of Polarized CO Emission from the Molecular Outflow in NGC 1333 IRAS 4A. , 525(2):L109–L112, Nov. 1999. doi: 10.1086/312345.

J. M. Girart, S. Viti, D. A. Williams, R. Estalella, and P. T. P. Ho. The molecular condensations ahead of Herbig-Haro objects. I. Multi-transition observations of HH 2. *A&A*, 388: 1004–1015, June 2002. doi: 10.1051/0004-6361:20020536.

J. M. Girart, R. Rao, and D. P. Marrone. Magnetic Fields in the Formation of Sun-Like Stars. *Science*, 313(5788):812–814, Aug. 2006. doi: 10.1126/science.1129093.

J. M. Girart, R. Rao, and D. P. Marrone. SMA observations of the magnetic fields around a low-mass protostellar system. , 313(1-3):87–90, Jan. 2008. doi: 10.1007/s10509-007-9592-7.

J. M. Girart, M. T. Beltrán, Q. Zhang, R. Rao, and R. Estalella. Magnetic Fields in the Formation of Massive Stars. *Science*, 324(5933):1408, June 2009. doi: 10.1126/science.1171807.

T. Gold. Polarization of Starlight. *Nature*, 169(4295):322, Feb. 1952. doi: 10.1038/169322a0.

A. A. Goodman, P. J. Benson, G. A. Fuller, and P. C. Myers. Dense Cores in Dark Clouds. VIII. Velocity Gradients. , 406:528, Apr. 1993. doi: 10.1086/172465.

S. P. Goodwin, A. P. Whitworth, and D. Ward-Thompson. Simulating star formation in molecular cloud cores. I. The influence of low levels of turbulence on fragmentation and multiplicity. *A&A*, 414:633–650, Feb. 2004. doi: 10.1051/0004-6361:20031594.

T. E. Graedel, W. D. Langer, and M. A. Frerking. The kinetic chemistry of dense interstellar clouds. , 48:321–368, Mar. 1982. doi: 10.1086/190780.

D. M. Graninger, O. H. Wilkins, and K. I. Öberg. Carbon Chains and Methanol toward Embedded Protostars. *ApJ*, 819(2):140, Mar. 2016. doi: 10.3847/0004-637X/819/2/140.

W. J. Gray, C. F. McKee, and R. I. Klein. Effect of angular momentum alignment and strong magnetic fields on the formation of protostellar discs. *MNRAS*, 473(2):2124–2143, Jan. 2018. doi: 10.1093/mnras/stx2406.

E. M. Gregersen, I. Evans, Neal J., S. Zhou, and M. Choi. New Protostellar Collapse Candidates: An HCO$^+$ Survey of the Class 0 Sources. *ApJ*, 484(1):256–276, July 1997. doi: 10.1086/304297.

E. M. Gregersen, I. Evans, Neal J., D. Mardones, and P. C. Myers. Does Infall End before the Class I Stage? , 533(1):440–453, Apr. 2000. doi: 10.1086/308665.

M. Guelin, W. D. Langer, R. L. Snell, and H. A. Wootten. Observations of DCO$^+$: the electron abundance in dark clouds. *ApJL*, 217:L165–L168, Nov. 1977. doi: 10.1086/182562.

M. Guelin, W. D. Langer, and R. W. Wilson. The state of ionization in dense molecular clouds. , 107:107–127, Mar. 1982.

S. Guilloteau, R. Bachiller, A. Fuente, and R. Lucas. First observations of young bipolar outflows with the IRAM interferometer : 2" resolution SiO images of the molecular jet in L 1448. , 265:L49–L52, Nov. 1992.

D. Harsono, J. K. Jørgensen, E. F. van Dishoeck, M. R. Hogerheijde, S. Bruderer, M. V. Persson, and J. C. Mottram. Rotationally-supported disks around Class I sources in Taurus: disk formation constraints. , 562:A77, Feb. 2014. doi: 10.1051/0004-6361/201322646.

T. W. Hartquist, J. H. Black, and A. Dalgarno. Cosmic ray ionization and the deuterium abundance. *MNRAS*, 185:643–646, Dec. 1978. doi: 10.1093/mnras/185.3.643.

I. T. Hasegawa, C. Rogers, and S. S. Hayashi. Observations of HCO$^+$ in B335. In G. D. Watt and A. S. Webster, editors, *Submillimetre Astronomy*, volume 158, page 175, Jan. 1990. doi: 10.1007/978-94-015-6850-0_64.

G. E. Hassel, E. Herbst, and R. T. Garrod. Modeling the Lukewarm Corino Phase: Is L1527 Unique? *ApJ*, 681(2):1385–1395, July 2008. doi: 10.1086/588185.

S. Hayakawa, S. Nishimura, and T. Takayanagi. Radiation from the Interstellar Hydrogen Atoms. *PASJ*, 13:184, Jan. 1961.

P. Hennebelle. Self-similar condensation of rotating magnetized self-gravitating isothermal filaments. , 397:381–391, Jan. 2003. doi: 10.1051/0004-6361:20021526.

P. Hennebelle and A. Ciardi. Disk formation during collapse of magnetized protostellar cores. *A&A*, 506(2):L29–L32, Nov. 2009. doi: 10.1051/0004-6361/200913008.

P. Hennebelle and S. Fromang. Magnetic processes in a collapsing dense core. I. Accretion and ejection. *A&A*, 477(1):9–24, Jan. 2008. doi: 10.1051/0004-6361:20078309.

P. Hennebelle, B. Commerçon, G. Chabrier, and P. Marchand. Magnetically Self-regulated Formation of Early Protoplanetary Disks. *ApJL*, 830(1):L8, Oct. 2016. doi: 10.3847/2041-8205/830/1/L8.

P. Hennebelle, B. Commerçon, Y.-N. Lee, and S. Charnoz. What determines the formation and characteristics of protoplanetary discs? , 635:A67, Mar. 2020. doi: 10.1051/0004-6361/201936714.

E. Herbst and W. Klemperer. The Formation and Depletion of Molecules in Dense Interstellar Clouds. *ApJ*, 185:505–534, Oct. 1973. doi: 10.1086/152436.

E. Herbst and E. F. van Dishoeck. Complex Organic Interstellar Molecules. *ARA&A*, 47(1):427–480, Sept. 2009. doi: 10.1146/annurev-astro-082708-101654.

J. Hernández, N. Calvet, C. Briceño, L. Hartmann, A. K. Vivas, J. Muzerolle, J. Downes, L. Allen, and R. Gutermuth. Spitzer Observations of the Orion OB1 Association: Disk Census in the Low-Mass Stars. *ApJ*, 671(2):1784–1799, Dec. 2007. doi: 10.1086/522882.

T. Hezareh, M. Houde, C. McCoey, C. Vastel, and R. Peng. Simultaneous Determination of the Cosmic Ray Ionization Rate and Fractional Ionization in DR 21(OH). *ApJ*, 684(2):1221–1227, Sept. 2008. doi: 10.1086/590365.

T. Hezareh, M. Houde, C. McCoey, and H.-b. Li. Observational Determination of the Turbulent Ambipolar Diffusion Scale and Magnetic Field Strength in Molecular Clouds. , 720(1):603–607, Sept. 2010. doi: 10.1088/0004-637X/720/1/603.

T. Hezareh, T. Csengeri, M. Houde, F. Herpin, and S. Bontemps. Probing the turbulent ambipolar diffusion scale in molecular clouds with spectroscopy. , 438(1):663–671, Feb. 2014. doi: 10.1093/mnras/stt2237.

A. E. Higuchi, N. Sakai, Y. Watanabe, A. López-Sepulcre, K. Yoshida, Y. Oya, M. Imai, Y. Zhang, C. Ceccarelli, B. Lefloch, C. Codella, R. Bachiller, T. Hirota, T. Sakai, and S. Yamamoto. Chemical Survey toward Young Stellar Objects in the Perseus Molecular Cloud Complex. , 236(2):52, June 2018. doi: 10.3847/1538-4365/aabfe9.

U. Hincelin, B. Commerçon, V. Wakelam, F. Hersant, S. Guilloteau, and E. Herbst. Chemical and Physical Characterization of Collapsing Low-mass Prestellar Dense Cores. *ApJ*, 822(1):12, May 2016. doi: 10.3847/0004-637X/822/1/12.

N. Hirano, O. Kameya, M. Nakayama, and K. Takakubo. Bipolar Outflow in B335. , 327:L69, Apr. 1988. doi: 10.1086/185142.

N. Hirano, O. Kameya, T. Kasuga, and T. Umemoto. Bipolar Outflow in B335: The Small-Scale Structure. , 390:L85, May 1992. doi: 10.1086/186378.

N. Hirano, S.-Y. Liu, H. Shang, P. T. P. Ho, H.-C. Huang, Y.-J. Kuan, M. J. McCaughrean, and Q. Zhang. SiO J = 5-4 in the HH 211 Protostellar Jet Imaged with the Submillimeter Array. , 636(2):L141–L144, Jan. 2006. doi: 10.1086/500201.

T. Hirota, M. Ohishi, and S. Yamamoto. A Search for Carbon-Chain-rich Cores in Dark Clouds. *ApJ*, 699(1):585–602, July 2009. doi: 10.1088/0004-637X/699/1/585.

J. A. Högbom. Aperture Synthesis with a Non-Regular Distribution of Interferometer Baselines. , 15:417, June 1974.

M. Houde, P. Bastien, R. Peng, T. G. Phillips, and H. Yoshida. Probing the Magnetic Field with Molecular Ion Spectra. , 536(2):857–864, June 2000a. doi: 10.1086/308980.

M. Houde, R. Peng, T. G. Phillips, P. Bastien, and H. Yoshida. Probing the Magnetic Field with Molecular Ion Spectra. II. , 537(1):245–254, July 2000b. doi: 10.1086/309035.

R. Hueso and T. Guillot. Evolution of protoplanetary disks: constraints from DM Tauri and GM Aurigae. , 442(2):703–725, Nov. 2005. doi: 10.1051/0004-6361:20041905.

A. M. Hughes, G. Duchêne, and B. C. Matthews. Debris Disks: Structure, Composition, and Variability. , 56:541–591, Sept. 2018. doi: 10.1146/annurev-astro-081817-052035.

C. L. H. Hull, R. L. Plambeck, W. Kwon, G. C. Bower, J. M. Carpenter, R. M. Crutcher, J. D. Fiege, E. Franzmann, N. S. Hakobian, C. Heiles, M. Houde, A. M. Hughes, J. W. Lamb, L. W. Looney, D. P. Marrone, B. C. Matthews, T. Pillai, M. W. Pound, N. Rahman, G. Sandell, I. W. Stephens, J. J. Tobin, J. E. Vaillancourt, N. H. Volgenau, and M. C. H. Wright. TADPOL: A 1.3 mm Survey of Dust Polarization in Star-forming Cores and Regions. , 213(1):13, July 2014. doi: 10.1088/0067-0049/213/1/13.

R. L. Hurt and M. Barsony. A Cluster of Class 0 Protostars in Serpens: an IRAS HIRES Study. *ApJL*, 460:L45, Mar. 1996. doi: 10.1086/309969.

M. Imai, N. Sakai, Y. Oya, A. López-Sepulcre, Y. Watanabe, C. Ceccarelli, B. Lefloch, E. Caux, C. Vastel, C. Kahane, T. Sakai, T. Hirota, Y. Aikawa, and S. Yamamoto. Discovery of a Hot Corino in the Bok Globule B335. *ApJL*, 830(2):L37, Oct. 2016. doi: 10.3847/2041-8205/830/2/L37.

M. Imai, Y. Oya, N. Sakai, A. López-Sepulcre, Y. Watanabe, and S. Yamamoto. Unveiling a Few Astronomical Unit Scale Rotation Structure around the Protostar in B335. , 873 (2):L21, Mar. 2019. doi: 10.3847/2041-8213/ab0c20.

A. Isella, J. M. Carpenter, and A. I. Sargent. Structure and Evolution of Pre-main-sequence Circumstellar Disks. *ApJ*, 701(1):260–282, Aug. 2009. doi: 10.1088/0004-637X/701/1/260.

A. A. Jaber, C. Ceccarelli, C. Kahane, and E. Caux. The Census of Complex Organic Molecules in the Solar-type Protostar IRAS16293-2422. *ApJ*, 791(1):29, Aug. 2014. doi: 10.1088/0004-637X/791/1/29.

N. Jackson. *Principles of Interferometry*, volume 742, page 193. 2008.

R. V. Jones and J. Spitzer, Lyman. Magnetic Alignment of Interstellar Grains. *ApJ*, 147:943, Mar. 1967. doi: 10.1086/149086.

M. Joos, P. Hennebelle, and A. Ciardi. Protostellar disk formation and transport of angular momentum during magnetized core collapse. *A&A*, 543:A128, July 2012. doi: 10.1051/0004-6361/201118730.

M. Joos, P. Hennebelle, A. Ciardi, and S. Fromang. The influence of turbulence during magnetized core collapse and its consequences on low-mass star formation. *A&A*, 554:A17, June 2013. doi: 10.1051/0004-6361/201220649.

J. K. Jørgensen, F. L. Schöier, and E. F. van Dishoeck. Physical structure and CO abundance of low-mass protostellar envelopes. , 389:908–930, July 2002. doi: 10.1051/0004-6361:20020681.

J. K. Jørgensen, F. L. Schöier, and E. F. van Dishoeck. Molecular inventories and chemical evolution of low-mass protostellar envelopes. , 416:603–622, Mar. 2004. doi: 10.1051/0004-6361:20034440.

J. K. Jørgensen, E. F. van Dishoeck, R. Visser, T. L. Bourke, D. J. Wilner, D. Lommen, M. R. Hogerheijde, and P. C. Myers. PROSAC: a submillimeter array survey of low-mass protostars. II. The mass evolution of envelopes, disks, and stars from the Class 0 through I stages. , 507(2):861–879, Nov. 2009. doi: 10.1051/0004-6361/200912325.

J. K. Jørgensen, A. Belloche, and R. T. Garrod. Astrochemistry During the Formation of Stars. , 58:727–778, Aug. 2020. doi: 10.1146/annurev-astro-032620-021927.

N. Kaifu, M. Ohishi, K. Kawaguchi, S. Saito, S. Yamamoto, T. Miyaji, K. Miyazawa, S.-I. Ishikawa, C. Noumaru, S. Harasawa, M. Okuda, and H. Suzuki. A 8.8–50GHz Complete Spectral Line Survey toward TMC-1 I. Survey Data. *PASJ*, 56:69–173, Feb. 2004. doi: 10.1093/pasj/56.1.69.

J. Kauffmann, F. Bertoldi, T. L. Bourke, I. Evans, N. J., and C. W. Lee. MAMBO mapping of Spitzer c2d small clouds and cores. *A&A*, 487(3):993–1017, Sept. 2008. doi: 10.1051/0004-6361:200809481.

J. Keene, J. A. Davidson, D. A. Harper, R. H. Hildebrand, D. T. Jaffe, R. F. Loewenstein, F. J. Low, and R. Pernic. Far-infrared detection of low-luminosity star formation in the BOK globule B 335. , 274:L43–L47, Nov. 1983. doi: 10.1086/184147.

S. J. Kenyon and L. Hartmann. Pre-Main-Sequence Evolution in the Taurus-Auriga Molecular Cloud. , 101:117, Nov. 1995. doi: 10.1086/192235.

S. J. Kenyon, L. W. Hartmann, K. M. Strom, and S. E. Strom. An IRAS Survey of the Taurus-Auriga Molecular Cloud. , 99:869, Mar. 1990. doi: 10.1086/115380.

J. Keown, S. Schnee, T. L. Bourke, J. Di Francesco, R. Friesen, P. Caselli, P. Myers, G. Williger, and M. Tafalla. Infall/Expansion Velocities in the Low-mass Dense Cores L492, L694-2, and L1521F: Dependence on Position and Molecular Tracer. , 833(1):97, Dec. 2016. doi: 10.3847/1538-4357/833/1/97.

A. Konigl and R. E. Pudritz. Disk Winds and the Accretion-Outflow Connection. In V. Mannings, A. P. Boss, and S. S. Russell, editors, *Protostars and Planets IV*, page 759, May 2000.

R. Krasnopolsky, Z.-Y. Li, and H. Shang. Disk Formation Enabled by Enhanced Resistivity. 716(2):1541–1550, June 2010. doi: 10.1088/0004-637X/716/2/1541.

R. Krasnopolsky, Z.-Y. Li, and H. Shang. Disk Formation in Magnetized Clouds Enabled by the Hall Effect. *ApJ*, 733(1):54, May 2011. doi: 10.1088/0004-637X/733/1/54.

K. M. Kratter, C. D. Matzner, M. R. Krumholz, and R. I. Klein. On the Role of Disks in the Formation of Stellar Systems: A Numerical Parameter Study of Rapid Accretion. , 708 (2):1585–1597, Jan. 2010. doi: 10.1088/0004-637X/708/2/1585.

M. E. Kress and A. G. G. M. Tielens. The role of Fischer-Tropsch catalysis in solar nebula chemistry. , 36(1):75–92, Jan. 2001. doi: 10.1111/j.1945-5100.2001.tb01811.x.

M. R. Krumholz and T. A. Thompson. Direct Numerical Simulation of Radiation Pressure-driven Turbulence and Winds in Star Clusters and Galactic Disks. *ApJ*, 760(2):155, Dec. 2012. doi: 10.1088/0004-637X/760/2/155.

Y. Kurono, M. Saito, T. Kamazaki, K.-I. Morita, and R. Kawabe. Unveiling the Detailed Density and Velocity Structures of the Protostellar Core B335. , 765(2):85, Mar. 2013. doi: 10.1088/0004-637X/765/2/85.

W. Kwon, I. W. Stephens, J. J. Tobin, L. W. Looney, Z.-Y. Li, F. F. S. van der Tak, and R. M. Crutcher. Highly Ordered and Pinched Magnetic Fields in the Class 0 Protobinary System L1448 IRS 2. , 879(1):25, July 2019. doi: 10.3847/1538-4357/ab24c8.

C. J. Lada. Star formation: from OB associations to protostars. In M. Peimbert and J. Jugaku, editors, *Star Forming Regions*, volume 115, page 1, Jan. 1987.

W. D. Langer and A. A. Penzias. 12C/ 13C Isotope Ratio in the Local Interstellar Medium from Observations of 13C 18O in Molecular Clouds. , 408:539, May 1993. doi: 10.1086/172611.

W. D. Langer, M. A. Frerking, and R. W. Wilson. Multiple Star Formation and the Dynamical Evolution of B335. *ApJL*, 306:L29, July 1986. doi: 10.1086/184698.

R. B. Larson. Numerical calculations of the dynamics of collapsing proto-star. , 145:271, Jan. 1969. doi: 10.1093/mnras/145.3.271.

R. Launhardt, A. M. Stutz, A. Schmiedeke, T. Henning, O. Krause, Z. Balog, H. Beuther, S. Birkmann, M. Hennemann, J. Kainulainen, T. Khanzadyan, H. Linz, N. Lippok, M. Nielbock, J. Pitann, S. Ragan, C. Risacher, M. Schmalzl, Y. L. Shirley, B. Stecklum, J. Steinacker, and J. Tackenberg. The Earliest Phases of Star Formation (EPoS): a Herschel key project. The thermal structure of low-mass molecular cloud cores. , 551:A98, Mar. 2013. doi: 10.1051/0004-6361/201220477.

C. J. Law, K. I. Öberg, J. B. Bergner, and D. Graninger. Carbon Chain Molecules toward Embedded Low-mass Protostars. *ApJ*, 863(1):88, Aug. 2018. doi: 10.3847/1538-4357/aacf9d.

A. Lazarian. Tracing magnetic fields with aligned grains. *JQSRT*, 106:225–256, July 2007. doi: 10.1016/j.jqsrt.2007.01.038.

V. J. M. Le Gouellec, C. L. H. Hull, A. J. Maury, J. M. Girart, Ł. Tychoniec, L. E. Kristensen, Z.-Y. Li, F. Louvet, P. C. Cortes, and R. Rao. Characterizing Magnetic Field Morphologies in Three Serpens Protostellar Cores with ALMA. *ApJ*, 885(2):106, Nov. 2019. doi: 10.3847/1538-4357/ab43c2.

C.-F. Lee. Molecular jets from low-mass young protostellar objects. *A&AR*, 28(1):1, Mar. 2020. doi: 10.1007/s00159-020-0123-7.

C.-F. Lee, N. Hirano, A. Palau, P. T. P. Ho, T. L. Bourke, Q. Zhang, and H. Shang. Rotation and Outflow Motions in the Very Low-Mass Class 0 Protostellar System HH 211 at Subarcsecond Resolution. , 699(2):1584–1594, July 2009. doi: 10.1088/0004-637X/699/2/1584.

C. W. Lee, P. C. Myers, and M. Tafalla. A Survey for Infall Motions toward Starless Cores. II. CS (2-1) and N_2H^+ (1-0) Mapping Observations. , 136(2):703–734, Oct. 2001. doi: 10.1086/322534.

C. M. Leung and R. L. Brown. On the interpretation of carbon monoxide self-absorption profiles seen toward embedded stars in dense interstellar clouds. , 214:L73–L78, June 1977. doi: 10.1086/182446.

H.-b. Li. Magnetic Field Continuity from 100 to 0.1 Parsec Scales. In *American Astronomical Society Meeting Abstracts #213*, volume 213 of *American Astronomical Society Meeting Abstracts*, page 347.06, Jan. 2009.

H.-b. Li and M. Houde. Probing the Turbulence Dissipation Range and Magnetic Field Strengths in Molecular Clouds. , 677(2):1151–1156, Apr. 2008. doi: 10.1086/529581.

H. B. Li, A. Goodman, T. K. Sridharan, M. Houde, Z. Y. Li, G. Novak, and K. S. Tang. The Link Between Magnetic Fields and Cloud/Star Formation. In H. Beuther, R. S. Klessen, C. P. Dullemond, and T. Henning, editors, *Protostars and Planets VI*, page 101, Jan. 2014. doi: 10.2458/azu_uapress_9780816531240-ch005.

Z.-Y. Li, R. Krasnopolsky, and H. Shang. Non-ideal MHD Effects and Magnetic Braking Catastrophe in Protostellar Disk Formation. *ApJ*, 738(2):180, Sept. 2011. doi: 10.1088/0004-637X/738/2/180.

D. N. C. Lin and J. E. Pringle. A viscosity prescription for a self-gravitating accretion disc. , 225:607–613, Apr. 1987. doi: 10.1093/mnras/225.3.607.

H. Linnartz, S. Ioppolo, and G. Fedoseev. Atom addition reactions in interstellar ice analogues. *arXiv e-prints*, art. arXiv:1507.02729, July 2015.

J. Llorca and I. Casanova. Formation of carbides and hydrocarbons in chondritic interplanetary dust particles: A laboratory study. , 33(2):243–251, Mar. 1998. doi: 10.1111/j.1945-5100.1998.tb01629.x.

L. W. Looney, L. G. Mundy, and W. J. Welch. Unveiling the Circumstellar Envelope and Disk: A Subarcsecond Survey of Circumstellar Structures. *ApJ*, 529(1):477–498, Jan. 2000. doi: 10.1086/308239.

A. López-Sepulcre, A. A. Jaber, E. Mendoza, B. Lefloch, C. Ceccarelli, C. Vastel, R. Bachiller, J. Cernicharo, C. Codella, C. Kahane, M. Kama, and M. Tafalla. Shedding light on the formation of the pre-biotic molecule formamide with ASAI. , 449(3):2438–2458, May 2015. doi: 10.1093/mnras/stv377.

M. M. Mac Low. Turbulent Structure of the Interstellar Medium. In S. Pfalzner, C. Kramer, C. Staubmeier, and A. Heithausen, editors, *The Dense Interstellar Medium in Galaxies*, volume 91, page 379, Jan. 2004. doi: 10.1007/978-3-642-18902-9_68.

M. N. Machida and T. Hosokawa. Evolution of protostellar outflow around low-mass protostar. *MNRAS*, 431(2):1719–1744, May 2013. doi: 10.1093/mnras/stt291.

M. N. Machida, S.-I. Inutsuka, and T. Matsumoto. Effect of Magnetic Braking on Circumstellar Disk Formation in a Strongly Magnetized Cloud. *PASJ*, 63:555, June 2011. doi: 10.1093/pasj/63.3.555.

D. Mardones, P. C. Myers, M. Tafalla, D. J. Wilner, R. Bachiller, and G. Garay. A Search for Infall Motions toward Nearby Young Stellar Objects. , 489(2):719–733, Nov. 1997. doi: 10.1086/304812.

R. D. Mathieu. The Rotation of Low-Mass Pre-Main-Sequence Stars (Invited Review). In A. Maeder and P. Eenens, editors, *Stellar Rotation*, volume 215, page 113, June 2004.

J. S. Mathis. The size distribution of interstellar particles. , 232:747–753, Sept. 1979. doi: 10.1086/157335.

M. J. Maureira, H. G. Arce, S. S. R. Offner, M. M. Dunham, J. E. Pineda, M. Fernández-López, X. Chen, and D. Mardones. A Turbulent Origin for the Complex Envelope Kinematics in the Young Low-mass Core Per-bolo 58. , 849(2):89, Nov. 2017. doi: 10.3847/1538-4357/aa91ce.

A. J. Maury, P. André, A. Men'shchikov, V. Könyves, and S. Bontemps. The formation of active protoclusters in the Aquila rift: a millimeter continuum view. *A&A*, 535:A77, Nov. 2011. doi: 10.1051/0004-6361/201117132.

A. J. Maury, P. André, S. Maret, C. Codella, F. Gueth, A. Belloche, S. Cabrit, and A. Bacmann. CALYPSO: An IRAM Plateau de Bure Survey of Class 0 Protostars. In *The Labyrinth of Star Formation*, volume 36 of *Astrophysics and Space Science Proceedings*, page 233, Jan. 2014. doi: 10.1007/978-3-319-03041-8_44.

A. J. Maury, J. M. Girart, Q. Zhang, P. Hennebelle, E. Keto, R. Rao, S. P. Lai, N. Ohashi, and M. Galametz. Magnetically regulated collapse in the B335 protostar? I. ALMA observations of the polarized dust emission. , 477(2):2760–2765, June 2018. doi: 10.1093/mnras/sty574.

A. J. Maury, P. André, L. Testi, S. Maret, A. Belloche, P. Hennebelle, S. Cabrit, C. Codella, F. Gueth, L. Podio, S. Anderl, A. Bacmann, S. Bontemps, M. Gaudel, B. Ladjelate, C. Lefèvre, B. Tabone, and B. Lefloch. Characterizing young protostellar disks with the CALYPSO IRAM-PdBI survey: large Class 0 disks are rare. *A&A*, 621:A76, Jan. 2019. doi: 10.1051/0004-6361/201833537.

J. M. Mayen-Gijon, G. Anglada, M. Osorio, L. F. Rodríguez, S. Lizano, J. F. Gómez, and C. Carrasco-González. Signatures of infall motions in the images of the molecular emission of G31.41+0.31 hot molecular core. , 437(4):3766–3775, Feb. 2014. doi: 10.1093/mnras/stt2172.

G. McCracken and P. Stott. Chapter 5 - magnetic confinement. In G. McCracken and P. Stott, editors, *Fusion (Second Edition)*, pages 45–58. Academic Press, Boston, second edition edition, 2013. ISBN 978-0-12-384656-3. doi: https://doi.org/10.1016/B978-0-12-384656-3.00005-2. URL https://www.sciencedirect.com/science/article/pii/B9780123846563000052.

C. F. McKee, P. S. Li, and R. I. Klein. Sub-Alfvénic Non-ideal MHD Turbulence Simulations with Ambipolar Diffusion. II. Comparison with Observation, Clump Properties, and Scaling to Physical Units. , 720(2):1612–1634, Sept. 2010. doi: 10.1088/0004-637X/720/2/1612.

R. R. Mellon and Z.-Y. Li. Magnetic Braking and Protostellar Disk Formation: The Ideal MHD Limit. , 681(2):1356–1376, July 2008. doi: 10.1086/587542.

R. R. Mellon and Z.-Y. Li. Magnetic Braking and Protostellar Disk Formation: Ambipolar Diffusion. , 698(1):922–927, June 2009. doi: 10.1088/0004-637X/698/1/922.

L. Mestel and J. Spitzer, L. Star formation in magnetic dust clouds. *MNRAS*, 116:503, Jan. 1956. doi: 10.1093/mnras/116.5.503.

T. J. Millar, A. Bennett, and E. Herbst. Deuterium Fractionation in Dense Interstellar Clouds. , 340:906, May 1989. doi: 10.1086/167444.

F. Motte and P. André. The circumstellar environment of low-mass protostars: A millimeter continuum mapping survey. *A&A*, 365:440–464, Jan. 2001. doi: 10.1051/0004-6361:20000072.

J. C. Mottram, E. F. van Dishoeck, M. Schmalzl, L. E. Kristensen, R. Visser, M. R. Hogerheijde, and S. Bruderer. Waterfalls around protostars. Infall motions towards Class 0/I envelopes as probed by water. , 558:A126, Oct. 2013. doi: 10.1051/0004-6361/201321828.

J. C. Mottram, E. F. van Dishoeck, L. E. Kristensen, A. Karska, I. San José-García, S. Khanna, G. J. Herczeg, P. André, S. Bontemps, S. Cabrit, M. T. Carney, M. N. Drozdovskaya, M. M. Dunham, N. J. Evans, D. Fedele, J. D. Green, D. Harsono, D. Johnstone, J. K. Jørgensen, V. Könyves, B. Nisini, M. V. Persson, M. Tafalla, R. Visser, and U. A.

Yıldız. Outflows, infall and evolution of a sample of embedded low-mass protostars. The William Herschel Line Legacy (WILL) survey. , 600:A99, Apr. 2017. doi: 10.1051/0004-6361/201628682.

P. C. Myers and E. F. Ladd. Bolometric Temperatures of Young Stellar Objects. , 413:L47, Aug. 1993. doi: 10.1086/186956.

P. C. Myers, G. A. Fuller, A. A. Goodman, and P. J. Benson. Dense Cores in Dark Clouds. VI. Shapes. , 376:561, Aug. 1991. doi: 10.1086/170305.

T. Nakano. Star Formation in Magnetic Clouds. , 494(2):587–604, Feb. 1998. doi: 10.1086/305230.

C. J. Nixon and J. E. Pringle. On the role of magnetic fields in star formation. , 67:89–96, Feb. 2019. doi: 10.1016/j.newast.2018.09.007.

C. Norman and J. Silk. Clumpy molecular clouds - A dynamic model self-consistently regulated by T Tauri star formation. *ApJ*, 238:158–174, May 1980. doi: 10.1086/157969.

K. I. Oberg. Photochemistry and astrochemistry: photochemical pathways to interstellar complex organic molecules. *arXiv e-prints*, art. arXiv:1609.03112, Sept. 2016.

S. S. R. Offner, E. J. Lee, A. A. Goodman, and H. Arce. Radiation-hydrodynamic Simulations of Protostellar Outflows: Synthetic Observations and Data Comparisons. *ApJ*, 743(1): 91, Dec. 2011. doi: 10.1088/0004-637X/743/1/91.

N. Ohashi, M. Hayashi, P. T. P. Ho, M. Momose, M. Tamura, N. Hirano, and A. I. Sargent. Rotation in the Protostellar Envelopes around IRAS 04169+2702 and IRAS 04365+2535: The Size Scale for Dynamical Collapse. , 488(1):317–329, Oct. 1997. doi: 10.1086/304685.

E. J. Opik. Stellar Associations and Supernovae. *Ir. Astron. J.*, 2:219, Dec. 1953.

Y. Osamura, H. Roberts, and E. Herbst. On the possible interconversion between pairs of deuterated isotopomers of methanol, its ion, and its protonated ion in star-forming regions. *A&A*, 421:1101–1111, July 2004. doi: 10.1051/0004-6361:20035762.

E. C. Ostriker and F. H. Shu. Magnetocentrifugally Driven Flows from Young Stars and Disks. IV. The Accretion Funnel and Dead Zone. , 447:813, July 1995. doi: 10.1086/175920.

Y. Oya, N. Sakai, Y. Watanabe, A. E. Higuchi, T. Hirota, A. López-Sepulcre, T. Sakai, Y. Aikawa, C. Ceccarelli, B. Lefloch, E. Caux, C. Vastel, C. Kahane, and S. Yamamoto. L483: Warm Carbon-chain Chemistry Source Harboring Hot Corino Activity. *ApJ*, 837 (2):174, Mar. 2017. doi: 10.3847/1538-4357/aa6300.

M. Padovani. Protostars: Forges of cosmic rays? In *Protoplanetary Disks Seen through the Eyes of New-Generation High-Resolution Instruments*, page 24, Dec. 2018. doi: 10.5281/zenodo.1892571.

M. Padovani and D. Galli. Effects of magnetic fields on the cosmic-ray ionization of molecular cloud cores. *A&A*, 530:A109, June 2011. doi: 10.1051/0004-6361/201116853.

M. Padovani and D. Galli. Cosmic-Ray Propagation in Molecular Clouds. In D. F. Torres and O. Reimer, editors, *Cosmic Rays in Star-Forming Environments*, volume 34 of *Astrophysics and Space Science Proceedings*, page 61, Jan. 2013. doi: 10.1007/978-3-642-35410-6_6.

M. Padovani, D. Galli, and A. E. Glassgold. Cosmic-ray ionization of molecular clouds. *A&A*, 501(2):619–631, July 2009. doi: 10.1051/0004-6361/200911794.

M. Padovani, A. Marcowith, P. Hennebelle, and K. Ferrière. Protostars: Forges of cosmic rays? , 590:A8, May 2016. doi: 10.1051/0004-6361/201628221.

M. Padovani, A. Marcowith, D. Galli, L. K. Hunt, and F. Fontani. The double signature of local cosmic-ray acceleration in star-forming regions. , 649:A149, May 2021. doi: 10.1051/0004-6361/202039918.

L. Pagani, M. Salez, and P. G. Wannier. The chemistry of H2D+ in cold clouds. , 258:479–488, May 1992.

L. Pagani, A. Bacmann, S. Cabrit, and C. Vastel. Depletion and low gas temperature in the L183 (=L134N) prestellar core: the N2H$\hat{+}$-N2D$^+$ tool. *A&A*, 467(1):179–186, May 2007. doi: 10.1051/0004-6361:20066670.

A. Palau, Q. Zhang, J. M. Girart, J. Liu, R. Rao, P. M. Koch, R. Estalella, H.-R. V. Chen, H. B. Liu, K. Qiu, Z.-Y. Li, L. A. Zapata, S. Bontemps, P. T. P. Ho, H. Beuther, T.-C. Ching, H. Shinnaga, and A. Ahmadi. Does the Magnetic Field Suppress Fragmentation in Massive Dense Cores? , 912(2):159, May 2021. doi: 10.3847/1538-4357/abee1e.

M. V. Penston. Dynamics of self-gravitating gaseous spheres-III. Analytical results in the free-fall of isothermal cases. , 144:425, Jan. 1969. doi: 10.1093/mnras/144.4.425.

J. E. Pineda, D. Segura-Cox, P. Caselli, N. Cunningham, B. Zhao, A. Schmiedeke, M. J. Maureira, and R. Neri. A protostellar system fed by a streamer of 10,500 au length. *Nature Astronomy*, 4:1158–1163, Jan. 2020. doi: 10.1038/s41550-020-1150-z.

R. E. Pudritz, R. Ouyed, C. Fendt, and A. Brandenburg. Disk Winds, Jets, and Outflows: Theoretical and Computational Foundations. In B. Reipurth, D. Jewitt, and K. Keil, editors, *Protostars and Planets V*, page 277, Jan. 2007.

D. Raghavan, H. A. McAlister, T. J. Henry, D. W. Latham, G. W. Marcy, B. D. Mason, D. R. Gies, R. J. White, and T. A. ten Brummelaar. A Survey of Stellar Families: Multiplicity of Solar-type Stars. , 190(1):1–42, Sept. 2010. doi: 10.1088/0067-0049/190/1/1.

J. Ramsey, P. Bjerkeli, D. Harsono, H. Calcutt, L. Kristensen, M. van der Wiel, J. Jorgensen, S. Muller, and M. Persson. Observing kinematics on AU-scales in B335 with ALMA. In *American Astronomical Society Meeting Abstracts #235*, volume 235 of *American Astronomical Society Meeting Abstracts*, page 364.16, Jan. 2020.

R. Rao, J. M. Girart, D. P. Marrone, S.-P. Lai, and S. Schnee. IRAS 16293: A "Magnetic" Tale of Two Cores. , 707(2):921–935, Dec. 2009. doi: 10.1088/0004-637X/707/2/921.

J. M. C. Rawlings, T. W. Hartquist, K. M. Menten, and D. A. Williams. Direct diagnosis of infall in collapsing protostars - I. The theoretical identification of molecular species with broad velocity distributions. , 255:471–485, Apr. 1992. doi: 10.1093/mnras/255.3.471.

E. Redaelli, F. O. Alves, F. P. Santos, and P. Caselli. Magnetic properties of the protostellar core IRAS 15398-3359. , 631:A154, Nov. 2019a. doi: 10.1051/0004-6361/201936271.

E. Redaelli, L. Bizzocchi, P. Caselli, O. Sipilä, V. Lattanzi, B. M. Giuliano, and S. Spezzano. High-sensitivity maps of molecular ions in L1544. I. Deuteration of N_2H^+ and HCO^+ and primary evidence of N_2D^+ depletion. , 629:A15, Sept. 2019b. doi: 10.1051/0004-6361/201935314.

E. Redaelli, O. Sipilä, M. Padovani, P. Caselli, D. Galli, and A. V. Ivlev. The cosmic-ray ionisation rate in the pre-stellar core L1544. , 656:A109, Dec. 2021. doi: 10.1051/0004-6361/202141776.

B. Reipurth and S. Mikkola. Formation of the widest binary stars from dynamical unfolding of triple systems. , 492(7428):221–224, Dec. 2012. doi: 10.1038/nature11662.

B. Reipurth, S. Heathcote, and F. Vrba. Star formation in Bok globules and low-mass clouds. IV. Herbig-Haro objects in B335. *A&A*, 256:225, Mar. 1992.

H. Roberts, G. A. Fuller, T. J. Millar, J. Hatchell, and J. V. Buckle. A survey of [HDCO]/[H_2CO] and [DCN]/[HCN] ratios towards low-mass protostellar cores. , 381:1026–1038, Jan. 2002. doi: 10.1051/0004-6361:20011596.

S. D. Rodgers and T. J. Millar. The chemistry of deuterium in hot molecular cores. , 280(4):1046–1054, June 1996. doi: 10.1093/mnras/280.4.1046.

S. I. Sadavoy and S. W. Stahler. Embedded binaries and their dense cores. , 469(4):3881–3900, Aug. 2017. doi: 10.1093/mnras/stx1061.

M. Saito, K. Sunada, R. Kawabe, Y. Kitamura, and N. Hirano. The Initial Conditions for Formation of Low-Mass Stars: Kinematics and Density Structure of the Protostellar Envelope in B335. , 518(1):334–345, June 1999. doi: 10.1086/307244.

N. Sakai, T. Sakai, T. Hirota, and S. Yamamoto. Abundant Carbon-Chain Molecules toward the Low-Mass Protostar IRAS 04368+2557 in L1527. *ApJ*, 672(1):371–381, Jan. 2008. doi: 10.1086/523635.

N. Sakai, T. Sakai, T. Hirota, and S. Yamamoto. Deuterated Molecules in Warm Carbon Chain Chemistry: The L1527 Case. *ApJ*, 702(2):1025–1035, Sept. 2009. doi: 10.1088/0004-637X/702/2/1025.

N. Sakai, T. Shiino, T. Hirota, T. Sakai, and S. Yamamoto. Long Carbon-chain Molecules and Their Anions in the Starless Core, Lupus-1A. *ApJL*, 718(2):L49–L52, Aug. 2010. doi: 10.1088/2041-8205/718/2/L49.

N. Sakai, Y. Oya, A. López-Sepulcre, Y. Watanabe, T. Sakai, T. Hirota, Y. Aikawa, C. Ceccarelli, B. Lefloch, E. Caux, C. Vastel, C. Kahane, and S. Yamamoto. Subarcsecond Analysis of the Infalling-Rotating Envelope around the Class I Protostar IRAS 04365+2535. *ApJL*, 820(2):L34, Apr. 2016. doi: 10.3847/2041-8205/820/2/L34.

T. Sakai, N. Sakai, K. Furuya, Y. Aikawa, T. Hirota, and S. Yamamoto. Chemical Compositions of Massive Clumps in Early Evolutionary Stages of High-Mass Star Formation. In R. Kawabe, N. Kuno, and S. Yamamoto, editors, *New Trends in Radio Astronomy in the ALMA Era: The 30th Anniversary of Nobeyama Radio Observatory*, volume 476 of *Astronomical Society of the Pacific Conference Series*, page 371, Oct. 2013.

D. A. Schleuning. Far-Infrared and Submillimeter Polarization of OMC-1: Evidence for Magnetically Regulated Star Formation. *ApJ*, 493(2):811–825, Jan. 1998. doi: 10.1086/305139.

D. M. Segura-Cox, L. W. Looney, J. J. Tobin, Z.-Y. Li, R. J. Harris, S. Sadavoy, M. M. Dunham, C. Chandler, K. Kratter, L. Pérez, and C. Melis. The VLA Nascent Disk and Multiplicity Survey of Perseus Protostars (VANDAM). V. 18 Candidate Disks around Class 0 and I Protostars in the Perseus Molecular Cloud. *ApJ*, 866(2):161, Oct. 2018. doi: 10.3847/1538-4357/aaddf3.

Y. Sekine, S. Sugita, T. Shido, T. Yamamoto, Y. Iwasawa, T. Kadono, and T. Matsui. An experimental study on Fischer-Tropsch catalysis: Implications for impact phenomena and nebular chemistry. , 41(5):715–729, May 2006. doi: 10.1111/j.1945-5100.2006.tb00987.x.

Y. L. Shirley, I. Evans, Neal J., J. M. C. Rawlings, and E. M. Gregersen. Tracing the Mass during Low-Mass Star Formation. I. Submillimeter Continuum Observations. , 131(1): 249–271, Nov. 2000. doi: 10.1086/317358.

F. H. Shu. Self-similar collapse of isothermal spheres and star formation. , 214:488–497, June 1977. doi: 10.1086/155274.

F. H. Shu and F. C. Adams. Star formation and the circumstellar matter of young stellar objects. In I. Appenzeller and C. Jordan, editors, *Circumstellar Matter*, volume 122, page 7, Jan. 1987.

F. H. Shu, F. C. Adams, and S. Lizano. Star formation in molecular clouds: observation and theory. , 25:23–81, Jan. 1987. doi: 10.1146/annurev.aa.25.090187.000323.

F. H. Shu, D. Galli, S. Lizano, and M. Cai. Gravitational Collapse of Magnetized Clouds. II. The Role of Ohmic Dissipation. *ApJ*, 647(1):382–389, Aug. 2006. doi: 10.1086/505258.

R. J. Smith, R. Shetty, A. M. Stutz, and R. S. Klessen. Line Profiles of Cores within Clusters. I. The Anatomy of a Filament. , 750(1):64, May 2012. doi: 10.1088/0004-637X/750/1/64.

R. L. Smith, K. M. Pontoppidan, and G. J. Herczeg. Observations of ^{12}C/^{13}C Fractionation In Embedded Protostars Using VLT-CRIRES. In *American Astronomical Society Meeting Abstracts #214*, volume 214 of *American Astronomical Society Meeting Abstracts*, page 422.05, May 2009.

R. L. Snell and R. B. Loren. Self-reversed CO profiles in collapsing molecular clouds. , 211: 122–127, Jan. 1977. doi: 10.1086/154909.

L. Spitzer and T. T. Arny. Physical Processes in the Interstellar Medium. *American Journal of Physics*, 46(11):1201–1201, Nov. 1978. doi: 10.1119/1.11466.

A. M. Stutz, M. Rubin, M. W. Werner, G. H. Rieke, J. H. Bieging, J. Keene, M. Kang, Y. L. Shirley, K. Y. L. Su, T. Velusamy, and D. J. Wilner. Spitzer and HHT Observations of Bok Globule B335: Isolated Star Formation Efficiency and Cloud Structure. , 687(1): 389–405, Nov. 2008. doi: 10.1086/591789.

B. Tabone, S. Cabrit, G. Pineau des Forêts, J. Ferreira, A. Gusdorf, L. Podio, E. Bianchi, E. Chapillon, C. Codella, and F. Gueth. Constraining MHD disk winds with ALMA. Apparent rotation signatures and application to HH212. *A&A*, 640:A82, Aug. 2020. doi: 10.1051/0004-6361/201834377.

M. Tafalla. Observations of Pre-Stellar Cores. In D. C. Lis, G. A. Blake, and E. Herbst, editors, *Astrochemistry: Recent Successes and Current Challenges*, volume 231, pages 17–26, Aug. 2005. doi: 10.1017/S1743921306007009.

Y.-W. Tang, P. T. P. Ho, P. M. Koch, and R. Rao. High-angular Resolution Dust Polarization Measurements: Shaped B-field Lines in the Massive Star-forming Region Orion BN/KL. *ApJ*, 717(2):1262–1273, July 2010. doi: 10.1088/0004-637X/717/2/1262.

V. Taquet, A. López-Sepulcre, C. Ceccarelli, R. Neri, C. Kahane, and S. B. Charnley. Constraining the Abundances of Complex Organics in the Inner Regions of Solar-type Protostars. *ApJ*, 804(2):81, May 2015. doi: 10.1088/0004-637X/804/2/81.

S. Terebey, F. H. Shu, and P. Cassen. The collapse of the cores of slowly rotating isothermal clouds. , 286:529–551, Nov. 1984. doi: 10.1086/162628.

J. J. Tobin, L. Hartmann, L. W. Looney, and H.-F. Chiang. Complex Structure in Class 0 Protostellar Envelopes. , 712(2):1010–1028, Apr. 2010. doi: 10.1088/0004-637X/712/2/1010.

J. J. Tobin, L. Hartmann, E. Bergin, H.-F. Chiang, L. W. Looney, C. J. Chandler, S. Maret, and F. Heitsch. Complex Structure in Class 0 Protostellar Envelopes. III. Velocity Gradients in Non-axisymmetric Envelopes, Infall, or Rotation? , 748(1):16, Mar. 2012. doi: 10.1088/0004-637X/748/1/16.

J. J. Tobin, L. Looney, Z.-Y. Li, C. J. Chandler, M. Dunham, D. Segura-Cox, S. Sadavoy, C. Melis, R. J. Harris, K. M. Kratter, and L. M. Perez. Protostellar Multiplicity in Perseus Characterized by the VLA Nascent Disk and Multiplicity (VANDAM) Survey. In *American Astronomical Society Meeting Abstracts #227*, volume 227 of *American Astronomical Society Meeting Abstracts*, page 205.03, Jan. 2016a.

J. J. Tobin, L. W. Looney, Z.-Y. Li, C. J. Chandler, M. M. Dunham, D. Segura-Cox, S. I. Sadavoy, C. Melis, R. J. Harris, K. Kratter, and L. Perez. The VLA Nascent Disk and Multiplicity Survey of Perseus Protostars (VANDAM). II. Multiplicity of Protostars in the Perseus Molecular Cloud. , 818(1):73, Feb. 2016b. doi: 10.3847/0004-637X/818/1/73.

K. Tokuda, T. Onishi, K. Saigo, A. Kawamura, Y. Fukui, T. Matsumoto, S.-i. Inutsuka, M. N. Machida, K. Tomida, and K. Tachihara. ALMA Observations of a High-density Core in Taurus: Dynamical Gas Interaction at the Possible Site of a Multiple Star Formation. , 789(1):L4, July 2014. doi: 10.1088/2041-8205/789/1/L4.

M. G. Tomasko and L. Spitzer. Heating of H I Regions by Energetic Particles. *The Astronomical Journal Supplement*, 73:37, Jan. 1968.

Y. Tsukamoto, K. Iwasaki, S. Okuzumi, M. N. Machida, and S. Inutsuka. Effects of Ohmic and ambipolar diffusion on formation and evolution of first cores, protostars, and circumstellar discs. *MNRAS*, 452(1):278–288, Sept. 2015. doi: 10.1093/mnras/stv1290.

T. Umebayashi and T. Nakano. Magnetic flux loss from interstellar clouds. *MNRAS*, 243: 103–113, Mar. 1990. doi: 10.1093/mnras/243.1.103.

J. P. Vallée. Cosmic magnetic fields - as observed in the Universe, in galactic dynamos, and in the Milky Way. , 48(10):763–841, Sept. 2004. doi: 10.1016/j.newar.2004.03.017.

N. van der Marel, L. E. Kristensen, R. Visser, J. C. Mottram, U. A. Yıldız, and E. F. van Dishoeck. Outflow forces of low-mass embedded objects in Ophiuchus: a quantitative comparison of analysis methods. *A&A*, 556:A76, Aug. 2013. doi: 10.1051/0004-6361/201220717.

E. F. van Dishoeck and J. H. Black. Comprehensive Models of Diffuse Interstellar Clouds: Physical Conditions and Molecular Abundances. *ApJS*, 62:109, Sept. 1986. doi: 10.1086/191135.

E. F. van Dishoeck and J. H. Black. The Photodissociation and Chemistry of Interstellar CO. , 334:771, Nov. 1988. doi: 10.1086/166877.

E. F. van Dishoeck, G. A. Blake, B. T. Draine, and J. I. Lunine. The Chemical Evolution of Protostellar and Protoplanetary Matter. In E. H. Levy and J. I. Lunine, editors, *Protostars and Planets III*, page 163, Jan. 1993.

M. L. van Gelder, B. Tabone, Ł. Tychoniec, E. F. van Dishoeck, H. Beuther, A. C. A. Boogert, A. Caratti o Garatti, P. D. Klaassen, H. Linnartz, H. S. P. Müller, and V. Taquet. Complex organic molecules in low-mass protostars on Solar System scales. I. Oxygen-bearing species. , 639:A87, July 2020. doi: 10.1051/0004-6361/202037758.

T. Vasyunina, A. I. Vasyunin, E. Herbst, H. Linz, M. Voronkov, T. Britton, I. Zinchenko, and F. Schuller. Organic Species in Infrared Dark Clouds. , 780(1):85, Jan. 2014. doi: 10.1088/0004-637X/780/1/85.

T. Velusamy, T. B. H. Kuiper, and W. D. Langer. CCS Observations of the Protostellar Envelope of B335. , 451:L75, Oct. 1995. doi: 10.1086/309691.

A. Verliat, P. Hennebelle, A. J. Maury, and M. Gaudel. Formation of protoplanetary disk by gravitational collapse of a non-rotating. In P. Di Matteo, O. Creevey, A. Crida, G. Kordopatis, J. Malzac, J. B. Marquette, M. N'Diaye, and O. Venot, editors, *SF2A-2019: Proceedings of the Annual meeting of the French Society of Astronomy and Astrophysics*, page Di, Dec. 2019.

A. Verliat, P. Hennebelle, A. J. Maury, and M. Gaudel. Protostellar disk formation by a nonrotating, nonaxisymmetric collapsing cloud: model and comparison with observations. *A&A*, 635:A130, Mar. 2020. doi: 10.1051/0004-6361/201936394.

R. Visser, E. F. van Dishoeck, S. D. Doty, and C. P. Dullemond. The chemical history of molecules in circumstellar disks. I. Ices. *A&A*, 495(3):881–897, Mar. 2009. doi: 10.1051/0004-6361/200810846.

R. Visser, S. D. Doty, and E. F. van Dishoeck. The chemical history of molecules in circumstellar disks. II. Gas-phase species. *A&A*, 534:A132, Oct. 2011. doi: 10.1051/0004-6361/201117249.

E. I. Vorobyov and S. Basu. Secular evolution of viscous and self-gravitating circumstellar discs. , 393(3):822–837, Mar. 2009. doi: 10.1111/j.1365-2966.2008.14376.x.

M. F. Walker. Studies of Extremely Young Clusters.VI. Spectroscopic Observations of the Ultraviolet-Excess Stars in the Orion Nebula Cluster and NGC 2264. , 175:89, July 1972. doi: 10.1086/151540.

D. Ward-Thompson, F. Motte, and P. Andre. The initial conditions of isolated star formation - III. Millimetre continuum mapping of pre-stellar cores. *MNRAS*, 305(1):143–150, May 1999. doi: 10.1046/j.1365-8711.1999.02412.x.

D. Ward-Thompson, L. Hartmann, and D. J. Nutter. Turbulence in Class 0 and I protostellar envelopes. , 357(2):687–690, Feb. 2005. doi: 10.1111/j.1365-2966.2005.08680.x.

D. M. Watson. The Distance to B335. *Research Notes of the American Astronomical Society*, 4(6):88, June 2020. doi: 10.3847/2515-5172/ab9df4.

J. C. Weingartner. On the Disalignment of Interstellar Grains. *ApJ*, 647(1):390–396, Aug. 2006. doi: 10.1086/505342.

J. C. Weingartner and B. T. Draine. Forces on Dust Grains Exposed to Anisotropic Interstellar Radiation Fields. , 553(2):581–594, June 2001. doi: 10.1086/320963.

J. C. Weingartner, B. T. Draine, and D. K. Barr. Photoelectric Emission from Dust Grains Exposed to Extreme Ultraviolet and X-Ray Radiation. *ApJ*, 645(2):1188–1197, July 2006. doi: 10.1086/504420.

T. Wilson, K. Rohlfs, and S. Huettemeister. *Tools of radioastronomy*. Springer-Verlag Berlin Heidelberg, 6 edition, 2013. doi: 10.1007/978-3-642-39950-3.

S. Wolf, R. Launhardt, and T. Henning. Magnetic Field Evolution in Bok Globules. *ApJ*, 592(1):233–244, July 2003. doi: 10.1086/375622.

S. Wolf, A. Schegerer, H. Beuther, D. L. Padgett, and K. R. Stapelfeldt. Submillimeter Structure of the Disk of the Butterfly Star. *ApJL*, 674(2):L101, Feb. 2008. doi: 10.1086/529188.

A. Wootten. Deuterated molecules in interstellar clouds. In M. S. Vardya and S. P. Tarafdar, editors, *Astrochemistry*, volume 120, pages 311–319, Jan. 1987.

A. Wootten, R. Snell, and A. E. Glassgold. The determination of electron abundances in interstellar clouds. , 234:876–880, Dec. 1979. doi: 10.1086/157569.

J. Wurster and B. T. Lewis. Non-ideal magnetohydrodynamics versus turbulence - I. Which is the dominant process in protostellar disc formation? *MNRAS*, 495(4):3795–3806, July 2020a. doi: 10.1093/mnras/staa1339.

J. Wurster and B. T. Lewis. Non-ideal magnetohydrodynamics versus turbulence II: Which is the dominant process in stellar core formation? *MNRAS*, 495(4):3807–3818, July 2020b. doi: 10.1093/mnras/staa1340.

J. Wurster, D. J. Price, and M. R. Bate. Can non-ideal magnetohydrodynamics solve the magnetic braking catastrophe? , 457(1):1037–1061, Mar. 2016. doi: 10.1093/mnras/stw013.

Y.-L. Yang, I. Evans, Neal J., A. Smith, J.-E. Lee, J. J. Tobin, S. Terebey, H. Calcutt, J. K. Jørgensen, J. D. Green, and T. L. Bourke. Constraining the Infalling Envelope Models of Embedded Protostars: BHR 71 and Its Hot Corino. *ApJ*, 891(1):61, Mar. 2020. doi: 10.3847/1538-4357/ab7201.

H.-W. Yen, S. Takakuwa, and N. Ohashi. High-Velocity Jets and Slowly Rotating Envelope in B335. , 710(2):1786–1799, Feb. 2010. doi: 10.1088/0004-637X/710/2/1786.

H.-W. Yen, S. Takakuwa, and N. Ohashi. Kinematics and Physical Conditions of the Innermost Envelope in B335. , 742(1):57, Nov. 2011. doi: 10.1088/0004-637X/742/1/57.

H.-W. Yen, S. Takakuwa, P. M. Koch, Y. Aso, S. Koyamatsu, R. Krasnopolsky, and N. Ohashi. No Keplerian Disk >10 AU Around the Protostar B335: Magnetic Braking or Young Age? , 812(2):129, Oct. 2015. doi: 10.1088/0004-637X/812/2/129.

H.-W. Yen, B. Zhao, I. T. Hsieh, P. Koch, R. Krasnopolsky, C.-F. Lee, Z.-Y. Li, S.-Y. Liu, N. Ohashi, S. Takakuwa, and Y.-W. Tang. JCMT POL-2 and ALMA Polarimetric Observations of 6000-100 au Scales in the Protostar B335: Linking Magnetic Field and Gas Kinematics in Observations and MHD Simulations. , 871(2):243, Feb. 2019. doi: 10.3847/1538-4357/aafb6c.

H.-W. Yen, B. Zhao, and P. M. Koch. Kinematics of neutral and ionzied gas in the candidate protostar with efficient magnetic braking B335. In *IAU General Assembly*, pages 120–120, Mar. 2020. doi: 10.1017/S1743921319003739.

H. Yoneda, Y. Tsukamoto, K. Furuya, and Y. Aikawa. Chemistry in a Forming Protoplanetary Disk: Main Accretion Phase. *ApJ*, 833(1):105, Dec. 2016. doi: 10.3847/1538-4357/833/1/105.

C. H. Young and I. Evans, Neal J. Evolutionary Signatures in the Formation of Low-Mass Protostars. , 627(1):293–309, July 2005. doi: 10.1086/430436.

C. H. Young, Y. L. Shirley, I. Evans, Neal J., and J. M. C. Rawlings. Tracing the Mass during Low-Mass Star Formation. IV. Observations and Modeling of the Submillimeter Continuum Emission from Class I Protostars. , 145(1):111–145, Mar. 2003. doi: 10.1086/345341.

B. Zhao, P. Caselli, Z.-Y. Li, R. Krasnopolsky, H. Shang, and F. Nakamura. Protostellar disc formation enabled by removal of small dust grains. *MNRAS*, 460(2):2050–2076, Aug. 2016. doi: 10.1093/mnras/stw1124.

B. Zhao, P. Caselli, Z.-Y. Li, and R. Krasnopolsky. Decoupling of magnetic fields in collapsing protostellar envelopes and disc formation and fragmentation. , 473(4):4868–4889, Feb. 2018. doi: 10.1093/mnras/stx2617.

S. Zhou. In Search of Evidence for Protostellar Collapse: A Systematic Study of Line Formation in Low-Mass Dense Cores. , 394:204, July 1992. doi: 10.1086/171572.

S. Zhou. Line Formation in Collapsing Cloud Cores with Rotation and Applications to B335 and IRAS 16293-2422. , 442:685, Apr. 1995. doi: 10.1086/175474.

S. Zhou, I. Evans, Neal J., H. M. Butner, M. L. Kutner, C. M. Leung, and L. G. Mundy. Testing Star Formation Theories: VLA Observations of H 2CO in the BOK Globule B335. *ApJ*, 363:168, Nov. 1990. doi: 10.1086/169327.

S. Zhou, I. Evans, Neal J., C. Koempe, and C. M. Walmsley. Evidence for Protostellar Collapse in B335. , 404:232, Feb. 1993. doi: 10.1086/172271.

N. Zielinski, S. Wolf, and R. Brunngräber. Constraining the magnetic field properties of Bok globule B335 using SOFIA/HAWC+. *A&A*, 645:A125, Jan. 2021. doi: 10.1051/0004-6361/202039126.

L. M. Ziurys, P. Friberg, and W. M. Irvine. Interstellar SiO as a Tracer of High-Temperature Chemistry. *ApJ*, 343:201, Aug. 1989. doi: 10.1086/167696.

Résumé

La formation des étoiles est un processus généralement bien compris, mais qui manque de détails et présente de nombreuses questions sans réponse. Certaines de ces questions concernent la manière dont la matière est accrétée et l'efficacité de ce processus, d'autres concernent l'évolution chimique du gaz au cours de l'évolution protostellaire et d'autres encore questionnent le rôle du champ magnétique dans ce processus. Le but de ce travail est de mettre des contraintes sur certains des processus physiques et chimiques qui se produisent dans un jeune coeur proto-stellaire au cours des premières étapes de l'effondrement, en essayant de répondre aux questions susmentionnées et sur la manière dont elles sont liées pour dicter le résultat de le processus de formation des étoiles.

Actuellement, l'un des meilleurs instruments pour observer les noyaux de formation d'étoiles est l'Atacama Large Millimeter Array, ou ALMA. Ce télescope permet d'observer des jeune coeurs qui sont noyées dans une enveloppe poussiéreuse et qui émettent une partie importante de sa luminosité dans le régime des longueurs d'onde millimétriques et submillimétriques. De plus, la technique interférométrique sur laquelle ALMA est basé, permet d'atteindre la résolution angulaire nécessaire pour étudier les objets protostellaires aux petites échelles des enveloppes internes. Par conséquent, pour mener à bien ce travail, nous avons utilisé des observations ALMA à haute résolution angulaire d'un objet protostellaire particulier, B335.

B335 est un Bok Globule isolé, qui contient une protoétoile de Classe 0 en son centre. Les objets de Classe 0 correspondent à la première étape de l'évolution protostellaire, après la formation de l'objet central. En raison de son isolement et de sa proximité relative, 164.5 pc, B335 a été largement étudié comme exemple prototypique du processus de formation d'étoiles de faible masse. Il a été utilisé comme source pour tester les théories de l'effondrement gravitationnel et a été suggéré comme un bon exemple d'effondrement magnétiquement régulé, car il présente une morphologie de champ magnétique sous forme de sablier, et aucun disque de plus de 10 au n'a été trouvé autour du l'object central. Dans le cadre du projet, nous avons obtenu des observations de l'émission thermique du continuum de poussière et l'émission de plusieurs raies moléculaires, par exemple, le CO et ses isotopologues $C^{18}O$ et $C^{17}O$, HCO^+ et ses isotopologues $H^{13}CO^+$ et DCO^+, HCN et isotopologues $H^{13}CN$, N_2D^+ et SO. Nous avons combiné les données avec différentes configurations ALMA pour permettre de sonder des échelles depuis l'enveloppe, vers 4000 au, jusqu'à la partie la plus intérieure, vers 150 au. Notre ensemble de données s'est avéré être de nature très hétérogène, ainsi que présenter une cinématique de gaz complexe, observée dans les profils de raies moléculaires.

L'objectif principal du travail était de mesurer les propriétés chimiques du gaz, telles que la fraction de deutération et d'ionisation, en utilisant DCO^+ (3-2) et $H^{13}CO^+$ (3-2) comme traceurs, et utilisez ces paramètres pour calculer l'échelle de diffusion ambipolaire, c'est-à-

dire l'échelle physique à laquelle les ions se découplent du champ magnétique, en utilisant $H^{13}CO^{+}$ (3-2) et $H^{13}CN$ (3-2). Cependant, dans nos observations d'isotopologues rares, nous avons détecté des profils de lignes à double pic. Ces profils de ligne sont normalement attribués à des lignes optiquement épaisses traçant une enveloppe qui s'effondre et peuvent être utilisés pour étudier les mouvements de chute dans les objets protostellaires. Étant donné que les molécules telles que $C^{17}O$ ou DCO^{+} sont peu abondantes, la présence de ces profils de raies dans les observations était inattendue et nécessitait une analyse plus approfondie avant de poursuivre l'objectif initial de la these. Nous avons utilisé nos observations de la transition $C^{17}O$ (1-0) pour obtenir des cartes spectrales, montrant l'évolution du profil de la raie à différents échelles de l'enveloppe par rapport au centre de la source, et avons constaté que le modèle de vitesse ne correspondent à ce que l'on attendrait d'un traceur optiquement épais dans un scénario d'effondrement sphérique symétrique. Nous avons utilisé ces faits pour étudier les mouvements de chute du gaz sur la source et modélisé les profils de ligne pour obtenir les principaux paramètres de la ligne, c'est-à-dire la vitesse, la dispersion de vitesse et l'opacité de la ligne principale. Nous avons dérivé l'opacité de la ligne en utilisant deux approches indépendantes: (i) nous avons estimé l'opacité attendue à partir de l'abondance estimée de $C^{17}O$ et avons trouvé une opacité de 0.7 et (ii) la modélisation du profil de la ligne, obtenu à partir du rapport d'intensité des différentes composantes hyperfines dans la transition $C^{17}O$ (1-0). Puisqu'il n'était pas possible de modéliser correctement les lignes en utilisant une seule composante de vitesse, en raison de l'existence des lignes à double pic, nous avons modélisé deux composantes de vitesse séparément, l'une décalée vers le bleu et l'autre décalée vers le rouge, en supposant qu'elles ne sont pas corrélées et qu'ils tracent du gaz avec des mouvements non symétriques, et obtiennent une opacité de 0.4 pour les deux composantes de vitesse. De plus, nous avons mesuré le rapport d'intensité des transitions $C^{17}O/C^{18}O$ (1-0), afin d'identifier d'éventuelles anomalies dans l'abondance de $C^{17}O$, en supposant que l'intensité est directement proportionnelle à l'abondance. Nous obtenons un rapport d'intensité qui correspond aux valeurs attendues du rapport d'abondance des deux traceurs, et concluons qu'aucun écart d'abondance n'est présent qui pourrait affecter l'opacité attendue du C17O (1-0). Pour pouvoir attribuer les deux composantes de vitesse aux mouvements de chute non symétriques, nous avons utilisé le profil de ligne de chaque composante de vitesse, obtenu avec la modélisation, et l'avons comparé au profil de ligne attendu provenant des mouvements de chute libre. Nous avons dérivé la composante thermique de la dispersion de vitesse et l'avons soustraite de la valeur totale observée pour obtenir une composante non thermique (potentiellement due aux mouvements de chute, outflows ou à la turbulence). Les valeurs de la composante non thermique, comprises entre 0.5 et 0.8 km/s, sont en accord avec celles obtenues pour les mouvements de chute libre du gaz, indiquant que les deux composantes de vitesse tracent bien des mouvements de chute. Nous avons donc proposé que les deux pics observés dans les profils de ligne proviennent de deux masses de gaz différentes avec une cinématique différente, c'est-à-dire que l'effondrement n'est pas symétrique. Nous proposons également que l'effondrement se produit le long des parois de la cavité. En effet, dans ces régions, le champ magnétique est parallèle aux mouvements de chute et offre moins de résistance au gaz qui s'écoule.

Étant donné que les profils à double pic étaient également présents dans les autres dérivés du CO que nous voulions utiliser pour notre analyse, c'est-à-dire DCO^{+} (3-2) et $H^{13}CO^{+}$ (3-2), et puisque DCO^{+} ne devrait pas être optiquement épais, nous avons supposé que les profils de ligne à double pic proviennent également de mouvements de chute non symétriques et nous avons poursuivi l'analyse de l'ionisation et le champ magnétique pour les deux composantes de vitesse séparément. Nous notons que dans ce cas, des effets tels que le filtrage des émissions à grande échelle et les mouvements de sortie du gaz ne peuvent pas être écartés de nos observations, puisque nous avons trouvé quelques indications de ceux-ci dans les cartes spectrales, c'est-à-dire une émission négative et une troisième composante de vitesse supplémentaire près de la cavité de sortie du gaz. Nous avons modélisé les profils de ligne de la même manière que nous l'avons fait pour $C^{17}O$ et avons obtenu des cartes pour la vitesse maximale et la dispersion de la vitesse. Étant donné que ni DCO^+ (3-2) ni $H^{13}CO^+$ (3-2) n'ont une structure hyperfine résolue, l'opacité des lignes n'a pas pu être obtenue à partir de la modélisation du profil de ligne. Nous avons calculé la fraction de deutération, [D]/[H], comme le rapport de densité de colonne de $DCO^+/H^{13}CO^+$, en supposant que l'abondance est directement proportionnelle à la densité de colonne, et en tenant compte du rapport de fractionnement de ^{13}C à ^{12}C ($f_{12C/13C}$ = 43). Dans la région externe de l'émission, nous avons obtenu des valeurs de deutération typiques des coeurs pré-stellaires ([D]/[H] $>$ 0.01). Étant donné que les valeurs de deutération, qui sont fixées pendant la phase pré-stellaire, peuvent durer 10^4 - 10^6 yr, la détection de ces valeurs est en accord avec l'âge de B335, estimé avec des mesures d'écoulement à 3×10^4 yr. Cependant, nous constatons que la région centrale et la partie nord de la source ont des valeurs de deutération plus faibles ([D]/[H] $<$ 0.01). Au cours de l'évolution protostellaire, les valeurs de la fraction de deutération devraient diminuer en raison de l'augmentation de la température et du rayonnement qui évaporent les molécules neutres en phase gazeuse, qui à leur tour détruiront les molécules deutérées. Par conséquent, la diminution des valeurs initiales de deutération peut être considérée comme la destruction locale des molécules deutérées au cours de la phase de Classe 0. Cette diminution peut également être observée dans nos cartes N_2D^+ (3-2), où les zones à faible taux de deutération ne présentent pas émission de N_2D^+.

À partir des valeurs de deutération, nous avons obtenu des cartes de la fraction d'ionisation, χ_e, en utilisant la méthode de Caselli et. al., 1998, et en supposant un facteur d'appauvrissement en C et O de 3. Dans la région centrale et la partie nord, nous avons obtenu de large valeurs de la fraction d'ionisation ($\chi_e > 10^{-6}$) et qui se situent dans la gamme supérieure dérivée pour les sources protostellaires. Afin d'évaluer la relation entre la fraction d'ionisation et le niveau de couplage du gaz avec le champ magnétique, nous avons comparé nos cartes de la fraction d'ionisation avec les cartes d'émission de poussières polarisées de B335 présentées dans Maury et. al., 2018, qui montre la morphologie du champ magnétique. Nous avons trouvé une bonne corrélation entre les régions d'haute d'ionisation et celles fortement polarisées. Nous considérons ce résultat comme une indication d'un bon couplage entre le gaz et le champ magnétique, puisque le gaz hautement ionisé se trouve préférentiellement là où le champ magnétique est bien organisé. Nous proposons deux origines pour la fraction d'ionisation de la source: (i) l'accélération des rayons cosmiques (CR) le long des lignes de champ magnétique. Lorsque des particules chargées à haute énergie provenant du milieu interstellaire (ISM) pénètrent dans le gaz, elles se déplacent en suivant de près les lignes de champ magnétique, ce qui augmente la probabilité de collisions ionisantes entre les CR et les particules de gaz et pourrait augmenter la fraction d'ionisation dans les régions à champ magnétique organisé. Cet effet pourrait produire la fraction d'ionisation observée dans la région nord de la source. (ii) À des densités élevées et lorsque le champ magnétique est fortement pincé, la propagation des CR le long des lignes de champ magnétique est supprimée et l'ionisation CR du milieu diminue. Par conséquent, les niveaux élevés d'ionisation que nous avons observés au centre de la source proviennent nécessairement d'autres effets. Nous proposons que ces niveaux d'ionisation soient produits par des chocs d'accrétion produits à proximité de la protoétoile, à mesure que la matière s'accumule dans l'objet central.

Enfin, nous avons tenté pour la première fois la dérivation de l'échelle de diffusion ambipolaire dans un objet protostellaire de Classe 0, en utilisant la méthode présentée dans Li & Houde, 2008. Nous avons d'abord tenté cette procédure en utilisant nos observations de $H^{13}CO^+$ (3-2) et $H^{13}CN$ (3-2). Car nos observations ne contenaient que des données à grande échelle ($\sim$ 3000 au), nous avons donc obtenu des données supplémentaires de l'archive ALMA du $H^{13}CO^+$ (3-2) et du $H^{13}CN$ (4-3) à petite échelle ($\sim$ 400-1000 au). Cependant, les données obtenues pour $H^{13}CN$ (4-3) présentaient un spectre très large et les deux composantes de vitesse n'étaient pas distinguables. Par conséquent, nous avons décidé d'utiliser à la place nos observations de $H^{13}CO^+$ (1-0) et du $C^{17}O$ (1-0) précédemment analysé. Afin d'obtenir des données à différentes échelles, nous avons lissé les données d'origine à 5 échelles de longueur croissantes supplémentaires. Nous modélisons les profils de raies pour les deux traceurs, les deux composantes de vitesse et à toutes les échelles considérées, et obtenons les valeurs de la dispersion de vitesse pour une région autour de la source de 411×1645 au, située le long du plan équatorial de la source (perpendiculaire à la direction d'écoulement), pour éviter les effets d'écoulement dans les profils de ligne. Nous avons pu observer qu'à toutes les échelles de longueur, la plage des valeurs de la dispersion de vitesse pour la molécule neutre, $C^{17}O$, était toujours plus grande que celles de l'ion, $H^{13}CO^+$. Cette situation serait attendue si les ions sont couplés au champ magnétique et souffrent moins d'autres processus, tels que la turbulence, que les molécules neutres. Par conséquent, nous considérons ce résultat comme une indication supplémentaire d'un bon couplage entre le gaz et le champ magnétique. À partir des dispersions de vitesse dans la région équatoriale, nous avons obtenu la dispersion de vitesse minimale, qui devrait être celle qui souffre le moins des effets de turbulence. D'après Li & Houde, 2008, la dispersion de vitesse minimale devrait augmenter différemment avec l'échelle de longueur pour les molecules ioniseeé et les neutres, suivant une loi de type Kolmogorov, et permettant de dériver l'échelle de diffusion ambipolaire à partir de l'ajustement de la dispersion de vitesse minimale à différentes échelles. Cependant, nous n'avons pas observé cette tendance sur la dispersion de vitesse minimale des traceurs, ce qui nous a empêchés de dériver l'échelle de diffusion ambipolaire. Nous proposons deux hypothèses pour expliquer pourquoi nous n'avons pas pu observer cette tendance: (i) notre gamme d'échelles est trop petite et la diffusion ambipolaire a le même effet dans la dispersion de vitesse sur toutes les échelles, et (ii) notre milieu est dominé par les mouvements gravitationnels et la l'évolution de la dispersion de vitesse avec l'échelle ne suit pas la loi de type Kolmogorov attendue. Il s'agit d'une hypothèse raisonnable puisque le modèle a été utilisé dans la littérature pour des mesures dans des nuages moleculaires, qui peuvent être dominés par des processus de turbulence, mais nous l'appliquons à une source où les mouvements de chute dominent les profils de raies. De plus, B335 a été suggéré comme source de classe 0 avec de faibles niveaux de turbulence, rendant encore plus difficile l'application du modèle à notre source.

En résumé, nous obtenons trois résultats principaux dans ce travail, avec des implications importantes pour la vision des mouvements de chute et du rôle du champ magnétique dans le processus de formation des étoiles : (i) nous avons obtenu la preuve d'un effondrement non symétrique à des échelles de ~ 400 à 800 au, (ii) nous avons obtenu des valeurs élevées de la fraction d'ionisation et observé une corrélation provisoire avec la morphologie du champ magnétique, et (iii) nous avons observé une différence significative entre les plages de valeurs de largeur de raie des molécules neutres et ioniques, qui suggèrent un bon couplage du gaz au champ magnétique. Finalement, une meilleure vision de l'interaction entre le gaz et le champ magnétique est obtenue, suggérant un bon couplage des deux et indiquant que l'effondrement dans B335 est fortement régulé magnétiquement.